



**Novel Hardware Systems and Signal Processing Techniques for
Propagation Measurement in IoT, Microwave and mmWave
Channels**

Edward Andrew Ball

A thesis by publication submitted in partial fulfilment of the requirements for the degree of
Doctor of Philosophy

The University of Sheffield
Faculty of Engineering
School of Electrical and Electronic Engineering.
Communications Research Group.

September 2024

Dedication

I dedicate this Thesis to the following people, who are sadly now are no longer here.

Firstly, to my late mother Lilian Joan Ball and father Alfred Ball for the love, support, and freedom to do what I wanted in life and their own sacrifices.

Also, in memory of the late Dennis and Anne Lowe for their encouragement of all my practical interests in childhood and for the supply of *Everyday Electronics* magazines and many salvaged electronic parts.

Finally, in memory of the late Harold Westwell for the many gifts of old radio bits just as they were needed in my numerous teenage amateur radio projects.

Acknowledgement

From a young age electronics, and in particular radio electronics, has always been my vocation and passion. However, many people have helped me on my way over the years, especially as it became a professional career.

Thanks go to all my colleagues at Cambridge Consultants Ltd, Tunstall Healthcare Ltd and The University of Sheffield for the chance to work on inspiring projects that have defined many key epochs in my life. Thanks go to my undergraduate, postgraduate and research students for opening a new door for me in passing knowledge on and helping them develop - and the pleasure that has been for me.

I thank The Communications Research Group here at Sheffield for welcoming me in 2015 and the various rich collaborations that have emerged. Special thanks go to Professor Alan Tennant for his friendly support and guidance, both in our research collaborations and his encouragement of me writing this Thesis.

And finally, thanks to Stephen Wan for all our years together and putting up with our house being full of radios and electronics paraphernalia.

Part of the research activity described in this Thesis emerged during a period I was funded by UKRI, grant number MRT043164/1 and I thank them for their support.

Abstract

Wireless communication systems rely on the radio channel. The characteristics of each channel define the limiting performance of the communications system, and so must be understood. This requires accurate measurement equipment to *sound* the channel in representative scenarios. *Channel Sounders* are themselves radio systems, thus benefitting from advances in RF engineering and signal processing.

This *thesis by publication* encompasses six novel, relevant, published works: contributing three portable channel sounders with field test results, and three RF systems applicable in sounders.

High performance, portable sounders for VHF / UHF and 28 GHz are created and subsequently used in novel use cases to elicit new channel propagation models. The VHF / UHF sounder had a measurement floor of -130 dBm. In suburban settings, it showed channel reflection delays did not exceed 1 μ s over 4 km. The 28 GHz sounder had a path loss measurement capability of 139 dB, and over 1km identified that near-ground, line-of-sight, path losses approximate free space.

Predicting the RF performance and power efficiency of downconversion mixers is vital in system design. A novel technique to predict the relationship between DC bias and local oscillator power is identified and related to RF mixer gain and linearity. The techniques predict conversion gain within 2.5 dB of measured PCB results at 26 GHz.

Three new works contribute to Time Modulated Arrays (TMAs). Cancellation of a non-steerable beam is the contribution of one work: achieving measured array gains within 1 dB of theory at 5.8 GHz. A receiving TMA is also created, uncovering a novel technique to combine TMA beam steering and subsampling— named the Subsampling TMA (STMA), with measured array gain within circa 2 dB of prediction. Finally, a 5.8 GHz channel sounder using a transmitting TMA is introduced - using a new signal processing approach enabling concurrent, time aligned, angle of departure channel measurements. The sounder measurement floor was -120 dBm.

TABLE OF CONTENTS

Abstract.....	iv
List of Figures	vii
List of Tables	ix
List of Publications	x
Declaration.....	xii
Glossary.....	xiii
1. Introduction	1
1. 1. Structure of Thesis	2
1. 2. The Need for Channel Sounding	2
1. 3. Channel Impulse Response	4
1. 4. Path Loss	4
1. 5. Fading.....	5
1. 6. Power Delay Profile and Delay Spread.....	5
1. 7. Coherence BW.....	6
1. 8. Angular Spread.....	6
1. 8. 1. Angle of Departure / Direction of Departure.....	7
1. 8. 2. Angle of Arrival / Direction of Arrival.....	7
1. 8. 3. Angular Spread	7
1. 9. Ricean K factor	7
1. 10. Channel Sounder Verification and Calibration.....	8
2. Channel Sounding Use Cases	9
2. 1. IoT Sounding.....	9
2. 2. Microwave Sounding.....	10
2. 3. mmWave Sounding	11
3. Channel Sounder Hardware, Algorithms and Existing Methods.....	14
3. 1. VNA Based Sounders.....	14
3. 2. Sounders Using RF Signal Generator + Oscilloscope / Spectrum Analyser or SDRs.....	15
3. 3. Bespoke Sounder Systems Incorporating SDR	16
3. 3. 1. Illustrative Architecture for a Bespoke Sounder Based on SDR	17
4. Linking of Published Papers to Thesis Research Theme	20
4. 1. Paper 1 – Portable VHF / UHF IoT Sounder.....	21
4. 2. Paper 2 – TMA C0 Canceller and Beam Steering	22
4. 2. 1. Approaches to Channel Sounding with Arrays.....	22
4. 3. Paper 3 – Analysis of 26 GHz Downconversion Mixer Design.....	23

4. 3. 1. Consideration of RX Mixers in a mmWave MIMO Sounder Application.....	23
4. 3. 2. Recent Works in Mixer Technology Applicable to Channel Sounders	25
4. 4. Paper 4 – 28 GHz Portable Channel Sounder and Close to Ground Sounding Usage	26
4. 4. 1. Frongoch Farm and National Spectrum Centre Tests	27
4. 5. Paper 5 – RX Subsampling TMA Concept and Prototype.....	32
4. 5. 1. STMA for use in Angle of Arrival Sounding RX	33
4. 6. Paper 6 – TX TMA Channel Sounder for Angle of Departure Soundings	33
4. 6. 1. AoD Angular Spread Measurement from the TX TMA Sounder	42
5. Paper 1 – Portable VHF / UHF IoT Sounder	45
6. Paper 2 – TMA C0 Cancellor and Beam Steering	60
7. Paper 3 – Analysis of 26 GHz Downconversion Mixer Design	73
8. Paper 4 – 28 GHz Portable Channel Sounder and Close to Ground Usage.....	95
9. Paper 5 – RX Subsampling TMA Prototype	108
10. Paper 6 – TX TMA Channel Sounder	124
11. Conclusion.....	130
11. 1. Paper 1 – Portable VHF / UHF IoT Sounder.....	130
11. 2. Paper 2 – TMA C0 Cancellor and Beam Steering	131
11. 3. Paper 3 – Analysis of 26 GHz Downconversion Mixer Design	131
11. 4. Paper 4 – 28 GHz Portable Channel Sounder and Close to Ground Usage.....	132
11. 5. Paper 5 – RX Subsampling TMA Prototype	132
11. 6. Paper 6 – TX TMA Channel Sounder	133
12. Recommendations for Future Work	135
12. 1. Recommendations per Paper	135
12. 1. 1. Paper 1 – Portable VHF / UHF IoT Sounder.....	135
12. 1. 2. Joint Consideration of Paper 2 and Paper 6 – TMA C0 Cancellor and Beam Steering / TX TMA Channel Sounder	135
12. 1. 3. Paper 3 – Analysis of 26 GHz Downconversion Mixer Design.....	135
12. 1. 4. Paper 4 – 28 GHz Portable Channel Sounder and Close to Ground Usage.....	136
12. 1. 5. Paper 5 – RX Subsampling TMA Prototype	136
12. 2. New Sounder Concept Areas	137
12. 2. 1. Joint Sounding and User Traffic	137
12. 2. 2. Sounders Operating At and Above mmWave Bands	137
12. 2. 3. Joint TX TMA and RX TMA Sounder Concept.....	137
13. References Additional to those of the Published Papers	141

List of Figures

FIGURE 1. 5G AND 6G MOBILE SPECTRUM [26].	2
FIGURE 2. EXAMPLES OF DIFFERENT REAL-WORLD RADIO CHANNEL SCENARIOS [IMAGES FROM PICKPIK, WIKIMEDIA, PEXELS, PIXABAY].	3
FIGURE 3. AN EXAMPLE MICROWAVE SOUNDER TX ARCHITECTURE.	17
FIGURE 4. AN EXAMPLE MICROWAVE SOUNDER RX ARCHITECTURE.	18
FIGURE 5. AN EXAMPLE MMWAVE SOUNDER TX ARCHITECTURE.	18
FIGURE 6. AN EXAMPLE MMWAVE SOUNDER RX ARCHITECTURE.	18
FIGURE 7. EXAMPLE 16 ELEMENT RX MIMO SYSTEM.	24
FIGURE 8. 16 WAY LO POWER SPLITTER USING CASCADES OF WILKINSON 3 DB SPLITTERS.	25
FIGURE 9. PROPAGATION TEST SITE ROUTES A, B, C, D, E, F, G, H, N AT THE NATIONAL SPECTRUM CENTRE, FRONGOCH FARM, ABERYSTWYTH [GOOGLE MAPS: MAP DATA ©2023 GOOGLE]. TX AND RX SYSTEMS TOGETHER SOUND 1 ROUTE.	27
FIGURE 10. ONE OF THE SOUNDER SYSTEMS IN A CART (ROUTE A). THE 28 GHZ HORN ANTENNA CAN BE SEEN IN STAND ON LEFT OF CART.	28
FIGURE 11. PROPAGATION SOUNDING AROUND THE EDGE OF A FARM DWELLING (ROUTE B).	28
FIGURE 12. PROPAGATION MEASUREMENT ALONG A ROAD AND INTO A WOOD (ROUTE C).	28
FIGURE 13. PROPAGATION GRAZING THE TOP OF TALL GRASSES (ROUTE D).	29
FIGURE 14. PROPAGATION OVER A BANK - TOWARDS A COW SHED (ROUTE E).	29
FIGURE 15. PROPAGATION IN PRESENCE OF METAL BUILDINGS (ROUTE H).	29
FIGURE 16. PROPAGATION THROUGH A WOODED SCRUB AREA (ROUTE N) – RX SITE.	30
FIGURE 17. PROPAGATION THROUGH A WOODED SCRUB AREA (ROUTE N) – TX SITE. RX SYSTEM IS ON THE OTHER SIDE OF WOOD. BOTH TX AND RX START NEAR THE GATE ON THE LEFT AND ARE MOVED AWAY FROM EACH OTHER TO INCREASE THE PATH LENGTH THROUGH THE WOOD.	30
FIGURE 18. ROUTE B MEASURED PROPAGATION DATA AND FITTED MODEL. (ROUTE B IS 178 M IN TOTAL LENGTH AND AROUND THE SIDE OF FARM BUILDINGS, ON A ROUGH ROAD).	31
FIGURE 19. ROUTE E MEASURED PROPAGATION DATA AND FITTED MODEL. (ROUTE E IS 240 M IN TOTAL LENGTH AND THROUGH AN OPEN, CLIPPED GRASSY FIELD, RISING UP TO A BROW AND THEN DESCENDING AGAIN BEHIND IT).	31
FIGURE 20. ROUTE N MEASURED PROPAGATION DATA AND FITTED MODEL. (ROUTE N IS 99 M IN TOTAL RADIO PATH LENGTH, THROUGH A WOODED SCRUB AREA).	32
FIGURE 21. AN RX TMA (E.G. STMA) CONVERTS FROM A CARRIER (C0 BORESIGHT BEAM AT CARRIER) TO A SET OF HARMONIC BEAMS, EACH CENTRED AT AN ANGLE OF ARRIVAL FOR THAT BEAM.	33
FIGURE 22. TMA SWITCH CONTROL – EXAMPLE FOR AN 8-ELEMENT ARRAY FOR USE IN TX SOUNDER.	34
FIGURE 23. TX TMA SIMULATION OF HARMONIC BEAM ANGULAR POSITIONS FOR A 6-ELEMENT ARRAY.	35
FIGURE 24. TX TMA SIMULATION OF HARMONIC BEAM ANGULAR POSITIONS FOR AN 8-ELEMENT ARRAY.	35
FIGURE 25. TX TMA SIMULATION OF HARMONIC BEAM ANGULAR POSITIONS FOR A 16-ELEMENT ARRAY.	35
FIGURE 26. PRBS MODULATED SIGNAL USED IN CHANNEL SOUNDING - AS APPLIED TO TMA INPUT.	36
FIGURE 27. TMA SPECTRAL EMISSION WITH CW CARRIER APPLIED – NOTE THE EXPECTED HARMONIC BEAM SPACING OF 1 MHZ.	36
FIGURE 28. TMA SPECTRAL EMISSION WITH PRBS MODULATED CARRIER APPLIED - ILLUSTRATIVE EXAMPLES FOR 2 DIFFERENT RX ANTENNA LOCATIONS SHOWING THE DIFFERENCE IN RX BEAM POWERS THAT WOULD REPRESENT AOD POWERS.	37
FIGURE 29. EXAMPLE SIMULATION OF EXTRACTED BEAM DELAYS AND POWERS SHOWING EACH BEAM HAS BEEN UNIQUELY RESOLVED. (HERE THE APPLIED SIGNAL WAS A 10 μ S INCREMENTAL PATH DELAY AND 2 DB INCREMENTAL PATH ATTENUATION.)	38
FIGURE 30. EXAMPLE SIMULATION OF EXTRACTED C0 BEAM DELAY.	38
FIGURE 31. EXAMPLE SIMULATION OF EXTRACTED C1P BEAM DELAY.	39
FIGURE 32. EXAMPLE SIMULATION OF EXTRACTED C1N BEAM DELAY.	39
FIGURE 33. EXAMPLE SIMULATION OF EXTRACTED C2P BEAM DELAY.	40
FIGURE 34. EXAMPLE SIMULATION OF EXTRACTED C2N BEAM DELAY.	40

FIGURE 35. EXAMPLE SIMULATION OF EXTRACTED C3P BEAM DELAY.	41
FIGURE 36. EXAMPLE SIMULATION OF EXTRACTED C3N BEAM DELAY.....	41
FIGURE 37. EXAMPLE TEST SITES FROM CAFÉ SCENARIO (LEFT) AND CORRIDOR SCENARIO (RIGHT), AS SEEN FROM EXAMPLE RX SDR LOCATIONS.	42
FIGURE 38. CALCULATED RMS AS FOR CAFÉ SCENARIO (TX ARRAY ROTATED IN STEPS FOR EACH TMA RUN, CONSTANT DISTANCE TO RX).....	43
FIGURE 39. CALCULATED RMS AS FOR CORRIDOR SCENARIO (TX ARRAY POINTED AT RX AND ONLY DISTANCE IS VARIED).	43
FIGURE 40. JOINT TX AND RX TMA SOUNDER CONCEPT.	138
FIGURE 41. JOINT TX AND RX TMA SOUNDER - RECOVERED SPECTRUM SHOWING HOW ALL THE POSSIBLE TX TMA BEAMS ARE RECEIVED IN EACH RX TMA BEAM (IF A REFLECTIVE PATH EXISTS TO SUPPORT EVERY REFLECTION).	138
FIGURE 42. SINGLE REFLECTION EXAMPLE.....	139
FIGURE 43. DOUBLE REFLECTION EXAMPLE.	139
FIGURE 44. RESOLVED RX TMA SPECTRUM SHOWING SINGLE REFLECTION SPECTRAL LOCATION - HENCE VIABLE TX AND RX BEAMS CAN BE IDENTIFIED.	140
FIGURE 45. RESOLVED RX TMA SPECTRUM SHOWING DOUBLE REFLECTION SPECTRAL LOCATION - HENCE VIABLE TX AND RX BEAMS CAN BE IDENTIFIED.	140

List of Tables

TABLE 1. OVERVIEW OF THE 6 PAPERS IN THIS THESIS.	21
TABLE 2. TMA AOD TEST SIMULATION SETTINGS.....	37

List of Publications

Below are the 6 papers (5 journal articles and 1 international IEEE conference paper) that form the core of this Thesis by Publication. Some of the papers have shared authorship, however I am the researcher and perform the scientific work and write-up in all cases. *For clarity, the contribution of my co-authors is stated for each paper below, where appropriate.*

Paper 1 [1] E. A. Ball, “Design and field trial measurement results for a portable and low-cost very-high-frequency / ultra-high-frequency channel sounder platform for Internet of things propagation research,” IET Microwaves, Antennas and Propagation, vol. 13, no. 6, pp. 714–724, May 2019. DOI <https://doi.org/10.1049/iet-map.2018.5827>. *I am sole author of this paper.*

Paper 2 [2] E. A. Ball and A. Tennant, “A Technique to Control the Harmonic Levels in Time-Modulated Antenna Arrays - Theoretical Concept and Hardware Verification Platform,” IEEE Transactions on Antennas & Propagation, vol. 68, no. 7, pp. 5375–5386, Jul. 2020. DOI <https://doi.org/10.1109/TAP.2020.2978894>. *I devised the research concept, conducted the research, created the prototypes, performed and led the lab tests, analysis and write-up. My co-author assisted in certain lab tests, discussions, reviewing and editing of the paper.*

Paper 3 [3] E. A. Ball, “Predicting the Performance of a 26 GHz Transconductance Modulated Downconversion Mixer as a Function of LO Drive and DC Bias,” Electronics (Switzerland), vol. 11, no. 16, Aug. 2022. DOI <https://doi.org/10.3390/electronics11162516>. *I am sole author of this paper.*

Paper 4 [4] E. A. Ball and S. D. Joseph, “A Portable 28-GHz Channel Sounder Platform and Measurement Results from Close-to-Ground Field Tests,” IEEE Open Journal of Instrumentation and Measurement, vol. 2, pp. 1–11, Mar. 2023. DOI <https://doi.org/10.1109/OJIM.2023.3259025>. *I devised the research concept, conducted the research, created the prototypes, performed and led the lab and field tests, analysis and write-up. My co-author assisted in discussions, reviewing and editing of the paper.*

Paper 5 [5] E. A. Ball, S. D. Joseph, and A. Tennant, “Receive Mode Time Modulated Antenna Array Incorporating Subsampling -Theoretical Concept and Laboratory Investigation,” IEEE Open Journal of Antennas and Propagation, 2023. DOI <https://doi.org/10.1109/OJAP.2023.3293123>. *I devised the research concept, conducted the research, created the prototypes, performed and led the lab tests and analysis and write-up. My co-authors assisted in certain lab tests, discussions, reviewing and editing of the paper.*

Paper 6 [6] E. A. Ball and S. David Joseph, “The Time Modulated Array for Channel Sounding Measurements – Concept and Initial Field Tests,” in Proceedings of 18th European Conference on Antennas and Propagation (EuCAP), Glasgow: IEEE, Mar. 2024, pp. 1371–1375. DOI <https://doi.org/10.23919/EuCAP60739.2024.10500956>. *I devised the research concept, conducted the research, created the prototypes, performed and led the lab tests, analysis and write-up. My co-authors assisted in discussions, reviewing and editing of the paper.*

Below are a set of *associated* publications in which I was involved, both in the research and as a co-author. They emerged during the Thesis research period, but are not submitted as part of this *thesis by publication*: -

- A journal article [7] reporting further measurement results from a new rural 28 GHz propagation sounding field test, using the sounder system developed in Paper 4.
- A conference paper [8] reporting further testing of the beam steering capability of the STMA system created and described in Paper 5.

- A conference paper [9] reporting initial lab results of a 73 GHz MMIC chip I designed, to be used in a 73 GHz TX TMA system demonstrator.

Declaration

I, the author, confirm that the Thesis is my own work. I am aware of the University's Guidance on the Use of Unfair Means (www.sheffield.ac.uk/ssid/unfair-means). This work has not been previously been presented for an award at this, or any other, university.

Glossary

AoA – Angle of Arrival

AoD – Angle of Departure

ACG – Array Control Gain

AS – Angular Spread

ADC – Analogue to Digital Converter

BJT – Bipolar Junction Transistor

BER – Bit Error Rate

BW - Bandwidth

BPF – Band Pass Filter

BPSK – Binary Phase Shift Keying

CBW – Coherence BW

DS – Delay Spread

DoD - Direction of Departure

DoA - Direction of Arrival

ETSI – European Telecommunications Standards Institute

EVM – Error Vector Magnitude

FSPL – Free Space Path Loss

Fp – TMA frame frequency (frequency at which the switching pattern repeats)

F_T – Transistor transition frequency (current gain = 1)

FCC – Federal Communications Commission

FET – Field Effect Transistor

HW – Hardware

ISM – Industrial Scientific Medical

ITU - International Telecommunication Union

IL – insertion Loss

IP1dB – Input 1dB compression point

InP – Indium Phosphide

LoS – Line of Sight

LNA – Low Noise Amplifier

MIMO – Multiple Input Multiple Output

MMIC – Microwave Monolithic Integrated Circuit

MPC – Multipath Components
NLoS – Non Line of Sight
NF – Noise Figure
NSC – National Spectrum Centre
OFDM – Orthogonal Frequency Division Multiplexing
PL – Path Loss
PRBS – Pseudo Random Binary Sequence
PN – Pseudo Noise
PDP – Power Delay Profile
pHEMT – Pseudomorphic High Electron Mobility Transistor
RX – Receiver
R_c – PRBS chip rate
SRD – Short Range Device
STMA – Subsampling Time Modulated Array
SDR – Software Defined Radio
SiGe – Silicon Germanium (transistor)
SW – Software
SNR – Signal to Noise Ratio
SPI – Serial Peripheral Interface
SLL – Side Lobe Level
TMA – Time Modulated Array
TX - Transmitter
ULA – Uniform Linear Array
VNA – Vector Network Analyser

1. Introduction

Over his professional career, the author has been fortunate to be involved in, or lead, the design of some challenging and fascinating RF hardware and radio systems. One common link between these various systems has been their need to be optimised for the available radio channel. Sometimes this has been for in-building systems, with many reflections. For other systems this has been outdoors, with few reflections.

To get the best from a radio system requires it to be optimised for the available channel. This requires accurate measurements of the channel, in the use-cases that will represent its intended deployment. The measurement of the channel response can be considered in simple terms of time domain (reflections) and frequency domain (usable bandwidth, spectral shape). However, the measurement of the associated parameters is far from trivial, often requiring either expensive lab equipment or the creation of complex, bespoke equipment.

In the research presented in this thesis and associated published papers, activities are presented on channel sounding hardware and supporting algorithms. This includes using the systems to perform measurements in the field. The full sounder systems described range from VHF/UHF to 28 GHz mmWave. In addition, hardware research for RF circuits and systems that have a more general application but can also be used in channel sounders are presented. How these systems could be used in channel sounders is discussed.

Modern society depends on radio systems more than ever. By the end of 2022 there were 1.3 billion predicted 5G connections across the globe [10]. However, the world is still not fully connected, and it is estimated that a third of the population are not yet connected to the internet, though as of late 2022 an estimated 5.3 billion people are using the internet [11]. This illustrates that much future growth in radio communications can still be expected.

Although spectrum is a finite resource, there seems to be a constant requirement to move services to new bands or repurpose familiar spectrum. An example is the recent emergence of cellular operator interest in 5G ‘mid bands’ (3.5 GHz – 6 GHz) and 6G ‘upper/mid bands’ (7 GHz – 24 GHz). Since the usage of the spectrum changes and so do the use cases then the channel models will also change.

5G technology has allowed operators and manufacturers to explore new scenarios, enabled by the now practical RF hardware that was not available until recent years. An example is the active research and trials in non-terrestrial networks [12]. LEO and GEO earth-space links have been studied for many years, but rarely before today for use cases involving mobile devices with small antennas.

Radio communication spectrum usage is also now extending up into mmWave frequencies (circa 30 GHz and upwards) and up into sub-THz frequencies (circa 100-300 GHz). A recent example of such usage demonstrated a D band link from a mobile phone sized prototype over 200 m and providing 2 Gbit/s link [10]. Many 5G mobile phones already have mmWave radio capability (circa 24-28 GHz or 39 GHz) and can be used on some commercial networks [11].

Good and accurate channel models enable realistic link budgets to be planned. This in turn can allow lowest possible TX powers for a use case and required performance, so leading to power efficient systems. As carrier frequencies increase this becomes increasingly important for the health and safety of the user who is exposed to the RF power. There have been attempts to model the safe thermal limits for RF exposure for some time, though only more recently has this been studied at mmWave [13]. Indeed, recent research is finding that even what was previously thought to be a safe level of exposure may still be high enough to potentially lead to biological effects [14].

The emergence of 6G as the successor to currently deployed 5G cellular systems has brought forward many new use cases, requiring research and new radio system development [15], [16], [17], [18], [19], [20].

This includes a new paradigm of joint communication and sensing [21], representing a very different set of potential propagation use cases. Link budget prediction in mmWave bands is now more practical than only a few years ago thanks to measurement campaigns and the resulting standards and recommendations [22], [23], [24].

In the future, radio systems using the THz bands are envisioned for mobile 6G communications over short links [25], [26]. Novel concepts allowing the THz communications to also be used to monitor the environment by examining the changes in absorption during communications use have been suggested [27]. The spectrum being considered for future enhancements to 5G and new 6G systems is shown in Figure 1 [26].

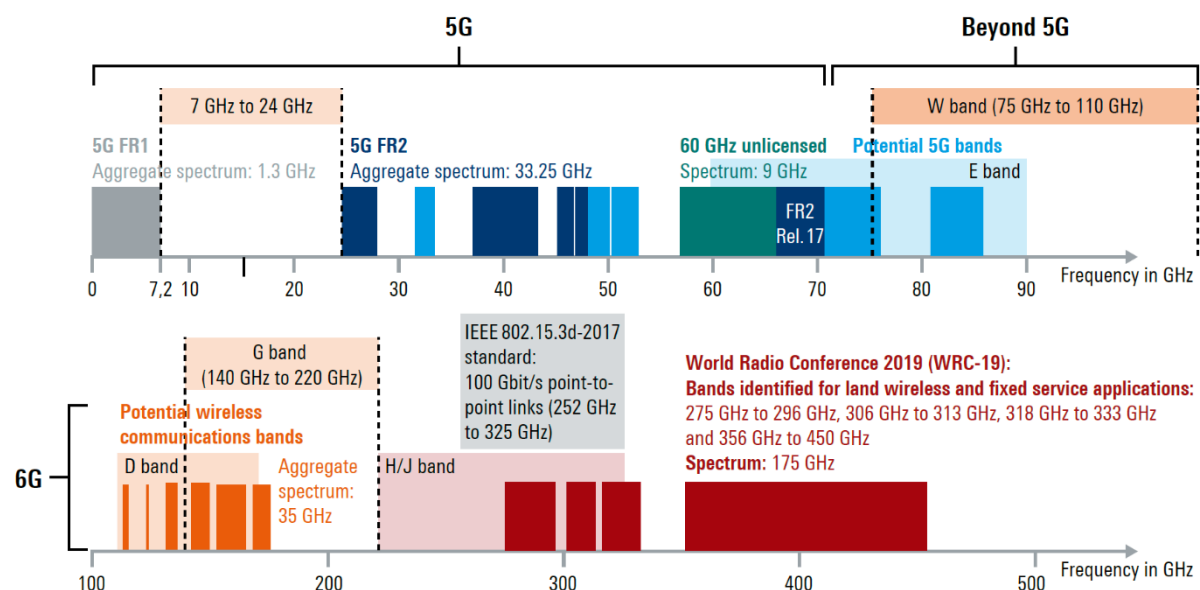


Figure 1. 5G and 6G mobile spectrum [26].

1. 1. Structure of Thesis

This thesis now continues in Chapter 1 with an introduction to the technical topic of channel sounding. In Chapter 2 some channel sounding use cases are introduced, illustrating the variety required, and the papers constituting this thesis are first introduced. Chapter 3 presents current strategies used to implement channel sounders, leading to some identified gaps in research. The relationships between the published papers and the overall thesis research theme are discussed in Chapter 4. The published papers are reproduced in Chapters 5-10 (author-accepted versions, due to copyright requirements of the publishers). Chapter 11 concludes the thesis with a discussion on the papers and recommendations for future work are made in Chapter 12.

1. 2. The Need for Channel Sounding

All radio communications systems use a channel. In wireless radio systems the air and radio-reflective environment defines the channel. For a radio system to operate at best performance, it must be optimally designed for the channel it will use. This can include considerations of antennas, link budget, modulation types, and channel equalisation. If the radio is properly designed for the channel, then it can make maximum use of the available capacity (bits/second/hertz) and minimise the required TX power for a required bit error rate (BER).

The maximum channel capacity C is found from the well-known Shannon Theorem (1), where BW is the channel bandwidth, S is the signal power and N is noise power (or interference).

$$C = BW \log_2 \left(1 + \frac{S}{N} \right) \text{ b/s} \quad (1)$$

Though useful for setting an upper performance limit, (1) assumes an ideal flat channel. Hence, the starting point for good radio design is a proper understanding of the real channel in a range of relevant bandwidths (BWs). This, in turn, requires techniques to measure the channel, which is the focus of this thesis. Channel sounding is important for all radio communications systems, from on-body and IoT through to mobile and satellite systems. There are very many radio channel realisations, with some examples shown in Figure 2.

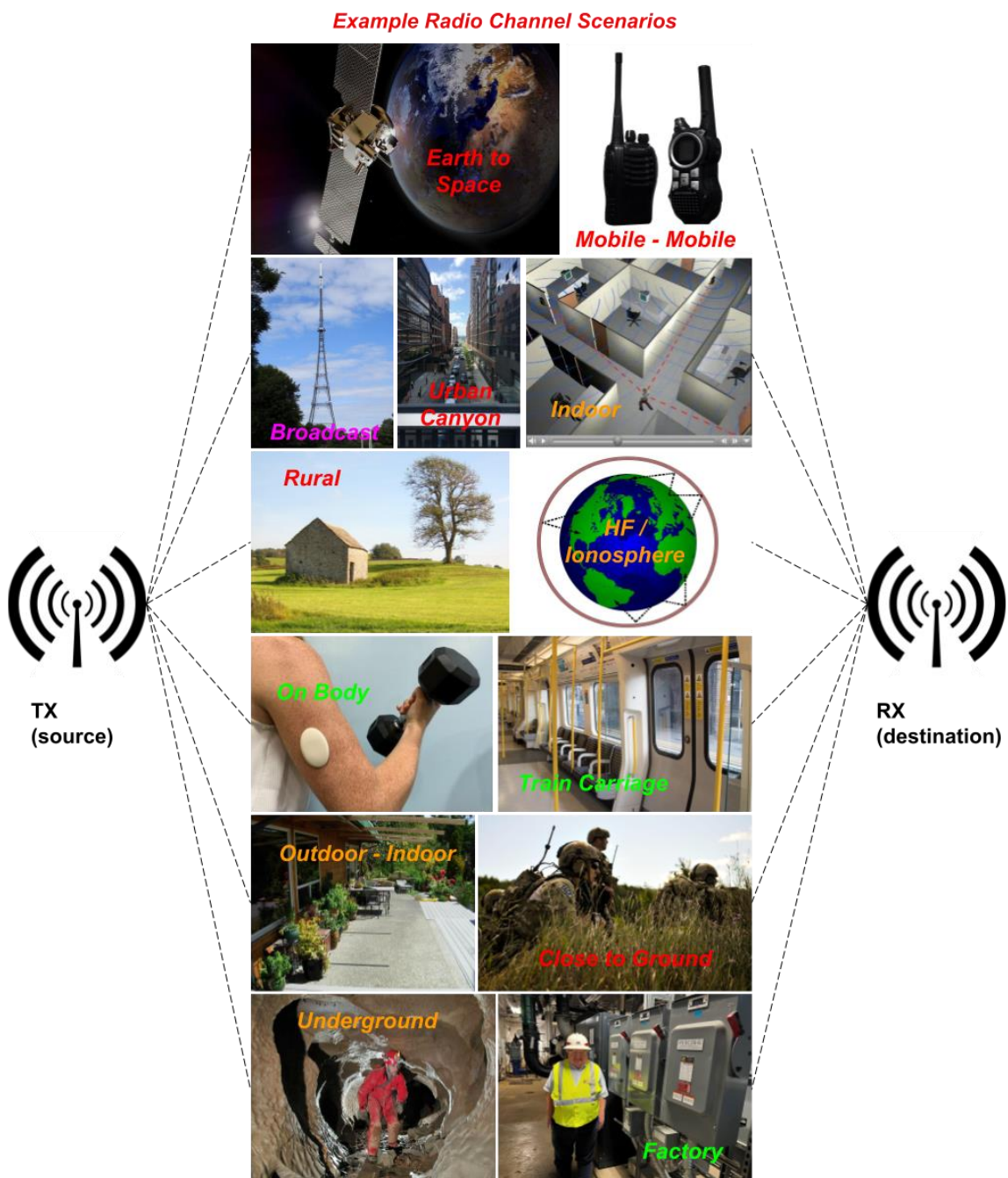


Figure 2. Examples of different real-world radio channel scenarios [images from PickPik, Wikimedia, Pexels, Pixabay].

The channel implicitly includes the operational scenarios and use cases that the radio system will inhabit. Therefore, it is also important that the channel is measured (sounded) in representative use cases. This can become extremely challenging for many use cases, where test kit may be too expensive or bulky to deploy, if available at all at the frequency of interest. Overall, this can lead to only generic channel soundings being possible, which may not fully represent the channel of interest.

The channel can depend on both permanent and temporal effects, for example some researchers have tried to model and predict channel propagation as a function of environmental conditions, such as weather [28]. The effect of propagation through trees and plant material can be very significant, with even wind effects on leaves causing a need for dedicated channel modelling [29].

Some of the key aspects in channel models and their measurement are now briefly discussed in the following subsections.

1. 3. Channel Impulse Response

The time domain channel impulse response can be represented by (2) [30], where τ_k is k th path delay of arrival and $\alpha_k e^{j\theta_k}$ is k th path amplitude and phase components. Parameter δ is the Dirac impulse function. It can be seen from (2) that a channel can be represented as a set of tap-delays with complex scalings.

$$h(\tau) = \sum_{k=1}^K \alpha_k e^{j\theta_k} \delta(\tau - \tau_k) \quad (2)$$

1. 4. Path Loss

The Path Loss (PL) is the RF attenuation provided by the channel. It is the key criteria in assessing a channel, since the target radio system will have a limit on what PL it can accept for a given minimum signal to noise ratio (SNR) for meeting a required error vector magnitude (EVM) or subsequent bit error rate (BER).

There are some common models used for PL, which will now be introduced. The PL is usually specified in dB, often as a log-normal equation model fitted to measured data using the *Floating Intercept* or *Close-In* models. The *Floating Intercept* form is shown in (3) [31].

$$PL_{FI}(d) = A + n10\log_{10}(d) + X_\sigma \text{ dB} \quad (3)$$

In (3) A is the fixed loss component, n is the log-distance scaling term for distance d and X is a Gaussian normal random variable with zero mean and standard deviation σ dB, usually representing log-normal shadowing effects. The parameters for the floating intercept model are obtained through fitting to the measured data.

An alternative PL format is the *Close-In* model, which has a similar form to (3) but uses a defined reference distance d_0 and is represented by (4) [32]. $PL(d_0)$ is the Free Space Path Loss (FSPL) at distance d_0 (commonly set to 1 m). Only parameter n needs to be found by fitting to data.

$$PL_{CI}(d) = PL(d_0) + n10\log_{10}\left(\frac{d}{d_0}\right) + X_\sigma \quad (4)$$

As the most basic and well-known example of PL, simple FSPL is modelled using (5). Though simple, it still provides an interesting comparison for any measured data and is often a good approximation for satellite links.

$$FSPL(d) = 20\log_{10}\left(\frac{4\pi d}{\lambda}\right) \text{ dB} \quad (5)$$

In (5) λ is the carrier wavelength, and the equation can be readily seen to map to the format of (4).

$$FSPL(d) = 20 \log_{10} \left(\frac{4\pi d_0}{\lambda} \right) + 20 \log_{10} \left(\frac{d}{d_0} \right) \text{ dB} \quad (6)$$

In scenarios where a single dominant reflection from ground is expected, a 2-ray reflective earth (RE) model can often be used, defined by (7) [33]. In (7), the height of the TX antenna is H_t and the height of the RX antenna is H_r . It should be noted that [7] is in practice a simplification and, for example, may not be valid for very high antennas with heights comparable to d .

$$PL_{RE}(d) = -20 \log_{10}(H_t H_r) + 40 \log_{10}(d) \text{ dB} \quad (7)$$

The choice of modelling approach will depend on the measured environment, data and approach of the researcher. It is common to compare field measured propagation data to different published propagation models. Fitting the measured data to several of the above models enables comparisons with the works of others. It is common to compare an extracted model from a field test to FSPL and RE, to help obtain an intuitive feel for the channel (no reflections, 2 ray RE, etc). Other formats of PL models are used in the literature, but (3) is sufficiently generic, practical and commonly used by researchers and so is used in this thesis.

1. 5. Fading

Fading represents changes to signal power that may vary with time, or small changes in location that are not related to PL geometry. Fading can be considered as *large-scale* fading (e.g. shadow fading due to path obstructions) and *small-scale* fading (leading to power delay profile, delay spread and angular spread).

In PL measurements using (3) or (4) X_σ for shadowing can be calculated using (8) [34], where W is the number of data points, PL_{data} is the path loss measured and PL_{model} is the path loss predicted by (3) or (4) with X_σ set to zero.

$$\sigma = \sqrt{\frac{1}{N} \sum_{k=1}^W \{PL_{data}(k) - PL_{model}(k)\}^2} \quad (8)$$

1. 6. Power Delay Profile and Delay Spread

When a signal passes through a reflective channel, the different transmission paths will give rise to differing times of signal arrival at the destination. These multiple delayed arrivals give rise to a spread in time – hence leading to a delay spread (DS). This arrival of the signals over time can be represented as a Power Delay Profile (PDP). The PDP is the magnitude squared of the complex impulse response.

The delay spread is sometimes characterised as groups of signal arrivals, with delay spread within each group and a discrete longer delay between the groups. This can be caused by (for example) reflections in an urban canyon from surfaces on several buildings, with each building providing its own group of reflections.

Delay spread measurement requires the sounder to be able to resolve the individual path delays. One technique is to use a Pseudo Random Binary Sequence (PRBS) carrier modulation in the transmitter (TX) and a correlating receiver (RX). The correlation between the known TX PRBS and the compound RX signal will produce a correlation impulse corresponding to each delay path.

Delay spread results can be evaluated to an RMS value for use in system design. Once a power delay profile is measured by a sounder, the mean excess delay T_m can be found using (9) [32], where $P(T_i)$ is the magnitude of the correlation peak at time delay T_i normalised to the primary (direct) ray, N is the number of discrete observable correlation peaks. Then, (10) and (11) [32] are used to calculate the RMS delay spread (DS_{RMS}).

$$T_m = \frac{\sum_{i=0}^{N-1} a_k^2 T_i}{\sum_{i=0}^{N-1} a_k^2} = \frac{\sum_{i=0}^{N-1} P(T_i) T_i}{\sum_{i=0}^{N-1} P(T_i)} \quad (9)$$

$$T_{sm} = \frac{\sum_{i=0}^{N-1} P(T_i) T_i^2}{\sum_{i=0}^{N-1} P(T_i)} \quad (10)$$

$$DS_{RMS} = \sqrt{T_{sm} - (T_m)^2} \quad (11)$$

From a radio communication system viewpoint, the delay spread can be used to help define the minimum acceptable symbol duration. If the RMS delay spread is a significant fraction (e.g. exceeding 10 %) of the symbol duration, the RX symbol will be subject to appreciable distortion due to the delayed arrivals. If the delay spread is insignificant compared to the symbol duration, then the channel will not notably distort the symbol. Some older radio systems used equalisers in the RX to help compensate the delay spread. Nowadays OFDM has gained popularity - with the cyclic prefix used to mitigate delays and narrow subchannels that appear spectrally flat (or require only simple equalisation).

1. 7. Coherence BW

The coherence BW (CBW) is a measure of the BW that will appear spectrally flat, in a reflective environment. (In general, *spectrally flat* is defined as a received signal magnitude that is not a function of carrier frequency.) CBW is inversely proportional to the RMS Delay Spread (DS_{RMS}) and commonly uses (12) to define the relationship, but there is no single definition of the scaling term p . Parameter p can vary from 0.5 to 7 for indoor scenarios, though other researchers have found setting $p = 5$ is a useful starting point [35] for approximation. The actual value of p will be dependent on the tested environment and can be found from a field test if CBW and DS_{RMS} have both been measured.

$$CBW \sim \frac{1}{p \cdot DS_{RMS}} \quad (12)$$

The CBW concept is central in modern communications systems which use OFDM. The OFDM subchannels are usually chosen to be sufficiently narrow (a small portion of overall TX spectrum) such that they only experience flat fading. The overall OFDM spectrum can be wide and so experience DS and hence suffer a ‘notchy’ channel, but the individual subchannels generally do not.

As a related parameter, *Coherence Time* is a measure of how long the channel characteristics remain static and unchanging.

1. 8. Angular Spread

When a directional antenna is used, it is possible to measure the angular propagation characteristics of the channel. These can be considered from the TX viewpoint (angle of departure - AoD) or the RX side (angle of arrival - AoA). Angular spread is simply the PDP and associated angle converted to an RMS figure of merit, as will be shown in the following subsections.

As an intermediate measurement, angular delay can also be measured (i.e. the full PDP at a particular AoA or AoD).

1. 8. 1. Angle of Departure / Direction of Departure

The signals emanating from the TX will radiate outwards depending on the directivity pattern of the TX antenna. If a channel is to be illuminated by a patterned TX antenna, or the TX beam is swept in some way, then the angle of departure (AoD) effect on the channel can be evaluated and a directional channel model made. The resolved AoD paths would also be seen all at once if an omnidirectional TX antenna were used, but a swept beam allows the individual paths to be identified.

1. 8. 2. Angle of Arrival / Direction of Arrival

The signals arriving at the RX can come from multiple directions, depending on the reflective environment between the TX and RX. These RX signal angles of arrival (AoA) provide additional characteristics for the channel and can also include DS. Insight from AoA (and AoD) can be used to help define antenna requirements for a communications system. For example, a high directivity antenna may help reduce TX illumination of reflecting surfaces and reduce RX exposure to reflections. Alternatively, if multiple AoAs are needed (e.g. for path diversity), an omnidirectional TX antenna and a steerable RX antenna may be more suitable.

1. 8. 3. Angular Spread

Once the PDP is known as a function of angle, for either the TX AoD or RX AoA, it becomes possible to consider the spread of the beam – known as the Angular Spread, referenced to the median angle of arrival (or departure). The RMS angular spread (S_A) can be calculated by (13), where a discrete set of multipath components (MPCs) and angles are known [36].

$$S_A = \sqrt{\frac{\sum_{k=1}^K (\theta_k - \mu_A)^2 \alpha_k^2}{\sum_{k=1}^K \alpha_k^2}} \quad (13)$$

In (13) θ_k is the angle of an observed MPC and α_k is the magnitude of the k th MPC. Parameter μ_A is the mean of the angle spread (AoA or AoD) and calculated using (14).

$$\mu_A = \frac{\sum_{k=1}^K \theta_k \alpha_k^2}{\sum_{k=1}^K \alpha_k^2} \quad (14)$$

A limit is usually set to threshold the MPCs that will be considered in the analysis. For example, only MPCs higher than -30 dB compared to the strongest component may be considered, or by using a noise threshold [37].

1. 9. Ricean K factor

In many propagation channels there will exist a dominant (often Line of Sight - LoS) ray and some lower amplitude multipath component rays, which may be Non Line of Sight (NLoS). The ratio of the power of the dominant ray to the local mean powers of these other MPCs is represented by the K-Factor [37]. The K-factor can be represented by (15) [34] and is an important parameter for characterising the multipath fading effect of a channel.

$$K = 10 \log_{10} \left(\frac{\alpha_1^2}{\frac{1}{L-1} \sum_{l=2}^L \alpha_l^2} \right) \quad (15)$$

In (15) α_1^2 is the power of LoS component (i.e the strongest component) and the denominator is the average power in the remaining (non-LoS) MPCs. When $K = 0$ there is no defined dominant signal – hence the channel has Rayleigh fading and when K is infinite there are no MPCs – hence only a LoS path exists.

1. 10. Channel Sounder Verification and Calibration

A channel sounder will often be used to characterise a channel prior to a radio communications system being designed specifically for that channel. Therefore, any errors in the operation of the sounder will translate to errors in the extracted channel model and so may lead to an imperfect design of the target radio system. Testing the operation of channel sounders in known reference environments, and against other sounders, is a growing area of research. To this end, a strategy for sanity checking sounder systems is proposed in [38].

Techniques to verify correct operation and benchmark channel sounder performance, such as using special test structures and calibration or verification artefacts for comparisons [39], or to allow a comparison in a defined (ground-truth) channel – without transporting multiple sounders to a common location are important. It is vital to de-embed the sounder from the channel model (i.e. by removing antenna artefacts, etc). In [40] candidate channel sounders are converted into mathematical model representations for comparison. The comparisons showed a stark difference in PL and delay spread accuracy from a set of tested sounders, suggesting accuracy issues already existed in some sounders.

Some channel sounders do not have coaxial connections that would facilitate direct TX to RX connection for a calibration step, hence an over the air calibration is required. An example is a 28 GHz sounder with a 2 GHz sounding BW [41] using SiGe ICs in a phased array and without conducted measurement connectors. The sounder in [41] used predistortion to implement the calibration correction, after the impulse response of an anechoic room was first measured as a known environment.

In [42] mmWave over the air verification of sounders is proposed using a controlled environment consisting of a compact antenna test range. In [43] an E band sounder is compared to a VNA using a set of predefined controlled test channels (LoS, LoS + reflectors, NLoS).

2. Channel Sounding Use Cases

The operational scenarios intended for a radio communication system define how the channel should be sounded. This can be limited by availability and suitability of equipment. The number of possible radio channel scenarios are very many and varied – perhaps ranging from complete in-body systems, through to deep space communications. As an unusual illustrative example, [44] describes a HF ionospheric characterisation system (2-36 MHz sounding BW), capable of measuring propagation channel group delay and angle of arrival for ionospheric paths.

In the following subsections, prior work examples of sounding use cases and associated sounders are presented and discussed. The relevance of the papers constituting this Thesis is also introduced.

2.1. IoT Sounding

Radio systems destined for use in Internet of Things (IoT) can have a very varied set of use cases, including:-

- Life-critical high reliability systems (monitoring vulnerable people in social care scenarios: fall detection, panic alarms, personal attack alarms, smoke alarms, ...)
- Long range low data rate (utility meter reading, remote control, industrial control, smart city infrastructure...)
- On-body medical and wellness (glucose monitor, pacemaker, smart watch, ...)
- Short range devices (Bluetooth LE, intruder alarm systems, garage door openers, ...)

IoT systems cover a wide span of frequencies, generally from low VHF to microwave. Many cost-sensitive IoT systems use Industrial Scientific Medical (ISM) and ETSI Short Range Devices (SRD) spectrum, such as 2.44 GHz and 868 MHz (Europe) or 915 MHz (USA).

An example of sounding measurements in UHF bands, focused on measuring coherence BW in both city and rural settings is reported in [35]. Equipment used included a standard lab measurement receiver.

Another published example relates to Industrial Internet of Things (IIoT) in evaluating the propagation channel for Power Grid IoT [45]. Channels are measured and models extracted for electrical substation scenarios at 3.35 GHz. PL, shadow fading, Ricean K factor, RMS delay spread, RMS angle spread of departure and RMS angle spread of arrival are found. Sounding equipment was based on RF lab test equipment (vector signal generators) and was time synchronised using rubidium clocks. Omnidirectional and phased array antennas (sweeping a sounding beam) with a 100 MHz BW OFDM sounding signal were used.

IoT systems can encompass a very wide range of use cases and so generic channel models are often not appropriate. For example, a fall detector that is under a person in a dwelling who has fallen has a very different radio channel to an industrial machine radio interface in a spacious but highly metallic factory. Some industrial uses of the IoT encompass very niche scenarios, such as on oil rigs [10].

Therefore, specific channel measurements tailored for the IoT use case of interest are very important. These may use generic RF lab equipment, but in some scenarios (e.g. on-body, awkward meter sites in basements, social care alarms, etc) the equipment is awkward to site in the ideal representative test location or is too valuable to be left unsupervised for any period. These scenarios can benefit from lower cost and portable bespoke sounder platforms. This was the stimulus for Paper 1 [1] and was also investigated in [46], [47].

2. 2. Microwave Sounding

In the microwave bands (1 GHz up to circa 6 GHz) sounders have been widely used as part of mobile phone system design for many years. Channel sounding is also included in some telecommunication standards as part of the phone's normal operation (such as use of pilot channels in 4G LTE OFDM frames) to dynamically track the operating environment and adapt to it.

The microwave bands are heavily congested and widely used: including all cellular communications, WiFi, Bluetooth, TV broadcast and some Low Earth Orbit (LEO) satellite systems. A wide set of use cases are potentially covered. Yet only uses closely related to broadcast and cellular communications have multiplicity of published and practical channel models, many provided by the ITU.

The field of microwave sounding has been widely reported in publications over the years, with some recent examples now presented to illustrate the variety of works.

MIMO sounding for outdoor to indoor channels using switched antenna array is reported in [48]. The RX array was cylindrical, and the TX array was a uniform linear array (ULA) on a rotor. Multitone sounding waveforms in the 2.5 GHz band were used. The TX was 5 m above a rooftop and the sounding RX was in a dwelling 150 m away. The authors obtain angular spread results and other channel parameters.

Angular spread in street environments, exploring the characteristics for both azimuth and elevation angular spread, were measured in [36] using a MIMO sounder. LoS and NLoS channels were measured. A key finding is that rather than a monotonous change in angular spread being observed as function of distance, various distance and location dependent responses were instead seen. The sounding signal used a pseudo noise modulated source at 2.6 GHz, giving a 62.5 MHz sounding BW. The sounder hardware was mobile on trolleys, with a mix of bespoke equipment and lab test kit. Angular power spread models were extracted, along with temporal and spatial power profiles.

Outdoor to indoor propagation measurements are important for all mobile communication systems. In [49] this topic is explored for urban microcells at 3.5 GHz. Azimuth and elevation angular spread of arrival were seen to have log-normal distribution and the time delay spread had a Rayleigh distribution. The sounding TX was mounted on a rooftop, with sounding RX equipment mobile in an adjacent building. The TX used 4x8 array of patches, each cross polarised. The authors proposed temporal models be considered as consisting of three groups of multipath components clusters: 1) main (strongest) group from direct propagation, 2) next group due to reflections from ground and walls, 3) the last group with MPCs from all other physical aspects of the test environment.

Measurements involving watertight metal doors (but with surrounding door frame metal work with air gaps) on a ship at 2.2 GHz using double directional MIMO measurements and a 100 MHz sounding BW are presented in [50]. An excess path loss of 25 dB due to the metal door was seen, but this was at times lower when the sounder was moved away from door, suggesting other signal paths exist. The stimulus for their work was to see if it was possible to replace ship cabling with wireless sensors – hence the need for soundings.

A drone air-to-ground channel sounder at 3.5 GHz is presented in [51]. The drone carried the TX Software Defined Radio (SDR). The RX ground station was an SDR and used an L shaped antenna array. RX propagation analysis software runs on an NI PXI SDR system with 100 MHz sounding BW.

Similar to IoT scenarios, sounders using lab RF test equipment can be used, but are not always practical or available. A vector network analyser (VNA) is an obvious choice for a channel sounder but these are expensive and bulky items. Also, long coaxial cables (or phase controlled wireless links) are needed to connect the measurement sites back to the instrument. To support innovation,

equipment is needed that can be used in other, less-investigated scenarios. Equipment is also needed that can be more compact, lower power or more cost-effective.

The hardware for creating a channel sounder shares much of what constitutes generic radio communications systems: Antenna arrays, RF mixers, Low Noise Amplifiers, Oscillators, filters, etc. As such, new developments in these hardware systems can open new avenues in channel sounding. New hardware can also make channel sounders more practical (compact / power efficient) for a scenario of interest.

Antenna arrays are useful in channel sounding as they can be used to improve the link budget and hence allow a longer range to be sounded or more MPCs resolved. Of course, the channel model extracted will implicitly include the array's directivity effects, potentially screening out off-axis reflections. Therefore, it is important that the antenna array is representative of what would be used in the finished communications product, where possible. Otherwise, the antenna should be de-embedded from the channel response.

In this thesis three new concepts in antenna arrays are presented, all making use of the Time Modulated Array (TMA) concept. In Paper 2 [2] the ability to steer a 5.8 GHz beam using a TMA and the ability to reduce the magnitude of an unwanted un-steered component is presented. Such an array could be used to implement a microwave channel sounder where a steered beam is required as part of the sounding activity.

In Paper 5 [5] a new concept using the TMA in RX mode at 2.4 GHz and including subsampling within the TMA operation is presented – named Subsampling TMA (STMA). This new concept could be used to reduce the complexity and cost in an RX sounder, where a steered RX beam is required. The STMA allows a lower carrier frequency SDR (or potentially direct connection to an ADC and digitiser) to be used.

In Paper 6 [6] the multiple harmonic beams generated by a TX TMA at 5.8 GHz are used to advantage and employed to simultaneously illuminate a channel. This can facilitate a rapid measurement of angle of departure dependency in a measured channel, without sweeping a beam.

2. 3. mmWave Sounding

Frequencies in mmWave bands (circa 28 GHz to beyond 100 GHz) have now become relevant to future mobile communications [52]. The 28 GHz band was earlier used for fixed wireless access and cellular backhaul but has now been deployed in many 5G mobile phones. For 6G standards, higher mmWave and even sub-THz bands are being considered for use in mobile devices, for communications to 200 m. Outside of cellular mobile use cases the emerging commercial chips now allow new products and concepts to be developed by industry and military, but channel models for novel use cases are needed.

Hence, the ability to measure channels in relevant and bespoke use case scenarios is important. The use of lab equipment can become prohibitive, due to its high cost and power requirements, hence bespoke sounder platforms are useful. Such systems can be used in unusual scenarios or high-risk scenarios where the loss of the sounder does not represent a high value and can be replaced (as opposed to a million-pound VNA). However, globally, lab facilities are being established that have the core equipment to perform such mmWave and higher frequency measurements [53], [54] and may be applicable if the risk of movement of equipment can be tolerated (or the use-case be sufficiently emulated in the laboratory setting).

In Paper 4 [4] a portable channel sounder is created and presented for the 28 GHz band, using recently available commercial RF chips. The sounder is used in novel scenarios for close-to-ground communications and reveals interesting results about the path loss for close-to-ground operation. The

sounder was also used in [55] as part of a rural field trial that would be extremely difficult to perform with conventional lab equipment.

The field of mmWave sounding has been a widely researched and published area. Some illustrative prior works will now be discussed, for different sounding scenarios.

In [56] a channel sounding campaign at 28 GHz was used to calibrate ray tracing. The authors also found that diffuse scattering accounted for 20 % of received power, though up to 40 % of received power being due to diffuse reflections had been suggested by others. Diffuse scattering is due to surface roughness being comparable to carrier wavelength and so leading to random directions of reflections. In contrast, diffraction is claimed to be negligible at mmWave due to the small Fresnel zones. Hence LoS propagation was proposed as the main mechanism, with diffuse scattering as the second most significant.

In [57] an early attempt to predict the complexity reduction that may be possible in a mmWave radio system was made – specifically investigating the reduction in hardware complexity that may be possible if a rich propagation channel was available (due to scattering).

For mmWave systems a wide sounding BW is often needed, to allow a sub ns delay resolution. This can be challenging to achieve. In [58] an alternative approach was taken, based on a 5.6 GHz OFDM sounder using a SDR with only 20 MHz instantaneous sounding BW. By using post processing, the sounding BW was concatenated to achieve an overall 200 MHz BW.

At 28 GHz foliage blockage measurements become important. In [59] a real time sounder using phased arrays and a switched beam to scan the channel are presented. The system was used to investigate delay spread and angular spread effects due to foliage. The system had a measurable PL of 169 dB and used a 400 MHz sounding BW using a multitone waveform. Foliage penetration loss models were extracted.

Outdoor to indoor loss can be significant at 28 GHz and above. In [60] (using the system of [59]) a building penetration loss of 10 dB to 23 dB was seen for the domestic dwellings tested. A key finding is penetration loss is not properly modelled by using traditional techniques of concatenating an outdoor and an indoor PL model, nor is it properly represented by just adding a fixed attenuation term to account for penetration loss.

Many recent works focus on the 5G spectrum at circa 28 GHz and 38 GHz. In [61] 5G related measurements at both these bands were evaluated for rooftop scenarios, inside a railway carriage, and for factory IIoT. Measured data was fitted to PL models using close in and floating intercept models and to 3D angular models. The system was based on NI PXI SDR equipment and could scan 19 discrete beam directions, selectable with 5 degree steps. The system used a 1 GHz sounding BW. TX and RX time synchronisation used the GPS 1 pps signal (now widely used in published channel sounders). From the reported measurements, strong reflection paths were seen in all scenarios – hence extracted PLs were all worse than FSPL. The measured RMS delay spread seen in an IIoT setting at 10.4 m separation between TX and RX was 110 ns, due to reflective metal structures. In [62] an indoor office environment was sounded at 6 GHz and 37 GHz, with obstructed LoS and NLoS paths compared, for a RX 1.1 m above the floor and the TX near the ceiling.

An investigation of 60 GHz channels (PL and angle of arrival) in a vehicle and outdoors are reported in [63]. The system had a measurement BW of 1.9 GHz and used a sliding correlator (with PN signal) and rotated directional horns to beam scan. Delay spreads of up to 36.6 ns and a PL exponent of 4.19 for outdoor NLoS was extracted. Outdoor LoS channels had below 1 ns delay spread and PL close to FSPL. The outdoor scenario mean delay spread was 6 ns. In-vehicle LoS PL was close to FSPL (mainly due to the short tested range). In general, NLoS links had a PL in range of 15 to 40 dB below

LoS links. Measurement equipment was based on commercial RF modules and supporting SDR lab kit.

Within an RX sounder at mmWave frequencies a downconverting mixer is usually required. The present generation of commercial SDR systems do not have direct digitisation capabilities at 28 GHz (or above), so analogue RF front-ends remain highly important for all mmWave radio systems. An RX mixer is critical in converting from an incoming RF signal to a usable and lower intermediate frequency (IF) signal. Until recently, commercially available packaged mixer chips at 28 GHz have not been available, so bespoke custom designs have always been required. The availability of a SiGe transistor that could be applied to mmWave mixing, for possible use in an RX sounder, is the topic in Paper 3 [3]. A key issue in mixer design is the local oscillator (LO) signal generation and particularly its RF power. Generating RF power for the LO becomes challenging at mmWave frequencies, hence techniques to help reduce the requirement are important. However, there is a dependency on LO power for mixer linearity. Since high linearity may not always be required, it is interesting to consider how the LO power can be controlled for a use case. This desire to reduce the LO power and also optimise the associated DC bias conditions through a mathematical understanding of the mmWave mixer transistor led to Paper 3 [3].

3. Channel Sounder Hardware, Algorithms and Existing Methods

This chapter introduces background concepts, some common hardware approaches and signal processing techniques used in realising channel sounders. Published examples of these various techniques are presented and discussed.

There are three major approaches to make a channel sounder, commonly seen in the literature :-

- Vector Network Analyser (VNA) based sounder with Inverse Fast Fourier Transform post processing.
- RF signal generator TX and high BW Oscilloscope or Spectrum Analyser RX, using correlation.
- Bespoke RF front end and SDR, using correlation algorithms.

Each of these approaches will now be considered based on prior works, with advantages and disadvantages discussed.

3.1. VNA Based Sounders

The VNA is an obvious and perhaps optimum tool for sounding a channel, as it will allow a swept calibrated response of amplitude and phase to be easily obtained. The self-contained nature of most VNAs is also easier to manage, rather than needing lots of smaller units and cables with attendant calibration issues.

A swept measured S_{21} can be obtained from the VNA and then the inverse Fast Fourier Transform be used on this data to obtain the channel time domain impulse response.

The main disadvantages of the VNA approach are the delicate nature of the instrument, the financial cost of the instrument, the difficulty or health and safety issues associated with transporting it to a test site use case, the need to handle a reference path (RF, fibreoptic cable or wireless link) between the two measurement ports and the associated calibration strategy. The power supply requirements and weather shielding for outdoor use are also issues. The problems in using a VNA become worse at mmWave frequencies. Here, the VNA can cost over £500k and may be deemed too vulnerable to take from the protection of a temperature and humidity-controlled lab. Although amplifiers can be used to boost the reference signals on longer cables, a point will be reached where the measurement is too noisy to use. Calibration over long cabled links also become problematic, requiring phase stable cabling or RF over fibre.

An example of a ‘long range’ channel sounder at mmWave using a VNA is given in [64]. The authors present a 10 GHz - 50 GHz sounder, using RF over optical fibre for its lower conducted signal loss but also then needing an additional phase compensation system. As reported, the theoretical sounding range was 238 m at 30 GHz when a 20 kHz VNA IF BW was used [64].

A novel use of a VNA and a ‘cubic virtual array’ is discussed in [65]. The main sounding measurement was performed by the VNA. A 3D positioner was used to move the sounding antenna in 3 dimensions, with it pausing at a new location for each sounding measurement. The process resulted in a virtual array which does not suffering from mutual coupling (since there is only 1 antenna). However, such a system can only be used when the channel is static (no doppler or temporal effects) since the mechanical scanning and repositioning of the sounding antenna is very slow.

At sub-THz frequencies, VNAs with frequency extenders have been used for short-range channel measurements or to longer ranges by using fibre optic reference links (RF over fibre) [66], even to links potentially to 600 m [67]. However, these systems are also subject to cost and mobility issues.

3. 2. Sounders Using RF Signal Generator + Oscilloscope / Spectrum Analyser or SDRs

Sounder systems can use SDR concepts either in an actual SDR platform, or on the signals captured from standard lab test kit. SDR concepts allow various sounding waveforms to be used, including OFDM, multitone, FM-CW, and sliding correlators using pseudo noise. The most basic measurement of using a spectrum analyser for simple measurements of PL are not considered here.

Arbitrary waveform RF signal generators are now cost effective and can be used as the TX unit for a sounder. Bespoke sounding patterns of an arbitrary nature (such as PRBS modulated BPSK) can readily be loaded into the signal generator and a sounding TX be quickly realised. On the RX side, a spectrum or signal analyser that has sampled data saving capability can be used, to capture the RX IQ waveform. Nowadays, fast sample rate oscilloscopes are also becoming available and popular as waveform digitisers.

Such general lab kit usage applied to sounding may be increasingly flexible and deployable, but the cost of the instruments can remain prohibitive, especially at mmWave frequencies. The ability to trial different sounding patterns and waveforms is useful, but this flexibility does still come with the cost of having to develop software systems to generate and then analyse the signals. Equipment power supply requirements can also be limiting.

Illustrative prior works using SDR approaches with lab equipment for channel sounding will now be introduced and discussed.

There are many sounder designs that use sliding correlators, with strategies to define optimal correlator design having been investigated [68]. The correlation approach is a popular method for obtaining the MPCs of a channel.

A real-time 28 GHz MIMO sounder using a phase array with horizontal and vertical steering (rather than a conventional rotating horn antenna) is presented in [69]. The TX and RX arrays consisted of 8x2 elements. Multitone sounding waveforms were used with a 400 MHz sounding BW. Lab test gear and commercial 28 GHz radio units were used to realise the system. The system was used to measure moving outdoor scatters (cars) and blocking objects. By using beam switching of the phased array the system could measure Direction of Departure (DoD), Direction of Arrival (DoA), delay and doppler effects.

In [70] a phased array MIMO channel sounder at 28 GHz with 2 μ s beam switching is described. A 28 GHz commercial RF frontend with National Instruments (NI) PXI system and modules were used to construct the system. Sounding used a multitone signal with 400 MHz sounding BW. As is becoming common for mmWave sounders, GPS-disciplined rubidium frequency references were used, giving a 10 MHz clock for RF reference and 1 pulse per second (PPS) signal aligned to Universal Time Coordinated (UTC) for synchronisation.

A 26 GHz MIMO sounder using a hybrid beamformer with 64 antennas at both the TX and at the RX is introduced in [71], using trolley-based RF lab equipment. Sounding BW was 56 MHz (leading to a 17.8 ns MPC delay resolution). The sounder could resolve AoA, AoD and PL.

In [72] a 73 GHz sounder, again based on PXI equipment, using a sliding correlator for angular or delay spread, (or real time spread spectrum mode for short range temporal monitoring) is presented. The sounding BW was 1 GHz (null-null). Beam steering was performed using rotatable horn antennas.

An 802.11 (2.4 GHz) SDR based channel sounder for industrial scenario wireless sounding is presented in [73]. The SDR had a 16.25 MHz sounding BW. A key novelty was the use of time

synchronisation over air, using time stamping from the Precision Time Protocol in the IEEE 1588 standard.

A 5.8 GHz battery powered and portable SDR based sounder is presented in [74]. The sounder used a doppler antenna concept, where each element was switched in turn to synthesise a doppler effect, allowing the resulting doppler frequency to measure the AoA of an RX signal.

A 300 GHz sounder based on commercial lab equipment is presented in [75], with a dedicated lab digitiser and commercial frequency extender units (VDI Ltd) used for up / down conversion.

A vector signal generator and vector signal analyser were used as the basis for a sounder at 6 GHz and 37 GHz in [62], allowing a PL comparison between both bands.

Modern lab oscilloscopes offer an alternative approach to digitising signals and also allow immediate and direct comparison measurements of phase and amplitude of a measured and reference signal. Oscilloscopes can be used in high mmWave channel sounders, when employed with up / down converters [76].

In [77] a lab signal generator and digitisers were used in conjunction with a 158 GHz analogue RF front end to create a MIMO channel sounder with 400 MHz BW. The sounder used OFDM signals with 120 kHz subchannels, as used in 3GPP standards for 5G NR.

3. 3. Bespoke Sounder Systems Incorporating SDR

With the advent of SDR and their now cost effectiveness at sub-6 GHz, a new breed of sounder can be realised. If sub-6 GHz conventional sounding is sufficient, then the entire system (TX and RX) can be implemented using such SDRs and only antennas, analysis and sounding software and calibration strategies need defining.

If higher operating frequencies are required then systems can be created though use of generic RF lab equipment (modularised amplifiers and mixers, signal generators, etc) or a fully bespoke (e.g. PCB based) design created using commercial RF parts. The advantage of the latter approach is the sounder can be compact and power efficient, as well as low cost. This can allow the sounder to be used in unconventional or risky scenarios where damage could happen, but important measurements are needed and can justify a limited cost.

Many published works use some hybrid of commercial lab RF equipment and bespoke circuit or module-based equipment to realise the sounder system. As seen in the literature, this is more common at mmWave frequencies where affordable commercial mmWave SDR hardware is not yet available. Below are some recent examples of bespoke and hybrid sounders at mmWave frequencies.

The work in [30] described a mobile mmWave 83.5 GHz channel sounder that measured complex amplitude, delay and AoA. Azimuth and elevation multipath components were measured with a delay resolution of 1 ns. The system is capable of indoor measurements to distances of circa 150 m LoS. GPS control and rubidium clocks were used for synchronisation between systems, which were constructed using lab test equipment and mmWave modules. The authors stated that manually rotated (directional horn) systems risk being too slow to capture temporal channel effects for a valid channel coherence time (i.e. while channel is not changing).

A 60 GHz sounder with 1 GHz sounding BW, using phased arrays, lab kit and bespoke hardware (HW) design is presented in [78]. The system measures AoA, AoD, and MPCs. The system was mounted on a robot for autonomous sounding in a test location. The phased array used 8x32 series fed arrays, connected to phase shifter and gain control chips as an RF front end. The sounding waveform was a PRBS with 1 ns chip duration. Supporting lab kit was used for TX and RX functions as well as signal processing.

In [79] a set of SiGe transceivers with beam steering were used to make a beam switching MIMO sounder. The sounder operated in the 60 GHz band with 2304 beam combinations (TX and RX total) [79]. The SiGe transceivers were used to create gain and phase controllable phased arrays. Signal generation and acquisition was performed using trolley-based lab equipment. A sounding BW of 400 MHz was achieved, using a 256 subcarrier multitone signal. Delay resolution was 2.5 ns [79]. The sounder took 200 ms to measure the channel [79].

A novel mock-handset was created in [80], operating at 21.5 GHz, used in channel sounding for measuring PL. The mock handset had a set of selectable antennas. The handset used a uniform linear array (ULA) based RX with 3 sub-arrays, each consisting of 8 elements. RF switches on the handset were used to select the antenna element to measure. A horn was used as a remote TX source, with a PN modulated signal transmitted. Correlation against the PN was used for sounding MPC extraction. Various indoor tests with different user holding styles were investigated using the system. A variation of 12 dB or more in PL was seen due to various users' holding orientations, and 4 dB variation between different individual users [80].

At higher mmWave and sub-THz bands, hybrid measurement systems are often seen using modules for frequency conversion and standard lab arbitrary waveform generation and digitization [81], or more bespoke solutions [82]. A system for E band sounding is presented in [83] which used modules, and an oscilloscope as the digitiser.

New FPGA based high performance SDR systems based on the Xilinx Ltd RFSoc applied to phased array designs [84] could also now become relevant for channel sounding. However, the RFSoc would still need mmWave up / down conversion modules or bespoke analogue design.

Since SDRs are now a well-established concept, it is inevitable that their performance will increase as the technology develops. There is already reported work considering SDR design for above 100 GHz [85]. However, at present, mmWave systems still require fully analogue front ends.

3.3.1. Illustrative Architecture for a Bespoke Sounder Based on SDR

The generic microwave SDR based sounder TX can be considered as shown in Figure 3 and the RX as shown in Figure 4. If the SDR is capable of generating sufficient TX power and has a sufficiently low noise figure (NF) to meet a required sounding link budget, then an external PA and LNA may not be needed.

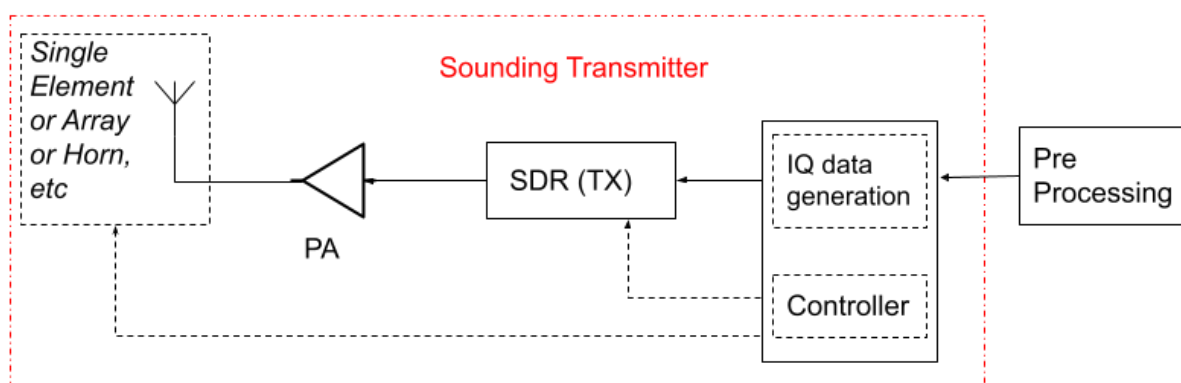


Figure 3. An example microwave sounder TX architecture.

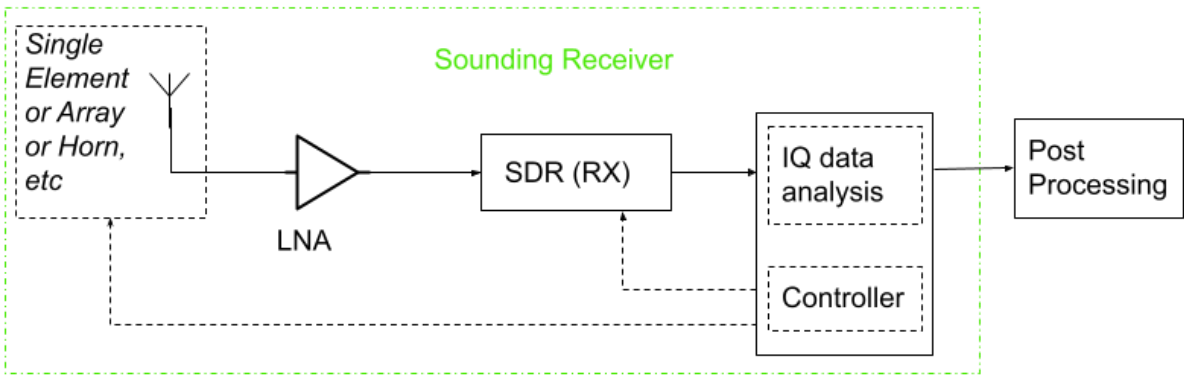


Figure 4. An example microwave sounder RX architecture.

If the SDR cannot generate or receive frequencies at the band to be sounded, then external up-conversion and downconversion stages are needed. This is shown in concept form for a mmWave TX in Figure 5 and for the RX in Figure 6. Analogue mmWave band pass filters may be required, to reject image signals, and are not shown.

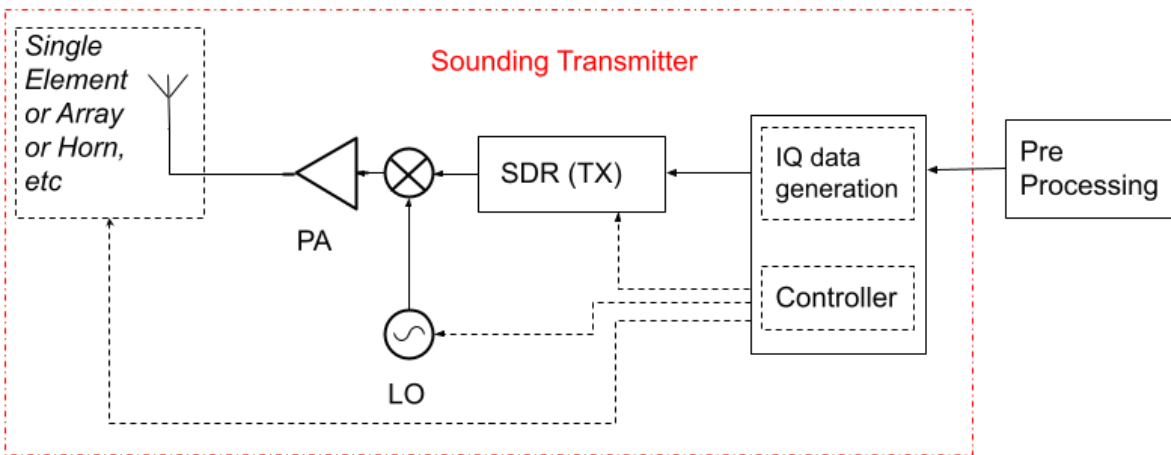


Figure 5. An example mmWave sounder TX architecture.

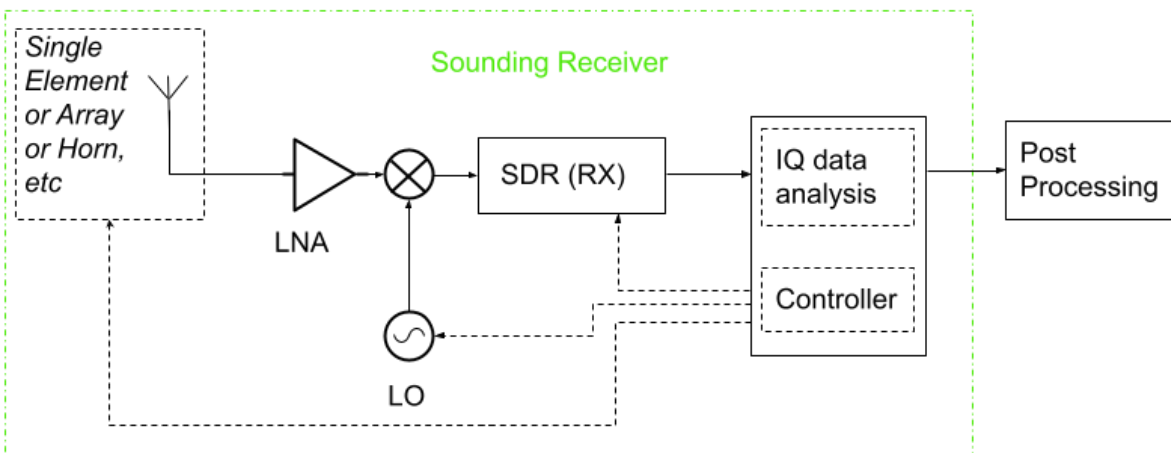


Figure 6. An example mmWave sounder RX architecture.

It can be shown that the sounder's link budget (defining the maximum measurable PL) can be calculated using the following equation :-

$$PL_{\text{sounder}} = (P_T + G_T + G_R) - (-174 + NF + 10 \log_{10}(BW) - PG + SNR_D) \text{ dB} \quad (16)$$

In (16), -174 is the thermal noise floor in dBm/Hz due to the Boltzmann constant k and the system operating temperature (i.e the kT) with a T of 290 Kelvin, P_T is the conducted TX power (dBm), G_T is the TX antenna gain (dBi), G_R is the receive antenna gain (dBi), NF is the RX system noise figure (dB), BW is the sounding bandwidth (Hz), PG is the processing gain (dB) for the sounding waveform and SNR_D is the signal-to-noise ratio required for detection (dB).

In this thesis a PRBS length M-sequence is used as the modulating signal in the sounders. For such a waveform the PG is given by (17). There are many other types of sounding waveforms that can be considered, including multitone and OFDM.

$$PG = 10 \log_{10}(M) \text{ dB} \quad (17)$$

From Figure 3 - Figure 6 and the subsystem terms in (16), it is clear that a channel sounder shares many similarities with other radio communications systems. Therefore, the research and design of all aspects of radio systems are relevant and important. This can include antennas and antenna arrays, PAs, LNAs, mixers, oscillators, filters and DSP algorithms. In this thesis, published works are presented in antenna arrays, mixers, sounding algorithms and full sounder implementations.

4. Linking of Published Papers to Thesis Research Theme

This Chapter introduces each of the published Papers (1-6) forming the main body of the Thesis. It also explains how each paper individually relates to the theme of the Thesis. The Chapter also discusses some of the original background that initially led to the work in each of the Papers. Therefore, how each publication specifically addresses and contributes to an aspect, or challenge, relating to channel sounding is discussed.

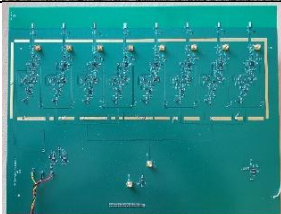
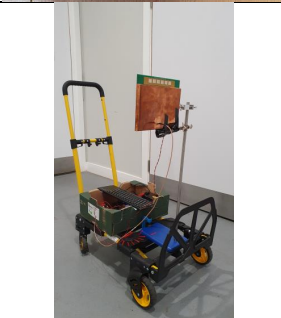
For the Papers focused on RF hardware, that could form part of a sounder, the discussion identifies how they could be applied in a sounder. To support comparison and highlight the significance of these Papers, some other competing strategies and prior works are also discussed.

Certain subsequent relevant work that occurred after the publication of the Papers is also presented, to further help explain the topics and clarify significance. Similarly, work that expands on the Papers to aid technical understanding is also included.

Channel sounders share many of the subsystems found in general RF communications systems. Therefore, the need for performance antenna arrays and RF mixers as modules is important and relevant to the novel hardware aspects of the thesis, in addition to the full sounder systems discussed.

An overview of the 6 Papers and their contribution and relevance to channel sounding is presented in Table 1.

Table 1. Overview of the 6 Papers in this Thesis.

Paper	System Picture	Purpose	Tested Operational Frequencies	Novelty / Contributions	Role in Channel Sounding
1 [1]		VHF / UHF sounder system.	71 MHz, 869.525 MHz	Hand portable system measuring PL and DS. Field test results.	This is a sounder system.
2 [2]		TX array (TMA).	5.8 GHz	Steerable TMA beam. Reduction of $C0$ beam. Prototype & Lab verification.	Could be used to steer a sounding TX beam.
3 [3]		RX mixer.	26 GHz	Mixer design models. A 26 GHz mixer prototype to verify models.	Could be used in a mmWave sounder as a downconverter stage.
4 [4]		28 GHz sounder system.	27, 27.2, 27.5, 27.65, 28, 29 GHz	Portable 28 GHz sounder system measuring PL and DS. Field test results.	This is a sounder system.
5 [5]		RX array (STMA).	2.4 GHz	Steerable TMA RX beam incorporating subsampling. Prototype & lab verification.	Could be used to steer a sounding RX beam.
6 [6]		5.8 GHz sounder system (using TMA).	5.8 GHz	TX TMA used to coherently illuminate multiple AoD beams. Ability to measure multi-beam PL & DS demonstrated. Field test results.	This is a sounder system.

4. 1. Paper 1 – Portable VHF / UHF IoT Sounder

Paper 1 [1] is a complete, calibrated, hand-held portable channel propagation measurement system operating at VHF and UHF. The focus here is on using low-cost, off-the-shelf, commercial hardware as far as possible with new, bespoke, signal processing algorithms and post-measurement analysis. The SDR used was the low-cost RTL-SDR with 2 MHz of capture BW, controlled by a Raspberry PI.

Measurements at 869 MHz and the (then) newly released Ofcom IoT segment at 71 MHz were the stimulus for the project, focused on complex, real-world pedestrian and car mobile use cases. The hand-held, dual band, hardware and algorithms extract the channel BW response and power delay profile of the channel.

The algorithms developed were later improved and modified for the system in Paper 4 [4]. An additional contribution of the paper is a new and simple approach to estimate the RMS delay spread assuming a 2-ray reflective earth model, when measuring power delay profiles with limited RX BW.

The measured field test data and resulting models help show the importance of performing tests in relevant use-cases and scenarios that could not be easily done using conventional lab-based equipment. City and suburban PL models are created for pedestrian and car mobile scenarios and results at both frequencies compared. The lack of observed channel reflections exceeding $1 \mu\text{s}$ over 4 km distances is an important finding and could simplify future IoT transceiver designs. The emerging models allow prediction of propagation characteristics in realistic IoT use-cases.

4. 2. Paper 2 – TMA C0 Canceller and Beam Steering

The Paper 2 [2] describes a practical and novel strategy for constructing and then controlling an antenna array to point an RF TX beam at 5.8 GHz in a desired direction, with a focus on both hardware and related control signal processing. The novel strategy does not use conventional methods, such as varactor-based phase shifters or vector modulators. In essence, this is a phased array that uses simple RF hardware based on switch functions and is simpler to control than conventional methods.

Starting from a proven methodology led to a new TMA concept and development of new analytical models for predicting the RF performance and array factor. The concept has been extensively verified using novel bespoke RF hardware in calibrated chamber measurements.

A key contribution of the paper is the method to reduce the un-steered (fixed beam) emission on the carrier frequency. Before now this has been a limiting issue with TX TMAs.

The described system uses commercial RF chips at 5.8 GHz, developed into a bespoke RF platform with a DSP MCU to implement necessary array control waveforms. Measured performance of the array with its new signal processing algorithms is given and compares favourably to expected theoretical performance.

This type of flat panel TMA antenna array could be used in a propagation measurement system to replace the standard-gain horns or Yagi antennas currently used, potentially offering a small form factor and with benefit of a fully digital control to steer the beam.

Some of the early concepts and hardware developed for this paper went on to become the groundwork for the Subsampling TMA of Paper 5 [5] and the 5.8 GHz TMA sounder system described in Paper 6 [6]. The described antenna array concept could support new and fast ways of channel measurement.

The multiple concurrent harmonic beam generation implicit in the TMA process is potentially useful in TX and RX channel sounding applications, as will also be discussed later.

4. 2. 1. Approaches to Channel Sounding with Arrays

This subsection presents recent works in propagation modelling that have made specific use of antenna arrays in novel ways, as alternatives to directional (e.g. horn) antennas. Multi-element phased arrays or MIMO arrays are now widely used, with either steered beams or switched beams performing the sounding measurement.

Channel models have been constructed based on observations using a mmWave planar array [86]. In [87] a square array was accessed one element at a time (hence time division multiplexing as beam switching) to sequentially sound a channel. The actual sequence for the selected antennas was optimised for best speed and performance. This represents a sequential form of a MIMO channel sounder.

Four linked sounding beams (linked – not independently controllable) were used in [88] for a 28 GHz channel sounder. The four beams were steered as a group. The sounder used bespoke SiGe chips as phased array beam former, with Gilbert cell mixers.

A dual polarized 28.5 GHz phased array operating as a switched beamformer in a channel sounder is described in [89]. The array size was 8x8 (64 elements). The system swept through each of the antennas and post-processing was then used to synthesise a recovered sounding beam. The authors suggest such an approach is faster to control overall (compared to steering a directional horn etc). SPI controlled analogue phase shifters were used at each antenna as part of the beam forming.

A MIMO switched antenna array for channel sounding, consisting of 256x128 elements, operating at 28 GHz is described in [90]. The antenna switching was implemented using a set of SP4T switches.

4. 3. Paper 3 – Analysis of 26 GHz Downconversion Mixer Design

RF downconverting mixers are used in many of the propagation measurement systems published, but their specific design is rarely considered. Techniques to theoretically predict downconversion mixer RF performance as a function of local oscillator (LO) drive power and DC bias are presented in Paper 3 [3]. The ability to trade off DC bias with LO power has been observed in practice before, but a full theoretical treatment had not been published for SiGe Bipolar Junction Transistors (BJTs).

The prediction of the RF performance of the mixer is important, to ensure suitability for an application. Until now, such prediction required extensive use of circuit simulation tools. Paper 3 [3] introduces a theoretical technique to help design pumped-transconductance mixers by jointly considering their DC bias and oscillator drive and thus helping trade them off. The technique can also facilitate dynamic control of a mixer performance for a given operational scenario. This can help save battery life and thus extend the operational life of a channel sounder or other system in the field. The theoretical concepts were developed using standard mathematical techniques and tested against Keysight ADS circuit simulations and also against a built hardware prototype at 26 GHz. The overall agreement between the theoretical and measured results verifies the technique.

4. 3. 1. Consideration of RX Mixers in a mmWave MIMO Sounder Application

The ability, at the design stage, to identify and trade-off the required LO power for a transistor bias condition allows proper design of a mmWave mixer in a transceiver at a power budget. Generation of high LO power is very challenging at mmWave and so the use of lowest possible power for communications or channel measurement in a scenario is important for extending battery life. The techniques can also be used to compare the expected performance of different transistors in a mixer.

The need for power efficient mmWave mixing can be illustrated with the aid of the following example. MIMO channel sounding is now widely used and reported [48], [69]. Consider a full MIMO channel sounder operating at 28 GHz, arranged as a 4x4 set of independent RX chains. Hence 16 coherent RX chains would be required, as shown in Figure 7.

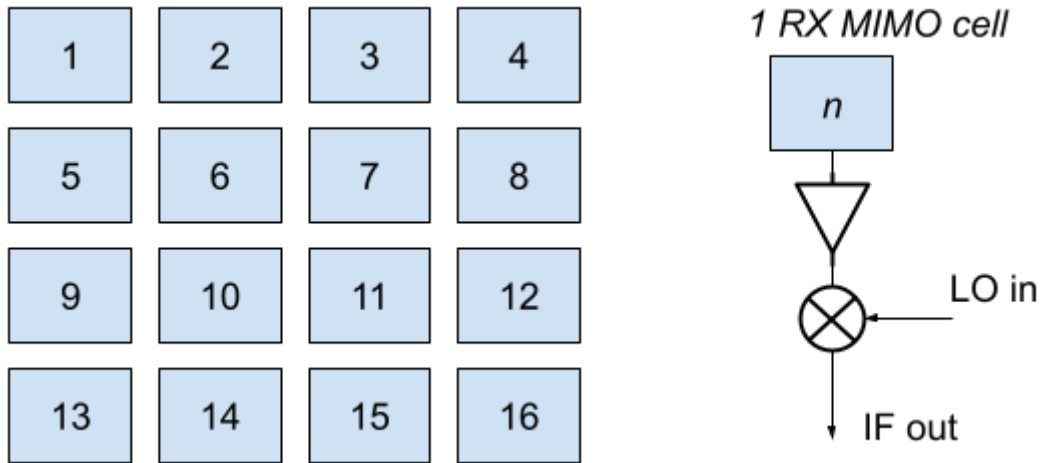


Figure 7. Example 16 element RX MIMO system.

In such a system, Analog to Digital (ADC) converters would be needed on each IF output of each chain, assuming the IF is digitised and IQ down conversion is performed in DSP. Here, we will just consider the mixer's impact. There are now some commercially available low mmWave mixer MMICs that are packaged (as opposed to bare die), such as the HMC264LC3B used in the system of Paper 4 [4]. The HMC264 chip has a 9 dB insertion loss (IL), requires an LO power of -4 dBm (0.4 mW) at half the LO frequency. It draws 25 mA at 3 V (75 mW) and at the time of writing costs circa £ 57 in low volumes. In contrast, the mixer as presented in Paper 3 [3] has an IL of 12 dB for a 0 dBm LO (1 mW) and draws 3 mA at 3V (9 mW) and the transistor costs circa £ 0.44. Since this was the first prototype, it is possible that improvements to IL could be achieved in subsequent revisions.

Additionally, from Paper 3 [3] it is shown that by varying the applied LO power and re-biasing the transistor, different input 1 dB compression points (IP1dB) and ILs can be achieved. This could allow a radio system (e.g. a sounder) to use the minimum LO power required for a particular sounding scenario based on required noise figure (NF) and linearity. Alternatively, with a fixed LO power, the DC bias can be used to control the IL – again allowing dynamic optimisation of the gain for a given scenario and power budget.

To further illustrate RF mixer issues, consider the overall power budget required for a 16 element mmWave MIMO sounder based on both the above mixer strategies. Since the mixers will all need to be phase coherent, they may use a common LO that is distributed through a set of Wilkinson splitters, or similar, as shown in Figure 8.

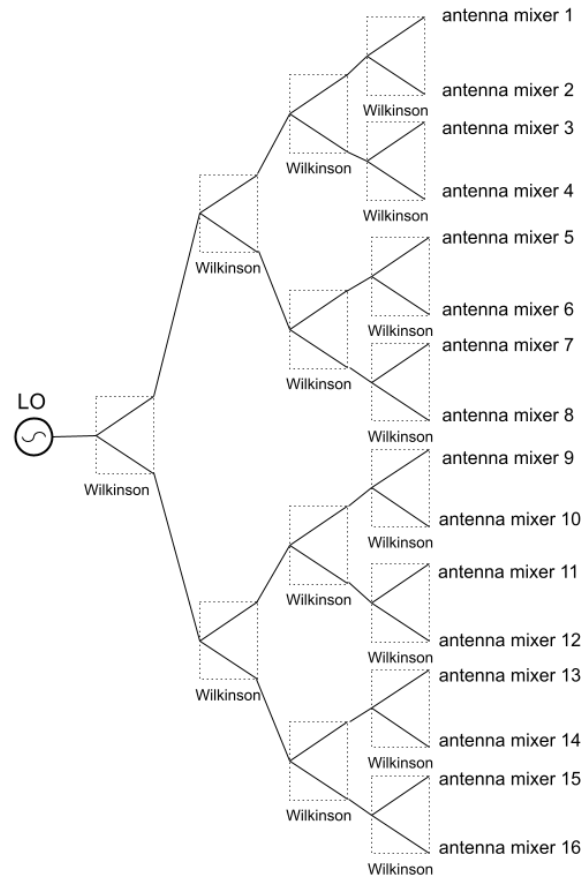


Figure 8. 16 way LO power splitter using cascades of Wilkinson 3 dB splitters.

An ideal, 2 output RF power splitter will send half the input power to each output port, hence a 3 dB insertion loss is incurred. The 12 dB minimum theoretical power splitting loss (4 x 3 dB) in Figure 8 implies an LO source power of 12 dBm (15.8 mW) would be required for the BFP740F mixers and 8 dBm (6.3 mW) for the HMC264LC3B mixers. However, 16 HMC264LC3B mixers will draw 1.2 W and cost £ 912. In contrast 16 mixers using BFP740Fs cost £ 7 and draws 0.144 W. Therefore, for large scale RX sounder systems, it is proposed that a set of BFP740F transistor-based mixers as presented in Paper 3 [3] would be a good option in terms of both cost and overall power consumption.

4. 3. 2. Recent Works in Mixer Technology Applicable to Channel Sounders

In this subsection, relevant prior works that have made specific use of mixers in mmWave systems that could be used as part of channel sounder designs are introduced - to illustrate relevance and importance of the topic. Mixers using SiGe are a key focus, as this relates directly to Paper 3 [3].

In this thesis, a single SiGe BJT device is modelled in mixer use. As an alternative, the nonlinear modelling of pHEMTs (i.e. FET topology) to address their use in mmWave mixers is introduced in [91]. However, pHEMT mixers have been a well-researched topic for many years.

Most of the recent published works use mixer designs based on the well-known Gilbert cell architecture. Whilst this is applicable to SiGe BiCMOS and general CMOS technologies (where multiple metal layers are available for signal routing) this type of mixer is hard to implement in MMIC designs that have only one metal layer. At present this prevents the application of the Gilbert cell to advanced III-V materials, such as InP, which are required for high sub-THz or THz operation. Hence, the continuing relevance and attraction in simple, single-device mixers as presented in this thesis.

SiGe is an important technology for low mmWave transceiver and mixer design and is now becoming more widely used, as illustrated by the following examples. A SiGe BiCMOS E band transceiver (71-76 GHz and 81-86 GHz) which incorporates a Gilbert cell in TX and RX stages is reported in [92]. A SiGe image reject mixer operating at up to 20 GHz for incorporation into self-aware systems is described in [93]. A self-aware system can apply a self-generated (hence known) test signal to itself to help calibrate itself and diagnose performance degradation in the field. Such a system can thus adapt itself to attempt to maintain a constant delivered RF performance. Transmit and receive mixers operating at 60 GHz and implemented in 130 nm SiGe are presented in [94]. The mixers draw 15 mW from DC supply and require a 0 dBm LO. A 28 GHz channel sounder using SiGe bespoke designed chips is presented in [88]. The bespoke SiGe chips implement a phased array beam former and also used a Gilbert cell mixer design. The sounder created four parallel sounding beams (linked – not independently controlled) that can sweep the channel.

SiGe is now increasingly capable of operation to high mmWave bands, due to transistor transition frequencies of circa 500 GHz becoming available. In [95] a 154 GHz mixer in SiGe using a modified Gilbert cell called a ‘micromixer’ was designed and tested. A 275 GHz RX chain using 130 nm SiGe with a modified Gilbert cell mixer topology was explored in [96]. The RX chip consumed 438 mW DC current. A D band (110-170 GHz) quadrature receiver in 130 nm SiGe and using a double balanced Gilbert cell mixer is presented in [97]. The receiver consumed 34 mW from the DC supply. A SiGe 90 nm 140-170 GHz receiver also using a Gilbert cell (requiring 3 dBm LO power) and overall drawing 136 mW DC power is described in [98].

At lower mmWave frequencies CMOS is applicable. In [99] a CMOS 5G (FR2 band) mixer operating at 24-40 GHz is presented. The mixer used coupled resonators within a double balanced mixer cell and drew 28.3 mW from the DC supply. In [100] a CMOS up and down conversion (bidirectional) mixer for FR2 allocation at 39 GHz is presented, drawing 39 mW. A double balanced Gilbert cell mixer in CMOS for 5G NR FR2 use at 24-40 GHz is presented in [101]. The mixer required a -10 dBm LO power and drew 50.9 mW DC.

4. 4. Paper 4 – 28 GHz Portable Channel Sounder and Close to Ground Sounding Usage

Paper 4 [4] is a complete propagation measurement system at 28 GHz and so the resulting bespoke RF hardware and signal processing is directly aligned with the overall focus of the thesis. The 28 GHz band is important for 5G and 6G communications. The recent availability of packaged commercial generic RF chips working at 28 GHz was a key reason to develop this sounder. All RF hardware was developed from scratch. The algorithm used is developed onwards from that described in Paper 1 [1]. One key enhancement is around the SDR used for both TX and RX signal generation. This paper uses an ADALM Pluto which is based on an Analog Devices AD9363 series SDR and provides faster sampling rate of 61.44 Msamp/s and operation to 3.8 GHz (here used as a 2 GHz IF for the 28 GHz front end).

The core contributions of the paper are twofold: 1) a new compact, hand-portable channel measurement system having the best dynamic range and RF hardware offering widest bandwidth of published sounders; 2) Measured data and extracted models for propagation scenarios close to ground at 28 GHz (no previous published data for such outdoor use case has been seen).

The sounder theoretical system design is fully presented. The built system is verified against expected RF performance using calibrated lab test kit. The field trial propagation measurements are compared to standard models and other published results, using log-normal modelling techniques.

The hardware design has been made open-source to support other researchers and industry working in the area needing low cost, high performance equipment [102]. The measured propagation results show that long range, close-to-ground communications at 28 GHz are possible with low loss: close to free

space path loss (FSPL). The new measurement data and resulting models at 28 GHz from the field tests show the usefulness of the bespoke sounding system in supporting unusual measurement scenarios.

The work of Paper 4 [4] led to a project at the National Spectrum Centre's Frongoch Farm site at the University of Aberystwyth, to investigate close-to-ground 28 GHz propagation in a rural environment.

4. 4. 1. Frongoch Farm and National Spectrum Centre Tests

The 28 GHz sounder system of Paper 4 [4] was later used in a measurement project at the National Spectrum Centre (NSC) [103], supported by QinetiQ. Tests were performed by Edward Ball, research associate (RA) Sumin David Joseph and PhD student Bill Gavin. Tests were performed on the 28th February 2023 to 1st March 2023. All sounding tests were performed at 27.65 GHz.

Extensive measurements of close-to-ground propagation around a rural farm setting were investigated, with path loss results obtained and PL models extracted. This allowed the system to uncover propagation characteristics at 28 GHz in scenarios that would be extremely challenging to perform using lab equipment. The routes tested (A, B, C, D, E, F, G, H, N) are illustrated in Figure 9. Examples of the tested routes are also shown in Figure 10 - Figure 17.

The tests using routes A-H were setup with a transmitter fixed at one end of a route to be tested and the sounding receiver then moved along the whole route - moving away from the TX and stopping at various distance intervals. At each stopping point, the RX was moved locally a few centimetres and the sounding measurement repeated a few times to capture any short-term or local fading effects. Distance was measured using a measuring wheel. Each sounding measurement took under 1 minute to complete, with the majority of the field test time taken by moving the equipment. For route N both the RX and the TX systems were moved as a pair (discussed below).

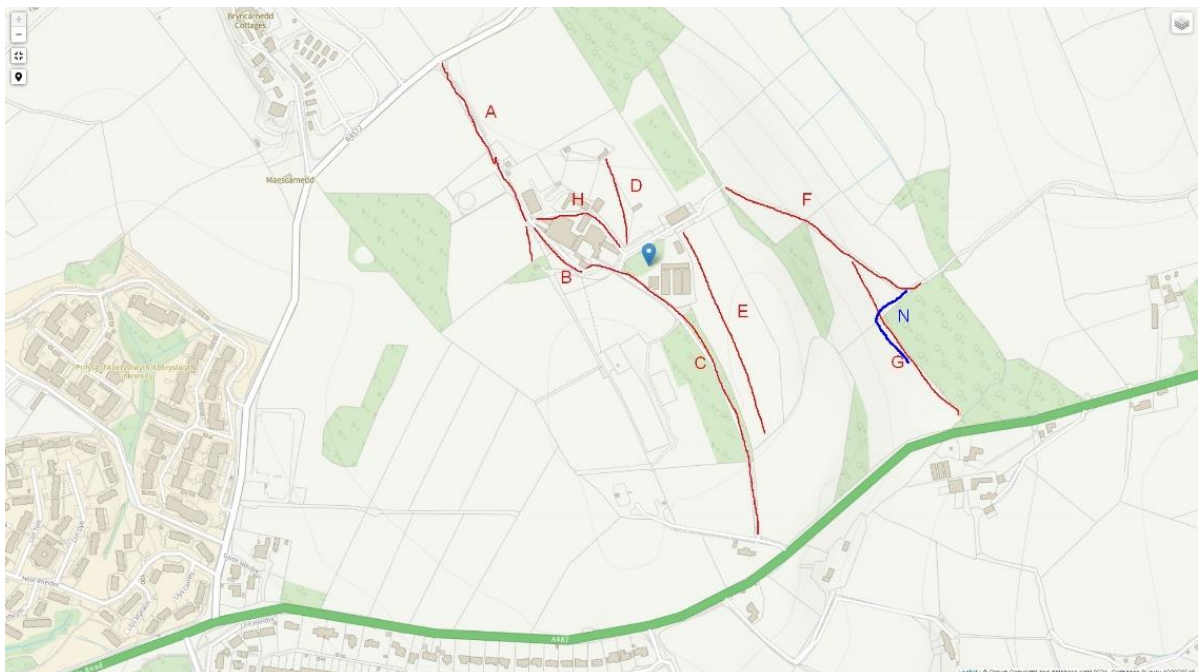


Figure 9. Propagation test site routes A, B, C, D, E, F, G, H, N at the National Spectrum Centre, Frongoch Farm, Aberystwyth [Google maps: Map data ©2023 Google]. TX and RX systems together sound 1 route.



Figure 10. One of the sounder systems in a cart (route A). The 28 GHz horn antenna can be seen in stand on left of cart.



Figure 11. Propagation sounding around the edge of a farm dwelling (route B).



Figure 12. Propagation measurement along a road and into a wood (route C).



Figure 13. Propagation grazing the top of tall grasses (route D).



Figure 14. Propagation over a bank - towards a cow shed (route E).



Figure 15. Propagation in presence of metal buildings (route H).



Figure 16. Propagation through a wooded scrub area (route N) – RX site.



Figure 17. Propagation through a wooded scrub area (route N) – TX site. RX system is on the other side of wood. Both TX and RX start near the gate on the left and are moved away from each other to increase the path length through the wood.

The tests and propagation models emerging from Frongoch are discussed in a paper authored by the RA [7]. However, some additional observed data and fitted models are presented and discussed below, as illustration.

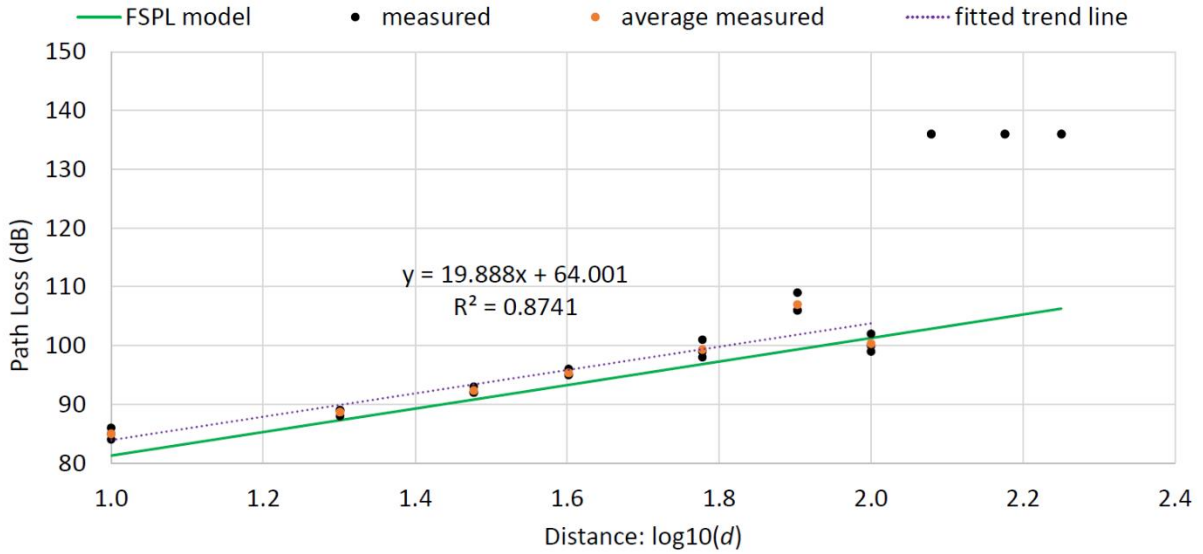


Figure 18. Route B measured propagation data and fitted model. (Route B is 178 m in total length and around the side of farm buildings, on a rough road).

In Figure 18, corresponding to Route B, we see the 27.65 GHz PL close to FSPL (5) for up to the 100 m TX-RX distance (after this point a building obscures the direct LoS path and the PL reaches the measurement floor – signified by the 3 PL results near 135 dB). Averaged results for a location are based on 10 individual measurements.

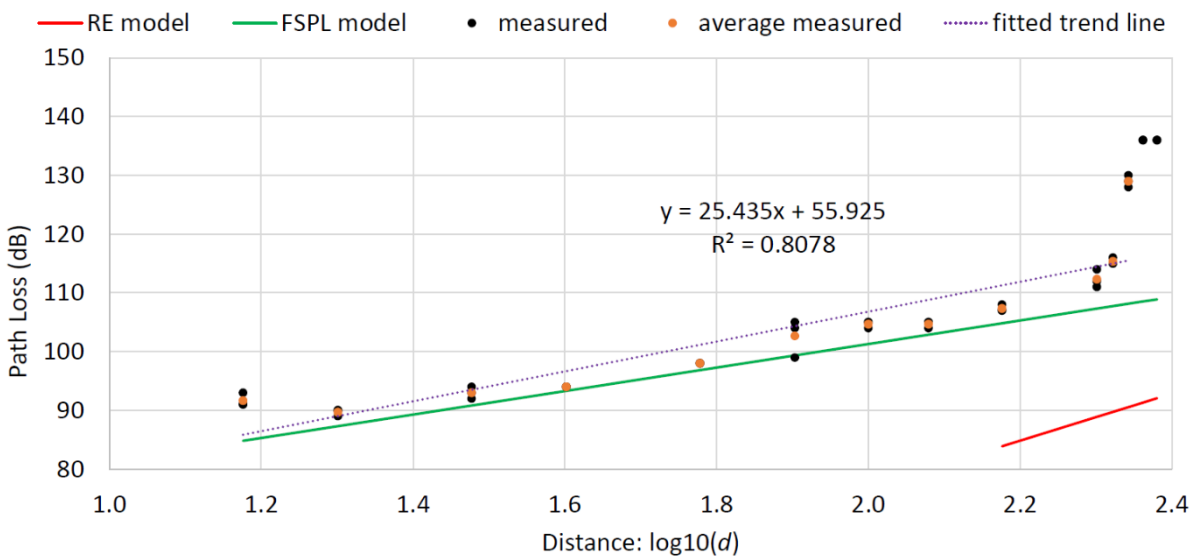


Figure 19. Route E measured propagation data and fitted model. (Route E is 240 m in total length and through an open, clipped grassy field, rising up to a brow and then descending again behind it).

In Figure 19, corresponding to Route E over clipped grazing grass, we see the PL is also close to FSPL up to the 200 m TX-RX distance. After this point the brow of a hill obscured the direct LoS path and so the PL quickly degrades to the sounder’s measurement floor. The RE model (7) was used.

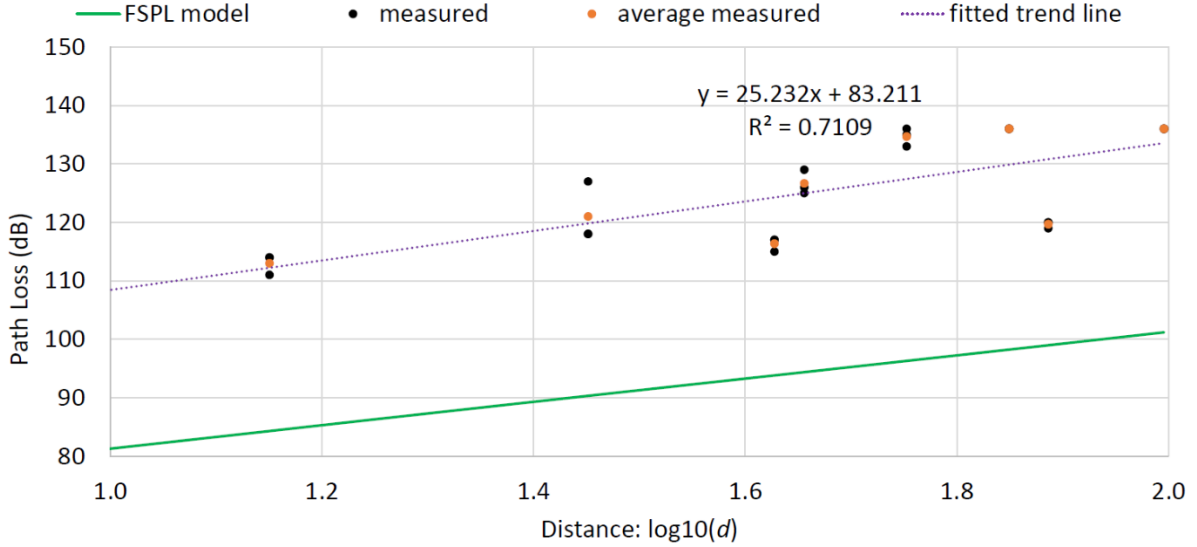


Figure 20. Route N measured propagation data and fitted model. (Route N is 99 m in total radio path length, through a wooded scrub area).

In Figure 20, corresponding to Route N through a wooded area, we again see a PL with similar slope to FSPL but with a higher fixed offset. For this test, both the TX and the RX were moved together as a pair. This was to create a radio signal path length through the wood representing the hypotenuse of a triangle (TX and RX moving along the edges of the wood – i.e. the other sides of the triangle). It can also be seen in Figure 20 that there is significant variation in readings (over short-changes in distance), which is due to the random chance of the LoS path being obscured (or not) by a tree trunk. In addition to the tree trunks, there is also additional scrub and bushes which lead to a general increased PL. It is proposed that a new bespoke model is needed to best represent this unusual PL scenario, possibly including a statistical parameter to represent the likelihood of a signal intercepting a trunk or not (based on a plantation density in an area of interest).

4. 5. Paper 5 – RX Subsampling TMA Concept and Prototype

The TMA concept, as first explored in Paper 2 [2], can also be applied in an RX context. Because of the inherent switching function used in the TMA, it is possible to include other functions in the RX TMA that can make use of the switch and Paper 5 [5] does this by incorporating a subsampling feature. This combining of the TMA and subsampling – named the *Subsampling TMA* (STMA) is a new and potentially powerful signal processing concept.

Paper 5 [5] shows how a phased array in RX with direct subsampling to a low IF can be realised by simple RF hardware (principally focused on an RF switch and sampling circuit). This concept can be extended to frequencies beyond the RF switch’s operating capabilities by use of a mixer-first strategy. This could potentially allow a reduced cost and complexity mmWave RX phased array to be realised.

In the context of a channel sounder, the STMA as published in Paper 5 [5] could be used to steer a single RX beam and so be used in a conventional channel sounding application, such as to identify AoAs. The beneficial simplifications here are that the STMA is digitally controlled, and a low IF is produced due to the subsampling- simplifying the required complexity of any attached sounding RX SDR.

Since publishing Paper 5 [5], an improved method to calculate the array conversion gain (ACG) of the STMA has been identified, reported in [8] and now shown in (18).

$$ACG = G_{cell} + 20 \log_{10}(N) + 20 \log_{10} \left(\frac{T_{ave}}{T_p} \right) \text{ dB} \quad (18)$$

In (18) G_{cell} is the gain of 1 STMA cell, N is the array size and T_{ave} is the average on time of all TMA cells in a frame period of length T_p . It can be seen in (18) that it is advantageous to maximise the T_{ave} .

4.5.1. STMA for use in Angle of Arrival Sounding RX

In channel sounding, a potentially useful novel feature of the STMA are the harmonic beams that are created at the IF output of the RX. Each of these discrete frequencies correspond to a particular phase applied to the incoming RF radiated signal at each element. This means that each RX harmonic beam seen at the IF corresponds to a phased array equivalent angle of arrival beam, allowing multiple arrival beams to be separated in frequency at the same time instant, as shown spectrally in Figure 21.



Figure 21. An RX TMA (e.g. STMA) converts from a carrier ($C0$ boresight beam at carrier) to a set of harmonic beams, each centred at an angle of arrival for that beam.

This use of the RX STMA would allow it to resolve the angles of arrival of multiple rays all in time coherence, since no RX beam sweeping is needed. This could allow temporal effects of a channel to be observed on the AoA, which is hard to do with a swept beam. This harmonic beam sounding concept is further investigated in TMA TX mode for Angle of Departure sounding in Paper 6 [6].

Direction of Arrival (DoA) and Direction of Departure (DoD) measurements are now commonly performed in channel sounding campaigns. As an example, in [104] the DoA was extracted from sequential observation using 32 antennas in an array, with each element used in sequences (one at a time) and with the array rotated in set angles. The concept was then used in a full channel sounder measurement system [105]. The AoA in a mobile setting was extracted in [106] using the ESPRIT technique, as an alternative to MUSIC. The sounder used 31 switched antennas, with each antenna observed in turn for the duration of a sounding PN sequence. However, these techniques all used sequential beam switching, which can be slow.

4.6. Paper 6 – TX TMA Channel Sounder for Angle of Departure Soundings

The TMA in TX mode generates a fan of harmonic beams. If the RF switch control waveforms are suitably designed (i.e. as a cascade of sequential switches being turned on and off in sequence) then the TX radiated harmonic beams are all present and have high power. As such, they can be used to illuminate a channel in different angles of departure simultaneously, as will now be discussed.

An example of the required RF switch control staircase waveform is shown in Figure 22, for an 8-element array.

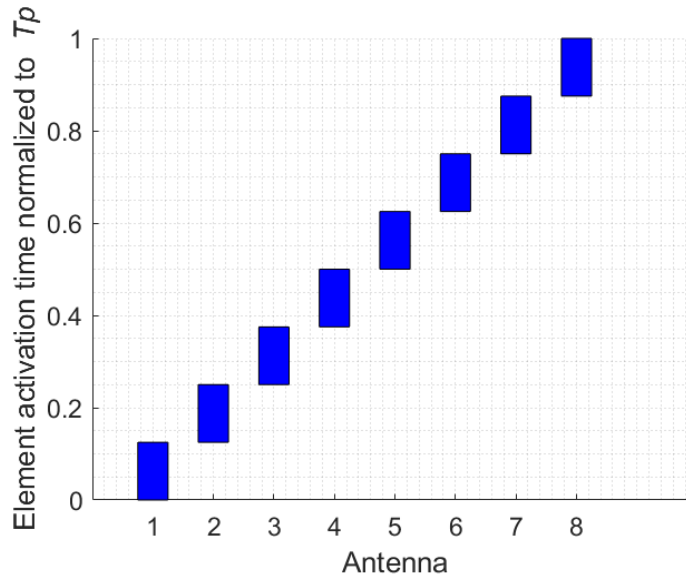


Figure 22. TMA switch control – example for an 8-element array for use in TX sounder.

This approach contrasts with conventional techniques that either steer a beam from a phased array or physically rotate a TX antenna. In prior works, AoA and AoD are commonly reported as measured in MIMO channel sounders by post-processing the switched beams emitted from each element in turn, [104], [105], [106]. Depending on the end application and if channel reciprocity is applicable, AoD may be used as a proxy for AoA at the same side of the link, if it is more convenient to measure.

When using separate mmWave oscillators at the TX and RX sides of a sounder, frequency drift and phase drift can be a problem. Many systems use the GPS 1PPS as a time synchronisation, benefitting from the precision of GPS atomic clock timing. However, this may not be possible indoors, with poor GPS reception. When long duration tests are needed (such as for sequential beam switching in channel sounding) mechanisms to compensate for the phase drift are important research topics. A technique to compensate the phase drift in an LO in a channel sounder used in angular measurements at mmWave over a long run of tests is presented in [107]. An advantage of the TMA architecture here is that multiple beams are transmitted at once, which will reduce the scan time required and so reduce or remove the need for such carrier phase drift correction.

The number of active elements in the TMA defines the available sounding angular range and the actual angle of emission for each TMA harmonic beam. Simulations of example beam locations illustrating this effect are shown in Figure 23 - Figure 25.

TMA 6 element beam pattern for channel illumination

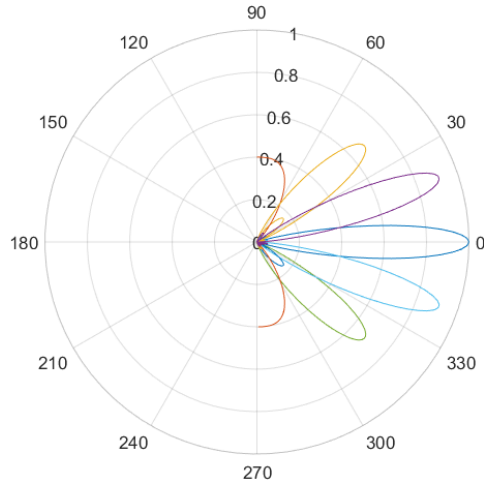


Figure 23. TX TMA simulation of harmonic beam angular positions for a 6-element array.

TMA 8 element beam pattern for channel illumination

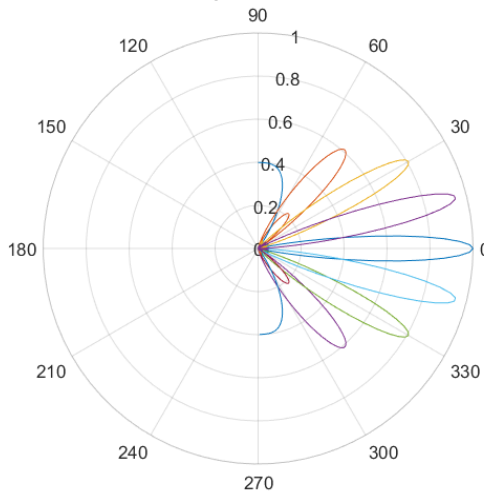


Figure 24. TX TMA simulation of harmonic beam angular positions for an 8-element array.

TMA 16 element beam pattern for channel illumination

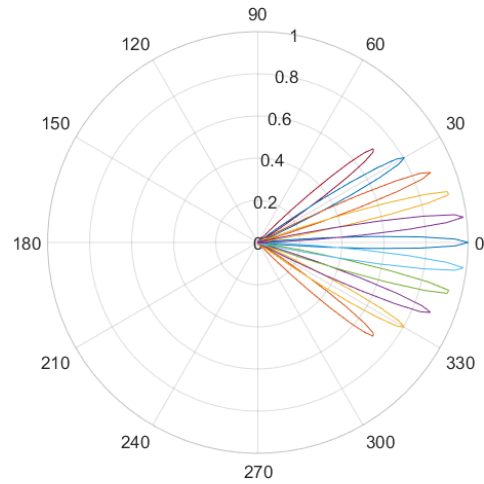


Figure 25. TX TMA simulation of harmonic beam angular positions for a 16-element array.

Since the TMA array is constructed of RF switches (or equivalent circuit functions), it is easy to dynamically select the actual number of active radiating elements by enabling or disabling groups of switches; and hence control the position of the harmonic beams as required for a particular sounding scenario.

In Paper 6 [6], a single modulated TX PRBS signal is generated by the TX SDR (an ADALM Pluto) and the TMA hardware then converts this to a set of harmonic beams. Paper 6 [6] additionally identifies the necessary relationship between the PRBS modulated sounding signal BW and the TMA frame frequency F_p . The initial TX spectrum for the PRBS modulated carrier prior to application to the TMA RF input is shown in Figure 26 and the unmodulated TMA TX signals (showing TMA CW harmonic beams) is seen in Figure 27, clearly showing the need to manage the sounder modulation BW.

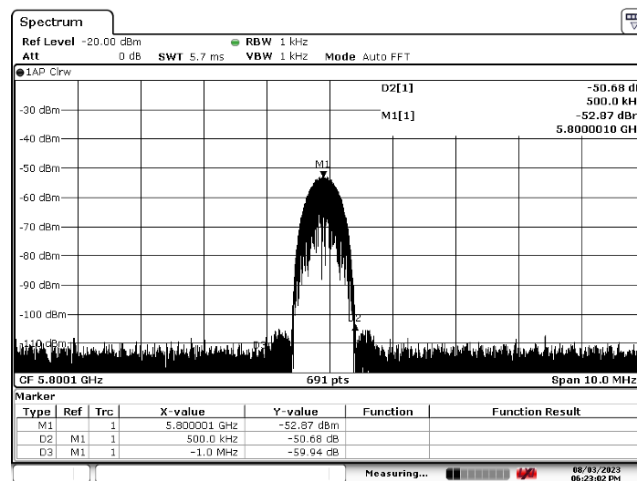


Figure 26. PRBS modulated signal used in channel sounding - as applied to TMA input.

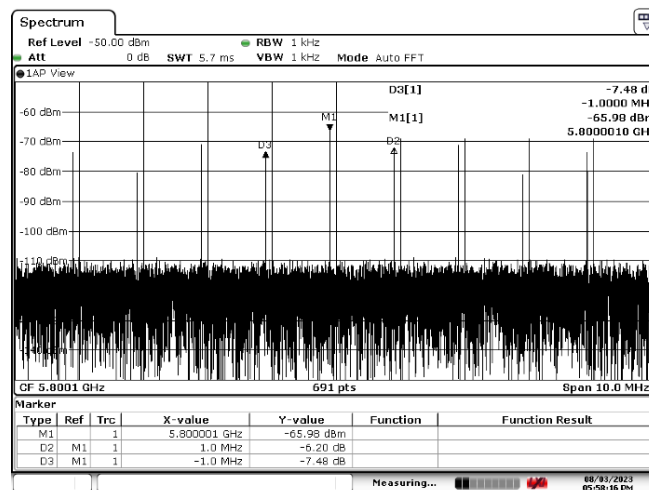


Figure 27. TMA spectral emission with CW carrier applied – note the expected harmonic beam spacing of 1 MHz.

When the input PRBS modulated 5.8 GHz carrier is applied to the TMA, the desired TX sounding beams are produced. Example spectrum analyser captured emission spectra for two different omnidirectional RX antenna locations are shown in Figure 28, showing illustrative differences in AoD beam powers that could be resolved by a sounding RX.

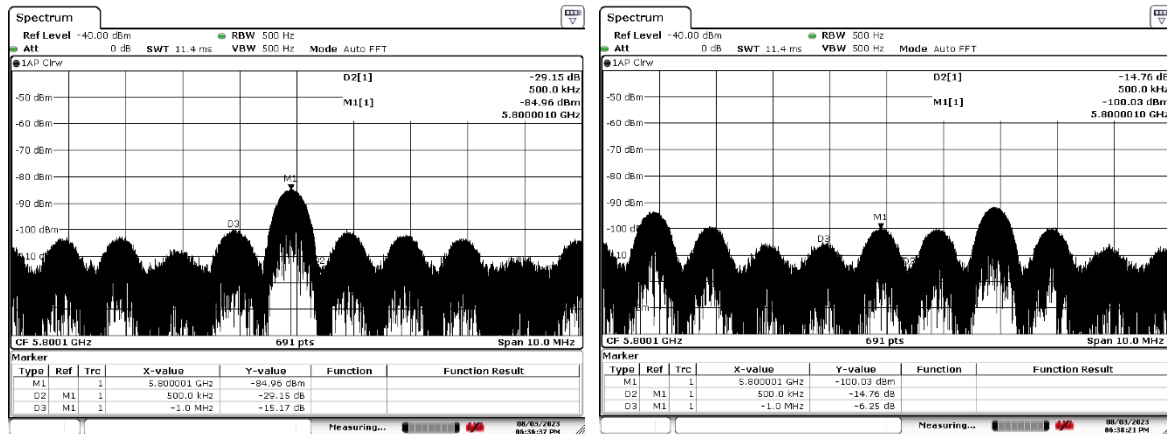


Figure 28. TMA spectral emission with PRBS modulated carrier applied - illustrative examples for 2 different RX antenna locations showing the difference in RX beam powers that would represent AoD powers.

Similar to Paper 1 [1], a correlation between the RX signal and the known TX PRBS is used to resolve the time domain delays, but now on each beam. A related key aspect in this paper is the demonstration of the frequency offset (implicitly applied to each sounding TX beam) due to harmonics of the TMA frame frequency F_p being correctly handled. This effect is accommodated in the sounding receiver by it correlating against the PRBS rotating at an IF offset of each multiple of the harmonic frequency F_p (i.e. specific to each beam).

The multi-beam sounding algorithm concept was initially tested using a Matlab simulation, using a test channel that applies a specified delay and amplitude scaling to each of the TMA harmonic beams. The simulation settings used are shown in Table 2 and the $C0$ beam RX power was set to -50 dBm. The simulation thus creates a scenario with user configurable delay and amplitude scaling for the propagation channel that is carrying each of the 7 TMA beams ($C0 - C3n$). This allows the algorithm’s ability to independently resolve each TMA beam’s power and delay to be demonstrated.

Table 2. TMA AoD test simulation settings.

Beam	Beam amplitude applied by test channel (dB)	Beam delay applied by test channel (μ s)
$C0$	0	30
$C1p$	-2	40
$C1n$	-4	50
$C2p$	-6	60
$C2n$	-8	70
$C3p$	-10	80
$C3n$	-12	90

In all cases the RX TMA sounder algorithm correctly extracts the composite delay channel impulses for all the beams, as shown in Figure 29, and extracts each individual beam’s impulse as shown in Figure 30 - Figure 36 (compared to simulation setup defined in Table 2).

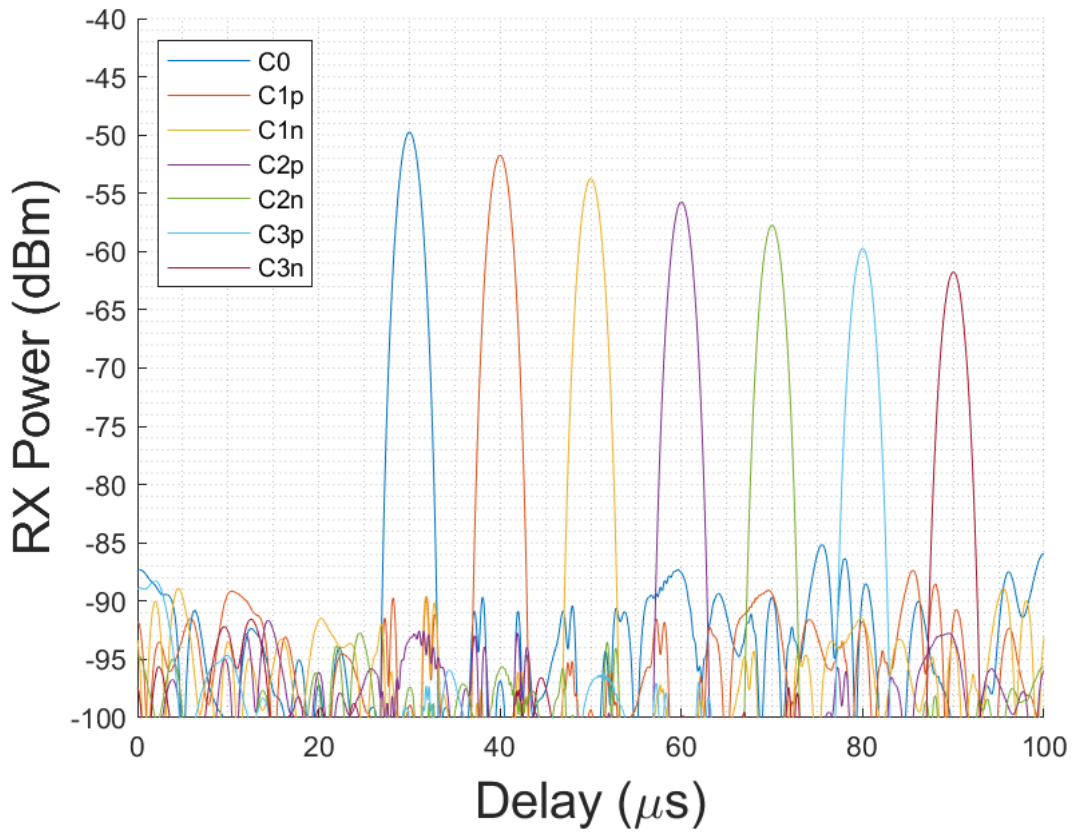


Figure 29. Example simulation of extracted beam delays and powers showing each beam has been uniquely resolved. (Here the applied signal was a 10 μs incremental path delay and 2 dB incremental path attenuation.)

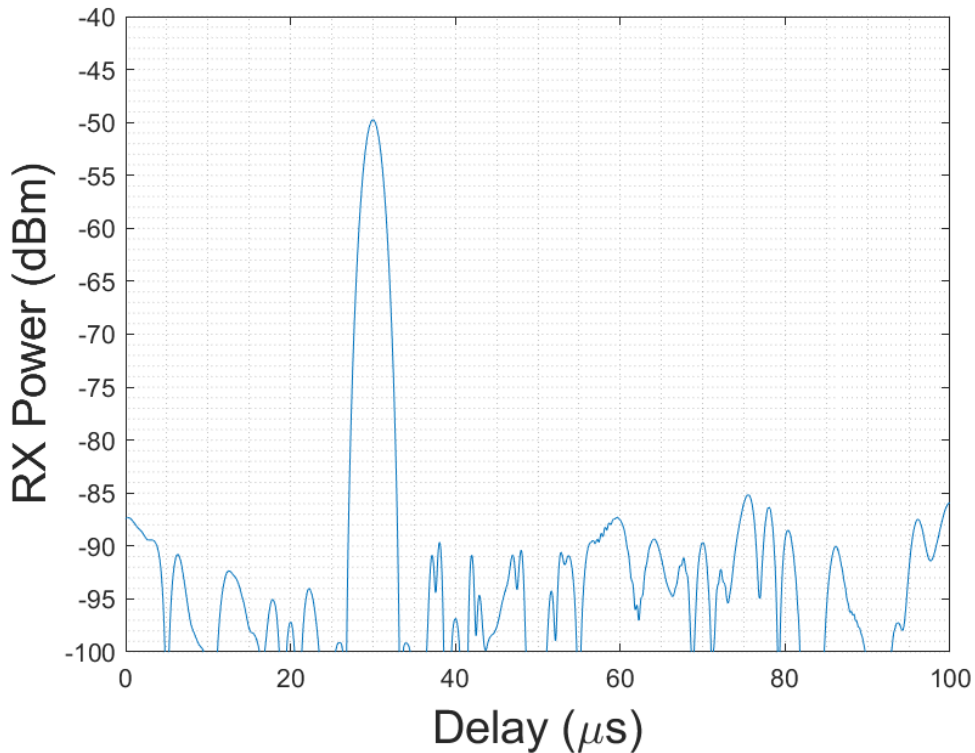


Figure 30. Example simulation of extracted C0 beam delay.

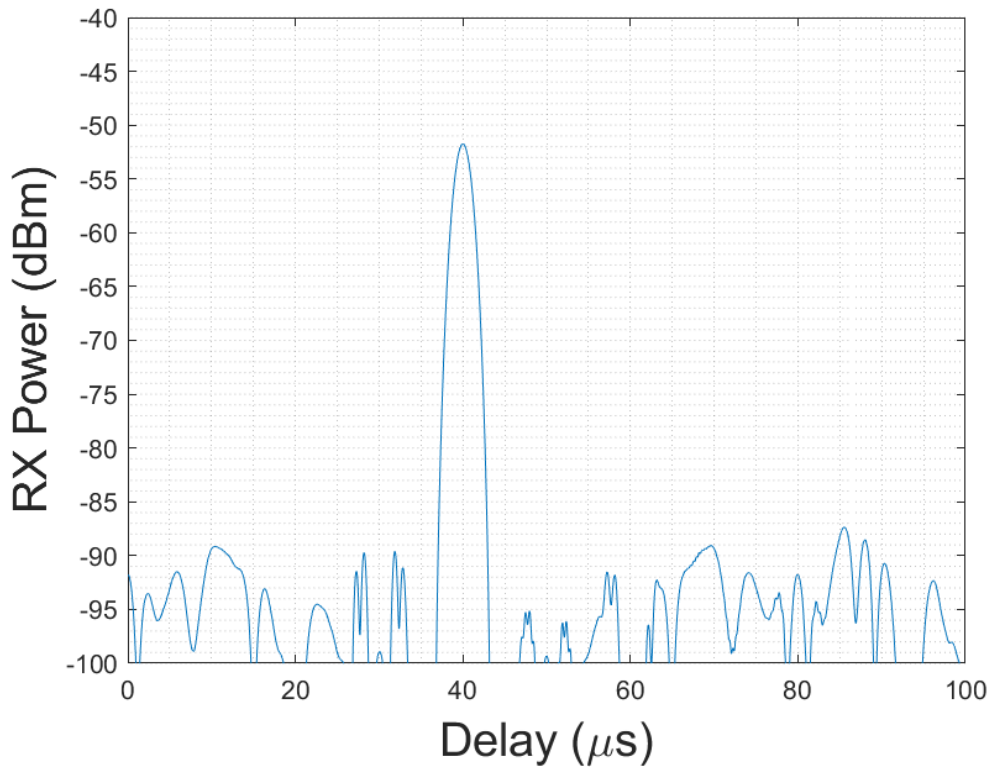


Figure 31. Example simulation of extracted C1p beam delay.

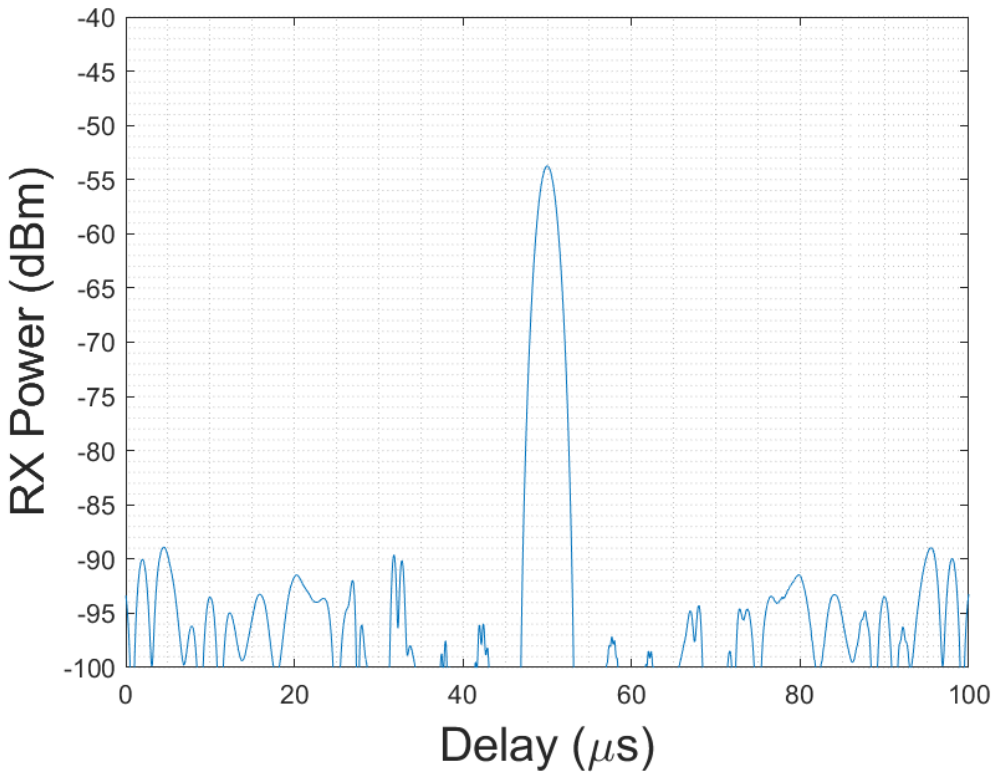


Figure 32. Example simulation of extracted C1n beam delay.

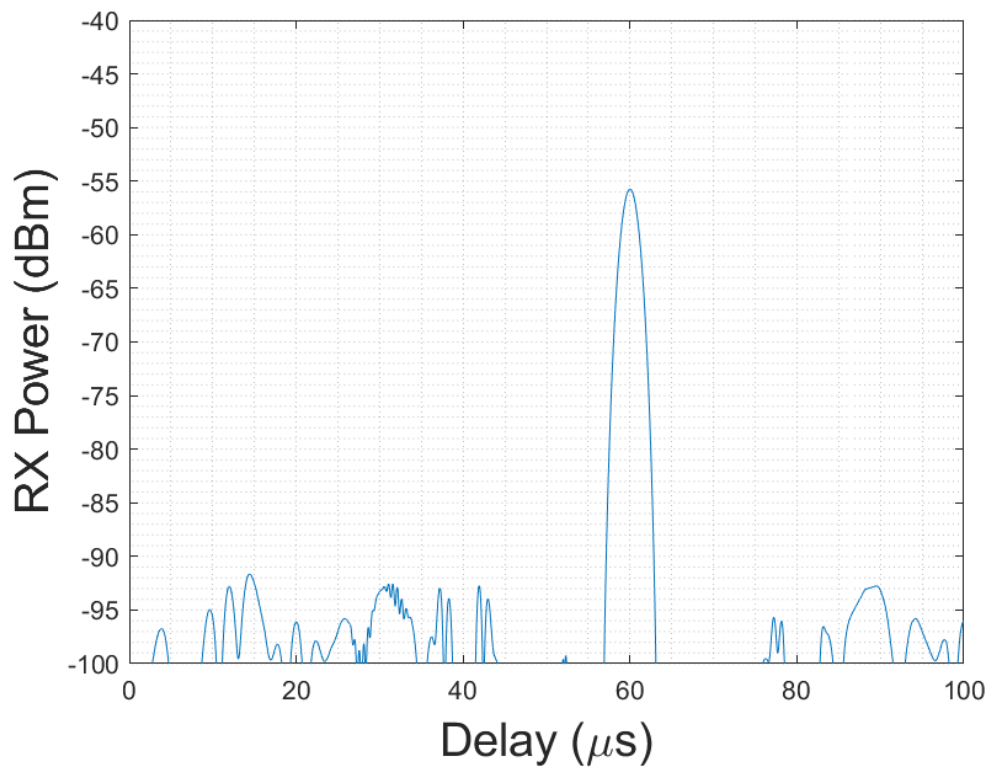


Figure 33. Example simulation of extracted C2p beam delay.

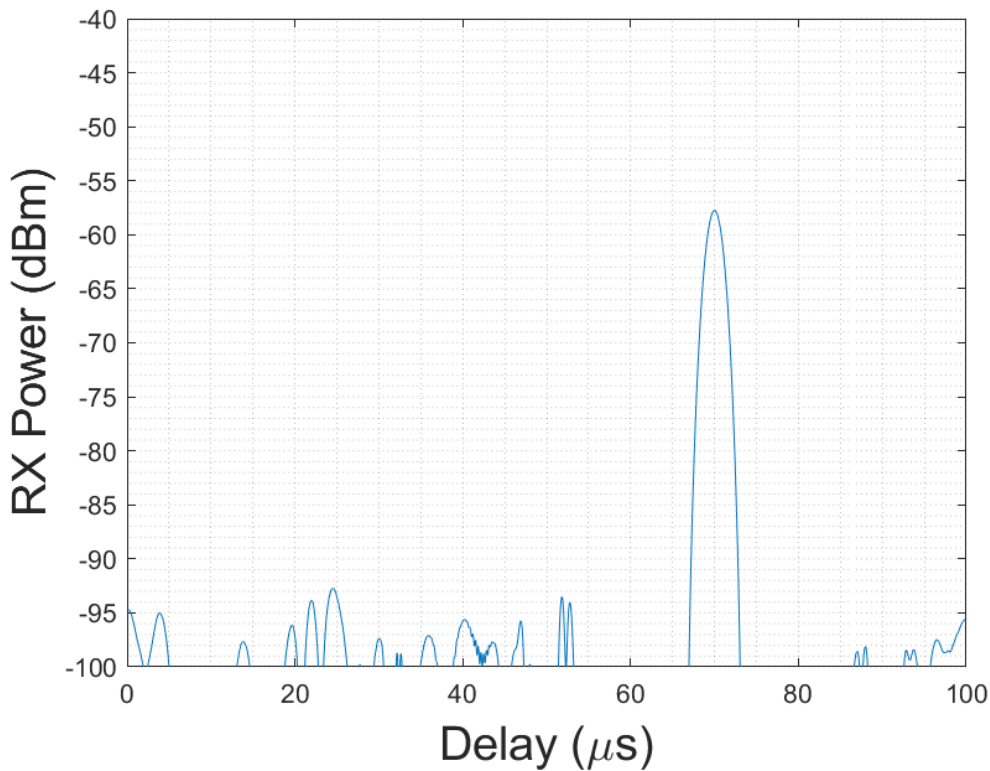


Figure 34. Example simulation of extracted C2n beam delay.

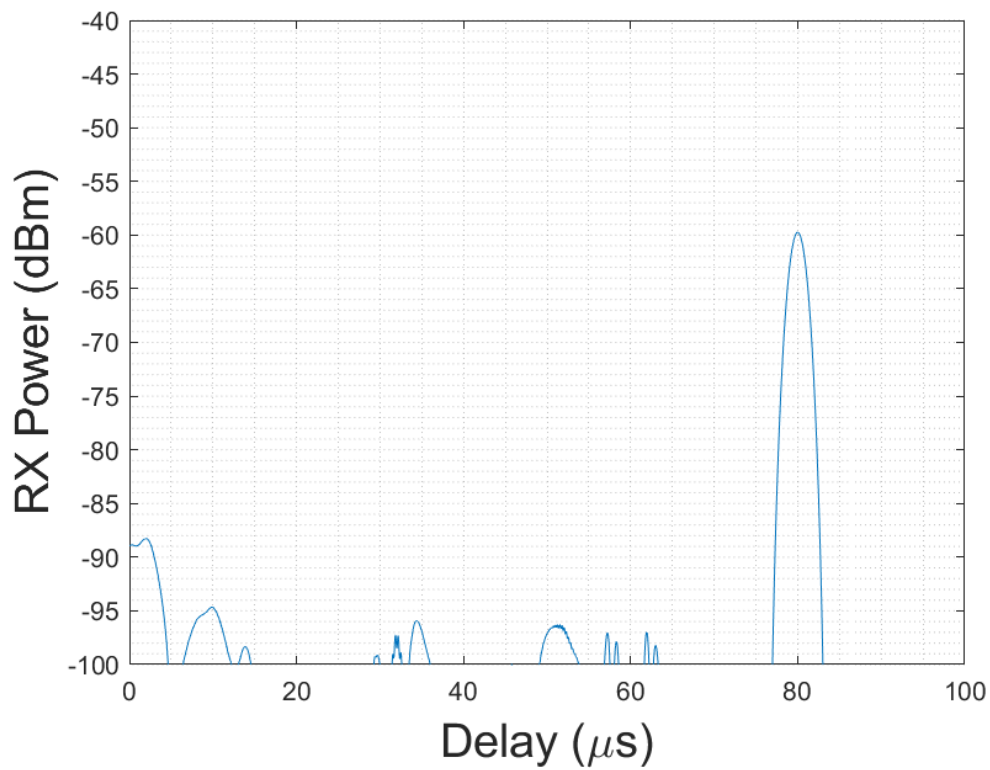


Figure 35. Example simulation of extracted C3p beam delay.

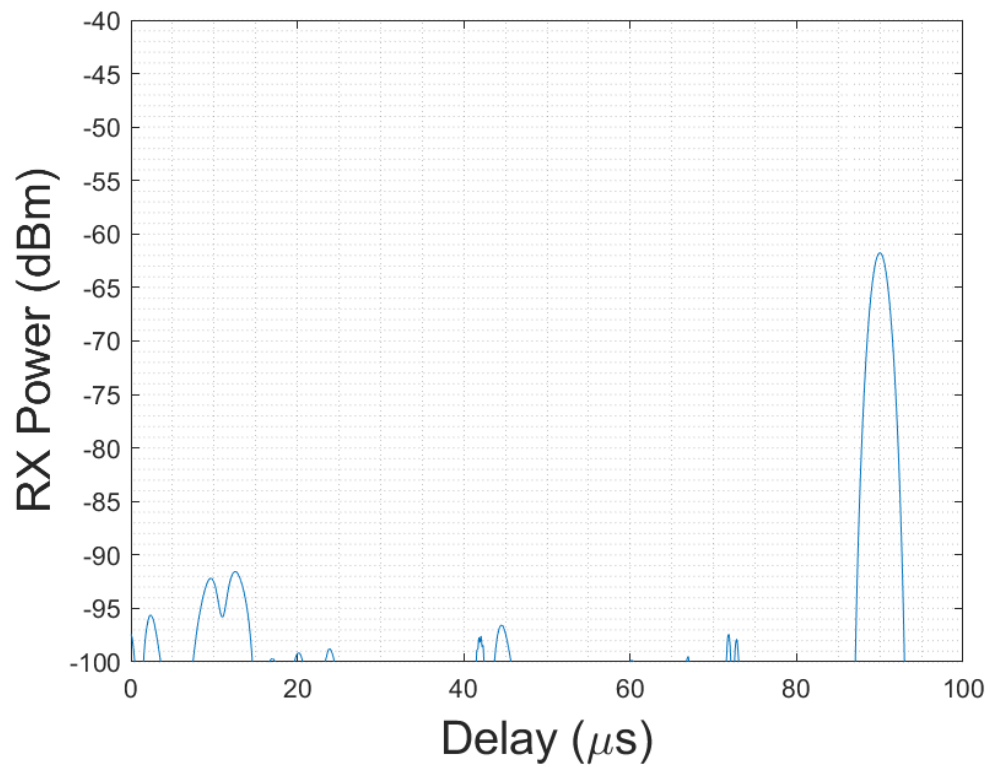


Figure 36. Example simulation of extracted C3n beam delay.

The work in Paper 6 [6] is the first demonstration of the TX TMA in a multi-beam channel sounder concept. The results for the measured indoor channels show reasonable agreement to ITU-R.P.1238-12 PL models, further confirming the usefulness of the approach.

The time domain resolution for the beam power delay profile is ultimately defined by the sampling rate of the SDR (which limits the sounding PRBS bit rate) and the switching speed of the TX TMA's RF switches (which limits F_p). In the current hardware the limiting factor is the RF switch (Analog Devices HMC7992). Future versions of the system should explore using faster RF switches, and potentially a faster sampling SDR, to enable improved indoor sounding with nano second delays as commonly required and reported by others.

However, an important contribution of Paper 6 [6] is the demonstration that the system can resolve delays *between* harmonic beams that are less than the theoretical limit imposed for detecting a delay on a single beam due to correlation of the PBRS bit period.

The use of the TMA in this new sounding concept allows a channel to be assessed in multiple discrete angles of departure at the same instant in time (thus providing temporal measurement coherence). This may allow certain time-dependent characteristics of a channel to be captured that could otherwise be missed when scanning a sounding beam.

4. 6. 1. AoD Angular Spread Measurement from the TX TMA Sounder

In Paper 6 [6], indoor testing was performed in a Café and a Corridor area, to show the applicability of the TMA in sounding real channels, as illustrated in Figure 38. Angular Spread (AS) assessments have subsequently been performed on the measured data and are now presented in this subsection.

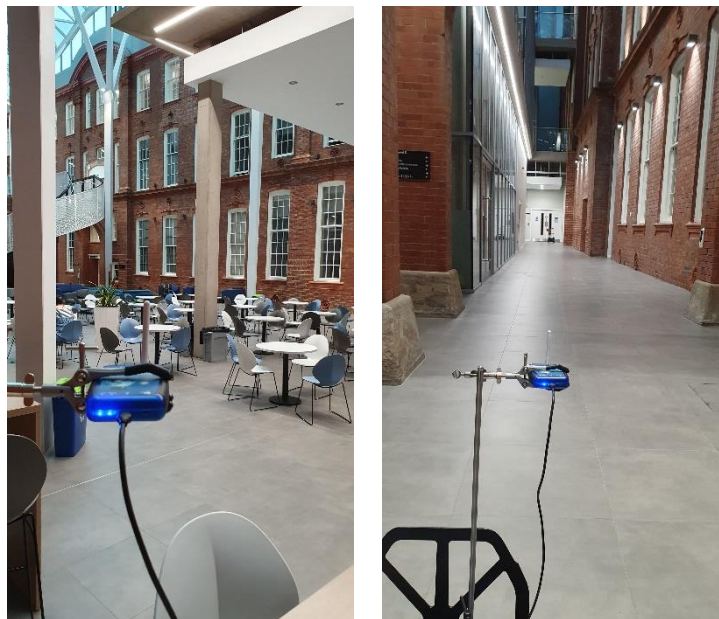


Figure 37. Example test sites from Café scenario (left) and Corridor scenario (right), as seen from example RX SDR locations.

An AS calculation is usually applied to the angularly resolved multipath components resulting from a sounding run. This could instead be inferred from sweeping a narrow beam at the TX or RX. In the TMA system, the sounder is illuminating a channel in several defined beam directions all at once. These discrete beams could be considered as (some of) the MPC paths that would exist if an omnidirectional TX antenna were used. Therefore, a limited calculation of the channel AS can be performed using the TMA sounder system as demonstrated.

The RMS AS calculation for the TMA sounder uses the method described in Section 1. 8. 3. The resulting RMS AS for the Café scenario as described in Paper 6 [6] is shown in Figure 38. As seen in the Paper, most of the MPCs in the measurements appear coincident in time for a given pointing angle, since most reflection delays were generally below the measurement resolution of the system.



Figure 38. Calculated RMS AS for Café scenario (TX array rotated in steps for each TMA run, constant distance to RX).

Figure 38 shows that AS is a minimum when the TX array is pointing directly at the RX, but tends to increase as the TX array is physically rotated away (possibly due to more opportunity for illumination of adjacent reflecting surfaces and a less dominant LoS beam).

The resulting RMS AS for the Corridor scenario as described in the paper is shown in Figure 39.

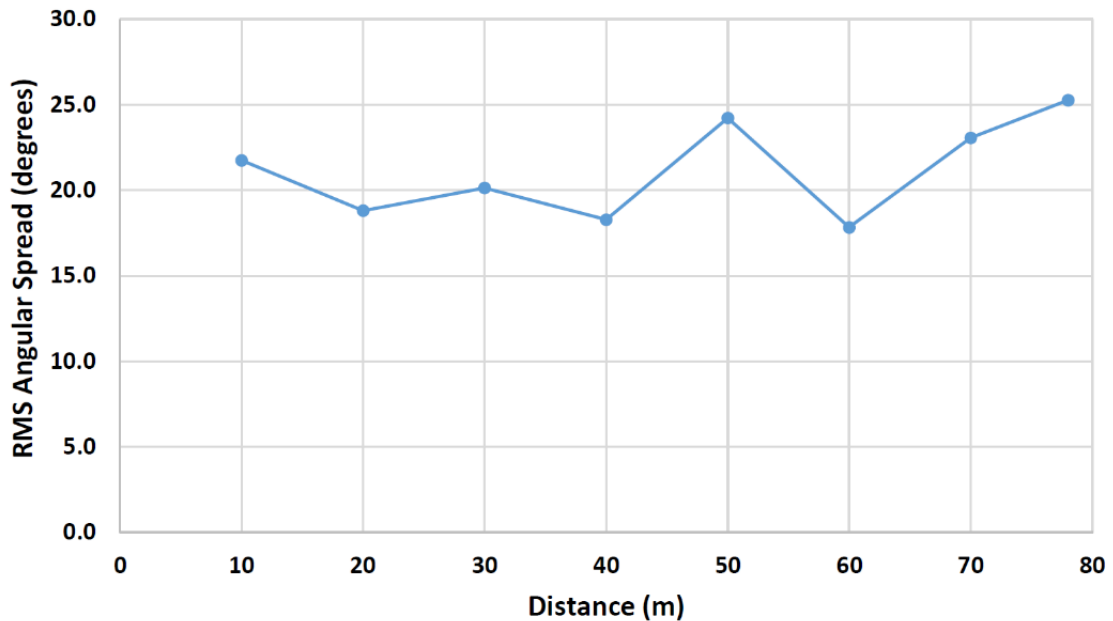


Figure 39. Calculated RMS AS for Corridor scenario (TX array pointed at RX and only distance is varied).

In the corridor scenario, the AS varies little over the 10 – 40 m test range (likely due to the TX array always pointing directly at the RX). However, a more notable (though still small) variation is seen at 50 m. This small change corresponds to a location where the mobile RX was moving from a region with only an adjacent brick wall as the suspected main source of reflections, to a region now also including adjacent structures of the nearby Café building. The AS also appears to be increasing after 60 m.

Both the above graphs show the applicability of the TMA for (at least) indicative AS measurements.

AS usually does not consider MPC delay. The novel feature of the TMA sounder's ability to resolve the delay between the harmonic beams could be used to extract AS as a function of path delay, when multiple beam MPCs are resolved. This could lead to a set of graphs for AS vs delay, all from a single measurement run.

5. Paper 1 – Portable VHF / UHF IoT Sounder

{Reproduced as published – author accepted version.}

© 2019 IET. Reprinted, with permission. E. A. Ball, “Design and field trial measurement results for a portable and low-cost very-high-frequency/ultra-high-frequency channel sounder platform for Internet of things propagation research,” IET Microwaves, Antennas and Propagation, vol. 13, no. 6, pp. 714–724, May 2019. DOI <https://doi.org/10.1049/iet-map.2018.5827>

(Published version [1].)

Design and field trial measurement results for a portable and low cost VHF / UHF channel sounder platform for IoT propagation research

E. A. Ball¹

¹Department of Electronic and Electrical Engineering, The University of Sheffield, Sheffield, S1 4ET, UK
e.a.ball@sheffield.ac.uk

Abstract: Propagation research is vital for informing the design of reliable VHF and UHF communications systems for the Internet of Things (IoT). In this paper, a cost-effective and highly portable system is proposed and then used to obtain propagation measurements in city and suburban scenarios at 71 MHz and 869.525 MHz. The system calculates the received power, power delay profile and channel frequency response. The portable sounding receiver uses readily available parts: an RTL-SDR (covering 27 MHz – 1.7 GHz) and a Raspberry Pi with touchscreen. The Pi implements all the channel sounding signal processing algorithms in Python, in near real-time. Extracted propagation data and models are presented, from example city and suburban field trials incorporating pedestrian and car use.

1. Introduction

Industrial and commercial interest and application of the Internet of Things (IoT) continues to grow, with both standards-based solutions and multiple proprietary systems jockeying for adoption. Emerging systems include NB-IoT and also 802.11ah “HaLow” [1] as well as the commercial LoRa [2] and Sigfox [3] systems. Even though systems are being brought to market, there still exist many fundamental research opportunities for antennas and propagation, in IoT specific use cases. There is also a need for practical systems to evaluate propagation performance and link budgets, for commercial applications and also for use in student teaching. A particular area of valuable research involves long range RF systems that are very low power and low cost, possibly powered by coin cells (e.g. CR2032) and supporting high reliability use cases, with multi-year life expectancy. Such devices could serve, for example, in connecting future city infrastructure or ubiquitous social care and healthcare systems.

VHF spectrum at 55-68 MHz, 70.5-71.5 MHz and 80.0-81.5 MHz has been promoted by Ofcom in the UK for use in IoT applications [4]. In the EU, Short Range Devices (SRD) spectrum in 863-870 MHz is widely employed for generic radio systems [5] and is where many commercial EU IoT systems currently operate. This is comparable to the 915 MHz Industrial Scientific & Medical spectrum widely used in the USA and Oceania.

Future high reliability and novel IoT radio systems may exploit multiple RF bands as well as reconfigurable modulation and cognitive radio aspects. This all requires fundamental, real world, understanding of the radio spectrum occupancy and usage, as well as propagation and noise floor characteristics for the bands.

To assist in the capture of IoT VHF and UHF propagation information, a low-cost, portable and frequency-agile system has been created and is described in this paper. The system consists of a fixed transmitter and a pedestrian portable Channel Sounding Receiver (CSR) [6]. The CSR allows near real-time capture and display of the channel response in operational environments, such as urban canyons or remote rural locations. The CSR system is built using an

RTL-SDR and Raspberry Pi 3B (R-Pi) with touchscreen- all powered by a USB battery power pack. The RTL-SDR imposes a maximum RF capture bandwidth (BW) of 2 MHz, but this is considered sufficient for our IoT propagation measurements since IoT radio systems for long range tend to not use multi-megahertz RF BWs (often significantly less).

This paper continues in section 2 with a discussion of IoT propagation; the channel sounding hardware used in section 3; channel sounding algorithm design in section 4 and lab testing of the system in section 5. Section 6 presents example measurements from a small scale city field trial campaign, followed in section 7 with results from a suburban measurement campaign. Section 8 presents models for the extracted propagation path loss data, suitable for use in IoT link budgets. Section 9 presents values for RMS delay spread, estimated from the field trial results.

The contributions of this paper are: 1) creation of a novel, low-cost, portable, near real-time channel sounding platform, 2) development of efficient algorithms for extracting the channel power delay profile and frequency response, 3) usage of the system to obtain example propagation data in suburban and city environments; leading to simple propagation models for use in IoT system design.

2. VHF / UHF Propagation and IoT Use Cases

The need for the CSR system emerged from our desire to be able to understand and model the propagation in various RF bands for specific use cases involving long range IoT communications. These use cases could include discreet body-worn miniature transceivers used for medical data telemetry and social care applications (fall detector alert systems, Alzheimer patient monitoring, etc). There are many other emerging diverse applications for the IoT, including control of industrial plant, city infrastructure and smart agriculture [7]. To be fully representative, the channel data should be extracted in the target use case (e.g. sitting, lying for social care applications) which requires compact and portable measurement equipment. Such insight is valuable for devising and creating novel future IoT systems, which may address un-met use cases. The VHF and UHF spectrum is particularly attractive for long range communications,

though antenna efficiency is often challenging. VHF and UHF propagation has been extensively studied over the years, for both commercial and military uses (e.g. [8], [9], [10]). There have also been investigations into short range applications [11].

Previously reported VHF and UHF RMS delay spreads have been observed to be typically in ranges of 100 ns to 2 μ s at distances of up to 2 km in various urban settings [12], [13], [14], [15] though occasionally reaching 5 μ s when indoor-outdoor transitions are included [16]. In contrast, the delay spreads in mountainous regions at VHF have achieved 8 μ s [13] to 30 μ s [17]. Propagation from devices with antennas near to ground, using VHF spectrum, has been shown to include significant path loss effects due to building roof line knife-edge diffraction [18].

Traditional path loss models focus on broadcast or cellular systems so are not relevant or representative of the use cases for IoT. New research is now developing propagation models for VHF systems that are close to ground for short range outdoor applications [19], [7], [15] and indoor-outdoor transitions [20], but the need for a compact and portable low cost CSR is clear, to provoke and enable further research.

Short range communications research has shown that multipath effects are less significant at VHF [19], [20] due to the reduced size of scatterers compared to the wavelength, manifesting itself as propagation with low delay spread.

In a general RF communications system it is highly desirable to use a symbol duration significantly longer than the RMS delay spread, since channel equalisation can be avoided. Such possible reductions of complexity are vital to cost-effective IoT applications. Since reported RMS delay spreads are typically less than 2 μ s therefore implies a 20 μ s minimum symbol duration would be desirable.

The CSR system proposed in this paper can be used to investigate and characterise propagation delay spread and channel conditions for any use case in the field and, although currently focused on 869 MHz and 71 MHz bands, could be deployed to measure anywhere within the frequency range of the RTL-SDR and companion transmitter or signal generator.

3. Channel Sounding Receiver Hardware

The channel sounding system consists of a transmitter and receiver. The transmitter is either an RF vector signal generator or a dedicated companion channel sounding transmitter (both are operated at a fixed location). The Channel Sounding Receiver (CSR) is highly portable and incorporates a display for channel impulse Power Delay Profile (PDP) and frequency response. In the tests presented here an Agilent E4437B signal generator is used as the TX signal source, loaded with waveform files created to suit the CSR. A dedicated companion transmitter has also been created and demonstrated at 71 MHz, which is the subject of future papers. The hardware used to make the CSR consists of:-

- Raspberry Pi 3B
- Raspberry Pi 7" or 3.5" touchscreen & case
- NooElec RTL-SDR with 0.5 ppm reference oscillator
- 5.4 Ahr portable USB battery pack

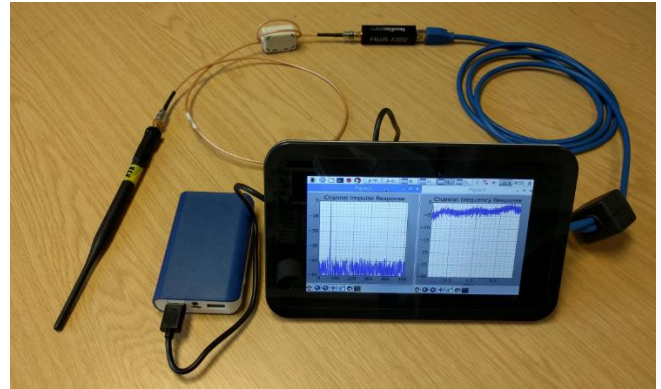


Fig. 1. RTL-SDR & 7" Touchscreen CSR, showing example 869 MHz channel PDP and frequency response.

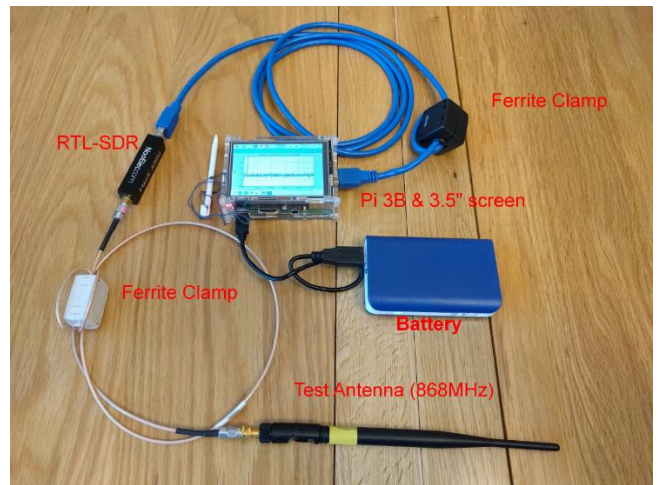


Fig. 2. RTL-SDR & 3.5" Touchscreen CSR, 869 MHz antenna attached.

The complete cost for the 3.5" touchscreen CSR variant is circa £85, making it extremely cost-effective for both research in VHF / UHF propagation and teaching applications. Both CSRs are shown in operation in Figs. 1 and 2. The use of a USB extension lead is important since it allows the RTL-SDR and its associated antenna to be placed optimally for the propagation trial and also helps separate it from sources of RF interference in the R-Pi. Ferrite clamps on both the USB cable and RG316 coax were also found to be essential: further reducing interference from the R-Pi that can otherwise desensitise the RTL-SDR, particularly at 71 MHz.

4. Channel Sounding Algorithm

The transmitting signal generator is used to illuminate the channel with a known BPSK modulated Pseudo Random Binary Sequence (PRBS). The same PRBS sequence is used in the CSR to perform a correlation against the received signal and thus extract the channel response. The CSR performs all the Digital Signal Processing (DSP) on the captured IQ data waveforms using Python and is able to display the extracted time domain and frequency domain plots to the user in near real time (under 5 seconds).

4.1 PRBS M-Sequence Selection

The system uses a PRBS-9 (511 bit) Maximum-length (M) sequence, providing a processing gain of 27 dB. The PRBS M-sequence is coded into the CSR in advance of the sounding activity, which avoids the need for any spreading code acquisition stages prior to sounding and thus reducing complexity. It is also beneficial to avoid the need for any frequency acquisition stage after data capture; further reducing complexity. Although the R-Pi is a capable platform for code development and execution, the avoidance of the above stages helps minimise the processing time in the field. The need for carrier frequency acquisition can be avoided by recognising that if the phase rotation of the RX IQ data (due to frequency errors) is less than 180 degrees over one complete PRBS frame then BPSK signals can be demodulated without error. The limiting relationship between maximum PRBS frame length and overall frequency error (composite of RX oscillator error and TX carrier error) is shown in (1).

$$\pi = \omega_e T_f \quad (1)$$

In (1), T_f is the duration (seconds) of a single PRBS frame and ω_e is the overall frequency error (rad/s) at the RX Intermediate Frequency (IF). The worst-case frequency errors are 0.5 ppm for the RTL-SDR and 1 ppm for the ESG4437B TX signal generator. The RTL-SDR is capable of sampling IQ data at 2 Msample/s, which would provide a direct conversion captured RF BW at the carrier of 2 MHz. To obtain the maximum channel temporal detail requires maximum illuminated BW, so a BPSK bitrate of 1 Mb/s was chosen, thus occupying the 2 MHz IF BW to the first sinc nulls. Clocking the PRBS symbols at 1 Mb/s and applying (1) predicts the CSR should tolerate IF frequency errors of up to 978 Hz. To achieve this long term would require GPS-lock of the TX signal generator and CSR, which is inconvenient. The RTL-SDR uses an internal temperature compensated crystal oscillator and the ESG4437B has a temperature controlled oven, so perceived carrier drift is minimal in practice, which allows the considerable simplification of applying an experimentally determined carrier offset correction to the TX signal. This ensures that the overall error at the CSR IF is manually controlled to below 978 Hz. The ESG4437B internal reference has proven to be very stable after warming up, hence this initial correction approach has proven acceptable for the duration of all measurement campaigns so far.

4.2 Correlation Technique in Channel Sounding Receiver

The CSR's main task is to perform a correlation between the received IQ data and the known TX PRBS sequence. This correlation can be performed in the time domain, but this is not computationally efficient. A more computationally efficient alternative is to perform the correlation of the two signals via the frequency domain [21], [22], [23] using convolution and then return the result back to the time domain. It is this Fast Fourier Transform circular

convolution (matched filter) approach that is employed in the CSR, described in (2).

$$C = IFFT[H(f)*G(f)] \quad (2)$$

In (2), $H(f)$ and $G(f)$ are the Fourier transforms of time series $h(n)$ and $g(n)$ respectively and $*$ denotes complex conjugation. C is the resulting cross-correlation array of the time series, resulting from the Inverse Fast Fourier Transform (IFFT) operation. Python code in the R-Pi interfaces to the RTL-SDR as well as implementing the required DSP algorithms and thus providing near real-time visualisation of the delay spread and frequency response of the propagation channel at a particular location. The CSR algorithm was written in Matlab and Python, allowing students to follow and modify the code. The RTL-SDR's internal RX gain is set to 49 dB and configured to capture samples representing 32 full PRBS frames, storing the captured data to file for analysis. The CSR algorithm to be described is based on a simplified version of those used in [21], [22], [23].

In the following descriptions, variables holding arrays of samples are italicised and in **bold**. Assume there are N complex samples per received PRBS frame (PRBS sequence length 511, oversampled by factor 2, i.e. $N = 1022$). The RX data from the RTL-SDR is partitioned into segments of length $2N$: ***rx_sequence_2N***[1..2N], which facilitates robust detection of at least one strong correlation peak, regardless of time offset in the captured RX data, compared to the TX PRBS. The overall captured RX data file is then processed in 16 such segments, each of length $2N$ samples, using the following pseudo-algorithm [6]:

1. Since the FFT input data must be periodic in time and the RX data is processed in lengths of $2N$, the TX correlation sequence of length N (for matched filtering) must be extended with zeros to length $2N$: ***tx_sequence*** = concatenate [***PRBS***, zeros(N)]
2. Compute the FFT of the time domain TX sequence: ***T*** = FFT(***tx_sequence***). This can be calculated in advance since it is fixed.
3. Select segment K in turn (0..15) of length $2N$ samples from the captured RX data ***rx_data***: ***rx_sequence_2N*** = ***rx_data***[$K2N : (K+1)2N-1$]
4. Compute the FFT of K th time domain RX segment: ***R*** = FFT(***rx_sequence_2N***)
5. Compute the conjugate of the frequency domain representation of received data: ***Rconj*** = conjugate(***R***)
6. Compute the delay profile for segment K by element-wise multiplying ***Rconj*** & ***T*** and then taking inverse FFT: ***time_response*** = IFFT(***Rconj.T***)
7. Finally, compute the delay profile magnitude of segment K : ***time_response_mag*** = abs(***time_response***)

The time domain samples in ***time_response_mag*** are then summed across each of the K frames, producing a single array for the composite Power Delay Profile (PDP) response

of the channel at the measurement location. The magnitude response of the 16 frames is used for combination since the impulses have a phase rotation, due to IF errors, which can otherwise reduce the combined SNR. Additionally, an FFT of the *time_response* array contains the frequency domain response of the channel for the K th frame (bins 1.. N for positive spectrum above carrier and bins $N+1..2N$ for negative spectrum below RX carrier). Similar to the time domain response, the magnitude of the 16 frequency domain responses can then be summed to produce a composite channel frequency response for the CSR's location.

The sinc response of the BPSK signal is imposed on the RX channel spectrum, requiring steps be taken to equalise it. The RTL-SDR was also found to add further non-linearity as a function of RX signal level. Thus, amplitude equalisation was required to address both issues. The BPSK frequency domain response, for use in equalisation (after inversion), at FFT bin x out of N is given by (3).

$$BPSK_response[x] = \left| \text{sinc}\left(\frac{x}{N}\right) \right|^n \quad (3)$$

From lab characterisation of the RTL-SDR, exponent n is selected based on the magnitude of the maximum time domain RX signal correlation peak, C_p , using (4a) or (4b).

$$n = 0.25 \ln(C_p) - 0.1 \quad (\text{if } C_p < 4500) \quad (4a)$$

$$n = 0.09 \ln(C_p) + 1.18 \quad (\text{if } C_p > 4500) \quad (4b)$$

C_p is the maximum value seen in *time_response_mag* array and also directly represents the RX RF power at the test location. The conversion of the correlation peak value C_p to an equivalent RF RX power is performed using (5).

$$RXpower = 10 \log_{10}(C_p) - 159.8 \text{ dBm} \quad (5)$$

The conversion offset value of -159.8 dBm in (5) was found experimentally during lab calibration and represents the composite gains of the RTL-SDR hardware and cable losses.

5. Testing of the Channel Sounding System

Prior to field use of the sounding system, it was subject to performance testing and calibration. Tests using a simulation model of a reflective channel were performed first, to validate the CSR algorithms. The simulated channel consisted of a primary ray with 1 reflection of delay 53 μ s and with the same amplitude. The correctly extracted impulse response is presented in Fig. 3a with a primary signal visible at 100 μ s offset and 1 reflection with path delta of 53 μ s. Fig. 3b shows the corresponding frequency response of the simulated channel. A 53 μ s delay in the channel model should present itself as spectral peaks and nulls with a period of 18.9 kHz and this matches well with Fig. 3b.

The ability of the CSR to resolve emulated reflections was also tested. Here, the ESG4437B produced the CSR's PRBS modulated BPSK signal and the signal from a separate (unsynchronised) VHF channel sounding transmitter were attenuated and then combined - representing a primary path

with 1 random reflection delay. The CSR was then used to extract the impulse response from the resulting composite signal. Since the signal generator and TX sounder were not synchronised, the time separation between impulses is random for each test. Fig. 4 shows the CSR captured impulse response for the 2 equal amplitude signals, resolved at 53 μ s apart. With the two signals at the same level, significant spectral nulling occurs, as would be expected. The nulls are visible in Fig. 4b, with 18.5 kHz spacing, which agrees well with the expected 18.9 kHz due to a reflection delay of 53 μ s and also with the results of Fig 3.

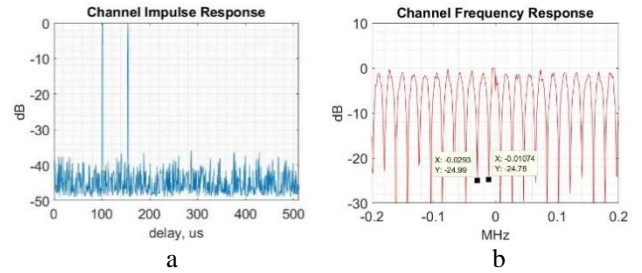


Fig. 3. Channel response with 1 simulated reflection at 53 μ s delay, from a 100 μ s primary signal. (a) PDP, (b) Frequency response with 18.6 kHz null spacing

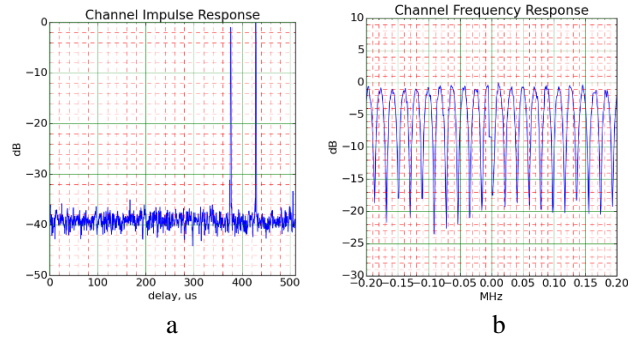


Fig. 4. Channel response for cabled emulation system, both signals at -95 dBm. (a) PDP, (b) Frequency response with 18.5 kHz null spacing

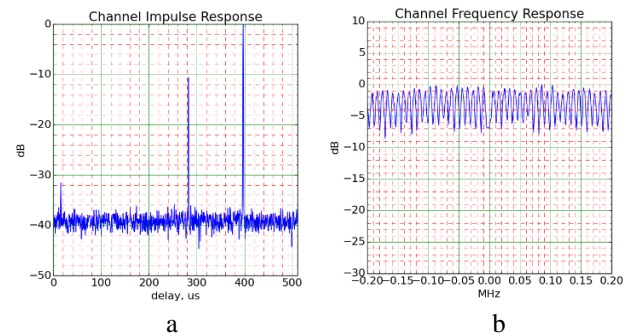


Fig. 5. Channel response for emulation system: signal generator at -105 dBm & sounder TX at -95 dBm. (a) PDP, (b) Close up of frequency response

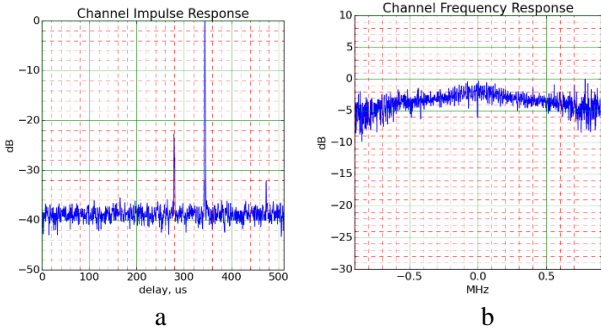


Fig. 6. Channel response for emulation system: signal generator at -115 dBm & sounder TX at -95 dBm. (a) PDP, (b) Frequency response

As the relative level of the emulated reflection decreases, the passband ripple in the channel response also decreases, as expected. With an emulated reflection of -10 dB, Fig. 5b shows circa 6 dB of ripple. As a final reflection emulation test, the emulated path amplitude difference was increased to 20 dB, resulting in the impulse response shown in Fig. 6. The resulting channel has circa 3 dB of passband ripple and the spectral nulls are now 15.5 kHz apart, which agrees well with the expected 15.4 kHz due to the 65 μ s reflection delay.

Overall, the above results show that the CSR system is working as expected. Note that in all time domain PDP figures, the absolute time delay of the primary correlation peak is random, due to the random initial M-sequence alignments between the TX and CSR RX. The CSR RX power measuring accuracy was tested with conducted signals, prior to use in the field. Table 1 presents the results of the CSR calculating the RX power, using (5).

Table 1 CSR RX Power Test

Conducted RF RX power at 71 or 869 MHz (dBm)	CSR detected power at 71 MHz (dBm)	CSR detected power at 869 MHz (dBm)
-80	-75	-76
-90	-87	-87
-100	-99	-100
-110	-109	-110
-120	-121	-122
-130	-131	-131

When a conducted signal without a reflections is received, the CSR is expected to produce a flat channel response and single correlation peak. This is confirmed for both bands in Figs. 7 and 8, using a test signal of -90dBm.

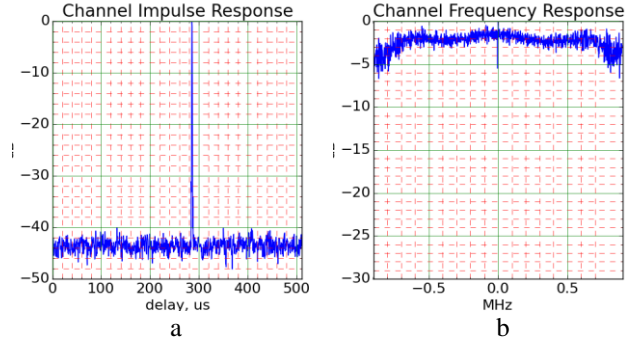


Fig. 7. 71 MHz Conducted channel response (-90dBm). (a) PDP, (b) Frequency response

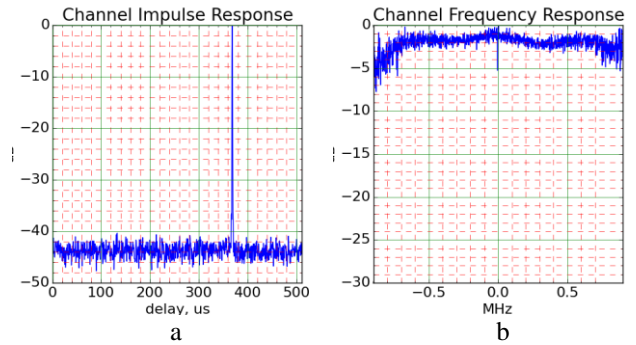


Fig. 8. 869 MHz Conducted channel response (-90dBm). (a) PDP, (b) Frequency response

The lab measured conducted sensitivity of the CSR is -125 dBm at 71 MHz and -130 dBm at 869.525 MHz, both for a displayed 10 dB correlation peak to noise ratio.

6. City Field Trials

One of the main purposes of the CSR is to facilitate rapid measurements of channel response and path loss in portable and mobile use cases. The frequencies investigated were centred on 71 MHz and 869.525 MHz, representing the two IoT bands of interest. To support pedestrian portable field tests, a commercial 868 MHz sleeved dipole whip antenna and a custom 71 MHz loop antenna were used, as shown in Fig. 9. For each case, the CSR test antenna was held at arm's length and with the radiating structure approximately at the operator's head height.

Initial field trials of the CSR in a pedestrian mobile test route through Sheffield city centre (53°22'50"N, 1°28'40"W) produced early results, select examples of which are reported in this section. The TX modulated source was the ESG4437B signal generator feeding a VHF folded dipole, or UHF whip, as appropriate, both mounted on a first floor office window.

The bespoke 71 MHz loop antenna had a BW of circa 200 kHz, which superimposed its response onto the extracted propagation channel response. The imposed BW limit can be seen, for example, on Fig. 10b. (This unwanted frequency response could be modelled and equalised from the CSR results, if required.)

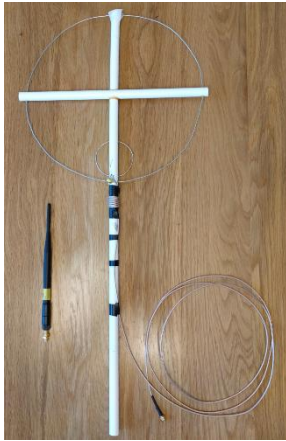


Fig. 9. Portable RX test antennas for 869 MHz (whip on left) and 71 MHz (loop on right).

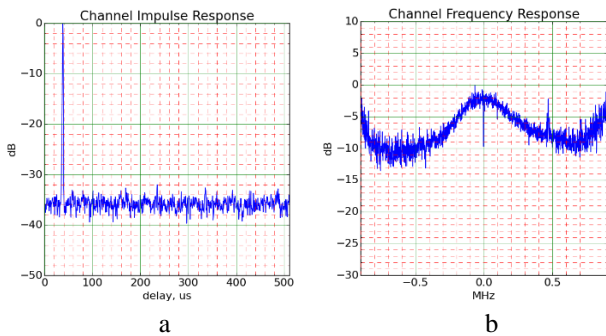


Fig. 10. 71 MHz Channel impulse response (76 m). (a) PDP, (b) Frequency response (central peak due to antenna BW)

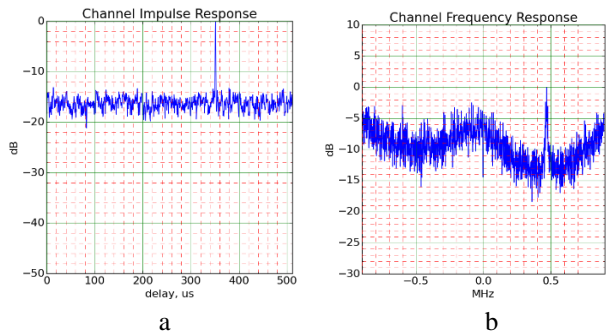


Fig. 11. 71 MHz Channel impulse response (190 m). (a) PDP, (b) Frequency response

Fig. 10 show an example channel impulse PDP and frequency response for measurements at 71 MHz with the CSR circa 76 m from the TX source. Fig. 11 show channel delay and frequency response for measurements at a non-line-of-sight street location circa 190 m from the sounder TX. Note the in-band tone interference on the extracted channel frequency response of Fig 11b.

Measurements were then taken on the same pedestrian mobile route incorporating the same test locations, using 869.525 MHz. The UHF test antenna used was broad band, so gave negligible shaping to the recovered spectrum. Fig. 12 shows an example channel responses extracted for a measurement location. The slope of the channel frequency

responses suggests a sub 1 μ s delay spread, which is plausible since no echo signal was seen resolved in the time domain. Delay spread calculations based on all observed PDPs are presented in section 9.

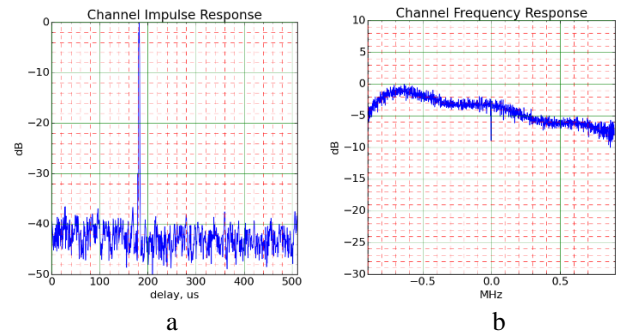


Fig. 12. 869 MHz pedestrian mobile channel response (76 m). (a) PDP, (b) Frequency response.

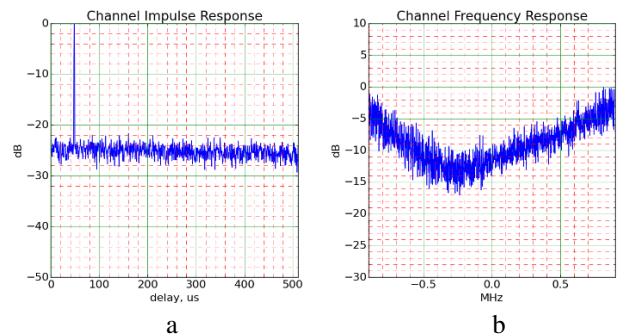


Fig. 13. 869 MHz pedestrian mobile channel response (152 m). (a) PDP, (b) Frequency response

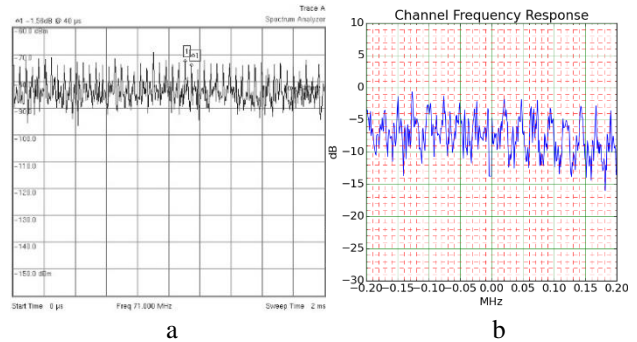


Fig. 14. Example interference observed in 71 MHz city tests. (a) MS2712E time domain (zero span), (b) Close up of resulting frequency response from CSR

Fig. 13 shows a single broad null, again suggesting a delay spread of significantly less than a 1 μ s. As before, no echo is seen with delay exceeding 1 μ s. Most of the measurements made during this test route showed a broadly flat channel response.

Although the delay spreads in the 71 MHz and 869 MHz examples are expected to be low (due to short distances), interesting channel frequency responses are still observed, which can inform use case link budget design. Extracted channel path loss models using the data are presented in section 8.

During the city tests, several locations were noted where interference was present (usually seen on the channel frequency response). During a subsequent investigation using a portable spectrum analyser (Anritsu Spectrum Master MS2712E) and antennas, the presence of sources of RF interference at various CSR field test locations was confirmed; with observed RX powers up to -100 dBm at 869.5 MHz and -80 dBm at 71 MHz (measured in a 10 kHz BW). The interference was often elaborate and intermittent, presenting as both an increase in white noise as well as additional random periodic events. A time domain example from a site with *only* periodic noise is shown in Fig 14a, as captured on the MS2712E and showing a periodicity of 40 μ s. The equivalent channel response recovered by the CSR is shown in Fig 14b, displaying a frequency domain periodicity due to the same interference of circa 25 kHz, as would be expected given the time domain signal. The sources of the interference could include commercial and domestic IT and lighting [24] systems as well as other legitimate users of the bands, such as EN 300 220 SRDs.

According to the manufacturer's data, the gains of the 869MHz whip antennas were 3 dBi and the gain of the 71MHz dipole was 0 dBd. The bespoke 71 MHz loop antenna's gain was calculated to be -2.2 dBi, with a bandwidth of 135 kHz, using standard loop design techniques [25]. The CSR system radiated power measurement accuracy was evaluated during field tests with antennas in operational positions; 4.5 m apart to approximate a reflection-less Free Space Path Loss propagation scenario. The conducted TX power feeding the specific TX antenna was -50 dBm. In this close-range test configuration, the CSR RX power was found to be within 1.2 dB of the expected power for 71 MHz (loop optimally orientated towards dipole), within 1.9 dB for the pedestrian 869 MHz system and within 2 dB for both 71 MHz and 869 MHz car setups- thus confirming that the overall cascaded antenna gains and system conversions are close to expectations and CSR system operation is acceptable.

The 71 MHz loop antenna is directional (maximum gain in the plane of the loop), so select propagation measurements have been performed taking measurements with both 90 degree orientations at each location.

7. Suburban Residential Field Trials

Measurements were also performed around a hilly residential area of Sheffield (53°21'50"N, 1°29'35"W) incorporating mixed housing, trees and vegetation. Two different measurement runs were executed: pedestrian mobile and car mobile. In both cases, the TX antennas were sited 4.3 m above ground at the rear of a dwelling, providing good RF illumination towards both the city and residential areas in the east of the city.

For tests at 71 MHz, a vertically polarised dipole antenna was mounted outside of the dwelling hosting the TX, as shown in Fig. 15. During UHF soundings, the VHF dipole was removed and replaced with a UHF sleeved dipole whip antenna.

7.1 Pedestrian mobile

The pedestrian mobile test route incorporated a journey around the streets near the dwelling. This use case could represent a user installed IoT system, with coverage required around the immediate neighbourhood. The figures presented in this section represent some of the notable channel responses obtained, rather than an exhaustive collection. The actual BW of the 71 MHz RX loop antenna is circa 200 kHz and superimposes its response on the measured channel response, as discussed in section 6.

In general, after accounting for the loop antenna's response, the propagation channel frequency response for the 71 MHz pedestrian mobile scenario was flat - but with some exceptions which are now presented in Figs. 16-17. The deep null on the right of Fig. 16a and on the left of Fig. 16b are in contrast with boosted signal on the other side of their respective plots (compared to the example reference response seen in Fig. 10). This suggests both constructive and destructive signal combination is occurring within the observed frequency range, but with a delay spread that is much less than 1 μ s. Fig. 17 shows a deep central null (nulling out the 71 MHz loop antenna's peak), also with interference.

Only one CSR test location provided an observable PDP reflection (value -20 dB). The spectrum for this location was flat, as would be expected for such a weak reflection.



Fig. 15. VHF TX antenna located at the first floor window of dwelling.

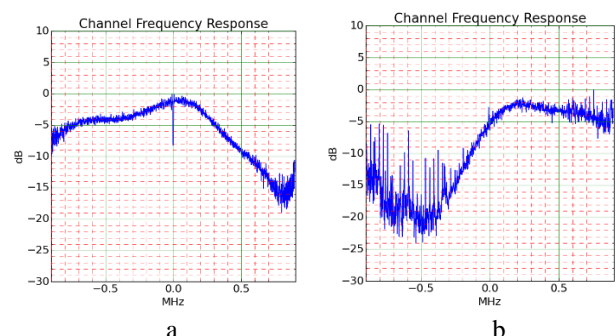


Fig. 16. 71 MHz pedestrian mobile channel response. (a) 198m (b) 314m, with interference

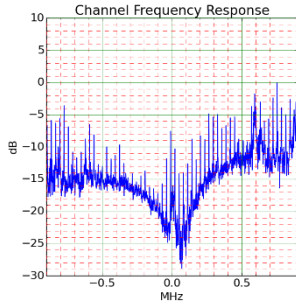


Fig. 17. 71 MHz pedestrian mobile channel response (414 m), with interference.

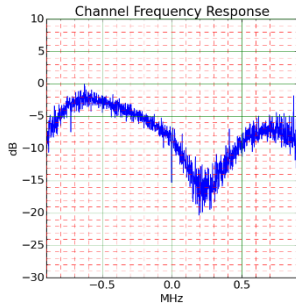


Fig. 18. 869 MHz pedestrian mobile channel response (107 m).

Measurements were also taken at 869.525 MHz on the same pedestrian test route. Fig. 18 shows a pronounced fade near the band centre and what could be the start of second nulls at +/- 1 MHz. However, at 869.525 MHz the fading was generally flat across the observed spectrum, though sometimes with shallow fades of depth 5dB.

Measurements were made for direct path distances of up to 500 m - with very few observable time domain reflections exceeding the 1 μ s resolution, and those that were present always being below -20 dB. This also manifests itself with only a small number of locations presenting with spectral nulls: operation at 71 MHz being more susceptible to such nulls.

7.2 Car mobile

For car mobile propagation measurements, a test route was devised consisting of a circuitous route extending radially to 5 km from the TX, through hilly, mixed suburban areas. This could represent a use case where a user installed IoT system is required to have coverage around a city region. The CSR RX antennas for 869.525 MHz and 71 MHz were quarter wavelength whips with magnetic mounts in the centre of the car roof. The test route included various elevations with respect to the TX site (differential heights ranging from +83 m to -50 m).

Figs. 19-20 show notable channel responses obtained at 71 MHz during the car test route. Fig. 19b shows the recovered 71 MHz frequency response is notably flatter, due to the use of a broad band UHF whip antenna, rather than the loop. Figs. 19-20 are typical of the VHF PDP and frequency responses in showing broadly flat spectrum and no resolvable reflections, to a 4 km range.

A small number of CSR test locations did present non-flat channel frequency responses, such as Fig. 21. As with previous measurements, the dimensions of the null suggest a sub-microsecond echo delay.

The same car route was then investigated at 869.525 MHz. The majority of spectra collected were either broadly flat or showing only modest shaping due to reflections. For example, Fig. 22 shows circa 5 dB of spectral slope across the measured band whereas Fig. 23 has a slight null of depth less than 5 dB.

There were some distant CSR RX locations providing very good signal levels yet still showing no significant reflections, for example Fig. 24. As also seen in previous tests, some locations did appear to suffer interference, occasionally presenting as tones.

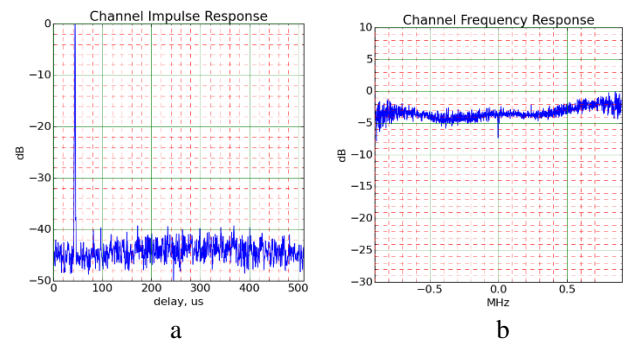


Fig. 19. 71 MHz car mobile channel response (2.87 km). (a) PDP, (b) Frequency response

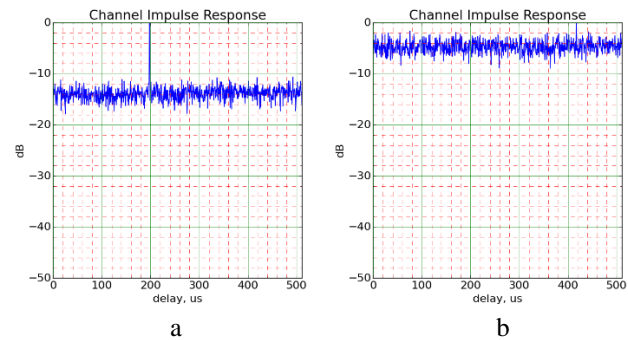


Fig. 20. 71 MHz car mobile PDP. (a) 4.05 km, (b) 4.5 km (limit of CSR sensitivity)

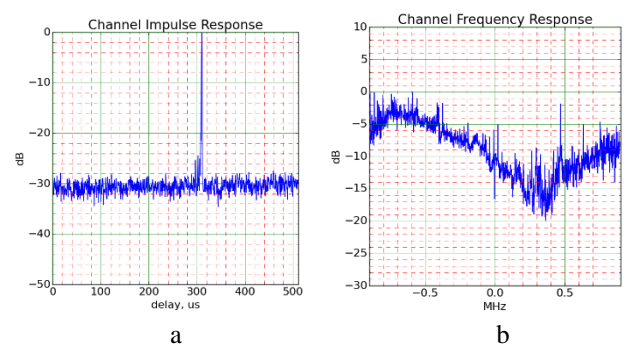


Fig. 21. 71 MHz car mobile channel response (418m). (a) PDP, with reflection at -25 dB (b) Frequency response

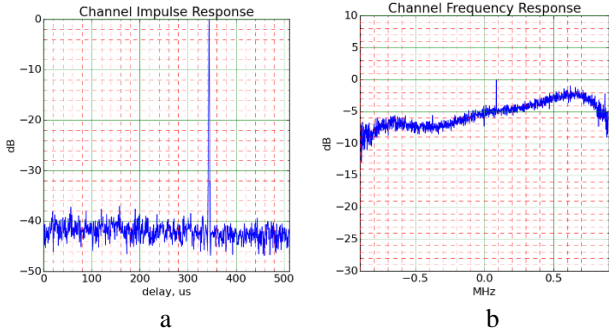


Fig. 22. 869 MHz car mobile channel response (107 m). (a) PDP, (b) Frequency response

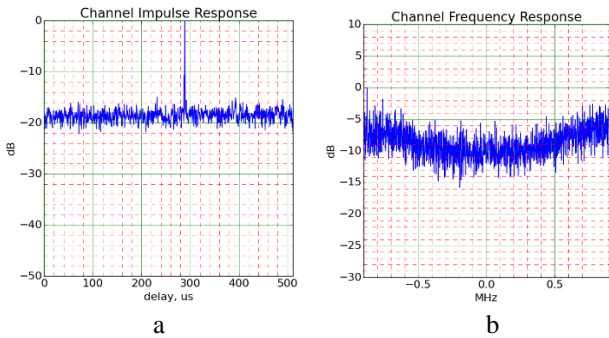


Fig. 23. 869 MHz car mobile channel response (2.71 km). (a) PDP, (b) Frequency response

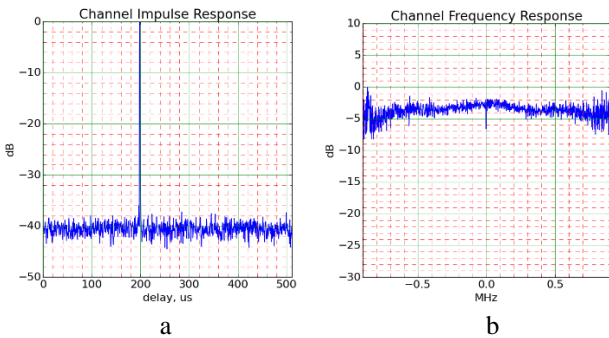


Fig. 24. 869 MHz car mobile channel response (2.87 km). (a) PDP, (b) Frequency response

Overall in the 71 MHz and 869.525 MHz car mobile tests it is again interesting to note that there are no significant reflections observed with delays exceeding 1 μ s, even with TX-RX distances extending beyond 4 km in hilly terrain. This may, in part, be due to the processing gain limitation of the CSR at longer ranges. However, the paucity of reflections over all distances is valuable information, possibly supporting the proposal of over-roof knife edge diffraction [18] being a key mechanism.

8. Extracted Propagation Models

Data was captured from several measurement journeys on each route (1 in summer and 2 in autumn). In addition to the PDP and channel frequency responses, received signal power is also calculated by the CSR, at all the field trial locations. The raw path loss data and proposed

straight line approximations are shown in Figs 25-30. Hata small city and suburban path loss models [10] are also included for reference, where applicable. (Note that the lower valid frequency for the Hata model is 150 MHz, so is included only for information on 71MHz figures). The straight line models are all fitted using a least squares approach.

The circled data points on Figs. 29-30 identify locations with a clear Line of Sight (LoS) path to the TX site, which are thus presenting low path loss, compared to adjacent locations. The general observed scattering of the data points is to be expected given the nature of the testing: signal paths partially occluded by various buildings, vegetation and trees, RX antennas at head height and with general movement of vehicles and people in the vicinity of the tests. Furthermore, relatively small changes in the CSR's location can open up different propagation paths. Additionally, for suburban car tests, locations had to be selected where it was safe to stop.

The data was measured at the same locations (within circa 2m) on 3 occasions: identified on Figs. 26-27 and Figs. 29-30 as [a] in summer, [b] and [c] in autumn. The suburban car based measurements show little variation due to the measurement runs. Autumn pedestrian tests using the 71MHz loop antenna were repeated for loop orientations of North/South (marked [N/S]) and East/West (marked [E/W]) to capture directionality effects on Fig. 25 and Fig. 28. The 869MHz suburban pedestrian tests appear to show a decrease in path loss in autumn; most likely due to the reduced foliage on the test route.

The log-normal (straight line) path loss P model described by (6) is used to fit the measured data to the test scenario distance d ; with model-specific coefficients u and n as presented in Table 2.

$$P = u + n \log_{10}[d] \text{ dB} \quad (6)$$

Path loss results reported in [19] at 64 MHz measured at 300 m showed losses of circa 97 dB over open flat concrete, 97-108 dB over grass and 100-108 dB for wooded areas. Comparable 71 MHz results presented in this paper show a loss of 96 dB for the suburban pedestrian (and 107 dB for the city scenario) at 300 m.

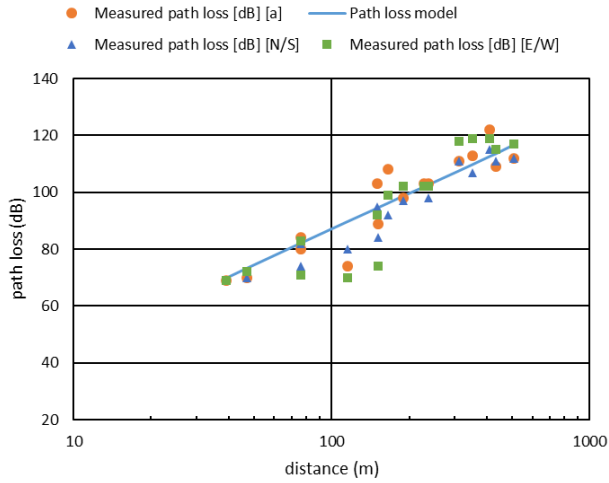


Fig. 25. City pedestrian 71 MHz path loss data and model.

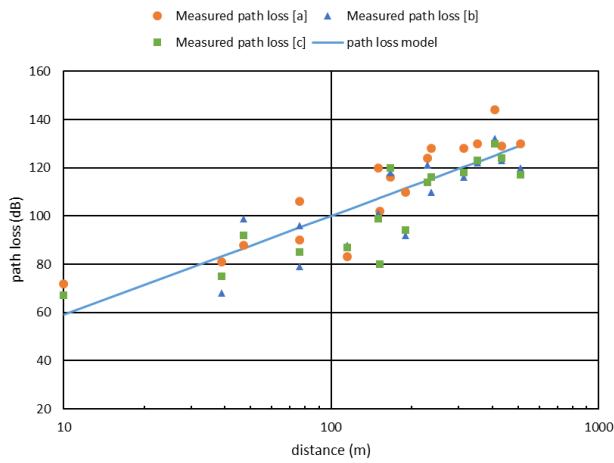


Fig. 26. City pedestrian 869 MHz path loss data and model.

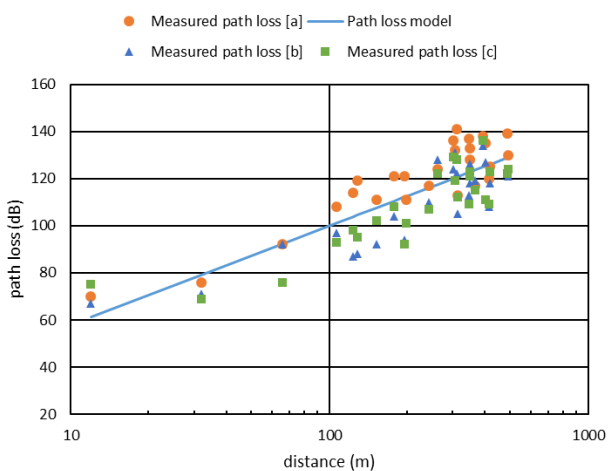


Fig. 27. Suburban pedestrian 869 MHz path loss data and model.

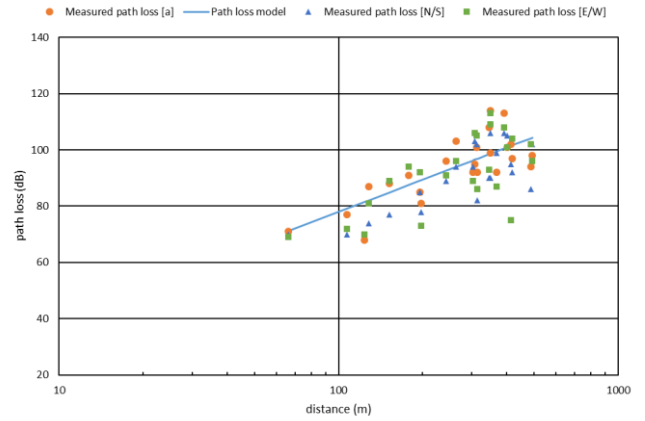


Fig. 28. Suburban pedestrian 71 MHz path loss data.

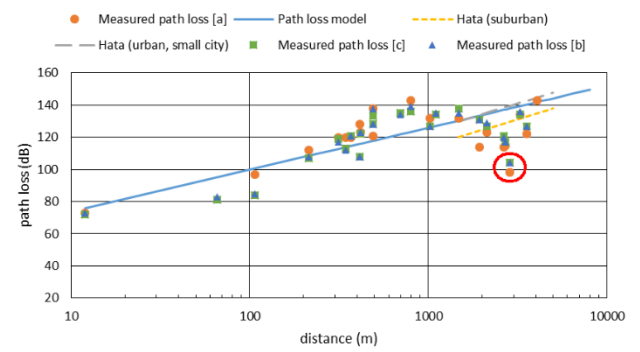


Fig. 29. Suburban car 869 MHz path loss data and model (distant locations with LoS to TX are marked by the circle).

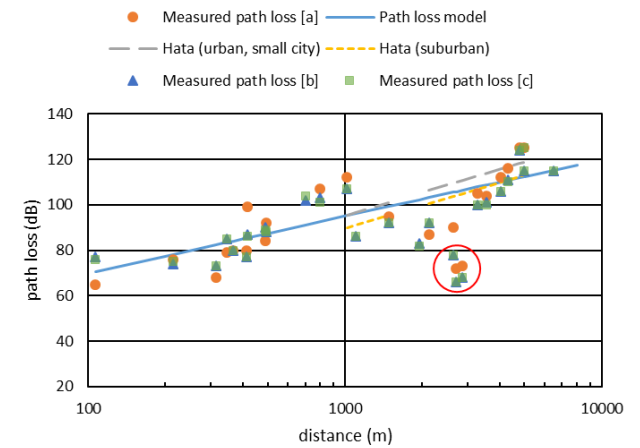


Fig. 30. Suburban car 71 MHz path loss data and model (distant locations with LoS to TX are marked by the circle).

Table 2 Path loss model coefficients

Propagation scenario	n	u (dB)
City Pedestrian 869	41	18
City Pedestrian 71	42	3
Suburban Pedestrian 869	42	16
Suburban Pedestrian 71	38	2
Suburban Car 869	26	48
Suburban Car 71	25	20

The Hata small city model at 869 MHz shows good agreement to the fitted model for car mobile data in Fig. 29 (but a 10 dB underestimation in the Hata suburban model). Although the Hata model is not valid below 150 MHz, it is interesting to compare its prediction for the 71 MHz propagation results in Fig. 30 and again it shows good agreement with the small city model at 1km, but is better represented by the Hata suburban model by 5km.

Considering a theoretical, frequency-dependent fixed-loss FL as defined in (7) gives a loss for 869.525 MHz of 31.2 dB and a loss of 9.4 dB for 71 MHz.

$$FL = 20 \log \left(\frac{4\pi}{\lambda} \right) \text{ dB} \quad (7)$$

The fixed loss term predicted by (7) overestimates the actual observed loss u for pedestrian scenarios by circa 14 dB at 869 MHz and circa 7 dB at 71 MHz. However, (7) also underestimates the loss u required for suburban car tests by 16.8 dB at 869 MHz and by 10.6 dB at 71 MHz. In the aim of creating a simple to use model, it is proposed that (7) be modified to include an additional fixed loss term that is the mean of the absolute error between (7) and u , i.e. a value 12 dB. The proposed fixed-loss model is shown in (8a) and (8b).

$$FL_{Pedestrian} = 20 \log \left(\frac{4\pi}{\lambda} \right) - 12 \text{ dB} \quad (8a)$$

$$FL_{Car} = 20 \log \left(\frac{4\pi}{\lambda} \right) + 12 \text{ dB} \quad (8b)$$

The standard deviation σ of the error between the measured data and associated fitted straight line model from Table 2 is shown in Table 3.

Table 3 Standard deviation of path loss model error

Propagation scenario	σ (dB)
City Pedestrian 869	10.7
City Pedestrian 71	6.6
Suburban Pedestrian 869	9.7
Suburban Pedestrian 71	8.4
Suburban Car 869	9.9
Suburban Car 71	8.5

Results in [15] for 77.5 MHz propagation measurement in a hilly city, identified a distance-dependent coefficient of 46.4 (aligning well with our city pedestrian model) and a standard deviation of 8.6 dB. Our suburban car results are influenced by significant path loss variations in the small data set. However, shadowing and small-scale fading effects are quite usual in such field measurements and the standard deviation of the data (from the model straight lines) are not out of the ordinary, compared to other trials. The reduced distance-dependent term n of Table 2 may be due to the existence of several near LoS paths existing between the TX and some of the RX sites - even at the furthest range, which may not have existed in [15].

The proposed path loss model in (6) is basic in form, but it is interesting to note that the pedestrian model coefficient n only varies between 38 and 42. This suggests that a simple 2-ray Reflective Earth propagation model,

based on the well-known $40 \log(d)$ approximation but also with addition of a theoretical fixed offset (8a) for u may be a pragmatic approach for general IoT city and suburban range planning. The n coefficient for the suburban car scenario is more favourable than in pedestrian scenarios, possibly due to a more uniform azimuth coverage and improved gain at low elevation of the monopole above the car roof ground plane, compared to the hand-held whip or loop antenna. It is also interesting to note that for the suburban car scenario, coefficient n only varies between 25 and 26. Fixed loss term u can be closely represented by (8b) in the suburban car scenario, overall also supporting a simple propagation model.

9. Extracted Delay Profile Models

The CSR produces PDP time domain delay profiles which can be used to extract RMS delay spread. However, the lack of any observable reflections with delays significantly exceeding 1 μ s has been remarkable during the field trials. This is in contrast with the findings of several others, as discussed in section 2, but perhaps does support the findings of [19], [20] and extends their applicability. During all the field trials, PDP data has been collected and examples showing close-in views of notable delay profiles on the correlation pulse are presented in Figs. 31–34. The PDPs produced during a conducted measurement are shown in Fig. 35 as a reference.

The PDPs produced from reference radiated measurements over a short range were also captured and found to be the same as in Fig. 35, apart for tests with the 71 MHz loop antenna. The reduced BW of the 71MHz loop antenna slews the PRBS bit transitions and extends the reference pulse, requiring a separate reference PDP for this setup, with 2 μ s width at the -10 dB point.

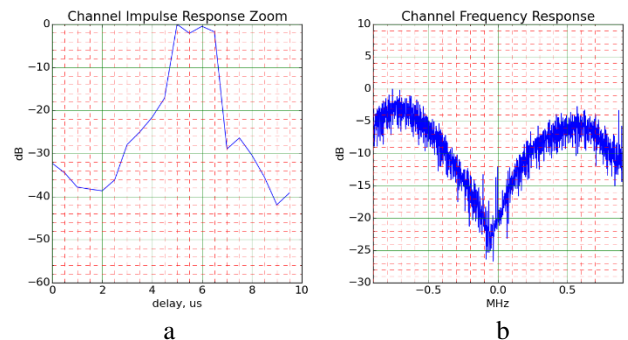


Fig. 31. 869 MHz City pedestrian channel response (47 m). (a) Close-in view of PDP, (b) Frequency response

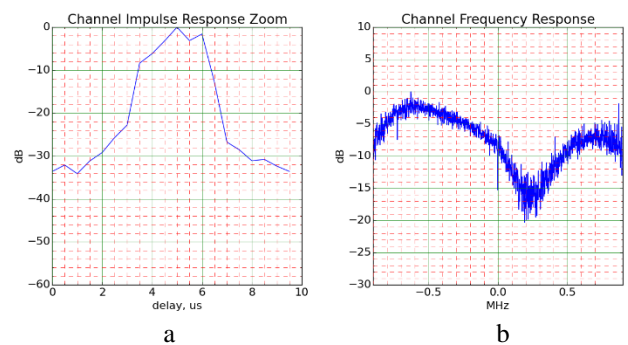


Fig. 32. 869 MHz Suburban pedestrian channel response (107 m). (a) Close-in view of PDP, (b) Frequency response

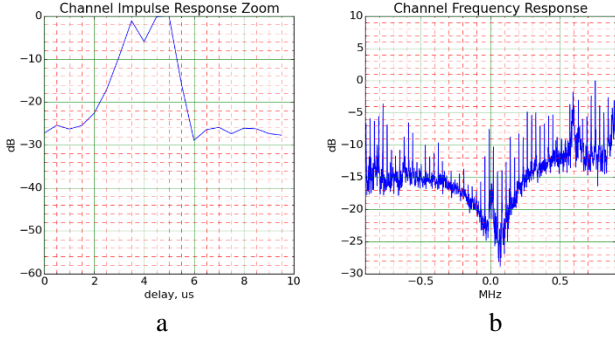


Fig. 33. 71 MHz Suburban pedestrian channel response (414 m). (a) Close-in view of PDP, (b) Frequency response

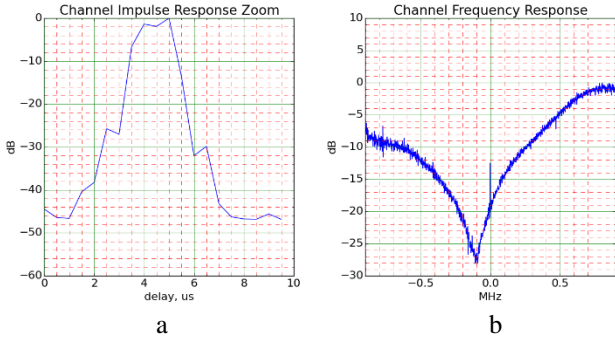


Fig. 34. 71 MHz Suburban car channel response (107 m). (a) Close-in view of PDP, (b) Frequency response

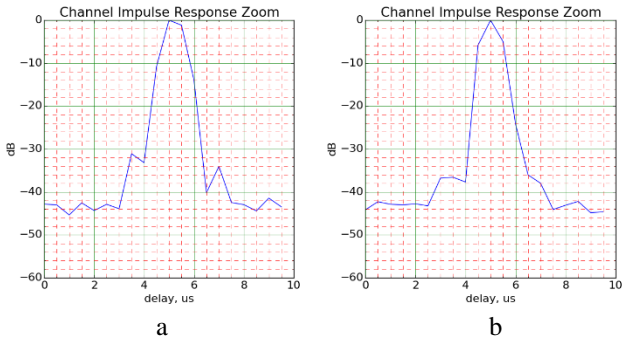


Fig. 35. Close-in PDP from conducted measurement at -90dBm (width of pulse at -10 dB point is 1.25 μ s). (a) 71MHz, (b) 869MHz

Given the low sample rate, care must be exercised in interpreting the close-in PDPs, when attempting to estimate the number of constituent rays and the delay spread. A small number of locations, such as Fig. 33a for example, do present what seems to resemble 2 PDP peaks. The approach taken in this section considers only the overall width of the recovered single PDP pulse, as a simplified method to estimate the RMS delay spread. By comparing the overall width of the obtained PDP correlation pulse at the -10 dB points to the width of the reference pulse at the -10 dB points, an estimation of the excess delay has been computed for those PDPs showing any pulse lengthening, as expressed in (9).

$$D = W_{radiated} - W_{conducted} \quad (9)$$

In (9), $W_{conducted}$ is 1.25 μ s (2 μ s for the 71MHz loop) and $W_{radiated}$ is the width of the observed PDP pulse at the same point (i.e. -10dB point). The concept is illustrated in Fig. 36.

Since the PRBS bit rate is 1 MHz and the RTL SDR sample rate is 2 MHz, the resolution of the PDP at low delay spreads is very limited, but it is still possible to extract some information. In general, the Mean Excess Delay can be expressed as [26]:-

$$T_m = \frac{\sum_{i=0}^{N-1} P(T_i)T_i}{\sum_{i=0}^{N-1} P(T_i)} \quad (10)$$

$P(T_i)$ is the level of the reflection's correlation peak at delay T_i , relative to the primary ray. The second moment of the power delay can be expressed as [26]:-

$$T_{sm} = \frac{\sum_{i=0}^{N-1} P(T_i)(T_i)^2}{\sum_{i=0}^{N-1} P(T_i)} \quad (11)$$

The RMS delay spread can then be calculated from [26]:-

$$\sigma_T = \sqrt{T_{sm} - (T_m)^2} \quad (12)$$

Since it was not possible, in general, to resolve the recovered CSR PDP data into distinct pulses, the simplifying model of 2 rays with the same amplitude has been used. Hence, the time separation between the ideal correlation peaks in the PDP is assumed to be the same as the measured difference in width of recovered pulse to reference pulse, D , as illustrated in Fig. 36.

It can then be shown that for this simple 2 ray case, the RMS delay spread simplifies to:-

$$\sigma_T = \frac{D}{2} \quad (13)$$

Using the above approach, estimates of RMS delay spreads observed in all the measured data have been calculated and are presented in Table 4. However, it should be noted that in the majority of field measurements, no discernible spreading of the PDP correlation pulse was observed at the -10 dB width points. (The lowest discernible value of D observed in the measured data was 0.15 μ s.)

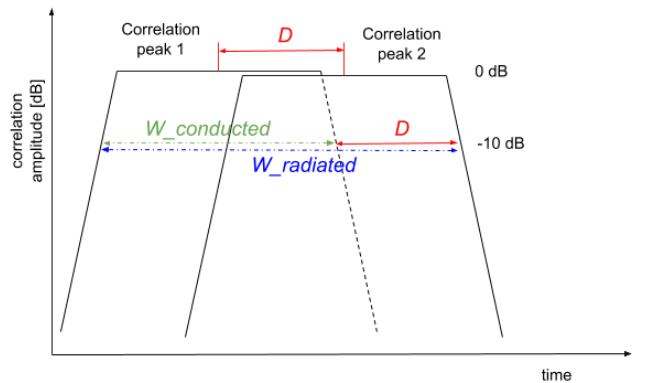


Fig. 36. Extracting D from an assumed 2 ray PDP.

Table 4 Maximum and typical observed RMS delay spreads

Propagation scenario	Maximum σ_T (μs)	Typical σ_T ranges (μs)
City Pedestrian 869	0.38	0 - 0.12
City Pedestrian 71	0.25	-
Suburban Pedestrian 869	0.88	0 - 0.12
Suburban Pedestrian 71	0.5	0 - 0.25
Suburban Car 869	0.12	-
Suburban Car 71	0.38	0 - 0.12

10. Conclusions & Future Work

The combination of the R-Pi, RTL-SDR and Python DSP code have proved themselves as a valuable, novel system for performing propagation research measurements for modest cost and with high portability. This is important in facilitating focused use case propagation research in the field, allowing extraction of maximum insight at each location. This also allows the rapid evaluation of antenna concepts in the field. The proposed system is also applicable to the teaching of radio propagation; allowing students to witness the effects in near real-time, via the touchscreen.

In addition to the channel power delay response and frequency response, the CSR's ability to calculate the path loss has allowed the creation of log-normal models for all the field trial scenarios. These extracted models have suggested that a basic 2 ray Reflective Earth distance-dependent model (augmented by a simple frequency-dependent loss term) may be pragmatic for pedestrian portable IoT use cases. A reduced distance-dependent coefficient appears sufficient to allow the model to also be used for the suburban car scenario, with more favourable path loss. The propagation model for suburban car at 71MHz is the most favourable.

It is surprising to note that no significant reflections with delays exceeding 1 μs have been observed, even with field test distances exceed 4 km over Sheffield's hilly terrain. This suggests the reflective environment in both the city scenario and long-range urban scenario are only subject to reflections immediately adjacent to the primary path. However, the lack of strong reflections exceeding 1 μs does align with the findings of some other researchers as discussed in section 2. The estimated delay spreads based on the correlation pulse lengthening have shown maximum delay spreads below 1 μs . Most of the recovered spectrum profiles have been flat, with only a few examples of deep, wide fading nulls observed (mainly in 71MHz pedestrian operation).

Interference to CSR measurements was experienced in some of the test locations, at both 71 MHz and 869.525 MHz. This is suspected due to domestic and commercial switched mode PSUs, PC equipment and LTE band 20 signals. The CSR's link budget is degraded by this interference, ideally requiring use of longer PRBS correlation sequences. This, in turn, would require more precise and stable oscillators at the TX and possibly within the CSR, at additional cost and complexity.

The low cost of the CSR lends itself to a multi-point test system, where several CSRs could be deployed at once and used to capture survey data in parallel from a common TX and thus used to build a propagation model faster than by touring with a single CSR. Another possible scenario is for multiple CSRs to be sited in various fixed locations and used to capture channel measurements periodically over a longer interval.

To increase both the RF carrier frequency and the sounding bandwidth, our next CSR will replace the RTL-SDR with new bespoke RX RF front ends for sub 6 GHz and 28 GHz, coupled to a Red Pitaya FPGA board sampling IQ signals at 125 MHz (hence an effective RF bandwidth of 125 MHz). Additionally, a new companion high BW sounding transmitter will be used. The Red Pitaya will be both controlled and provide RX IQ signals to be analysed to the R-Pi. The R-Pi will implement the same DSP code and graphical interface as described in this paper. The future system will further enable valuable, portable propagation measurements to be performed cost-effectively for new bands of interest.

11. References

- [1] Domazetović, B., Kočan, E., Mihovska, A.: 'Performance evaluation of IEEE 802.11ah systems'. 2016 24th Telecommunications Forum (TELFOR), Belgrade, Serbia, Nov. 2016, pp. 1-4
- [2] Lavric, A., Petrariu, A. L.: 'LoRaWAN communication protocol: the new era of IoT'. 2018 International Conference on Development and Application Systems (DAS), Suceava, Romania, May 2018, pp.74-77
- [3] Mroue, H., Nasser, A., Hamrioui, S., Parrein, B., Motta-Cruz, E., Rouyer, G.: 'MAC layer-based evaluation of IoT technologies: LoRa, SigFox and NB-IoT'. 2018 IEEE Middle East and North Africa Communications Conference (MENACOMM), Lebanon, Lebanon, April. 2018, pp. 1-5
- [4] Ofcom, 'VHF radio spectrum for the Internet of Things (Statement)'. 2016.
- [5] Bagal, S., Desai, P., Gulavani, A., Patil, R. A.: 'Considerations for wireless communication at 868MHz'. 2014 Annual IEEE India Conference (INDICON), Pune, India, Dec. 2014, pp. 1-5
- [6] Ball, E. A.: 'Portable and low cost channel sounding platform for VHF / UHF IoT propagation research'. Loughborough Antennas & Propagation Conference (LAPC 2017), Loughborough, UK, November 2017, pp.1-5
- [7] Stewart, J., Stewart, R., Kennedy, S.: 'Internet of Things – propagation modelling for precision agriculture applications'. 2017 Wireless Telecommunications Symposium (WTS), Chicago, USA, April. 2017, pp. 1-8
- [8] Allsebrook, K., Parsons, J. D.: 'Mobile radio propagation in British cities at frequencies in the VHF and UHF bands', IEEE Trans. on Vehicular Technologies, 1977, 26, pp. 313-323
- [9] Vigneron, P. J., Pugh, J. A.: 'Propagation models for mobile terrestrial VHF communications'. MILCOM Conference, San Diego, USA, Nov. 2008, pp. 1-7
- [10] Hata, M.: 'Empirical formula for propagation loss in land mobile radio services'. IEEE Trans. on Vehicular Technology, 1980, 29, (3), pp. 317-325

- [11] Dagefu, F. T., Verma, G., Rao, C. R., et al., 'Measurement and characterization of the short-range low-VHF channel'. WCNC Conference, New Orleans, USA, March 2015, pp. 177-182
- [12] Pugh, J. A., Bultitude, R. J. C., Vigneron, P. J.: 'Mobile propagation measurements with low antennas for segmented wideband communications at VHF'. 12th ANTEM Conference, Montreal Canada, July 2006, pp. 1-4
- [13] Fischer, J., Grossmann, M., Felber, W., Landmann, M.: 'A novel delay spread distribution model for VHF and UHF mobile-to-mobile channels'. 2013 7th European Conference on Antennas and Propagation (EuCAP), Gothenburg, Sweden, April 2013, pp. 469-472
- [14] Pugh, J. A., Bultitude, R. J. C., Vigneron, P. J.: 'Propagation measurements and modelling for multiband communications on tactical VHF channels'. MILCOM 2007 - IEEE Military Communications Conference, Orlando, USA, Oct. 2007, pp 1-7
- [15] Bedeer, E., Pugh, J., Brown, C., Yanikomeroglu, H.: 'Measurement-based path loss and delay spread propagation models in VHF/UHF bands for IoT communications'. 2017 IEEE 86th Vehicular Technology Conference, Toronto, Canada, Sept. 2017, pp. 1-5
- [16] Karam, M., Turney, W., Baum, K. L., et al.: 'Outdoor-indoor propagation measurements and link performance in the VHF/UHF bands'. 2008 IEEE 68th Vehicular Technology Conference, Calgary, Sept. 2008, pp.1-5
- [17] Safer, H., Berger, G., Seifert, F.: 'Wideband propagation measurements of the VHF-mobile radio channel in different areas of Austria'. 5th International Symposium on Spread Spectrum Techniques and Applications, Sun City, South Africa, Sept. 1998, pp. 502-506
- [18] Sasaki, M., Yamada, W., Sugiyama, T.: 'VHF band path loss model for low antenna heights in residential areas'. The 8th European Conference on Antennas and Propagation (EuCAP 2014), The Hague, Netherlands, April 2014, pp. 2092-2094
- [19] Sizov, V., Gashinova, M., Zakaria, N., Cherniakov, M.: 'VHF communication channel characteristics over complex wooded propagation paths with applications to ground wireless sensor networks', IET Microw. Antennas Propag., 2013, 7, (3), pp. 166-174
- [20] Dagefu, F. T., Verma, G., Rao, C. R., et al.: 'Short-range low-VHF channel characterization in cluttered environments', IEEE Trans. On Antennas and Propag., 2015, 63, (6), pp. 2719-2727
- [21] Fannin, P. C., Molina, A., Swords, S. S., Cullen, P. J.: 'Digital signal processing techniques applied to mobile radio channel sounding'. IEE Proceedings F - Radar and Signal Processing, 1991, 138, (5), pp. 502-508
- [22] Charles, S. A., Ball, E. A., Whittaker, T. H., Pollard, J. K.: 'Channel sounder for 5.5GHz wireless channels'. IEE Proceedings in Communications, 2003, 150, (4), pp. 253-258
- [23] MacCurdy, M., Gabrielson, R., Spaulding, E., et al.: 'Automatic animal tracking using matched filters and time difference of arrival'. Journal of Communications, 2009, 4, (7), pp. 487-495
- [24] Landa, I., Blázquez, A., Vélez, M., Arrinda, A.: 'Indoor measurements of IoT wireless systems interfered by impulsive noise from fluorescent lamps'. 11th European Conference on Antennas and Propagation (EuCAP), Paris, France, May 2017, pp. 2080-2083
- [25] Balanis, C. A.: 'Antenna Theory' (Wiley Interscience, 3rd Edition, 2005)
- [26] Rappaport, T. S.: 'Wireless Communications Principles & Practice' (Prentice Hall, New Jersey, 1996)

6. Paper 2 – TMA C0 Canceller and Beam Steering

{Reproduced as published - author accepted version.}

© 2020 IEEE. Reprinted, with permission, from Edward A. Ball, and Alan Tennant, “A Technique to Control the Harmonic Levels in Time-Modulated Antenna Arrays—Theoretical Concept and Hardware Verification Platform”, IEEE Transactions on Antennas and Propagation, published 12th March 2020.

DOI <https://doi.org/10.1109/TAP.2020.2978894>

(Published version [2])

A Technique to Control the Harmonic Levels in Time Modulated Antenna Arrays – Theoretical Concept and Hardware Verification Platform

Edward A. Ball, *Member, IEEE* and Alan Tennant, *Member, IEEE*

Abstract—This paper presents techniques into prediction and control of the radiated harmonic levels in time modulated antenna arrays (TMAs). The effect of ramping on the controlling switching waveform, due to slew in the RF switches, is analyzed first. This is followed by a novel technique for controlling and reducing the fundamental carrier component (due to the Fourier series 0 Hz term) that is always produced by TMAs. A new bespoke, steerable, TMA RF hardware test platform is presented, using three gain states to pragmatically implement the proposed carrier reduction technique. The platform implementation utilizes binary logic control interfaces to the TMA, rather than analogue control interfaces. Laboratory measurements using the test platform demonstrate a 16.5dB reduction (limited by PCB emissions) in the level of the fundamental carrier component relative to the steered first harmonic, from a possible reduction of 21.3dB. The array gain for the first harmonic beam is 2dBi.

Index Terms—Time Modulated Antenna Arrays, Fourier series, RF hardware platform, Microwave circuits.

I. INTRODUCTION

THERE IS TODAY much ongoing research into beamforming techniques for use in next generation 5G communications, including a focus on mmWave radio for mobile applications [1]. From a future mobile device's perspective, it can be argued that only a single active beam may be required at any particular instant; significantly relaxing the technical challenge and cost in implementing a radio using beamforming.

The time modulated antenna array (TMA) [2], [3], [4], [5], [6] can be used to generate a beam at a desired angle without the use of vector modulators or phase shifters, though it seems rarely used in practice. TMAs create a steerable beam, using only RF switching elements and can create or receive multiple beams carrying different modulated data [7], [8] or steer nulls in the direction of interference [9], [10], [11], [12]. The TMA has also been investigated for use in direction finding systems [13], [14] by analyzing signal harmonic characteristics. TMAs are also applicable to radar systems [15], [16] and can incorporate both a radar function in the boresight beam and a communications function in the other beams, using a single system [17], [18], [19]. The TMA has also seen application in reflector arrays [20], for diversity reception systems [21], and multiple beam communications [22]. Recently TMAs

have found use in generating orbital angular momentum waves [23], [24] and circular polarization [25]. Most systems use only the boresight beam or possibly the first harmonic beam, with increased beam steer angles requiring the use of higher order harmonics for realizable switching timings.

In this paper we devise concepts to predict and control the level of the harmonic beams including, for the first time to our knowledge, a new technique to control or cancel the fundamental beam at boresight. In section II of this paper we briefly introduce the concept of TMAs and then go on to predict the magnitude of a harmonic beam as a function of RF switch ramping time between on and off states, due to slew rate. We then propose a new way of controlling the harmonic fundamental beam magnitude due to the Fourier series 0 Hz term, using a bipolar gain stage. Section III introduces a 5.8GHz RF hardware switching architecture, using three gain states and phase inversions per array element to implement the required bipolar gain, leading to a novel RF TMA test platform. In section IV we present measured data from radiated chamber tests of the six element TMA array. We conclude the paper in section V.

The contributions of this paper are threefold: 1) mathematical model for the prediction of harmonic levels in TMAs due to RF switching slew; 2) Novel algorithm and RF hardware technique to null out the TMA fundamental component at the carrier frequency without affecting the harmonic beam steering; and 3) proof of concept test results from laboratory tests using the bespoke RF hardware platform.

II. HARMONIC LEVELS IN TIME MODULATED ARRAYS

TMAs use switching time to control the direction of a harmonic beam carrying RF energy. Often in TMA design, the fundamental component at the carrier is the focus of attention and all other harmonics are to be curtailed. There has been some research into controlling the magnitude of these harmonic levels, for example using trapezoid switching waveforms and cosine switching waveforms [26], [27], though these can require complex circuitry to implement the required analogue control waveforms. There has also been investigation into the control of the instantaneous emission level [28], which can be significant in TMAs. In this paper we only consider the average emission level, as would be perceived by a receiver of the beam from a linear array.

A. TMA with RF Switching Slew

The Array Factor (AF) for an array of N isotropic radiating elements in a TMA can be described by (1) [5], where $F_n[U_k(t)]$ is the Fourier coefficient of the n th harmonic of the time domain switching waveform U on the k th antenna element.

$$AF(\theta, t) = e^{j[\omega_c + n\omega_p]t} \cdot \sum_{k=1}^N F_n[U_k(t)] e^{j\varphi_k} \quad (1)$$

The time modulation of the RF signal at element k can be represented as a series of Fourier coefficients, multiplied with harmonics of the switching frequency ω_p , then up-converted to the carrier frequency ω_c . The term $e^{j\varphi_k}$ is an element-specific phase shift, due to antenna element spacing and evaluated beam angle and can be expressed using (2), where k is the element number, d is the spacing between the elements and θ is the azimuth beam angle direction being evaluated.

$$\varphi_k = (k - 1) \frac{2\pi}{\lambda} \cdot d \cdot \sin(\theta) \quad (2)$$

In the rest of this paper we refer to the n th Fourier coefficient of the switching waveform n th harmonic, for a particular element k , as $Cn_k = F_n[U_k(t)]$ and the overall magnitude of the combined AF due to the n th harmonic as Cn .

Although there has been some prior research into deliberately shaping the switching waveform $U_k(t)$, such as [27], AF TMA models commonly assume an infinite slew rate on the transition of the RF signal from radiating element k 'on' state to element 'off' state. In this ideal case, the fundamental Fourier term $C0_k$ can be represented by (3), where T_k is the element on-time and T_p is the frame period, with $\omega_p = \frac{2\pi}{T_p}$.

$$C0_k = \frac{T_k}{T_p} \quad (3)$$

In practical systems, an RF switching ramp time of zero seconds is not achievable. Fig. 1 shows a more typical time domain waveform for $U_k(t)$, with period T_p and the switch's 'on' duration time T_k , with ramping durations T_r and T_f .

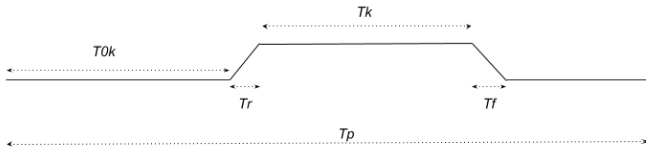


Fig. 1. $U_k(t)$ example time domain form, including ramping T_r and T_f .

Next are presented the equations for the Fourier coefficients that include the effect of RF switching slew: T_r 'off-to-on' and T_f 'on-to-off' transitions. Equation (4) describes the $C0_k$ term and (5) the Cn_k term, for a particular ramped element k in the TMA.

$$C0_{k_ramp} = \frac{T_r}{2T_p} + \frac{T_k}{T_p} + \frac{T_f}{2T_p} \quad (4)$$

From (4), the Fourier coefficient $C0_k$ for the k th element with switching slew can be seen to include the expression of the ideal (zero ramping) from (3) and additional terms associated with the ramping slew. The magnitude of the Fourier coefficient of the n th harmonic from the k th element can be predicted using (5).

$$Cn_{k_ramp} = \left\{ \frac{e^{-jn\omega_p T_{0k}} [e^{-jn\omega_p T_r} - 1] + \frac{je^{-jn\omega_p (T_{0k} + T_r)}}{2\pi n}}{T_p T_r n^2 \omega_p^2} \right\} + \left\{ \frac{\sin\left(\frac{n\pi T_k}{T_p}\right)}{n\pi} e^{-jn\pi\left(\frac{2T_{0k}}{T_p} + \frac{T_k}{T_p} + \frac{2T_r}{T_p}\right)} \right\} + \left\{ \frac{e^{-jn\omega_p (T_{0k} + T_r + T_k)}}{n^2 2\pi \omega_p T_f} [1 - e^{-jn\omega_p T_f}] - \frac{je^{-jn\omega_p (T_{0k} + T_r + T_k)}}{2\pi n} \right\} \quad (5)$$

Hence, (4) and (5) allow the prediction of the harmonic levels as a function of switching ramp times T_r and T_f . Fig. 2 shows an example AF for a six element Dolph-Chebyshev weighted array, designed for -20dB sidelobes on the first harmonic and steering the harmonic beam to +10 degrees, with T_p set to 1 μ s, T_r and T_f set to 1ns (i.e. 0.1% of switching period T_p).

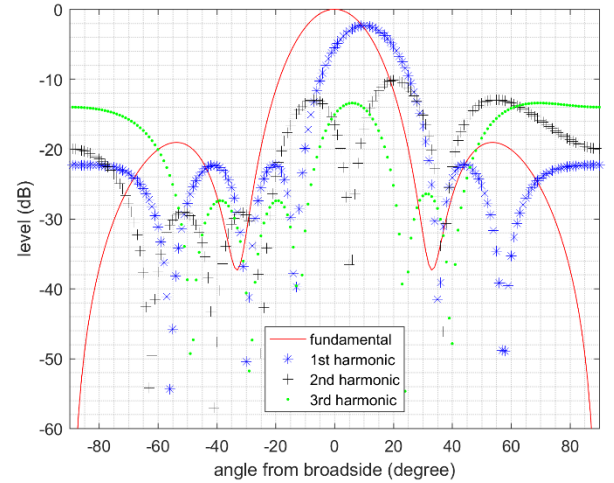


Fig. 2. Six element TMA AF for fundamental and positive harmonics 1 to 3. T_r and T_f set to 0.1% of T_p , first harmonic beam set to +10 degrees.

As an example of the effect of switching slew, let T_r and T_f now increase to 200ns (20% of T_p). As would be expected, the magnitude of the harmonic levels predicted by (5) are significantly reduced, as shown in Fig. 3.

In some circumstances it may be desirable to precisely control the magnitudes of the higher harmonic beams: control of T_r and T_f , or adjusting T_k for a given T_r and T_f , are ways this could be achieved.

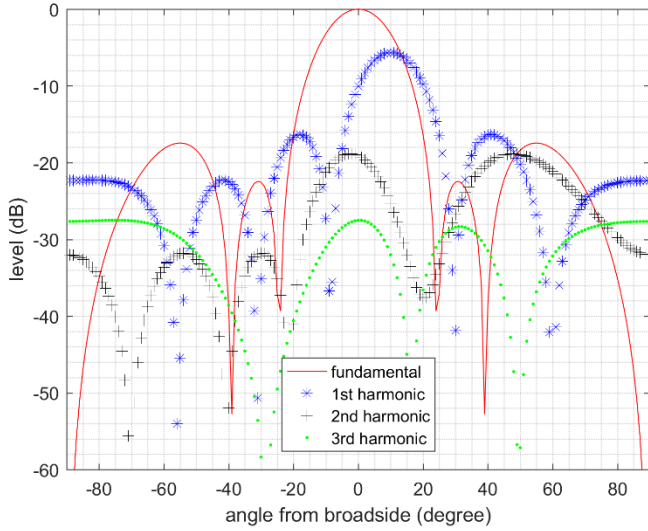


Fig. 3. Six element TMA AF for fundamental and positive harmonics 1 to 3. T_r and T_f set to 20% of T_p , first harmonic beam set to 10 degrees.

The dominant, non-steerable, beam due to Fourier $C0$ component is also strongly evident in Fig. 2 and Fig. 3. This could be a limitation in using the TMA in some practical implementations, also representing a waste of energy on the non-steerable beam. We now go on to consider how the $C0$ level emission may be controlled and reduced.

B. Use of Bipolar $U_k(t)$ to Reduce Fundamental $C0$ Emission

It will be noticed from (3) that since 0 Hz coefficient $C0$ can never be zero for practical array timings, there will always exist a strong emission on array boresight, which may be undesirable.

Other researchers have investigated simulated TMA techniques to control or reduce the levels of harmonics and sidelobes (often focusing on maintaining *only* the $C0$ beam). Techniques usually manipulate switch timings, with use of computer optimization to reduce the sidelobe levels [29], [30], [31], [32].

In this paper we offer an alternative strategy, using dedicated simple hardware and a simple algorithm to reduce the $C0$ beam, whilst also still supporting steering of other harmonic beams. One way to remove the $C0$ contribution at each element is to arrange for a two-state amplifier with gains chosen such that the combined average of $U_k(t)$ over one cycle of T_p is zero. Let the k th element amplifier have linear gain states Ra_k (positive) and Rb_k (negative) at the antenna element. The resulting equations for the Fourier coefficients at element k in this bipolar gain scenario are shown in (6) and (7).

$$C0_k = \frac{T_k}{T_p} (Ra_k - Rb_k) + Rb_k \quad (6)$$

$$Cn_k = \left(\frac{Ra_k - Rb_k}{\pi n} \right) e^{-jn\pi \left(\frac{2T_{0k}}{T_p} + \frac{T_k}{T_p} \right)} \sin \left(\frac{n\pi T_k}{T_p} \right) \quad (7)$$

If $C0_k$ is set to zero in (6), a relationship between Ra_k and Rb_k can be obtained for the k th element that should remove the $C0$ term, as now shown in (8).

$$\frac{Ra_k}{Rb_k} = 1 - \frac{T_p}{T_k} \quad (8)$$

A simulation of the AF resulting from modified Fourier coefficients (6) and (7) to point a first harmonic beam at +10 degrees and using element specific gains Ra_k and Rb_k from (8) applied to (1) is shown in Fig. 4. (T_r and T_f are set to zero). For this simulation six antenna elements were used ($k = 1..6$), all Ra_k values were set to 0dB, 0 degrees phase and Rb_k values were found using (8) as follow:-

$$Rb1 = Rb6 = -13.1\text{dB}, 180 \text{ degrees}$$

$$Rb2 = Rb5 = -8.1\text{dB}, 180 \text{ degrees}$$

$$Rb3 = Rb4 = 0\text{dB}, 180 \text{ degrees}$$

Using the proposed technique, Fig. 4 clearly shows the cancellation of the fundamental $C0$ emission as desired. Fig. 4 also shows visible minor effects on the shape of the remaining beams, due to the $C0$ canceller, compared to the normal TMA.

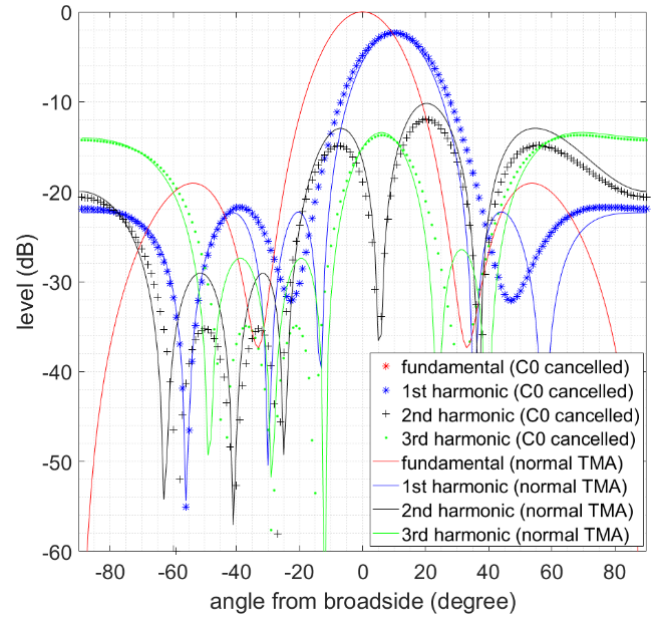


Fig. 4. Six element TMA AF for fundamental and positive harmonics 1 to 3. Harmonic beams shown for normal TMA mode and $C0$ cancellation mode, first harmonic beam set to 10 degrees. Fundamental $C0$ carrier component cancelled.

Key attractions of the TMA are its low cost and low implementation complexity, in contrast to using phase shifters or vector modulators commonly used in antenna arrays for beam steering. It is therefore proposed that calculating and controlling gain Rb_k and Ra_k on a per-element basis is highly unattractive, due to the complexity of element RF hardware - hence a pragmatic approach is required. The ideal values of Rb_k vary with element and desired beam angle, but we have observed that their average value across the array is constant per harmonic, regardless of the beam pointing angle.

Furthermore, we have found that all values of Rb_k can be quantized to a subset of just two values ($Rb1q, Rb2q$) and still provide useful (though imperfect) cancellation of the fundamental whilst steering beams in the first three harmonics. Considering the first, second and third harmonic beams, example values of $Rb1q$ and $Rb2q$ which led to better than 10dB CO cancellation across the array pattern were found by simulation and are described in linear form by (9) and (10). In (10) $mean(Rb)$ is the average of all elements' ideal Rb_k values, as found using (8), and Rb_mid is the ideal value of Rb for the centre element in the array. Ra was chosen and fixed the same for all elements at 0dB.

$$Rb1q = -Ra \quad (9)$$

$$Rb2q = mean(Rb) - \frac{Rb_mid}{6} \quad (10)$$

The choice between $Rb1q$ or $Rb2q$ for the gain to be used for Rb_k in element k was then made based on comparing the ideal value of Rb_k to the value $mean(Rb)$ as follows:

```

if ( $Rb_k < mean(Rb)$ )
   $Rb_k = Rb1q$ 
else
   $Rb_k = Rb2q$ 
end

```

When pointing the second or third harmonic beam, a simpler mapping just using $Rb2q$ was found sufficient: $Rb_k = Rb2q$. Further improvements in the technique to select $Rb1q$ and $Rb2q$ may be possible but have not been trialed, and may possibly require numerical solutions. However, the technique proposed has been sufficient to support investigation of our CO cancellation concept.

Example AFs using an array of six elements are shown in Fig. 5 for a first harmonic beam pointed at +18 degrees and Fig. 6 for a second harmonic beam at +35 degrees. The following Rb_k values were used for the first harmonic beam generation, using (9), (10) and the proposed $Rb1q Rb2q$ algorithm:-

$Rb1 = Rb6 = -8.6\text{dB}$, 180 degrees
 $Rb2 = Rb5 = -8.6\text{dB}$, 180 degrees
 $Rb4 = Rb3 = 0\text{dB}$, 180 degrees

The required values for generating CO reduction when pointing the second harmonic beam were:-

$Rb1 = Rb6 = -16.8\text{dB}$, 180 degrees
 $Rb2 = Rb5 = -16.8\text{dB}$, 180 degrees
 $Rb4 = Rb3 = -16.8\text{dB}$, 180 degrees

Hence, it is therefore proposed that by use of RF switches and fixed gain states in the TMA, the fundamental carrier (un-steered) CO emission can be reduced, whilst maintaining beam steering across the remaining harmonics.

III. TMA RF HARDWARE TEST PLATFORM

TMA generally requires fast RF switching, with a slew rate significantly faster than the switching frequency if higher harmonics are to be available for beams. The effect of switching slew on harmonic energy levels has been shown in (4) and (5). Furthermore, to obtain harmonic beams with a wide spectral spacing requires a high switching frequency.

To allow us to investigate our CO cancelling algorithm and assess the real-world performance, a 5.8GHz transmitting (TX) test platform with six novel switched antennas has been created.

A. Design of 5.8GHz RF Switching Cell and Test Platform Hardware

As described thus far, we propose to modify the TMA $Uk(t)$ waveform to be bipolar, with a single fixed positive gain state (Ra) and two fixed negative gain states ($Rb1q, Rb2q$) with the same values available for use at each element. From (8) it can be seen that the ratio of stage gains are key, hence the absolute gains can be scaled to convenient practical values.

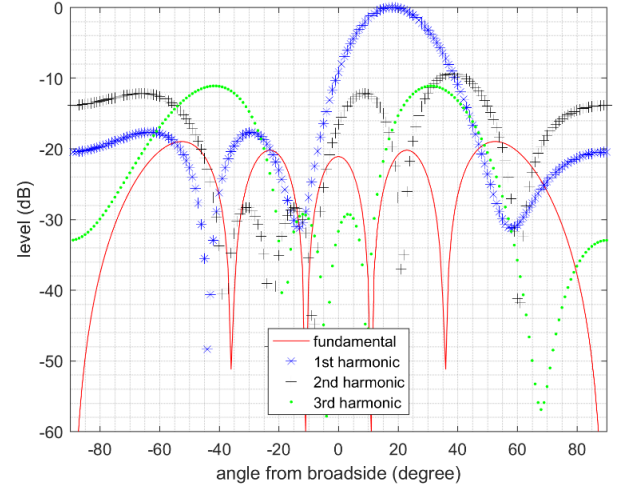


Fig. 5. Six element TMA AF for fundamental and positive harmonics 1 to 3, with first harmonic beam pointing at +18 degrees. TMA bipolar gain quantized to $Ra, Rb1q, Rb2q$. Carrier beam suppressed by 20dB.

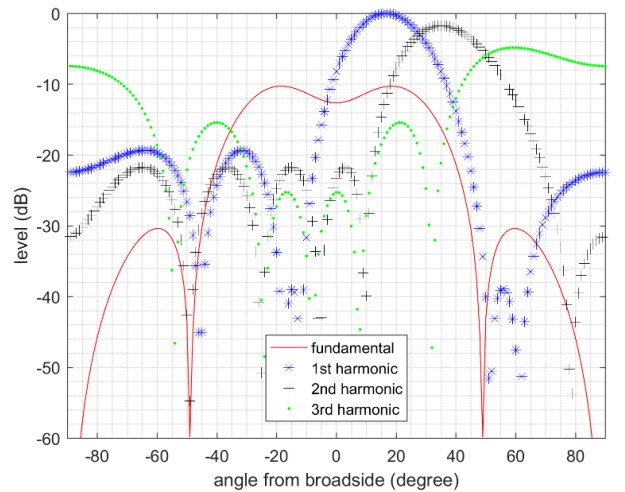


Fig. 6. Six element TMA AF for fundamental and positive harmonics 1 to 3, second harmonic beam pointing at +35 degrees. TMA bipolar gain quantized to $Ra, Rb1q, Rb2q$. Carrier beam suppressed by 10dB.

The proposed test platform consists of six identical stages (or cells), each using three gain states: $Ra = 0\text{dB} / 0$ degree phase, $Rb1q = 0\text{dB} / 180$ degree phase and $Rb2q = -10\text{dB} / 180$ degree phase. Simulations of the expected AF patterns when using the quantized gains for a desired first harmonic beam at 18 degrees are shown in Fig. 7, which shows similar AF to Fig. 5, though with further $C0$ nulling on boresight.

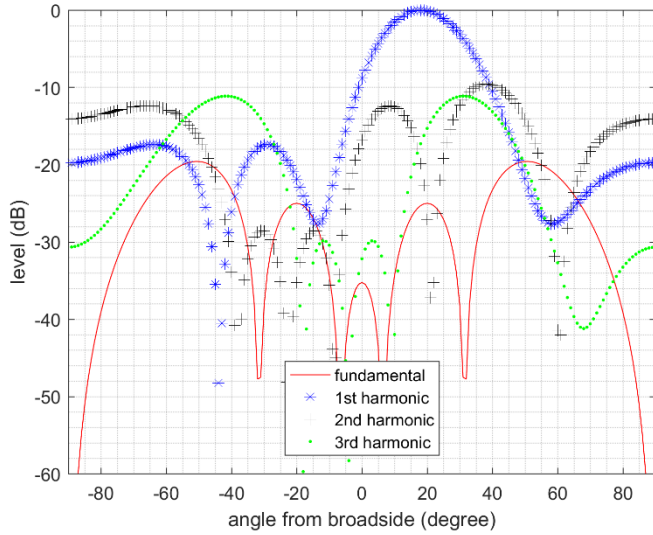


Fig. 7. Fundamental reduction for a six element array, first harmonic beam pointing at 18 degrees, fixed $Rb2q = Rb1q - 10\text{dB}$.

The individual cell RF hardware used to implement the required switched gains and phase is shown in Fig. 8. The single switching cell was designed based on an Analog Devices HMC7992 single pole 4-throw RF switch [33], with a resistive attenuator pad to implement level control for $Rb2q$ and coplanar waveguide PCB tracking to implement the required phase inversions for $Rb1q$ and $Rb2q$, with reference to Ra . The output of the cell branches are combined via a simple three-way Wilkinson combiner. The HMC7992 switch has the advantage of providing a 50 ohm termination to all ports, including the unselected ports. This simplifies the design of the Wilkinson output combiner network due to all ports seeing correct termination regardless of switch state. Finally, an RF amplifier using an Analog Devices ADL5611 [34] was used at the output to drive the cell's patch antenna. The switching cell was then duplicated six times to create the six element array. A six way feed network of Wilkinson splitters was created to distribute the input 5.8GHz RF signal to all the cells.

The switching control and sequencer for the TMA was implemented using a Microchip DSPIC (DSPIC33EP512GP806) [35], clocked internally at 140MHz and providing a sample rate of 2Msamples/s in the form of a 12 bit parallel word to control switch states for all the HMC7992 switches. The DSPIC hence defines the overall frame length T_p , as well as T_k and T_{0k} . The DSPIC produces 70 discrete samples per each frame, resulting in a T_p of 35 μs .

Fig. 9 shows the structure of the complete system, including RF input signal distribution.

The completed PCB consists of an FR4 substrate 1.6mm thick with two copper layers and with an overall PCB size of 210mm by 160mm. The radiating elements are conventional 5.8GHz patch antennas, with centre spacing of 19mm.

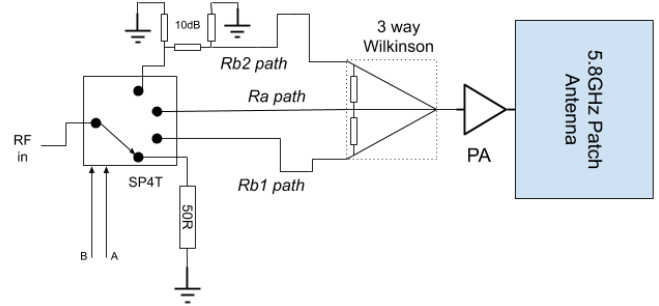


Fig. 8. A single TMA cell with Ra , $Rb1q$ and $Rb2q$ paths selected by RF switch.

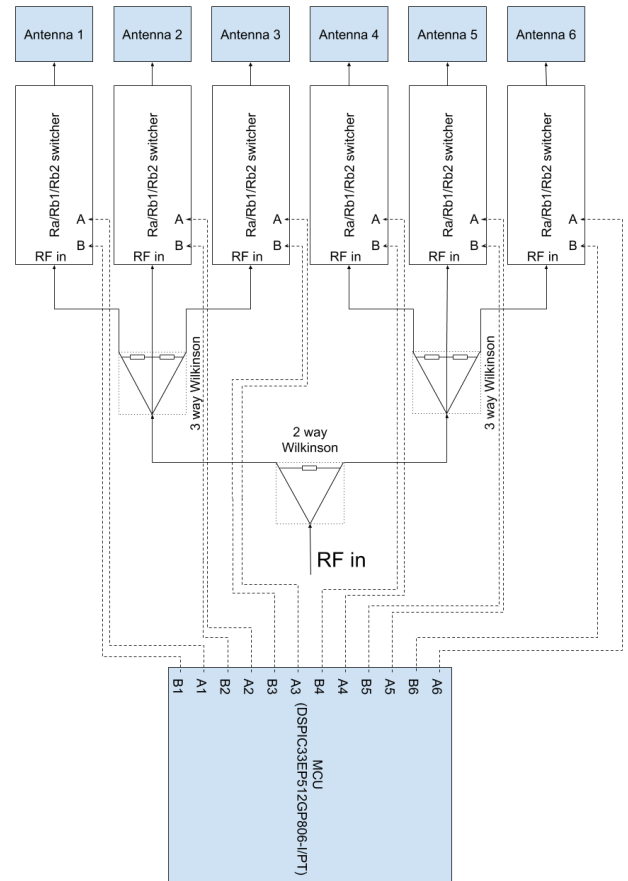


Fig. 9. Full TMA RF hardware system, using six stages and DSPIC MCU pattern sequencer.

B. Generation of Switching Patterns for TMA Hardware Platform

Trial switching patterns were generated in Matlab and then loaded into the DSPIC. The switching patterns were created using (1) and (2) to obtain a chosen n harmonic beam to point in a desired angular direction. The AF for the array

with particular element timings can therefore be expressed by (11).

$$AF(\theta, t) = e^{j[\omega_c + n\omega_p]t} \cdot \sum_{k=1}^N e^{j\varphi_k} \cdot \frac{\sin\left(n\pi \frac{T_k}{T_p}\right)}{n\pi} \cdot e^{-jn\pi\left(2\frac{T_{0k}}{T_p} + \frac{T_k}{T_p}\right)} \quad (11)$$

The derivation of equations used to calculate the element-specific timings T_k and T_{0k} for a particular frame period T_p are based on the approach in [5], but now extended here to use an arbitrary desired harmonic n , as shown in (12) and (13).

$$T_k = T_p \cdot \frac{\arcsin(G(k))}{n\pi} \quad (12)$$

$$T_{0k} = T_p \cdot \left[\frac{(k-1)d_\lambda \sin(\theta_t)}{n} - \frac{T_k}{2T_p} \right] \quad (13)$$

In (12) and (13), $G()$ is a desired Dolph-Chebyshev array of weights for the overall array pattern [36], n is the desired harmonic beam (1 for first harmonic, 2 for second, etc) to point in desired angular direction θ_t , and d_λ is the element spacing divided by wavelength (0.5 used for half-wavelength spaced elements). Dolph-Chebyshev array weights were chosen to achieve a 20dB sidelobe level.

The *maximum* beam steering angle possible for a particular harmonic can be defined as the point when any of the array's RF switches have an on time ($T_{0k} + T_k$) exceeding the frame period T_p . Such an occurrence would cause the switch to be turned off after the end of the current frame duration – which is clearly an invalid configuration. For our system, the steering range is -19 degrees to $+19$ degrees for the first harmonic and -46 degrees to $+46$ degrees for the second harmonic.

It should also be noted that the expected array gain for the harmonic beam from (1) and (7) can be calculated and compared for different Rb_k values, including the conventional TMA with no CO cancellation (i.e. Rb_k equals zero).

C. Initial Testing of TMA Hardware Platform

The built TMA PCB was first tested using 5.8GHz conducted RF signals feeding each cell, to test their phase and amplitude alignments. The results of this commissioning test are shown in Table I, overall showing good agreement with the desired amplitude and phase shifts required for Ra , $Rb1q$ and $Rb2q$ for each cell. The expected conducted gain for the Ra path was -4 dB (due to FR4 PCB tracking, Wilkinson splitters, etc) and the mean Ra path gain measured was -6 dB. When combined with a typical patch antenna gain, this leads to a predicted element cell radiated gain of circa -3 dB.

The typical measured RF power ramp duration T_f was 90ns and the T_r duration was 100ns, as measured using a Rohde & Schwarz FSIQ26 spectrum analyser in 0 Hz mode. Given our T_p of 35 μ s and (5) suggests that the RF switches will not enforce notable attenuation on the harmonic beams.

The measured mean gain difference between $Rb1q$ and Ra paths was -0.6 dB and the mean gain difference between $Rb2q$ and Ra paths was -10.3 dB. The mean phase error for the required 180 degree shift between $Rb1q$ and Ra paths was -0.2 degrees and for $Rb2q$ to Ra paths was 1.0 degree. This overall gave confidence that the TMA system was functioning adequately and absolute gain and phase alignment between cell stages was acceptable.

The return loss and coupling between the 5.8GHz patch antennas was also measured. The return loss for each antenna was found to be better than 10dB and the isolation due to mutual coupling was better than 13dB between adjacent elements.

Simulations were run to investigate the expected performance of the cancellation algorithm when using the measured PCB values for all elements' Ra , $Rb1q$ and $Rb2q$. Fig. 10 shows the expected AF for the carrier fundamental and first harmonic beam when pointed at $+18$ degrees; still providing 20dB of rejection relative to the carrier, as also seen in Fig. 5.

TABLE I
MEASURED CELL STAGE GAINS AND PHASE SHIFTS

Stage k	Gain Delta $Rb1q(k)$ - $Ra(k)$ (dB)	Gain Delta $Rb2q(k)$ - $Ra(k)$ (dB)	Phase Delta $Rb1q(k)$ - $Ra(k)$ (degrees)	Phase Delta $Rb2q(k)$ - $Ra(k)$ (degrees)
1	-2.4	-10.4	-179	-180
2	2.3	-10	-173	-178
3	0.3	-9.5	-187	-180
4	-1	-10	-180	-181
5	-1	-10.6	-182	-181
6	-1.6	-11.2	-180	-174

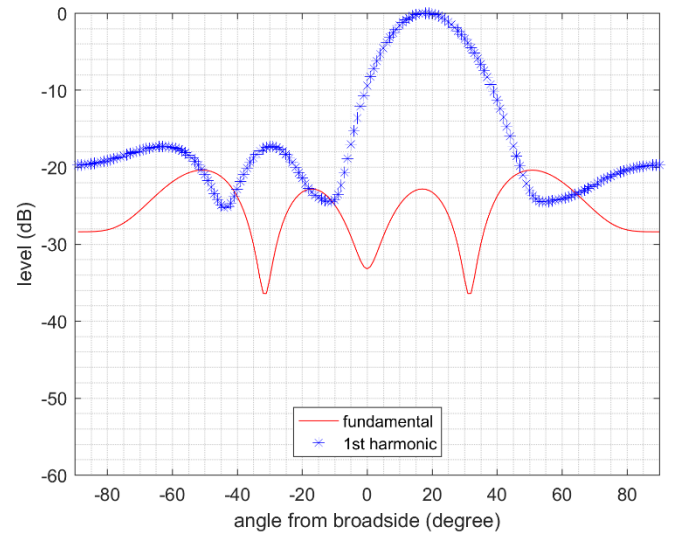


Fig. 10. Six element TMA simulated AF for fundamental and first positive harmonic. Harmonic beam pointing at $+18$ degrees. TMA bipolar gain quantized to measured PCB values for Ra , $Rb1q$, $Rb2q$. Fundamental suppressed by 20dB.

IV. TMA RADIATED CHAMBER TESTS

The TMA PCB was tested in an anechoic chamber in the University of Sheffield's Communications Research

Group. Tests evaluated the magnitude of the fundamental ($C0$), first ($C1$) and second ($C2$) harmonic beam patterns. The measurement system consisted of a Gigatronics 2540B 5.8GHz CW signal source, Rohde & Schwarz FSV40-N Spectrum Analyser and AEL H-1498 measurement horn antenna. The H-1498 measurement antenna was mounted on a movable arch, pointing down vertically from above towards the TMA under test, thus allowing measurement of the radiated energy at various azimuth angles (test PCB facing upwards). Due to limitations of the measurement system, one measurement horn was used to measure emissions for clockwise rotations of the arch and another identical horn for anti-clockwise rotation. The measurement system is shown in Fig. 11, with an example measurement shown in Fig. 12a. Fig. 12b shows the RF side of the assembled TMA PCB. The distance d between the measurement horn(s) and the TMA PCB was 56cm. Since this is an anechoic measurement environment and far-field, simple free space path loss (FSPL) can be used at the measurement wavelength λ , using (14).

$$FSPL = 20 \log_{10} \left(\frac{4\pi d}{\lambda} \right) \text{ dB} \quad (14)$$

The manufacturer's specification of the H-1498 horn antenna gain (circa 8dBi), a calculation of 43dB for the FSPL between the TMA PCB and measurement horn and a measurement of the overall cable loss allowed an estimation of the radiating gain of the TMA as an antenna array system to be made. Therefore, the measurement figures in this section show the measured radiated gain in dBi, after accounting for the measurement losses in the system. This is useful in allowing an absolute comparison between various radiated levels and also comparing to theoretical simulations. Background noise was circa 70dB below measured main-lobe powers.

Tests were first performed without any screening can fitted to the PCB and with a desired $C1$ first harmonic beam steered to +18 degrees, first without and then with the $C0$ cancellation algorithms operational, with results shown in Fig. 13 and Fig. 14 respectively. Since, at this stage, no RF screening enclosure was fitted to the PCB, the reduction in achieved $C0$ cancellation was suspected to be due to radiation directly from the circuitry, prior to the patch antennas, thus limiting the dynamic range of the chamber measurements. To investigate this, the outputs from each TX stage were terminated in 50 ohm loads and their antennas isolated. The emissions emanating from the board were then measured and indeed confirmed to be significant. The effect of this leakage from the PCB (mainly from the input Wilkinson distribution network) was characterised and found to impose a measurement floor to the antenna gain calculations, as presented in Table II.

TABLE II
GAIN MEASUREMENT FLOOR DUE TO PCB LEAKAGE
EMISSIONS

Measurement angle (degrees)	Fundamental ($C0$) measurement floor (dBi)	1 st harmonic ($C1$) measurement floor (dBi)	2 nd harmonic ($C2$) measurement floor (dBi)
0	-10	-30	-28
-10 / +10	-10	-30	-44
-20 / +20	-20	-40	-37
-40 / +40	-20	-33	-37

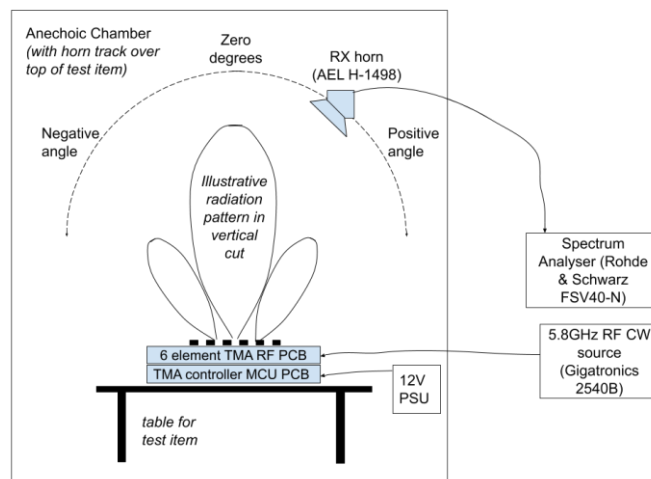


Fig. 11. Laboratory TMA radiated measurement system.

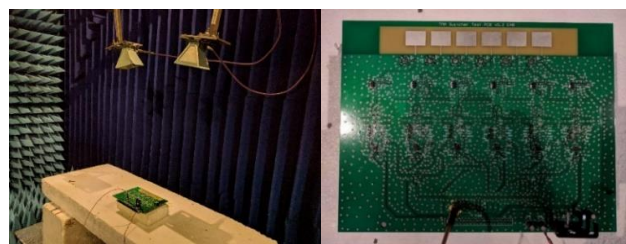


Fig. 12. TMA RF hardware testing. (a) example TMA pattern measurement being taken, (b) built TMA test system, with DSPIC on reverse of PCB.

To help reduce the compromising of the measurements due to carrier leakage, a screening can was then fitted over the entire RF circuitry. Tests were again performed with a desired $C1$ first harmonic beam steered to +18 degrees, without and then with the $C0$ cancellation algorithms operational, with results shown in Fig. 15 and Fig. 16 respectively. Comparing the $C0$ traces on Fig. 14 and Fig. 16 shows a circa 5dB reduction in carrier seen on the boresight, confirming that PCB leakage had been an issue. Figs. 14 and 16 also show the predicted theoretical radiated gain (isotropic reference) of the array from (11), for comparison. Unless stated, all subsequent reported measurements are using the screened PCB system.

Tests were then performed for a desired $C1$ harmonic beam steered to -18 degrees both without and with the $C0$ cancellation algorithms operational, with results shown in Fig. 17 and Fig. 18 respectively. In all cases the $C0$ magnitude is reduced on boresight by our technique and the

main lobe of the $C1$ steered beam broadly follows the gain and beam shape from the AF predictions.

Comparing Fig. 15 to Fig. 16 also shows an increase in the desired first harmonic $C1$ beam. However Fig. 16 appears to also show circa 5dB less than expected $C0$ cancellation was achieved on the PCB, for reasons we discuss later.

The TMA was then configured to produce a desired beam at +35 degrees, using the second switching harmonic, $C2$. The results for this scenario when the fundamental $C0$ signal is present unmodified and then when the $C0$ canceller is operational are shown in Fig. 19 and Fig. 20 respectively.

In Fig. 20 the level of cancellation of the $C0$ beam is less than that obtained when steering the first harmonic beam, such as in Fig. 16. This is expected and due to the compromise made in quantizing element gains Rb_k and Ra_k to common Ra , $Rb1q$ and $Rb2q$ fixed gain states, as discussed in Section IIB. Improved $C0$ cancellation would require either more Rb states or variable control of gains Rb_k and Ra_k per element.

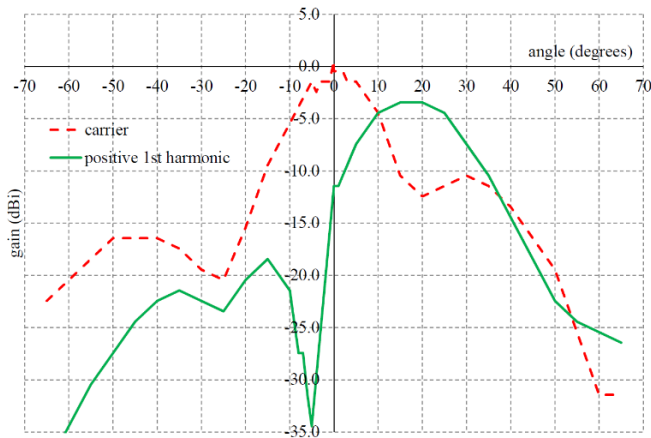


Fig. 13. Measured radiated gain of TMA when pointing first positive harmonic beam to +18 degrees in conventional TMA pattern operation (no PCB screening can).

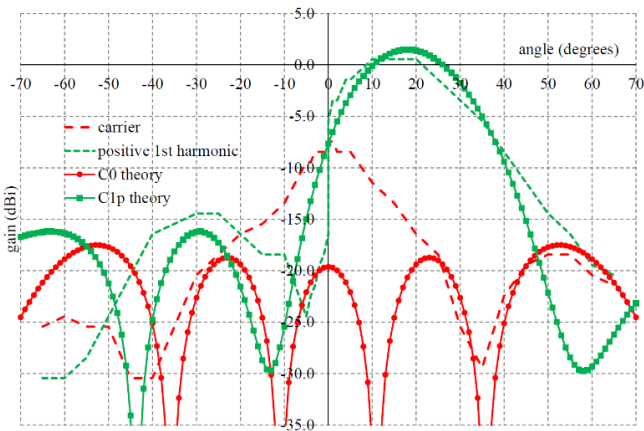


Fig. 14. Measured radiated gain of TMA pointing first positive harmonic beam to +18 degrees with $C0$ canceller activated (no PCB screening can).

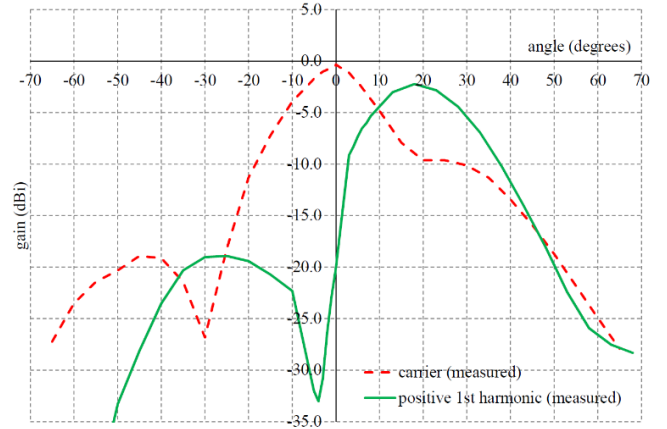


Fig. 15. Measured radiated gain of TMA when pointing first positive harmonic beam to +18 degrees in conventional TMA pattern operation (with PCB screening can).

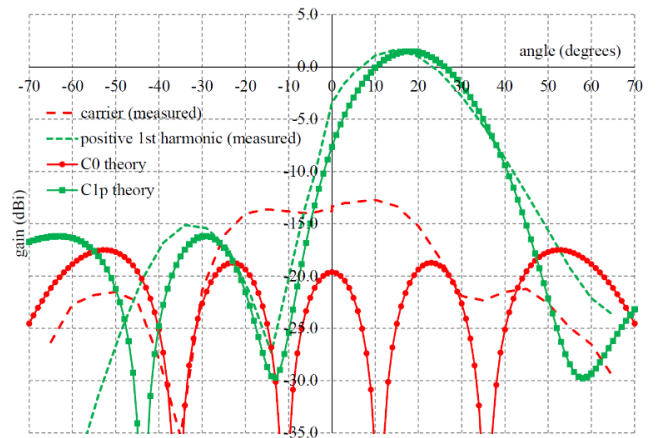


Fig. 16. Measured radiated gain of TMA pointing first positive harmonic beam to +18 degrees with $C0$ canceller activated (with PCB screening can).

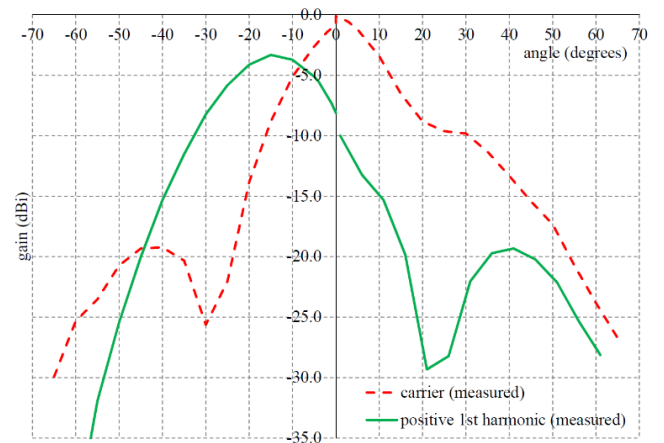


Fig. 17. Measured radiated gain of TMA pointing first positive harmonic beam to -18 degrees in conventional TMA pattern operation (with PCB screening can).

Comparing Fig. 19 and Fig. 20 does show that the fundamental emission on boresight due to $C0$ has been reduced by circa 10dB and the beam pattern also follows the trend predicted in AF simulations. The wanted $C2$ emission has increased and also closely follows AF simulations.

To allow comparisons, the $C2$ and $C0$ emissions without the screening can fitted are shown in Fig. 21. An improvement in $C0$ cancelation due to the screening can is seen in Fig. 20, also showing a close trend to theoretical predictions for $C0$.

With the screening can refitted, the TMA was then configured to produce a desired $C2$ beam at -35 degrees, again using the second harmonic. The results for this scenario when the fundamental $C0$ signal is present and then when the $C0$ canceller is operational are shown in Fig. 22 and Fig. 23 respectively.

Note that Figs. 16, 18, 20, 21 and 23 also show the predicted gain (isotropic reference) of the array from (11), for comparison. Here, the predicted gain of (11) uses actual PCB measured values for Ra , $Rb1q$ and $Rb2q$, extracted from each of the six cells.

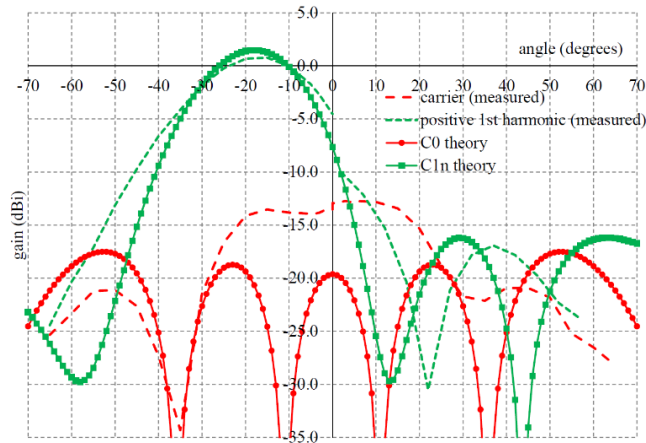


Fig. 18. Measured radiated gain of TMA pointing first positive harmonic beam to -18 degrees with $C0$ canceller activated (with PCB screening can).

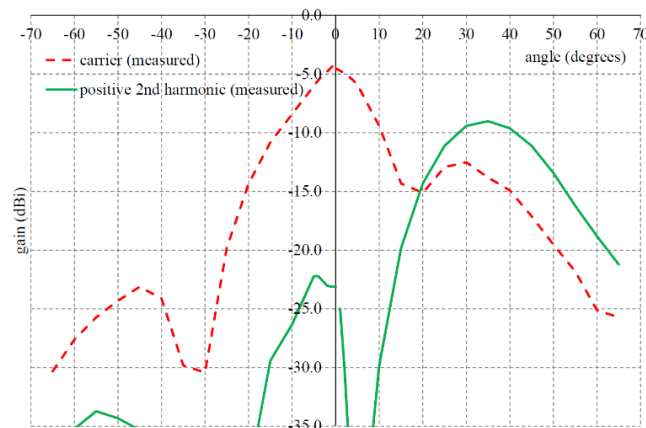


Fig. 19. Measured radiated gain of TMA pointing second positive harmonic beam to $+35$ degrees in conventional TMA pattern operation (with PCB screening can).

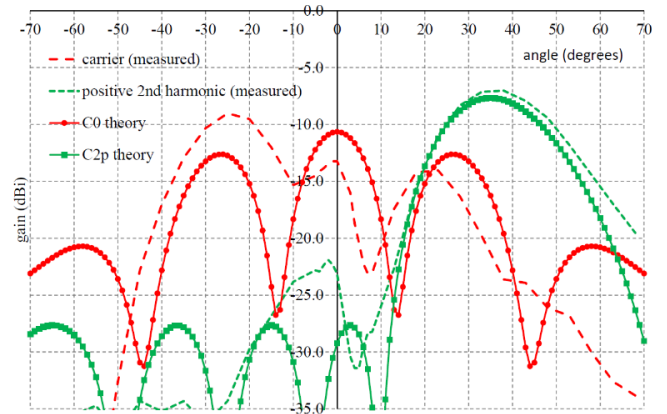


Fig. 20. Measured radiated gain of TMA pointing second positive harmonic beam to $+35$ degrees with $C0$ canceller activated (with PCB screening can).

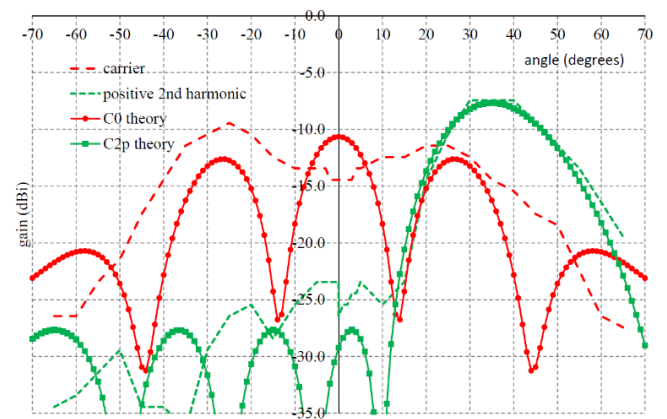


Fig. 21. Measured radiated gain of TMA pointing second positive harmonic beam to $+35$ degrees with $C0$ canceller activated (no PCB screening can).

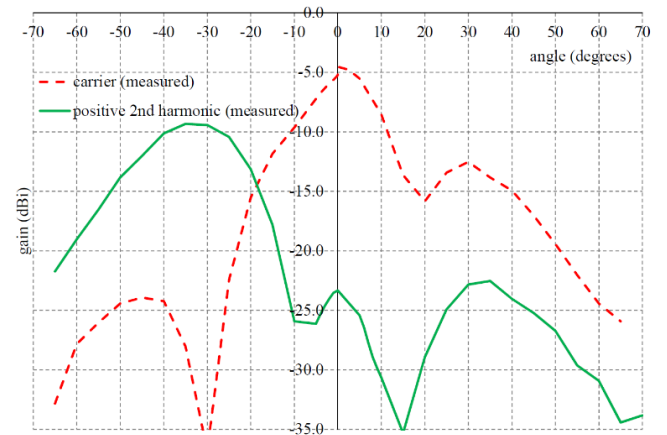


Fig. 22. Measured radiated gain of TMA pointing second positive harmonic beam to -35 degrees in conventional TMA pattern operation (with PCB screening can).

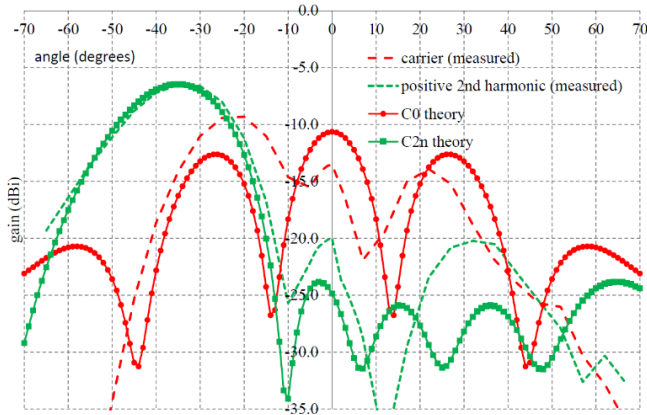


Fig. 23. Measured radiated gain of TMA pointing second positive harmonic beam to -35 degrees with $C0$ canceller activated (with PCB screening can).

From Fig. 22 and Fig. 23 it is clear that the $C0$ canceller is reducing the strength of the fundamental emission on boresight by circa 8dB and also following the trend predicted by the AF simulations. Similarly, the desired $C2$ beamwidth and gain are closely matching AF calculations and the performance is also broadly similar to the AF as seen in Fig. 20 (using the opposite beam).

The fundamental radiated performance of three antennas and associated circuit cells (A1, A3, A6) within the array was also characterised, to investigate their basic patterns, with results shown in Fig. 24. The expected radiated gain of a cell is -3dBi (based on measured average Ra gain of -6dB, a theoretical PCB patch antenna directivity of 6dBi and FR4 radiating efficiency of -3dB) - which agrees well with the boresight gains measured for A1, A3 and A6. The radiated RF leakage without DC power applied is also shown in Fig. 24. It is clear that whilst there are some differences between the individual measured antenna cells (contributed to by the spread in Ra circuit performance as well as possible antenna radiating pattern differences), the patterns are still broadly similar. The leakage from the PCB without DC power applied is also evident and imposes a fundamental floor on radiated $C0$ boresight cancellation of circa -18dBi. From subsequent tests we have found that RF radiation from the feed coax close to the PCB SMA connector, and the use of spot-solder joints (rather than seam solder joints) around the screening can are both still leading to some higher than desired carrier leakage.

The reduction of the $C0$ beam can be predicted using (6). With the actual PCB values used for $Rb1q$, $Rb2q$, Ra and chosen switch timings, we would expect to see 20dB reduction in the $C0$ emission, when using the 18 degree $C1$ harmonic beam. We would expect to see a 10.6dB reduction in $C0$ emission when using the 35 degree $C2$ harmonic beam. However, the measured $C0$ reduction is 12.6dB when the 18 degree first harmonic beam is selected and worst-case 5dB (9.1dB when only considering $C0$ at boresight) when the 35 degree second harmonic beam is selected. Fig. 24 suggests that the unwanted PCB emissions from carrier leakage could

be limiting the performance of the $C0$ cancellation, as observed in Fig. 16, Fig. 18, Fig. 20 and Fig. 23.

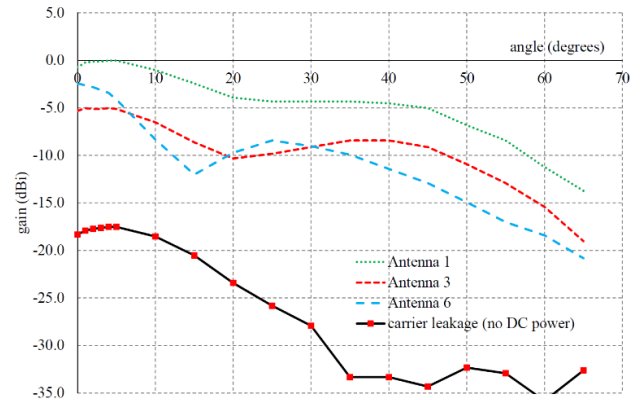


Fig. 24. Measured radiated gain pattern (half of pattern) for three TMA antenna cells (Ra path and a single antenna tested in turn, all other antennas off). Carrier leakage with PCB unpowered is also shown.

Also, note that due to the choice of values made for $Rb1q$, $Rb2q$ and Ra , the existing PCB design is theoretically, and in practice, more suited to $C0$ cancellation when pointing the $C1$ beam, rather than when using the $C2$ beam. This difference can, for example, be seen by comparing Fig. 16 and Fig. 20 or indeed Fig. 5 and Fig. 6.

It is interesting to note that when the $C0$ reduction algorithm is operational, as well as attenuating the radiated energy in the boresight $C0$ beam, there is also an increase in energy in the harmonic beams. This can be predicted using (7) using the actual timings and Ra , $Rb1q$ and $Rb2q$ values obtained from the PCB. The expected gain enhancement of the first harmonic beam is 4.1dB and for the second harmonic beam an enhancement of 2.3dB is expected. In practice we see an enhancement of 3.9dB for the first harmonic and 2.8dB for the second harmonic beam.

Overall, with the limitations of the PCB as-built, we are achieving an effective decrease in $C0$ emission of 16.5dB relative to the first harmonic beam $C1$, which from theory should be 21.3dB if $C0$ RF PCB leakages were insignificant. We achieve a decrease in effective $C0$ emission of worst-case 7.6dB (11.8dB if only $C0$ boresight is considered) relative to the second harmonic beam $C2$, which broadly agrees with the theoretical prediction of 10.8dB.

The measured equivalent isotropic gain of the $C0$ cancelled TMA system is +2dBi for the first harmonic beam and -6dBi for the second harmonic beam. A comparable phased array (using the same PCB RF amplifiers, splitters and antennas, but assuming phase shifters are used instead of the TMA RF switches) would be expected to have a gain of +4.6dBi. The 2.6dB loss in first harmonic beam gain can be considered an *implementation loss* for the TMA. Such a loss may be acceptable for many applications, given the lower cost of the hardware and simpler digital control supported, possibly also mitigated by using a larger array of elements.

V. CONCLUSION

This paper has presented new TMA techniques to predict and control the magnitude of the fundamental carrier (C_0) beam whilst still steering higher-order radiated harmonic beams (C_1 , C_2). These techniques will enable TMA system to become more useful to industrial and commercial radio system designers.

The algorithmic concepts have been demonstrated and tested using a new, bespoke, RF hardware platform operating at 5.8GHz, with test results generally showing good agreement with theory. The sensitivity of the TMA radiated performance to PCB RF leakage emissions has been identified as a limiting factor.

Further work is now planned to operate the TMA platform at higher switching rates and to develop techniques to control multiple harmonic beam levels. For this we are developing an FPGA platform to control the TMA, replacing the DSPIC. This faster switching platform will then allow us to investigate further harmonic control, such as using pulse-splitting techniques as investigated in [37]. Higher switching rates are vital to spectrally separate the generated harmonics, thus supporting transport of user modulated data on an RF channel. The higher switching rates will also allow us to vary T_k as a means to control harmonic levels using (5) in systems where T_r and T_f are fixed, which is the usual case for RF switches.

There is currently much interest in beam steering for future 5G and mmWave mobile systems. To be commercially viable, such systems must be cost-effective and very power efficient. The simple and low cost RF hardware TMA concepts described in this paper may be applicable to such future handset antenna arrays, which could be pointing traffic to only a single base station at a given instant.

Although this paper has focused on a transmitter TMA, the concept of the triple-gain-state RF switch circuitry could also be applied for receiving arrays using low noise amplifiers, or indeed in a transceiver array.

REFERENCES

- [1] S. Kuttu, and D. Sen, "Beamforming for millimeter wave communications: an inclusive survey," *IEEE Communications Surveys & Tutorials*, vol. 18, no. 2, pp. 949-973, Dec. 2015.
- [2] W. H. Kummer, A. T. Villeneuve, T. S. Fong, and F. G. Terrio, "Ultra-low sidelobes from time-modulated arrays," *IEEE Transactions on Antennas and Propagation*, vol. 11, no. 6, pp. 633-639, Nov. 1963.
- [3] Y. Tong, and A. Tennant, "Simultaneous control of sidelobe level and harmonic beam steering in time-modulated linear arrays," *Electronics Letters*, vol. 46, no. 3, pp. 201-202, Feb. 2010.
- [4] W-Q. Wang, H. C. So, and A. Farina, "An overview on time/frequency modulated array processing," *IEEE Journal of Selected Topics in Signal Processing*, vol. 11, no. 2, pp. 228-246, March, 2017.
- [5] G. Li, S. Yang, Y. Chen, and Z. Nie, "A novel beam scanning technique in time modulated linear arrays," *2009 IEEE Antennas and Propagation Society International Symposium*, Charleston, 2009, pp. 1-4.
- [6] P. Rocca, G. Oliveri, R. J. Mailloux, and A. Massa, "Unconventional phased array architecture and design methodologies - a review," *Proceedings of the IEEE*, vol. 104, no. 3, pp. 544-560, March, 2016.
- [7] Y. Tong, and A. Tennant, "A two-channel time modulated linear array with adaptive beamforming," *IEEE Transactions on Antennas and Propagation*, vol. 60, no. 1, pp. 141-147, Jan. 2012.
- [8] E. T. Bekele, L. Poli, L. Manica, P. Rocca, A. Massa, S. Yang, and Q. Zhou, "Advances on time-modulated arrays for cognitive radio," *7th European Conference on Antennas and Propagation (EuCAP)*, Gothenburg, 2013, pp. 344-346.
- [9] W. C. Barott, and S. Fucharoeb, "Experimental time-modulated beamformer for interference mitigation in a radio spectrometer," *IEEE Journal of Selected Topics in Signal Processing*, vol. 11, no. 2, pp. 271-281, March, 2017.
- [10] L. Poli, P. Rocca, G. Oliveri, and A. Massa, "Adaptive nulling in time-modulated linear arrays with minimum power losses," *IET Microwaves, Antennas & Propagation*, vol. 5, no. 2, pp. 157-166, January, 2011.
- [11] G. Bogdan, M. Jarzynka, and Y. Yashchyshyn, "Experimental study of signal reception by means of time-modulated antenna array," *21st International Conference on Microwave, Radar and Wireless Communications (MIKON)*, Krakow, 2016, pp. 1-4.
- [12] G. Bogdan, Y. Yashchyshyn, and M. Jarzynka, "Time-modulated antenna array with lossless switching network," *IEEE Antennas and Wireless Propagation Electronics Letters*, vol. 15, pp. 1827-1830, March, 2016.
- [13] J. Chen, R. Jin, H. Fan, J. Geng, X. Liang, and C. He, "Wideband direction-finding based on time-modulated antenna arrays," *IEEE 4th Asia-Pacific Conference on Antennas and Propagation (APCAP)*, Kuta, 2015, pp. 48-49.
- [14] A. O'Donnell, W. Clark IV, J. Ernst, and R. McGwier, "Analysis of modulated signals for direction finding using time modulated arrays," *IEEE Radar Conference (RadarConf)*, Philadelphia, 2016, pp. 1-5.
- [15] D. Ni, S. Yang, Y. Chen, and J. Guo, "A study on the application of subarrayed time-modulated arrays to MIMO radar," *IEEE Antennas and Wireless Propagation Letters*, vol. 16, pp. 1171-1174, November, 2017.
- [16] G. Li, S. Yang, and Z. Nie, "A study on the application of time modulated antenna arrays to airborne pulsed doppler radar," *IEEE Transactions on Antennas and Propagation*, vol. 57, no. 5, pp. 1578-1582, May, 2009.
- [17] J. Euzière, R. Guinvarc'h, M. Lesturgie, B. Uguen, and R. Gillard, "Dual function radar communication time-modulated array," *2014 International Radar Conference*, Lille, 2014, pp. 1-4.
- [18] J. Euzière, R. Guinvarc'h, I. Hinostroza, B. Uguen, and R. Gillard, "Time modulated array for dual function radar and communications," *IEEE International Symposium on Antennas and Propagation & USNC/URSI National Radio Science Meeting*, Vancouver, 2015, pp. 806-807.
- [19] J. Euzière, R. Guinvarc'h, and I. Hinostroza, "Optimizing communications in TMA for radar," *IEEE International Symposium on Antennas and Propagation (APSURSI)*, Fajardo, 2016, pp. 705-706.
- [20] Y. Wang, and A. Tennant, "Experimental time-modulated reflector array," *IEEE Transactions on Antennas and Propagation*, vol. 62, no. 12, pp. 6533-6536, December, 2014.
- [21] R. Maneiro-Catoira, J. Brégains, J. A. García-Naya, L. Castedo, P. Rocca, and L. Poli, "Performance analysis of time-modulated arrays for the angle diversity reception of digital linear modulated signals," *IEEE Journal of Selected Topics in Signal Processing*, vol. 11, no. 2, pp. 247-258, March, 2017.
- [22] L. Poli, P. Rocca, G. Oliveri, and A. Massa, "Harmonic beamforming in time-modulated linear arrays," *IEEE Transactions on Antennas and Propagation*, vol. 59, no. 7, pp. 2538-2545, July, 2011.
- [23] A. Tennant, and B. Allen, "Generation of OAM radio waves using circular time-switched array antenna," *Electronics Letters*, vol. 48, no. 21, pp. 1365-1366, October, 2012.
- [24] C. Sun, S. Yang, and Y. Chen, "Generation of orbital angular momentum (OAM) waves using time-modulated circular arrays," *IEEE International Workshop on Electromagnetics: Applications and Student Innovation Competition (iWEM)*, Nanjing, 2016, pp. 1-2.
- [25] A. Reyna, L. I. Balderas, and M. A. Panduro, "Time-modulated antenna arrays for circularly polarized shaped beam patterns," *IEEE Antennas and Wireless Propagation Letters*, vol. 16, pp. 1537-1540, January, 2017.

- [26] R. Maneiro-Catoira, J. Brégains, J. A. García-Naya, and L. Castedo, "Enhanced time-modulated arrays for harmonic beamforming," *IEEE Journal of Selected Topics in Signal Processing*, vol. 11, no. 2, pp. 259-270, March, 2017.
- [27] E. T. Bekele, L. Poli, P. Rocca, M. D'Urso, and A. Massa, "Pulse-Shaping Strategy for Time Modulated Arrays - Analysis and Design," *IEEE Transactions on Antennas and Propagation*, vol. 61, no. 7, pp. 3525-3537, July, 2013.
- [28] P. Rocca, L. Poli, and A. Massa, "Instantaneous directivity optimisation in time-modulated array receivers," *IET Microwaves, Antennas & Propagation*, vol. 6, pp. 1590-1597, November, 2012.
- [29] P. Rocca, and A. Massa, "Innovative Approaches for optimized Performance in Time-Modulated Linear Arrays," *Antennas and Propagation Society International Symposium*, Charleston, 2009, pp. 1-4.
- [30] L. Poli, P. Rocca, and A. Massa, "Beam pattern optimization in time-modulated linear arrays," *IEEE International Symposium on Phased Array Systems and Technology*, Waltham, 2010, pp. 876-878.
- [31] S. Yang, Y. B. Gan, and A. Qing, "Sideband suppression in time-modulated linear arrays by differential evolution algorithm," *IEEE Antennas and Wireless Propagation Letters*, vol. 1, pp. 173-175, 2002.
- [32] L. Poli, P. Rocca, L. Manica, and A. Massa, "Handling sideband radiations in time-modulated arrays through particle swarm optimization," *IEEE Transactions on Antennas and Propagation*, vol. 58, no. 4, pp. 1408-1411, April, 2010.
- [33] Analog Devices Ltd HMC7992 datasheet Available: <https://www.analog.com/en/products/hmc7992.html>
- [34] Analog Devices Ltd ADL5611 datasheet Available: <https://www.analog.com/en/products/adl5611.html>
- [35] Microchip Semiconductors Ltd dsPIC33EP512GP806 datasheet Available: <https://www.microchip.com/wwwproducts/en/dsPIC33EP512GP806>
- [36] C. A. Balanis, "Chapter 6", in *Antenna Theory - Analysis and Design*. 3rd ed. New Jersey, Wiley-Interscience, 2005.
- [37] L. Poli, P. Rocca, F. Viani, and A. Massa, "Advanced harmonic radiations design in time-modulated antenna arrays," *2015 IEEE International Symposium on Antennas and Propagation & USNC/URSI National Radio Science Meeting*, Vancouver, 2015, pp. 812-813.



Edward A. Ball (M 2008–present) Edward (Eddie) became a Member of IEEE in April 2008 and was born in Blackpool, United Kingdom in November 1973. Eddie graduated in 1996 with a 1st Class Master of Engineering Degree in Electronic Systems Engineering, from the University of York, York, United Kingdom.

After graduating, he worked in industry for 20 years, first spending 15 years working as Engineer, Senior RF Engineer and finally Principal RF Engineer at Cambridge Consultants Ltd in Cambridge, UK. He then spent 5 years as Principal RF Engineer and Radio Systems Architect at Tunstall Healthcare Ltd in Whitley, UK. In November 2015 he joined the Department of Electronic and Electrical Engineering at the University of Sheffield, Sheffield, United Kingdom, where he now works as Reader in RF Engineering. His research interests cover all areas of radio technology, from RF system design, RF circuit design (sub-GHz to mm-wave) and the application of radio technology to real-world industrial and commercial problems. He has a particular passion for RF hardware design.

Mr. Ball is a member of the IET and is a Chartered Engineer.



Alan Tennant (M 1992–present) received the B.Eng. degree in Electronic Engineering and Ph.D. degree in Microwave Engineering from the University of Sheffield, Sheffield, U.K., in 1985 and 1992, respectively.

Previously, he was with BAE Systems, Stevenage, U.K. He then joined DERA, where he worked on phased-array antenna systems before taking up an academic post with Hull University, Hull, U.K. He returned to Sheffield University in 2001 as a Senior Lecturer with the Communications and Radar

Group and is now Professor, where he is involved in research into techniques, materials, and signal processing for adaptive radar signature management, novel three-dimensional phased-array antenna topologies, acoustic array systems, and new research into time-modulated array antennas. He has published over 100 academic papers including several invited papers on adaptive stealth technology. His research has attracted substantial funding from both industry and government sources.

7. Paper 3 – Analysis of 26 GHz Downconversion Mixer Design

{Reproduced as published - author accepted version.}

© 2022 MDPI. Reprinted with permission. “Predicting the Performance of a 26 GHz Transconductance Modulated Downconversion Mixer as a Function of LO Drive and DC Bias”, published 11th August 2022.

DOI <https://doi.org/10.3390/electronics11162516>

(Published version [3].)

Predicting the Performance of a 26 GHz Transconductance Modulated Downconversion Mixer as a function of LO Drive and DC Bias

Edward A. Ball

Department of Electronic & Electrical Engineering, The University of Sheffield, UK; e.a.ball@sheffield.ac.uk

Abstract: The dependency of RF performance on the local oscillator (LO) drive amplitude and DC bias is an important topic for RF mixers, especially as carrier frequency increases and generation of RF power thus becomes more complex. The prediction of mixer performance, without initial reliance on full circuit simulations, can provide important insights. In this work, mathematical models without the prior use of circuit simulation are developed, leading to a strategy to predict the conversion gain (G_c), DC current, 1 dB input compression point (IP1dB) and third order input intercept point (IIP3) for a SiGe bipolar transistor transconductance mixer. The models show the possibility to trade-off LO RF power and DC bias to achieve a desired performance. The concepts allow a prediction of the necessary DC bias required to support a chosen LO level and desired conversion transconductance or linearity. The mathematical model results, circuit simulation results, and measured hardware results from a 26 GHz prototype of a single-ended mixer are presented and compared, showing good agreement. In a lab-measured example, LO power reduction from +10 dBm to +3 dBm resulted in only a 1 dB reduction in conversion gain, by modifying the DC bias as predicted. The peak conversion gain predicted by the models is within 2.0 dB of circuit simulation and 2.5 dB of measured PCB results. The RMS error for predicted DC current, compared to circuit simulation, is 1.9 mA or better.

Keywords: RF; Conversion gain; Linearity; Mixer design; bipolar transistor circuits; simulation

Citation: Ball, E.A. Title. *Electronics* 2022, 11, x.
<https://doi.org/10.3390/xxxxx>

Academic Editor: Firstname
Lastname

Received: date
Accepted: date
Published: date

Publisher's Note: MDPI stays neutral with regard to jurisdictional claims in published maps and institutional affiliations.



Copyright: © 2022 by the authors. Submitted for possible open access publication under the terms and conditions of the Creative Commons Attribution (CC BY) license (<https://creativecommons.org/licenses/by/4.0/>).

1. Introduction

The millimeter wave (mmWave) 5G bands at n258 (26GHz) and n257 (28GHz) are examples of the increasing adoption of mmWave frequencies for 5G and future 6G wireless communications [1]. A particular focus for mmWave systems is massive MIMO [2] which will require a multiplicity of low power RF hardware solutions at each antenna element. However, the operation of radios in the mmWave bands still requires power efficient and cost-effective RF circuit techniques to realize practical radio systems.

Whilst RF mixers can be designed and performance accurately predicted using CAD tools from the outset, this can lead to a loss of understanding of what affects the mixer performance. This is where mathematical models for circuit operation become valuable and allow fundamental insights into why particular effects or performance is seen.

Most mixer design strategies nowadays focus on FETs, due to their use in MMICs and CMOS designs. Such designs are well documented, with many published recent examples in CMOS at 28 GHz [3] and for 5G FR2 [4], 2.4 GHz [5], and increasingly at 60 GHz [6].

It is well known that the local oscillator (LO) drive power used for a frequency mixer can affect its gain, linearity and noise figure (NF). However, the generation of significant LO power at mmWave frequencies is today still complex, costly, and DC power inefficient. There is continued research interest in using simple, novel, and power-efficient RF

architectures at mmWave, because of the generally higher DC bias currents and device costs as operational frequencies increase.

1.1. Paper Motivation

Development of mathematical models to allow the RF performance of a mmWave single-ended bipolar junction transistor (BJT) mixer design to be investigated, based on a known transistor, without the initial use of a circuit simulator. Existing published literature has focused extensively on FET mixers, with less recent attention on BJT mixers. This paper investigates the viability of trading LO RF power with DC bias in an SiGe NPN RF BJT transconductance modulated mixer, significantly expanding and improving the models and measurements developed in [7]. Mathematical models to predict the IF current generated by the mixing operation within the transistor are developed, leading to a prediction of the conversion transconductance (g_{m_c}) and conversion gain (Gc), 1 dB input compression point (IP1dB) and third order input intercept point (IIP3). The concepts are demonstrated using a commercial SiGe BJT.

Prediction of required DC bias for given LO power. A model is created for predicting the required DC base bias (V_b) to achieve a desired conversion transconductance with a chosen LO power, to allow the trading of RF performance in a predictable way. The concept can also be used to predictably control the conversion gain by adjusting V_b . Conventional mixer design approaches tend to set the DC bias and optimize the LO power for the best RF performance [8 - 10]. To the author's best knowledge, the mathematical prediction of RF mixer performance by jointly selecting LO power and V_b has not been extensively explored previously, particularly relating to SiGe BJTs, although empirical relationship results have been observed and reported, for example [11].

Investigation into the use of low-cost commercial BJT in mmWave downconverting mixer. Although the focus of this paper is on the performance prediction of single transistor downconversion mixer at 26 GHz, a hardware prototype was created using a commercial packaged transistor. This useful prototype has facilitated lab testing.

1.2. Background

Most recent literature for downconversion transistor-based mixer analysis and design are focused on CMOS, mainly using the Gilbert Cell architecture, (for example [12] at 24 GHz), though these can have poor performance at mmWave frequencies [13]. The related circuit analytical design often focuses on noise reduction techniques, with examples at 3.1GHz [14] and 5G 27.5 GHz – 43.5 GHz [15]. Linearity improvement techniques are also popular research topics for CMOS, such as for IIP3 in 802.15.4 at 2.4GHz [16] or for second order input intercept point (IIP2) improvement [17]. Published works tend rely on subsequent circuit simulation for validation of trialed design techniques.

Single device (i.e., single-ended) downconverting mixers using GaAs transistors have been widely reported, for example [18] demonstrating a 6-26 GHz mixer requiring 13 dBm LO and [19] demonstrating a 5-30 GHz mixer requiring 15 dBm LO. However, SiGe devices can generally operate at lower bias current than GaAs and are readily available as discrete surface mount devices.

Only a few prior works fully develop and consider mixers with first-principles analysis techniques, such as for IIP2 and DC offset control [20], FET modelling [21], MOSFET modelling (100 MHz - 1.5 GHz) [22] - generally all at carrier frequencies below 6 GHz. Where LO waveforms at the drain or collector are considered, standard models of clipped sinusoids are relied on, such as for 5G 24 GHz – 40 GHz [23], leading to transconductance mixer models. For Gilbert Cell mixers, a hard switching waveform is assumed for commutation, such in WLAN 2.4 GHz [24]. However, the Gilbert Cell architecture is more complex than the mixer used in this paper, requiring three or more active devices.

Very few reported works compare the mathematical model results jointly to *both* circuit simulation *and* to a built prototype (3 steps), which makes it hard to assess the relative accuracies of approaches. They instead commonly focus on only comparisons between CAD simulation and lab measurements.

The mixer collector current is often modelled as a Taylor series in device transconductance, such as at 2.4 GHz [25], 1.7 GHz [26], 500 MHz – 3.1 GHz [14] and this is the approach also taken in this paper for linearity analysis.

SiGe is an important semiconductor material for future mmWave communications systems due to its high performance and suitability for system integration [27- 29]. Examples of its relevance to mixers are demonstrated in [30] for a 40 GHz mixer with 2 dBm LO drive. However, there are few recent works that consider BJT mixer design and analysis, even though this is relevant to SiGe BiCMOS at mmWave frequencies. This is because most mmWave designs have traditionally use GaAs PHEMTs or more recently CMOS (both using FET based models). Reported SiGe mixer designs are usually part of a larger integration, such as a front-end chip, with examples at 28 GHz for a phased array [31], IIP2 calibration techniques for 900 MHz WCDMA [32], 5G 26GHz & 28GHz receiver [33] and at 2 GHz [34]. However, the applicability of SiGe for higher mmWave operation is beginning to be reported in mixers, such as for 60 GHz ISM [35], a 0 dBm LO drive mixer at 60 GHz [36], and [37] presenting a 60 GHz Gilbert Cell with 3 dBm LO drive.

A design strategy for a single balanced BJT mixer in IC is provided in [38], though this uses 3 transistors. Also, like many Gilbert Cell designs, it also assumes the upper transistors act as switches with a 50 % duty cycle. This is a simplification not used in this paper for the LO current model, with the whole waveform considered.

Reported results that compare modern CAD mixer circuit simulation to measured data at mmWave often show very good accuracies, often with circa 1 dB error for conversion gain, e.g.: 77 GHz & 94 GHz mixer [39], 60GHz [40], 5G 28 GHz [41], WIMAX [42], 5G 24 GHz – 30 GHz [43], 26 GHz – 40 GHz [44], though with up to 5 dB error for some designs [45]. Circa 3 dB simulator-referenced prediction errors for NF are reported, e.g. 77 GHz & 94 GHz [39], 5G 24 GHz – 40 GHz [45] and 5G 28 GHz [41]. Fewer lab measurement to simulation comparisons of linearity have been published. However, [43] demonstrates IP1dB linearity measurements for a SiGe BiCMOS 5G 24 GHz – 30 GHz mixer with LO operating at 20 GHz, which differs from simulations by circa 1dB.

A rare example that compares a calculated 950 MHz mixer conversion gain to measurements is reported in [46], showing a 1.5 dB overestimate from the calculation.

In general in the literature, mathematical models are used in the initial design process for selecting circuit values, with the CAD simulator then used to validate the design. The errors between models or simulations and measurements are often considered minor if circa 1 dB. However, the key requirements for a mixer (G_c , NF, IIP3) all have a great impact on the overall system performance. A difference of 1-3 dB can be significant for these parameters, hence the importance of model accuracy and a good understanding of the causes for performance, which theoretical models can provide.

1.3. Paper Contribution & Structure

The contributions of this paper are as follows: 1) new mathematical design models for predicting RF mixer IF and DC currents and hence G_c , considering both the base LO drive A_L and DC base bias V_b without circuit simulation. 2) Models for predicting the IP1dB and IIP3 levels due to A_L and V_b . 3) A model to guide the selection of base bias V_b , given a defined LO amplitude A_L and desired conversion transconductance $g_{m,c}$. 4) Comparison and validation of the modelling approach to conventional circuit time-domain simulation and a measured hardware prototype single-ended 26 GHz mixer.

The paper is organized as follows: in Section 2, the models for the collector current are introduced and in Section 3, mathematical models for the IF current are developed. The hardware test prototype is introduced in Section 4. In Section 5, the mathematical

models are compared to circuit simulation results and hardware lab trials. Section 6 concludes the paper.

2. Transistor Collector Current Mathematical Models

To facilitate a practical analysis, a commercial transistor was selected as the basis of the investigation and the resulting mixer design. The SiGe transistor BFP740FH6 from Infineon Ltd. was selected, with a transition frequency (F_T) of 45 GHz. The first step in modeling the mixer operation is to create a representative collector current model. This requires an understanding of the device I-V characteristics at DC and at the center frequency of the LO. For the proposed mixer, an LO of 21 GHz was used. The conceptual representation of this initial test circuit for time-domain simulation is shown in Figure 1a. To allow a fully mathematical model to be created, a circuit model for the transistor's basic operation was developed, as shown in Figure 1b, based on the Gummel Poon (GP) model [47].

The total collector current (combined AC and DC currents) caused by the base-emitter voltage, is represented by I_o . I_o can thus represent $I_{bm} = I_o(V_b)$ due to DC base bias V_b , or $I_{pk} = I_o(A_L + V_b)$ due to the combined base AC LO signal and DC bias. The parameters of the GP model were obtained directly from vendor's data sheets. All components shown in Figure 1b must be included to capture the AC and DC operation of the transistor.

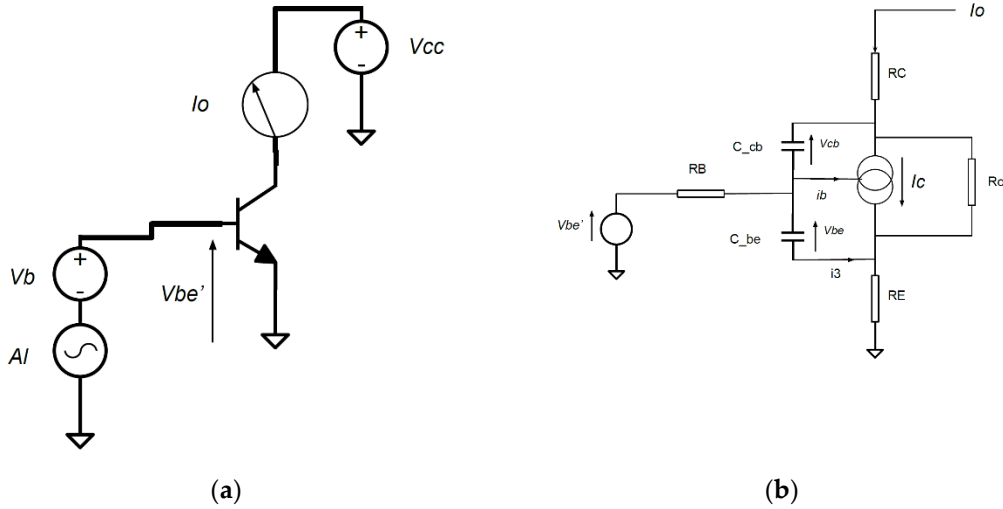


Figure 1. BJT model used: (a) Initial simulation circuit to extract I_o vs V_b and A_L ; (b) Mathematical model for transistor operation, using Gummel Poon BJT parameters.

The next step in building the mathematical model is to represent the relationship for I_o at the LO as a function of an externally applied total voltage V_{be}' , applied between the external base and emitter BJT pins. (Note: term V_{be} is the total voltage seen between the internal base-emitter junction.) V_{be} can be related to V_{be}' using conventional circuit analysis techniques. I_o is determined via mathematical circuit analysis and the GP BJT model, relating V_{be}' to V_{be} and I_o . The BJT internal collector current I_c is related to V_{be} using Equation (1). In Equations (1) – (7), all terms are standard GP parameters, with values obtained from the BJT vendor's data sheet model.

$$I_c \approx \frac{I_s}{NqB} \left(e^{\left[\frac{V_{be}}{NFV_T} \right]} - 1 \right) \quad (1)$$

The GP term NqB of Equation (2) is important for capturing the effects of current reduction due to DC bias and the LO AC drive.

$$NqB = \frac{q_{1s}}{2} (1 + \sqrt{1 + 4q_{2s}}) \quad (2)$$

The GP parameters q_{1s} in Equation (3) represents the base-width modulation and q_{2s} in Equation (4) represents high-level injection effects (including Kirk effect approximation).

$$q_{1s} = \frac{1}{1 - \frac{V_{be}}{V_{AR}} \frac{V_{bc}}{V_{AF}}} \quad (3)$$

$$q_{2s} = \frac{I_s}{I_{KF}} \left(e^{\left[\frac{V_{be}}{N_F V_T} \right]} - 1 \right) + \frac{I_s}{I_{KR}} \left(e^{\left[\frac{V_{bc}}{N_R V_T} \right]} - 1 \right) \quad (4)$$

The GP internal capacitors C_{be} of Equation (5) and C_{bc} of Equation (6) are also crucial in capturing the AC effects of the resulting collector current.

$$C_{be} = \frac{C_{JE}}{\left(1 - \frac{V_{be}}{V_{JE}}\right)^{M_{JE}}} + \frac{TFF \cdot I_s}{N_F \cdot V_T \cdot NqB} e^{\left[\frac{V_{be}}{N_F V_T} \right]} \quad (5)$$

$$C_{bc} = \frac{C_{JC}}{\left(1 - \frac{V_{bc}}{V_{JC}}\right)^{M_{JC}}} + \frac{TR \cdot I_s}{N_R \cdot V_T \cdot NqB} e^{\left[\frac{V_{bc}}{N_R V_T} \right]} \quad (6)$$

The GP parameter TFF represents the transit time and is defined by Equation (7).

$$TFF = TF \left(1 + XTF \left[\frac{I_c}{I_c + ITF} \right]^2 e^{\left[\frac{V_{bc}}{1.44 V_T} \right]} \right) \quad (7)$$

Parameters C_{bc} , C_{be} , and NqB all have the effect of reducing the collector current achieved for a given V_{be} for AC signals, leading to differing performance at AC and DC. The GP parameters used in the model for the BFP740F are listed in Table 1.

Figure 2 shows the equivalent AC comparison of the mathematical model compared to a Keysight ADS simulation as per Figure 1, showing a good fit over most of the range of interest for A_L and V_b and so confirming the viability of the approach. This means the collector current due to LO can be accurately predicted and includes DC and AC effects, without CAD circuit simulation. It will be seen later that the LO waveform is vital to accurate mixer modelling. Figure 2 also shows the root mean square error (RMSE) between the ADS simulation and the model.

In general, let the applied external (base-emitter) voltage V_{be}' consists of three components: a base DC bias V_b , the LO signal of form $A_L \cdot \cos(\omega_L \cdot t)$ and the incoming RF signal $A_R \cdot \cos(\omega_R \cdot t)$, combined for analysis as represented in Equation (8).

$$V_{be}' = V_b + A_L \cdot \cos(\omega_L t) + A_R \cdot \cos(\omega_R t) \quad (8)$$

3. IF Current Mathematical Models

The prediction of the IF transconductance mixer current produced by the nonlinear action of the transistor is central to the calculations in this paper. This knowledge allows the proper and full consideration of base LO amplitude A_L and base DC bias V_b on the creation of the IF current to be explored, supporting predictions of conversion transconductance g_{m_c} and IP1dB, etc. The mixer model uses the peak collector current $I_o(A_L + V_b)$ and DC current $I_o(V_b)$ obtained using the device circuit mathematical model for the transistor described in Section 2. These current amplitudes are then applied to subsequent time-domain mathematical models representing the mixer action – this being more suitable for subsequent simple mathematical manipulation.

Table 1. Gummel Poon Model Parameters for BFP740F.

BJT Model Parameter	Value	Unit	Description
I_s	1.249e-15	A	Transport saturation current
N_F	1.002	-	Forward current emission coefficient
N_R	1.01	-	Reverse current emission coefficient
V_T	25.9	mV	kT/q (25.9mV at 300K)
V_{AR}	1.229	V	Reverse Early voltage
V_{AF}	380.1	V	Forward Early voltage
IKF	0.1898	A	Forward Beta high current roll-off
IKR	0.02753	A	Reverse Beta high current roll-off
C_{JE}	0.2531	pF	Base-emitter zero-bias depletion cap
V_{JE}	0.9286	V	Base-emitter built-in potential
M_{JE}	0.06125	-	Base-emitter junction exponential factor
TF	2.331	pS	Ideal forward transit time
XTF	1.159	-	TF bias dependence coefficient
ITF	0.3991	A	TF high current parameter
V_{TF}	0.5242	V	TF dependency on V_{bc}
C_{JC}	54.52	fF	Base-collector zero-bias depletion cap
V_{JC}	0.4808	V	Base-collector built-in potential
M_{JC}	0.5812	-	Base-collector junction exponential factor
TR	1.532	nS	Ideal reverse transit time
RC	4.1	Ohm	Internal collector resistance
RE	0.18	Ohm	Internal emitter resistance
RB	7.0	Ohm	Zero bias internal base resistance
R_o	V_{AF}/I_c	Ohm	Output resistance
BF	987.1	-	Forward max Beta

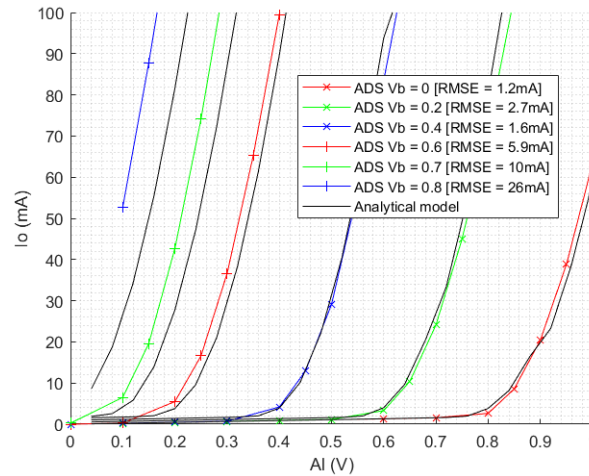


Figure 2. Comparison of peak AC I_o vs A_L for test ADS circuit simulation and GP mathematical model, showing good agreement.

3.1. LO Currents

A conceptually valuable and well-known approach to modeling the operation of a transconductance mixer starts with the simple assumption that the collector current due to the LO produces a clipped sinusoidal waveform [48], [49], as shown in Figure 3. I_{pk} is found using the model Equations (1) – (8) for $I_o(A_L+V_b)$, providing the peak collector current due to the combined effect of base DC bias V_b and the AC LO signal A_L , as applied to the external base-emitter. A simple time-domain sinusoidal current model, defined as $i(t) = I_{bm} + (I_{pk} - I_{bm}) \cdot \cos(\theta)$ is then used for subsequent mixer modeling, where θ is the phase of the LO in the cycle, I_{pk} is the peak collector current, and I_{bm} is the DC current due to V_b . Note that for all practical BJTs, there will be negligible current flowing in the period T_1 to $T_r - T_1$ because the collector will be off – hence the use of a clipped sinusoid model.

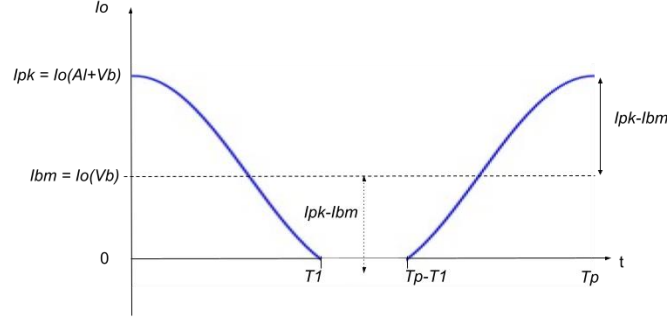


Figure 3. BJT collector LO current I_o approximated by $I_{bm} + I_o(AL+Vb)\cos(\theta)$.

From Figure 3, parameter T_p is the period of the LO cycle and T_1 is the time, as measured from the start of the waveform, where the collector current has fallen to a negligible value (i.e., transistor V_{be}' below knee). However, it has been found that as V_b is reduced and A_L increased significantly, the collector current waveform is better modeled by $(I_{pk} - I_{bm}) \cdot \cos(2\theta)$. Between these states, transitional definitions are required, allowing the collector current time-domain model to better represent the actual transistor current waveform. The time-domain representation of this new fitting can be defined by Equations (9) - (11) which incorporates parameter k , which can vary from 1.0 – 2.0 thus representing $(I_{pk} - I_{bm}) \cdot \cos(k \cdot \theta)$.

$$I_{Tk} = I_{bm} + (I_{pk} - I_{bm}) \cdot \cos\left(\frac{2 \cdot k \cdot \pi \cdot t}{T_p}\right), \text{ for } t = 0..T_1 \quad (9)$$

$$I_{Tk} = I_{bm} + (I_{pk} - I_{bm}) \cdot \cos\left(2\pi[1 - k] + \frac{2 \cdot k \cdot \pi \cdot t}{T_p}\right), \text{ for } t = T_p - T_1..T_p \quad (10)$$

$$I_{Tk} = 0, \text{ for } t = T_1..T_p - T_1 \quad (11)$$

The Fourier coefficient for the resulting first harmonic C_1 current is then represented by Equation (12) and Equation (13) for DC C_0 . Equation (12) defines C_{1k} when k is not equal to 1; when k equals 1 Equation (14) should be used.

$$C_{1k} = \frac{2I_{bm}}{\pi} \sin\left(\frac{2\pi T_1}{T_p}\right) + \frac{(I_{pk} - I_{bm})}{\pi} \left\{ \frac{\sin\left[\frac{2\pi T_1(k+1)}{T_p}\right]}{k+1} + \frac{\sin\left[\frac{2\pi T_1(k-1)}{T_p}\right]}{k-1} \right\} \quad (12)$$

$$C_{0k} = \frac{2I_{bm}T_1}{T_p} + \frac{(I_{pk} - I_{bm})}{k\pi} \left[\sin\left(\frac{2k\pi T_1}{T_p}\right) \right] \quad (13)$$

$$C_{11} = \frac{2I_{bm}}{\pi} \sin\left(\frac{2\pi T_1}{T_p}\right) + \frac{2(I_{pk} - I_{bm})T_1}{T_p} + \frac{(I_{pk} - I_{bm})}{2\pi} \left[\sin\left(\frac{4\pi T_1}{T_p}\right) \right] \quad (14)$$

Parameter T_1 can be defined by the simple geometry of the collector current waveform or the applied base voltage waveform V_{be}' . Considering Equation (8) and ignoring the negligible contribution from A_R , the point where V_{be}' intercepts BJT DC knee voltage V_{tt} (circa 0.75V) can be used to define T_1 , using Equation (15). Although V_{tt} can be hard to predict in a real device, for the purposes of the simple model here it can be predicted as required from Equation (1).

$$T_1 = \frac{T_p}{2\pi} \arccos\left(\frac{V_{tt} - V_b}{A_L}\right) \quad (15)$$

The equivalent steady-state DC current I_{bm} , the middle of the collector current amplitude cycle in Figure 3, is determined from Equation (1) by considering only V_b ,

without an AC A_L signal applied. The value of k for a particular time T_i and T_p is determined using Equation (16), where m and f are linear parameters for a straight-line approximation, dependent only on V_b .

$$k = V_b \cdot m + f \quad (16)$$

The values for m and f are found via time domain comparison over one LO period, using BJT instantaneous current I_o using Equations (1) – (8) when compared to Equation (9) and Equation (10) over the V_b and A_L ranges of interest. They do not require circuit simulation and only need evaluating once for a design. The BFP740F extracted values are $m = -1.75 \text{ V}^{-1}$ and $f = 2.6$.

3.2. Relating A_L to Required Port LO Power

The mathematical models are driven by the LO amplitude A_L and DC bias V_b , both applied directly at the base. In practice, the LO power will be applied to a port away from the transistor, passing through various LO/RF combining networks and RF matching, before reaching the base. An approximation of the actual LO power required at the port can be calculated using the following steps:-

1. Select a target A_L and V_b and let the mathematical model Equation (13) produce the resulting equivalent DC current draw C_{0k} .
2. Use C_{0k} and the BJT small-signal S parameters to estimate the base input reflection coefficient Γ_i Equation (17), with Γ_L set to -1, representing a collector short circuit to ground at the LO, as required for good mixer operation.

$$\Gamma_i(C_{0k}) = S_{11} + \frac{S_{12}S_{21}\Gamma_L}{1-S_{22}\Gamma_L} \quad (17)$$

Then, convert from Γ_i to the equivalent base input impedance $Z_i(C_{0k})$ and then to the equivalent base shunt input resistance R_p .

3. Use A_L as applied to R_p to calculate the RF LO power LOP_b , as would be seen at the base.
4. Translate the power LOP_b back to the connector port, accounting for any expected intermediate RF stage insertion losses, due to combiners, etc.

The above approach has been used in this study and shows good agreement with Keysight ADS simulations for A_L vs. applied port LO power.

3.3. Extracting the Transconductance Mixing Current

The C_{1k} Fourier component Equation (12) can be converted to a transconductance at the LO using Equation (18). C_{1k} and A_L are both ‘large signals’, however they both properly capture the transistor operation in the large signal regime and so (18) is a valid approach for the time varying transconductance due to the LO in the BJT.

$$gm_{LO} = \frac{C_{1k}}{A_L} \quad (18)$$

The product of the LO modulated transconductance, Equation (18), and the RF signal entering the mixer at the carrier, $A_R \cdot \cos(\omega_R t)$, will result in an IF current, due to the conversion transconductance. This product of the RF input voltage and the time varying transconductance is fundamental to the mixer’s operation [48, 50]. The conversion transconductance at one of the resulting sidebands can then be represented by Equation (19).

$$gm_{c_max} = \frac{gm_{LO}}{2} \quad (19)$$

Note that gm_c is a function of both A_L and I_{pk} (itself a function of A_L and V_b) and as such the transistor is not operating in a class-A linear bias due solely to V_b .

The resulting IF current is then the product of Equation (19) and the applied RF voltage A_r . The resulting DC current C_{0k} may result in the BJT's effective input and output match changing from the initial design target (used to create the matching networks). Therefore, the BJT input and output match change, due to a change in the effective bias, must be considered when evaluating the resulting conversion gain. A simple strategy for this is to consider the effect of the impedance change at the base (RF) and collector (IF) and represent it as a reduction in effective conversion gain, with respect to the target design value, which would usually be a conjugate match. This effect is incorporated into the model using Equation (20), Equation (21) and Equation (22).

$$gm_c = gm_{c,max} \cdot M_B(C_{0k}) \cdot M_C(C_{0k}) \quad (20)$$

$$M_B(C_{0k}) = \frac{R_b(C_{0k})}{\sqrt{(R_{b,target} + R_b(C_{0k}))^2 + (X_{b,target} + X_b(C_{0k}))^2}} \quad (21)$$

$$M_C(C_{0k}) = \frac{R_{c,target}}{\sqrt{(R_{c,target} + R_c(C_{0k}))^2 + (X_{c,target} + X_c(C_{0k}))^2}} \quad (22)$$

Parameter R_b is the real part of the base impedance, X_b is the imaginary part and with the *target* assumed to be the conjugate of the base impedance at the target design DC current. Similarly, parameter R_c is the real part of the collector impedance, X_c is the imaginary part, and the *target* is collector conjugate impedance at the DC operating target.

3.4. IP1dB & IIP3 Prediction Models

The IP1dB for the mixer can be predicted as a function of A_L and V_b , using the LO currents for the fundamental (C_{1k}) and third harmonic (C_{3k}) and then relating them, as will now be introduced. A conventional approach is to define the IF current using derivatives of the conversion transconductance using a Taylor series [51], [52], represented at the IF frequency by Equation (23). This model assumes there are no memory effects present.

$$I_{c_{IF}} = I_{C0} + A_r \cdot gm_1 + A_r^2 \cdot gm_2 + A_r^3 \cdot gm_3 + \dots \quad (23)$$

Where, conversion transconductance $gm_1 = \frac{d(I_{c_{LO}})}{d(V_{AL})}$, $gm_2 = \frac{d^2(I_{c_{LO}})}{d(V_{AL})^2}$, $gm_3 = \frac{d^3(I_{c_{LO}})}{d(V_{AL})^3}$ are evaluated from the collector current due to the LO. Once the conversion transconductances are known, the IP1dB Equation (24) and IIP3 Equation (25) can be obtained directly for the equivalent base RF voltages.

$$A_{R_{IP1dB}} = \sqrt{\frac{gm_1}{gm_3} \left(10^{\frac{-1}{20}} - 1 \right)} \quad (24)$$

$$A_{R_{IIP3}} = \sqrt{\frac{gm_1^4}{gm_3^3}} \quad (25)$$

A technique will now be introduced that relates the magnitudes of the found Fourier LO harmonics C_{1k} , C_{3k} to the currents that would be produced by a simple Taylor exponential expansion and hence leading to the required gm_1 and gm_3 . The technique starts by defining the IF collector current from only the LO, as passed through the simple BJT AC model Equation (26) and then expanding into a Taylor series using Equation (27).

$$I_{C_{LO}} = I_{DC} \cdot e^{\frac{A \cos(\omega_{LO})}{V_T}} \quad (26)$$

$$I_{C_{LO}} = 1 + A \cos(\omega_{LO}) + \frac{A^2}{2} \cos^2(\omega_{LO}) + \frac{A^3}{6} \cos^3(\omega_{LO}) + \dots \quad (27)$$

Expanding Equation (27) and collecting terms produces Equation (28).

$$I_{C_{LO}} = \left(1 + \frac{A^2}{4}\right) + \left(A + \frac{3A^3}{24}\right) \cos(\omega_{LO}) + \frac{A^2}{4} \cos(2\omega_{LO}) + \frac{A^3}{24} \cos(3\omega_{LO}) + \dots \quad (28)$$

Considering the fundamental LO term means we can immediately state that $C_{1k} = A$ and considering the third harmonic term $C_{3k} = \frac{A^3}{24}$. We can then find parameter A by evaluating the ratio of C_{3k}/C_{1k} , using Equation (29).

$$A = \sqrt{\frac{24C_{3k}}{C_{1k}}} \quad (29)$$

The magnitude of the third-harmonic collector current component C_{3k} can be determined using Equation (30), based on the techniques from Section 3.1.

$$C_{3k} = \frac{2I_{bm}}{3\pi} \sin\left(\frac{6\pi T_1}{T_p}\right) + \frac{(I_{pk} - I_{bm})}{\pi} \left\{ \frac{\sin\left[\frac{2\pi T_1(k+3)}{T_p}\right]}{k+3} + \frac{\sin\left[\frac{2\pi T_1(k-3)}{T_p}\right]}{k-3} \right\} \quad (30)$$

By considering the current generation action of Equation (28), we can now also directly state Equations (31) & (32) to relate the current components in terms of required transconductance.

$$gm_1 A_L = A \quad (31)$$

$$gm_3 A_L^3 = \frac{3A^2}{24} \quad (32)$$

As a penultimate step, the required ratio of gm_1/gm_3 can be found using Equation (33) and Equation (29).

$$\frac{gm_1}{gm_3} = \frac{8A_L^2}{A^2} \quad (33)$$

The base-referred IP1dB equivalent voltage amplitude is then determined by Equation (24). The base RF voltage corresponding to the 3rd order input intercept point can also now be predicted using Equation (25).

3.6. Selecting V_b for a Fixed A_L and Conversion Transconductance

A key aim of the research was to identify the V_b required to support a particular desired conversion transconductance with a defined LO power. To lead to this, the expressions for $k = 1$ and $k = 2$ versions of Equation (12) using Equation (15) were derived. Applying the simplifying approximation of $I_{pk} > I_{bm}$ and $V_b < V_{tt}$ for practical mixers, allows usable simple expressions to emerge. However, in general we will not know early in a design whether to use $k = 1$ or $k = 2$ variants, so for a pragmatic approach an average is used. In addition, knowing that $0 < (V_{tt} - V_b) < A_L$ allows a further simplification. We also know from Equation (18) and Equation (19) that $C_{1k} = 2A_L gm_c$. The above strategy leads to Equation (34) to define a simple relationship between V_b and a given A_L and the desired gm_c . (To further simplify Equation (34) NqB can reasonably be approximated to 1.)

$$Vb_m = V_T \log_e \left[\frac{2\pi \cdot gm_c \cdot A_L \cdot NqB}{I_s \left(2 + \left[\frac{\pi + 11}{4 + 12} \right] e^{\left(\frac{A_L}{V_T} \right)} \right)} \right] \quad (34)$$

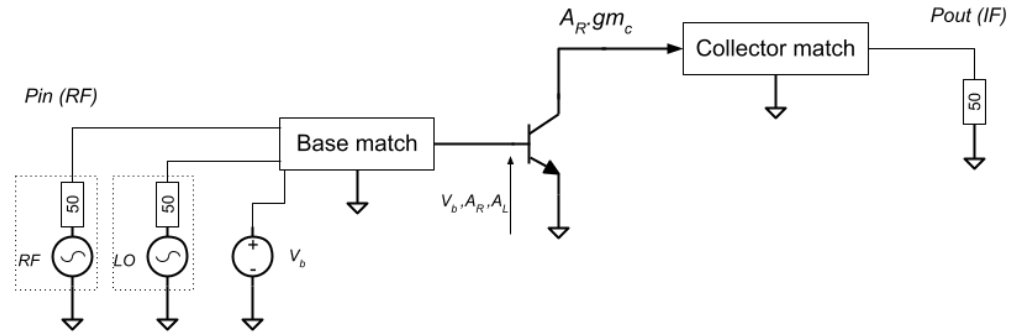


Figure 4. Mixer signal locations.

It may be tempting to rearrange Equation (34) to obtain gm_c for a given Vb and A_L but this should be avoided. (The applied simplifications would lead to an overestimate of gm_c if used in this way. Accurate prediction of gm_c requires full use of models as described in Sections 3.1 - 3.3)

Once proposed input and output matching circuits are known, the conversion gain can be predicted and thus converted to a trial gm_c , following the architecture of Figure 4.

4. Trial Mixer Hardware for Model Validation

To evaluate the accuracy of the proposed IF current model (and subsequent conversion gain) required a BFP740F mixer prototype. The key requirement to ensure relevance to the mathematical model is that the mixer is base-driven for both the LO and RF signals and the IF current is extracted from the collector. A Keysight ADS circuit and planar EM simulation was created for the single-ended transistor mixer, as shown Figure 5, designed using conventional RF techniques.

The mixer LO range was 19 - 23 GHz and the RF range was 24 - 28 GHz. Rogers RO4003C substrate was used (0.5 mm thick, ϵ_r of 3.55, loss tangent of 0.0027). The input RF and LO signals are combined using a rat-race and then passed through a base conjugate matching network.

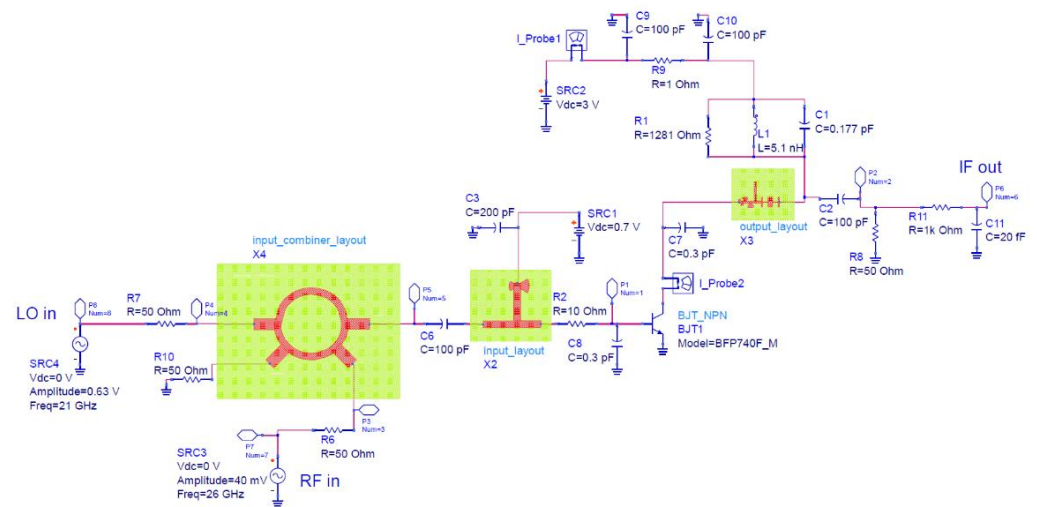


Figure 5. Single-ended 26 GHz mixer schematic.

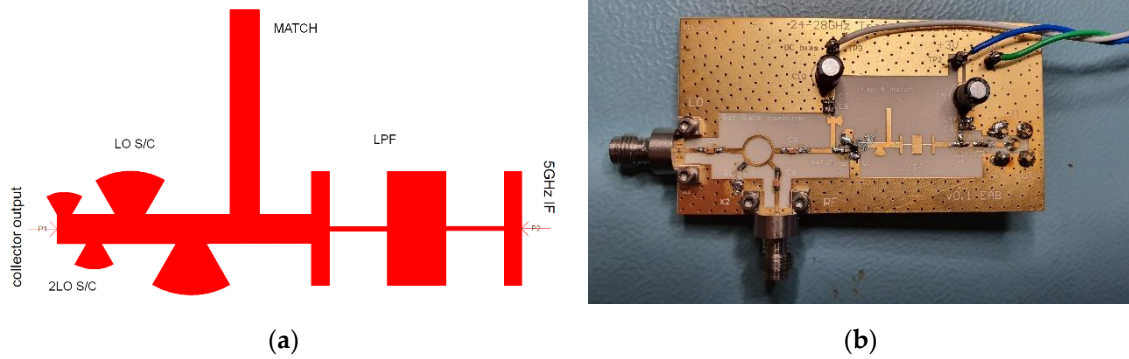


Figure 6. Single-ended 26 GHz mixer: (a) output network; (b) Built PCB (LO port on left and RF port on lower left, IF on right).

The output matching network is particularly important for transconductance mixers. Figure 6a shows the architecture used, with radial stub short circuits (S/C) at the collector port for the LO fundamental and its second harmonic, followed by an IF matching circuit and low pass filter (LPF). The collector network was biased at 3V. To fully evaluate the mixer concepts, a 26 GHz PCB prototype was created from the developed ADS design. The assembled single-ended mixer PCB is presented in Figure 6b.

5. Comparison Between Mathematical Models, Circuit Simulations and Measured PCB

The achievable RF performance and $A_L - V_b$ trade-offs were explored using the PCB prototype mixer with 3 V collector bias. Unless stated, single frequency lab tests used a 21 GHz LO with port LO drive powers of 10, 7, 3 and 0 dBm. Unless stated, the RF signal was set to 26 GHz at -20 dBm, resulting in a 5 GHz IF. The RF signal generator was an Agilent E8247C and the LO signal generator was a Gigatronix 2540B. IF signals were measured using a Rohde & Schwarz FSV40N spectrum analyser.

5.1. Initial Insights from Mathematical Model

The mathematical models based on Equations (1) - (22) were first used to explore the choice of V_b and A_L on the produced IF current magnitude, resulting conversion gains and DC current draw. DC bias V_b was swept from 0 to 0.9 V and amplitude A_L swept from 0 to 0.9 V, with RF input amplitude A_R fixed. The resulting mixer IF conversion gains are shown in Figure 7a and the DC current draw in Figure 7b. A ridge for local optimum conversion gain can be seen in Figure 7a, starting at low V_b / high A_L and showing a relationship between V_b and A_L pairings for local optimum gain over the surface. There is also a clear upper peak gain area centered near $V_b \sim V_{tt}$. The region adjacent to the peak gain also shows further possible tradeoff between A_L and V_b for a desired conversion gain near to peak.

The DC current consumption predicted by the mathematical model in Figure 7b highlights a rapid increase associated with increasing conversion gain towards maximum. Figure 7a shows that for a given fixed value of A_L and simply adjusting V_b , a wide range of conversion gains can be achieved. It is proposed that in many systems it will be easier to vary V_b to control performance, whilst A_L (LO power) will be fixed due to practical circuit implementation issues. By considering Figure 7a it can be seen that by adjusting V_b for a given A_L , the gain can be peaked, confirming what has been reported experimentally by others [11]. By jointly considering Figure 7a and Figure 7b allows operational points to be found for A_L and V_b that give close to peak conversion gain but allow DC current to be minimized.

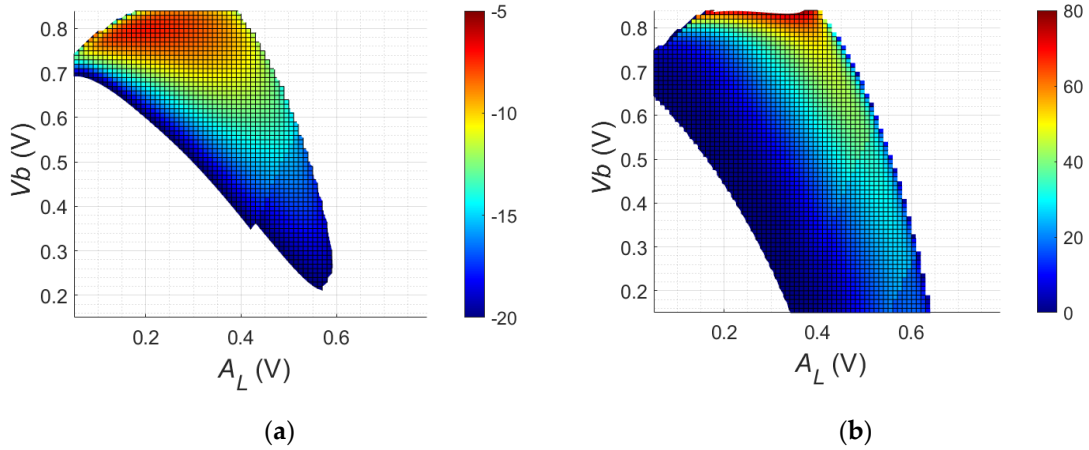


Figure 7. Mathematical model: (a) conversion gain (dB); (b) DC current draw (mA).

An example of predicting V_b for a given A_L using model Equation (34), compared to the ADS circuit time-domain simulation, is presented in Figure 8. This shows good agreement between the model Equation (34) and the ADS circuit simulation, for achieving a 30 mS transconductance.

Figure 9a shows the simulation using Equation (24) to calculate IP1dB is sensitive to both V_b and A_L (LO power), with higher A_L and higher V_b generally improving the achieved IP1dB, as might be expected. The input RF voltage corresponding to IIP3 can also now be predicted, using Equation (25), and is shown in Figure 9b, showing a similar trend. The P1dBI and IIP3 can also be seen to be more sensitive to V_b for lower LO powers.

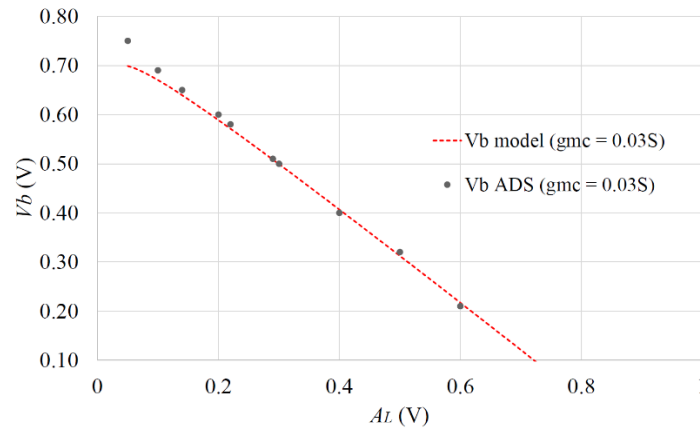


Figure 8. Comparison of Equation (34) vs. ADS simulation for V_b & A_L to obtain 30 ms g_m .

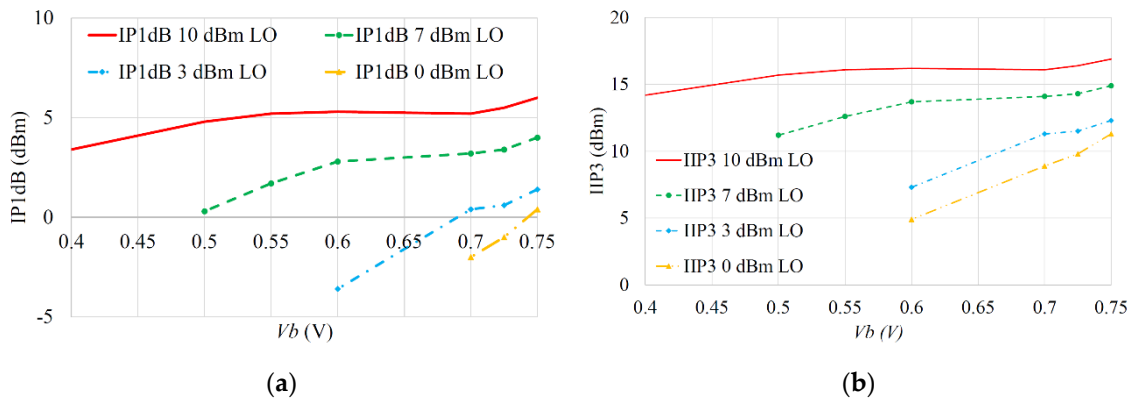


Figure 9. Linearity models as function of V_b and LO power: (a) IP1dB; (b) IIP3.

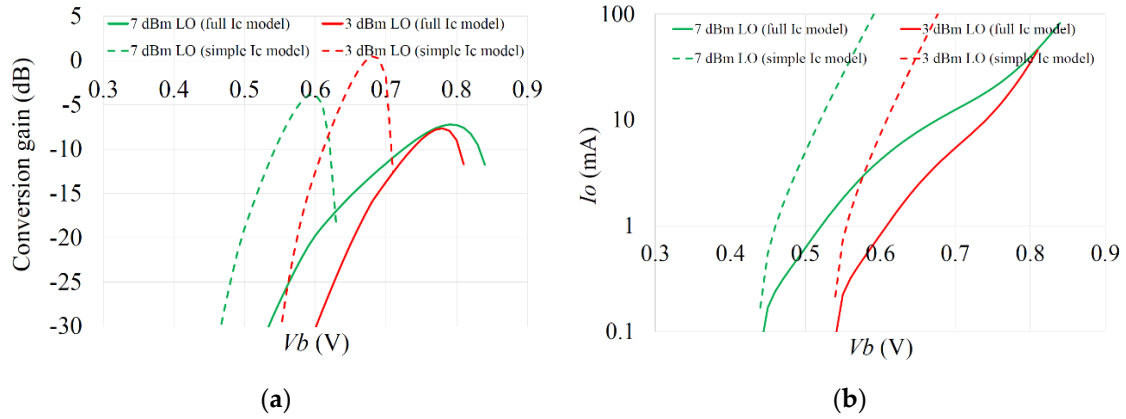


Figure 10. Comparison of effect of simple and full model for collector current, as function of V_b and LO power on: (a) Conversion gain; (b) DC current.

The collector current full model consisting of Equations (1) – (7) and Figure 1b are necessarily complex to sufficiently represent the current. Figure 10a shows conversion gain and Figure 10b DC current at 7 dBm and 3 dBm LO powers, when comparing the results for the full collector current model and a simpler version just using Equation (1). The simple collector current model leads to significant overestimate of collector current so cannot be used. Thus, comparisons using the full model are shown in Section 5.2.

5.2. Lab Comparison Measurements of Hardware Mixer Prototype

The input rat-race combiner was tested within the implemented mixer, giving an LO to RF port isolation of 10 dB from 19 GHz to 25 GHz and 21 dB from 20 GHz to 23 GHz. The results of [7] show that simply defining a fixed consumed DC current and then adjusting V_b and A_L to achieve the DC current will not result in constant gain. Thus, lab tests for this paper swept V_b for each LO drive level and measured the resulting conversion gain..

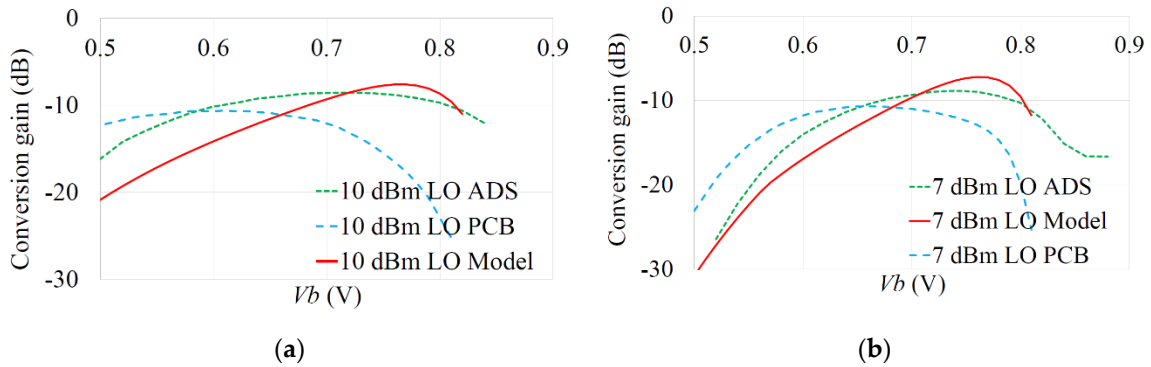


Figure 11. Model, ADS and measured PCB comparisons of mixer conversion gain as a function of V_b at: (a) 10 dBm LO drive; (b) 7dBm LO drive.

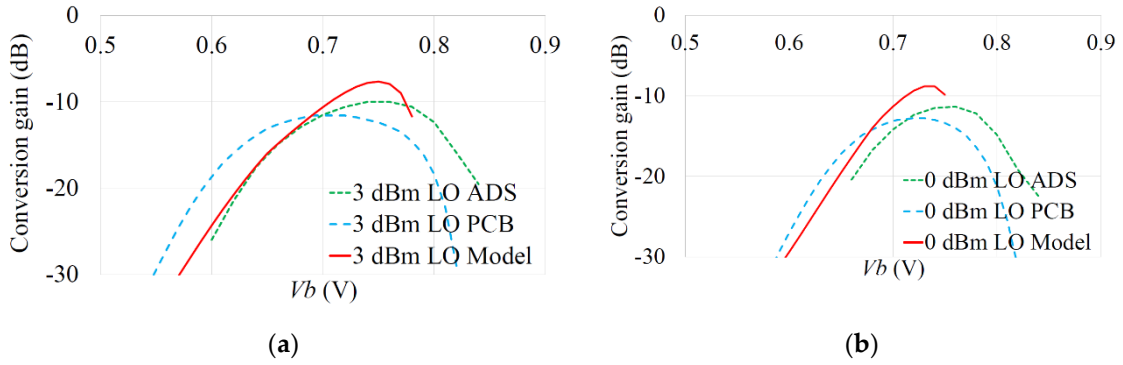


Figure 12. Model, ADS and measured PCB comparisons of mixer conversion gain as a function of V_b : (a) 3 dBm LO drive; (b) 0 dBm LO drive.

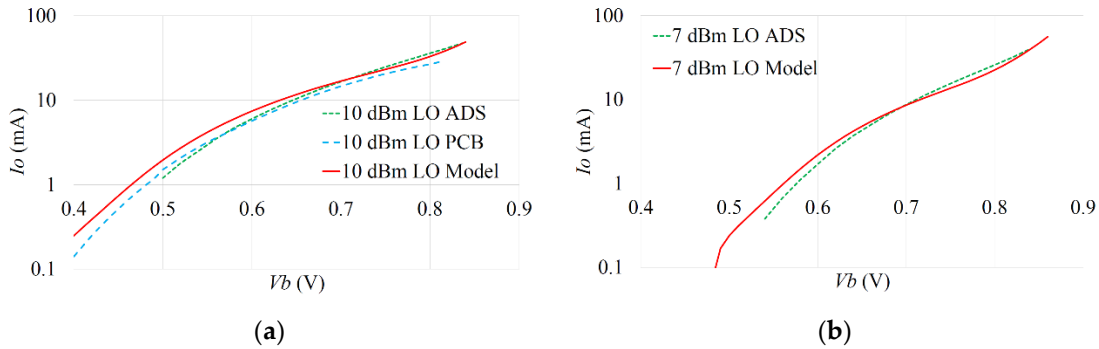


Figure 13. Model, ADS and PCB comparison of mixer DC draw as a function of V_b and LO drive at: (a) 10dBm; (b) 7dBm.

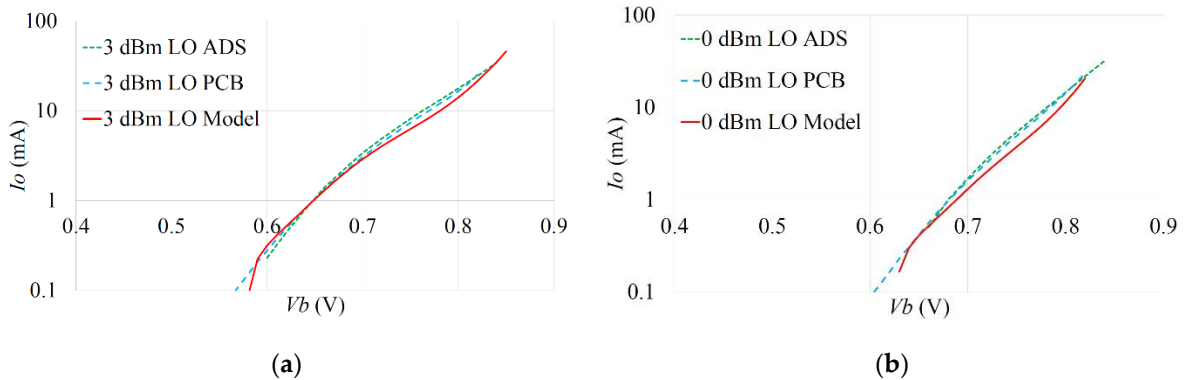


Figure 14. Model, ADS and PCB comparison of mixer DC draw as a function of V_b and LO drive at: (a) 3dBm; (b) 0dBm.

The resulting trade-off between the LO drive A_L and bias V_b for a desired conversion gain can be observed in Figures 11 – 12, comparing the mathematical model, Keysight ADS simulation and measured results. The DC current draw was also measured for the mixer configurations and is presented in Figures 13 – 14. The various RMSE for the conversion gain and DC current are presented in Table 2. The errors in predicting the peak conversion gain are presented in Table 3. The DC currents show good agreement between the mathematical model, circuit simulations and measured PCB results, with RMSE errors better than 2 mA between the model and circuit simulations.

Table 2. RMSE fitting error for conversion gain & DC current.

	10 dBm LO	7 dBm LO	3 dBm LO	0 dBm LO	
Gc: Model-PCB	8.0	6.0	4.3	2.7	dB
Gc: ADS-PCB	5.2	5.5	5.3	5.2	dB
Gc: Model-ADS	3.0	1.8	1.3	2.7	dB
DC Draw: Model-PCB	2.4	-	1.1	1.2	mA
DC Draw: ADS-PCB	3.4	-	0.7	0.6	mA
DC Draw: Model-ADS	1.6	1.6	1.9	1.7	mA

Table 3. Error in peak conversion gain prediction.

	10 dBm LO	7 dBm LO	3 dBm LO	0 dBm LO	
Gc: Model-PCB	0.9	1.6	2.4	2.5	dB
Gc: ADS-PCB	3.0	3.5	3.9	4.0	dB
Gc: Model-ADS	2.0	1.8	1.6	1.4	dB

The general shape of the gain curves from the model, ADS simulation and PCB results show reasonable trend agreement. From Table 3, the model predicted peak Gc is within 2.0 dB of circuit simulation results and within 2.5 dB of measured PCB results. From Table 2, the RMSE of the model Gc compared to the measured PCB is similar to that due to full circuit simulation. The remaining error is possibly because, for simplicity, the model does not include all BJT current limiting aspects (which may require use of much more complex transistor models, such as Mextram and thus losing the convenience of the simple GP model). The F_T of the BFP740F is 45 GHz (typical) so the relatively close operational frequency of the mixer and tolerancing of the real device may have also led to some of the differences seen compared to the measured data. An increased sensitivity to LO power on conversion gain, for operation close to F_T , is seen in [53] for a Gilbert Cell architecture and this could also be an issue.

The published works discussed in Section 1.2 typically report a measurement to simulation error of circa 1 dB. However, there are very few published works that provide results of *theoretical predictions* of conversion gain or linearity as a function of base / gate DC bias and LO power. There are also very few works that have investigated the relationship between LO power *and* base / gate bias, which was a key motivator for this paper. In [8] the authors report conversion gain for an indium–phosphide (InP) double heterojunction BJT mixer with fixed bias operating in fundamental mode at 140 GHz, with an error in predicted Gc ranging from 0 dB to circa 10 dB over a range of LO powers. Table 2 shows a better prediction accuracy over a range of biases and powers (though at a lower carrier frequency). In [9] the authors show a InP High Electron Mobility Transistor acting as a mixer at 85 GHz and showing a decreasing conversion loss as LO power is increased, for two gate bias voltages. For high LO powers the conversion loss converges, as also seen in this work in Figures 11 & 12. In [9] a 5 dB reduction in Gc is seen as the bias is reduced, a trend also predicted and seen in this paper. The authors of [10] present results for a GaAs (FET) mixer at 7.8 GHz, showing Gc measurements and theoretical predictions agreeing within circa 0.5 dB. This is notably better than the results in this work, but are at a lower frequency and with a FET technology rather than BJT. In [11] an E band SiGe BJT ring mixer is reported, with circuit simulation results showing that bias and LO amplitude can be traded (e.g. 0.3 V LO amplitude & 0.7 V bias give similar Gc to 0.7 V LO & 0.5 V bias) - as also proposed in this work and seen in Figures 11 & 12. However, no theoretical calculation prediction of gain is provided. The authors of [11] report the measured conversion gain differs by circa 3 dB from that simulated. In [21] the gm_c of a FET VHF

mixer is seen to increase for increasing bias and increasing LO amplitude – as also seen here with the BJT.

By adjusting the base DC bias V_b , the single-ended mixer LO power was reduced from +10 dBm to +3 dBm, while suffering only a 1 dB drop in the conversion gain and benefitting from a 2 mA drop in DC draw. The accuracy of predicting V_b using Equation (34) was assessed, compared to the V_b required for the test PCB, in the lab for a desired gain and LO power. The error in predicting the required V_b over the range of LO powers was found to be less than 10 %.

The measured PCB mixer conversion gain is negative largely owing to losses in the input combiner rat-race and network feeding the transistor base and choice of transistor. However, it should be noted that a negative conversion gain is common in simple single-device mixers operating at frequencies in the tens of gigahertz. Whilst it would be theoretically possible to de-embed the active part of the mixer so that it can be considered in isolation from passive circuits, it would still be necessary to include the effect of these losses when measuring and comparing to the test PCB. Therefore, the measurements reported here are compared to the RF ports of the built PCB and include the effect of all losses, allowing a direct comparison.

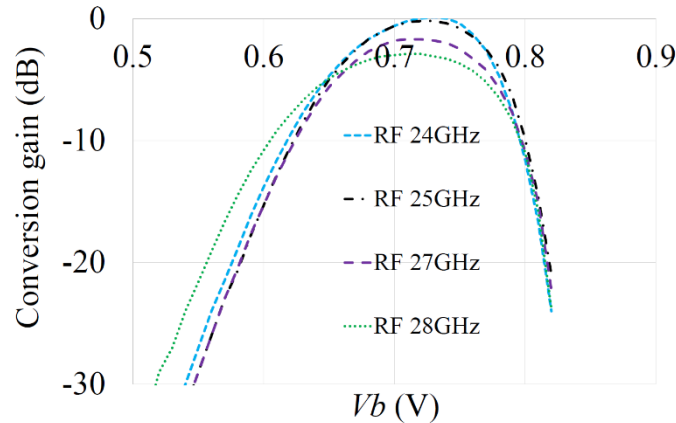


Figure 15. Measured gain (normalized to gain at 26 GHz) across range 24 – 28 GHz as function of V_b (3 dBm LO drive)

Figure 15 shows results from lab measurements of the mixer’s G_c across the RF input range 24 GHz – 28 GHz with a 3 dBm LO and with various applied V_b (results are normalized to the G_c at 26 GHz). This shows the mixer’s measured conversion gain dependency on V_b is not a strong function of frequency - suggesting the single mathematical model can be used over the band.

A comparison of IP1dB for the prototype mixer and the model Equation (24) is presented in Figure 16a, showing good agreement between the mathematical model and laboratory measurements for all tested LO powers, with a model error of circa 1 dB. Figure 16b shows the comparison between the measured IIP3, an ADS harmonic balance (HB) simulation and Equation (25). Since the model underestimates the IP1dB, it could be expected to also underestimate the IIP3 by a similar amount. In practice, the model underestimates IIP3 by circa 5 dB. It is interesting to note that whereas the model tends to underestimate the IIP3 by 5 dB (or less) the ADS HB simulation tends to overestimate it by 5 dB. These results point to a general difficulty in modeling mixer nonlinearity, which can be sensitive to DC bias as also seen in [21], or possibly due to memory effects. However, the predicted IIP3 trend is correct and a ~ 5dB uncertainty may be acceptable in early-stage designs. The authors of [20] show that IIP2 increases as LO power increases, to a certain point, as also seen in Figure 16b though for IIP3. This improvement in linearity for increasing LO power and sensitivity to V_b is also predicted in Figure 9a and 9b.

Additionally [21] confirms the 3rd order products reduce as LO drive increases, leading to an increased IIP3.

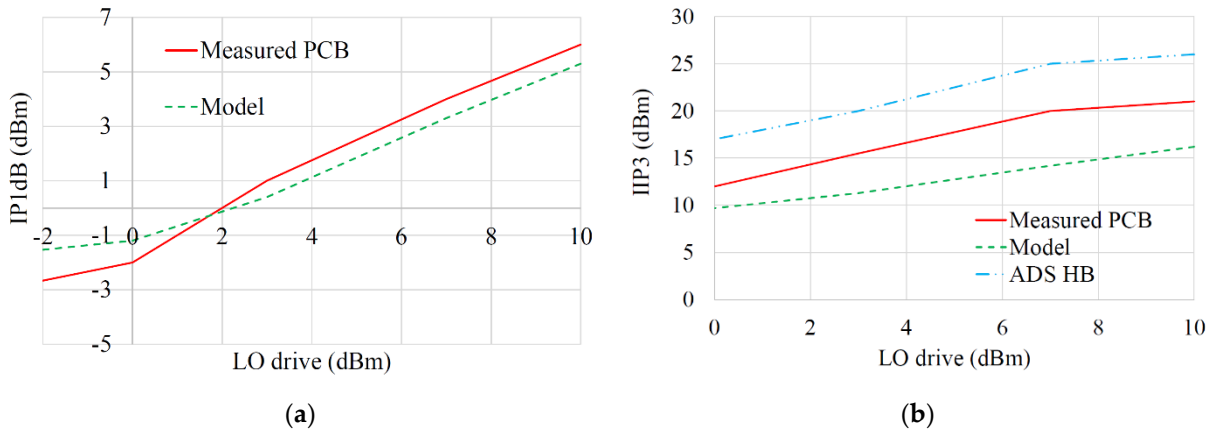


Figure 16. Measured and mathematical model comparison for IP1dB & IIP3 as function of LO drive level (V_b chosen to achieve peak gain for each tested LO drive power): (a) IP1dB; (b) IIP3.

The RF input 3 dB bandwidth of the mixer was measured for an IF at 5 GHz and found to be 1.4 GHz (+10 dBm LO power). The IF 3 dB bandwidth of the mixer was also measured, and found to be 900 MHz, with an LO of 21 GHz and +10 dBm LO power.

5.3. Noise Figure Measurements

Since the mixer has circa 10dB conversion loss (CL), this will dominate any noise figure (NF) results. This was confirmed by measuring the single sideband (SSB) NF and associated conversion loss on the prototype for 10 dBm and 0 dBm LO powers, as shown in Figure 17. The NF was measured using a noise diode (Keysight 346CK01) and spectrum analyzer with LNA (Keysight PXA N9030B) and evaluating the added noise from the mixer. The SSB NF of the mixer can be seen to be within 1 dB of the conversion loss, as expected. It is also worth noting from Figure 17 that if V_b is carefully selected (based on maximizing G_c), only a 2dB degradation in NF will be suffered yet the LO power can be reduced by 10 dB.

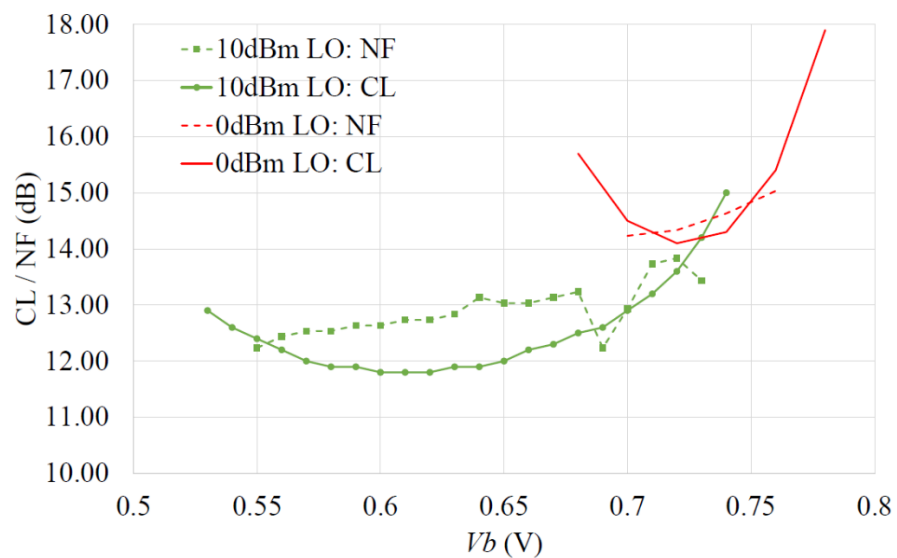


Figure 17. Measured mixer SSB NF and conversion loss (CL) for 10 dBm and 0 dBm LO drive.

6. Conclusions

It is shown that G_c , DC draw, IP1dB and IIP3 that can be achieved from a SiGe bipolar transistor downconverting mixer can be predicted to useful accuracy using the developed, simple mathematical models without recourse to full circuit simulation. Furthermore, an equation to predict the required V_b , for a base LO drive A_L , to achieve a desired conversion transconductance is presented. The transconductance mixer mathematical models were compared to Keysight ADS circuit simulations and prototype hardware.

During tests, the mathematical model predicts peak conversion gain within 2.0 dB of circuit simulation results and within 2.5 dB of measured PCB results. The conversion gain RMSE between the model and circuit simulation is 3 dB worst-case, 1.3 dB best-case. The RMSE between predicted DC current and circuit simulation is below 2 mA. The model predicts IP1dB to 1 dB and IIP3 to circa 5 dB accuracies, with respect to the measured PCB.

Another key finding is that for operation below the peak G_c , the LO drive power can be traded for V_b bias while maintaining a defined conversion gain. An equally important finding is that conversion gain can be optimized by V_b as LO power is reduced and this can be predicted. This is an important finding because LO power is often challenging to generate at mmWave frequencies and impacts battery life of portable products. This also allows system designers using front-end mixers to configure them for a particular operational gain scenario, dynamically degrading gain and linearity where acceptable, to save power.

Although the model agrees well with simulation and measured results, some of the differences between the measured results and the mathematical models are likely due to the use of standard commercial uncharacterized surface-mount packaged transistors. The lab prototype used to validate the models also serves to demonstrate that a practical 26 GHz mixer can be realized using a low cost packaged transistor and conventional PCB design.

In general, mixer use-cases will likely have a primary design criterion based on NF / G_c or IIP3 / P1dBi or obtaining best overall RF performance for a given available LO power. Hence, using the developed mathematical models, the following mixer scenarios can be investigated early in a design before embarking on a full circuit design:

- NF / G_c : best settings for A_L , V_b can be found and resulting IIP3 / P1dBi predicted;
- IIP3 / P1dBi: best settings for A_L , V_b can be found and resulting NF / G_c predicted;
- Fixed LO power: Achievable NF, G_c , IIP3, P1dBi and DC power as function of V_b can be predicted;
- Fixed DC power: Achievable NF, G_c , IIP3, P1dBi as function of LO power can be predicted.

Funding: This research was funded by UKRI, grant number MR/T043164/1. The APC was funded by the UKRI.

Conflicts of Interest: The author declares no conflict of interest.

References

1. Hong, W.; Jiang, Z.H.; Yu, C.; Hou, D.; Wang, H.; Guo, C.; Hu, Y.; Kuai, L.; Yu, Y.; Jiang, Z.; et al. The Role of Millimeter-Wave Technologies in 5G/6G Wireless Communications. *IEEE Journal of Microwaves* **2021**, *1*, 101–122, doi:10.1109/jmw.2020.3035541.
2. Chataut, R.; Akl, R. Massive MIMO Systems for 5G and beyond Networks—Overview, Recent Trends, Challenges, and Future Research Direction. *Sensors (Switzerland)* **2020**, *20*.
3. Yang, T.Y.; Chiou, H.K. A 28 GHz Sub-Harmonic Mixer Using LO Doubler in 0.18-Mm CMOS Technology. In Proceedings of the Digest of Papers - IEEE Radio Frequency Integrated Circuits Symposium; 2006; Vol. 2006, pp. 209–212.
4. Chang, Y.T.; Lin, K.Y. A 28-GHz Bidirectional Active Gilbert-Cell Mixer in 90-Nm CMOS. *IEEE Microwave and Wireless Components Letters* **2021**, *31*, 473–476, doi:10.1109/LMWC.2021.3061658.
5. Kumar, S.; Saraiyan, S.; Dubey, S.K.; Pal, S.; Islam, A. A 2.4 GHz Double Balanced Downconversion Mixer with Improved Conversion Gain in 180-Nm Technology. *Microsystem Technologies* **2020**, *26*, 1721–1731, doi:10.1007/s00542-019-04718-3.

6. Varonen, M.; Kärkkäinen, M.; Kantanen, M.; Halonen, K.A.I. Millimeter-Wave Integrated Circuits in 65-Nm CMOS. *IEEE Journal of Solid-State Circuits* **2008**, *43*, 1991–2002, doi:10.1109/JSSC.2008.2001902.
7. Ball, E.A. Investigation into the Relationship Between Conversion Gain, Local Oscillator Drive Level and DC bias in a SiGe Transistor Transconductance Modulated Mixer at 24-28 GHz. In Proceedings of IEEE Texas Symposium on Wireless & Microwave Circuits and Systems, Waco, USA, 18th May 2021. 10.1109/WMCS52222.2021.9493227.
8. Yan, Y.; Bao, M.; Gunnarsson, S.E.; et al. A 110-170-GHz Multi-Mode Transconductance Mixer in 250-nm InP DHBT Technology. *IEEE Trans. on Microwave Theory and Techniques* **2015**, *63*, 2897–2904. 10.1109/TMTT.2015.2459676.
9. Ning, X.; Yao, H.; Wang, X.; Jin, Z. A W-Band Single-Ended Downconversion / Upconversion Gate Mixer in InP HEMT Technology. In Proceedings of 2013 IEEE International Conference on Microwave Technology and Computational Electromagnetics, Qingdao, China, 25th August 2013. 10.1109/ICMTCE.2013.6812434
10. Pucel, R.A.; Masse, D.; Bera, R. Performance of GaAs MESFET Mixers at X Band. *IEEE Trans. on Microwave Theory and Techniques* **1976**, *24*, 351–360. 10.1109/TMTT.1976.1128854.
11. Del Rio, D.; Gurutzega, I.; Rezola, A.; et al. A Wideband and High-Linearity E-Band Transmitter Integrated in a 55-nm SiGe Technology for Backhaul Point-to-Point 10-Gb/s Links. *IEEE Trans. on Microwave Theory and Techniques* **2017**, *65*, 2990–3001. 10.1109/TMTT.2017.2664833.
12. Chen, J. da; Wang, W. jun A K-Band Low-Noise and High-Gain Down-Conversion Active Mixer Using 0.18-Mm CMOS Technology. *Wireless Personal Communications* **2019**, *104*, 407–421, doi:10.1007/s11277-018-6027-4.
13. Beigizadeh, M.; Nabavi, A. Design of a High Gain and Highly Linear Common-Gate UWB Mixer in K-Band. *Analog Integrated Circuits and Signal Processing* **2014**, *78*, 501–509, doi:10.1007/s10470-013-0132-9.
14. Solati, P.; Yavari, M. A Wideband High Linearity and Low-Noise CMOS Active Mixer Using the Derivative Superposition and Noise Cancellation Techniques. *Circuits, Systems, and Signal Processing* **2019**, *38*, 2910–2930, doi:10.1007/s00034-019-01023-2.
15. Heidari, T.; Nabavi, A. Design and Analysis of a Wideband Compact LNA-Mixer in Millimeter Wave Frequency. *Analog Integrated Circuits and Signal Processing* **2020**, *105*, 371–383, doi:10.1007/s10470-020-01737-3.
16. Gladson S, C.; Bhaskar, M. A Low-Power RF Mixer with Harmonic Cancellation for IEEE 802.15.4 Portable, Wearable Wireless Applications. *AEU - International Journal of Electronics and Communications* **2020**, *124*, doi:10.1016/j.aeue.2020.153335.
17. Sivonen, P.; Vilander, A.; Pärssinen, A. Cancellation of Second-Order Intermodulation Distortion and Enhancement of IIP2 in Common-Source and Common-Emitter RF Transconductors. *IEEE Transactions on Circuits and Systems I: Regular Papers* **2005**, *52*, 305–317, doi:10.1109/TCSI.2004.841571.
18. Nguyen, T.T.; Fujii, K.; Pham, A-V. Highly Linear Distributed Mixer in 0.25- μm Enhancement-Mode GaAs pHEMT Technology. *IEEE Microwave and Wireless Components Letters* **2017**, *27*, 1116–1118. 10.1109/LMWC.2017.2750071.
19. Nguyen, T.T.; Riddle, A.; Fujii, K.; Pham, A-V. Development of Wideband and High IIP3 Millimeter-Wave Mixers. *IEEE Trans. on Microwave Theory and Techniques* **2017**, *65*, 3071 - 3079. 10.1109/TMTT.2017.2669042.
20. Kivekäs, K.; Pärssinen, A.; Halonen, K.A.I. Characterization of IIP2 and DC-Offsets in Transconductance Mixers. *IEEE Transactions on Circuits and Systems II: Analog and Digital Signal Processing* **2001**, *48*, 1028–1038, doi:10.1109/82.982353.
21. Surana, D.C.; Gardiner, J.G. Gain and Distortion Properties of FET Mixers and Modulators. *IEEE Transactions on Electromagnetic Compatibility* **1974**, EMC-16, 29–38, doi:10.1109/TEMC.1974.303320.
22. Korotkov, A.S. Double-Balanced Mixer Based on MOSFETs. *Russian Microelectronics* **2011**, *40*, 128–140, doi:10.1134/S1063739711020053.
23. Bae, B.; Han, J. 24-40 GHz Gain-Boosted Wideband CMOS Down-Conversion Mixer Employing Body-Effect Control for 5G NR Applications. *IEEE Transactions on Circuits and Systems II: Express Briefs* **2022**, *69*, 1034–1038, doi:10.1109/TCSII.2021.3119995.
24. Amirabadzadeh, S.; Bijari, A.; Alizadeh, H.; Mehrshad, N. Performance Improvement of a Down-Conversion Active Mixer Using Negative Admittance. *Circuits, Systems, and Signal Processing* **2021**, *40*, 22–49, doi:10.1007/s00034-020-01477-9.
25. Ataei Siah Bidi, A.; Karimi, G. Design of High Linearity Inductor-Less Active CMOS Mixer Based on Volterra Series Analysis. *Circuits, Systems, and Signal Processing* **2020**, *39*, 4810–4828, doi:10.1007/s00034-020-01407-9.
26. García, J.A.; de La Fuente, M.L.; Zamanillo, J.M.; Mediavilla, A.; Tazón, A.; Pedro, J.C.; Carvalho, N.B. Intermodulation Distortion Analysis of FET Mixers under Multitone Excitation. In Proceedings of the 2000 30th European Microwave Conference, EuMC 2000; IEEE Computer Society, 2000.
27. Xu, H.; Chen, J.; Wu, X.; Peng, C.; Yu, J.; Yuan, B. A 32–40 GHz 4-Channel Transceiver with 6-bit Amplitude and Phase Control. *AEU Int. J. Electron. Commun.* **2021**, *139*, 153925. <https://doi.org/10.1016/j.aeue.2021.153925>.
28. Avenier, G.; Diop, M.; Chevalier, P.; Troillard, G.; Loubet, N.; Bouvier, J.; Depoyan, L.; Derrier, N.; Buczko, M.; Leyris, C.; et al. 0.13 μm SiGe BiCMOS Technology Fully Dedicated to Mm-Wave Applications. *IEEE Journal of Solid-State Circuits* **2009**, *44*, 2312–2321, doi:10.1109/JSSC.2009.2024102.
29. Wietstruck, M.; Marschmeyer, S.; Schulze, S.; Tolunay Wipf, S.; Wipf, C.; Kaynak, M. Recent Developments on SiGe BiCMOS Technologies for Mm-Wave and THz Applications. In Proceedings of the 2019 IEEE MTT-S International Microwave Symposium (IMS); IEEE: Boston, June 2 2019; pp. 1126–1129.
30. Pruvost, S.; Telliez, I.; Dambrine, G. ; et al. A 40 GHz Single-Ended Down-Conversion Mixer in 0.13 μm SiGeC BiCMOS HBT. *IEEE Microwave and Wireless Components Letters* **2005**, *15*, 496–498. 10.1109/LMWC.2005.852773.
31. Wang, X.; Guo, B.; Wu, J.; Gong, J. A 28 GHz Front-End for Phased Array Receivers Simulated in 180 Nm CMOS. In Proceedings of the 2020 IEEE International Conference on Semiconductor Electronics (ICSE); IEEE: Kuala Lumpur, July 28 2020; pp. 1–4.

32. Kivekäs, K.; Pärssinen, A.; Ryyänen, J.; Jussila, J.; Halonen, K. Calibration Techniques of Active BiCMOS Mixers. *IEEE Journal of Solid-State Circuits* **2002**, *37*, 766–769, doi:10.1109/JSSC.2002.1004581.
33. Fonte, A.; Plutino, F.; Moquillon, L.; Razafimandimby, S.; Pruvost, S. 5G 26 GHz and 28 GHz Bands SiGe:C Receiver with Very High-Linearity and 56 DB Dynamic Range. In Proceedings of the 2018 13th European Microwave Integrated Circuits Conference (EuMIC); IEEE: Madrid, September 23 2018; pp. 57–60.
34. Kivekas, K.; Parssinen, A.; Jussila, J.; Ryyänen, J.; Halonen, K. Design of Low-Voltage Active Mixer for Direct Conversion Receivers. In Proceedings of the ISCAS 2001 - 2001 IEEE International Symposium on Circuits and Systems, Conference Proceedings; 2001; Vol. 4, pp. 382–385.
35. Reynolds, S.K. A 60-GHz Superheterodyne Downconversion Mixer in Silicon-Germanium Bipolar Technology. *IEEE Journal of Solid-State Circuits* **2004**, *39*, 2065–2068, doi:10.1109/JSSC.2004.835838.
36. Mazor, N.; Sheinman, B.; Katz, O.; Levinger, R.; Bloch, E.; Carmon, R.; Ben-Yishay, R.; Elad, D. Highly Linear 60-GHz SiGe Downconversion/Upconversion Mixers. *IEEE Microwave and Wireless Components Letters* **2017**, *27*, 401–403, doi:10.1109/LMWC.2017.2678426.
37. Qayyum, J.A.; Albrecht, J.D.; Ulusoy, A.C. A Compact V-Band Upconversion Mixer with -1.4-dBm OP1dB in SiGe HBT Technology. *IEEE Microwave and Wireless Components Letters* **2019**, *29*, 276–278. 10.1109/LMWC.2019.2901395.
38. Sweet, A.A. *Designing Bipolar Transistor Radio Frequency Integrated Circuits*, 1st ed.; Artech House: Norwood, USA, 2008; pp. 200–205.
39. Reynolds, S.K.; Powell, J.D. 77 and 94-GHz Downconversion Mixers in SiGe BiCMOS. In Proceedings of the 2006 IEEE Asian Solid-State Circuits Conference, ASSCC 2006; 2006; pp. 191–194.
40. Choi, C.; Son, J.H.; Lee, O.; Nam, I. A +12dBm OIP3 60-GHz RF Downconversion Mixer with an Output-Matching, Noise- and Distortion-Canceling Active Balun for 5G Applications. *IEEE Microwave and Wireless Components Letters* **2017**, *27*, 284–286, doi:10.1109/LMWC.2017.2661964.
41. Testa, P.V.; Szilagyi, L.; Xu, X.; Carta, C.; Ellinger, F. A Low-Power Low-Voltage Down-Conversion Mixer for 5G Applications at 28 GHz in 22-Nm FD-SOI CMOS Technology. In Proceedings of the Asia-Pacific Microwave Conference Proceedings, APMC; Institute of Electrical and Electronics Engineers Inc., December 8 2020; Vol. 2020-December, pp. 911–913.
42. Bhatt, D.; Mukherjee, J.; Redouté, J.M. Low-Power Switched Transconductance Mixer and LNA Design for Wi-Fi and WiMAX Applications in 65 Nm CMOS. *IET Microwaves, Antennas and Propagation* **2018**, *12*, 1736–1744, doi:10.1049/iet-map.2017.0798.
43. Yang, S.; Hu, K.; Fu, H.; Ma, K.; Lu, M. A 24-to-30 GHz Ultra-High-Linearity Down-Conversion Mixer for 5G Applications Using a New Linearization Method. *Sensors* **2022**, *22*, 3802, doi:10.3390/s22103802.
44. Xu, L.; Wang, Z.; Li, Q. Design of a Broadband Millimeter-Wave Monolithic IQ Mixer. *Journal of Infrared, Millimeter, and Terahertz Waves* **2010**, *31*, 593–600, doi:10.1007/s10762-010-9615-2.
45. Lee, D.; Lee, M.; Park, B.; Song, E.; Lee, K.; Lee, J.; Han, J.; Kwon, K. 24-40 GHz MmWave Down-Conversion Mixer with Broadband Capacitor-Tuned Coupled Resonators for 5G New Radio Cellular Applications. *IEEE Access* **2022**, *10*, 16782–16792, doi:10.1109/ACCESS.2022.3149311.
46. Xavier, B.A.; Aitchison, C.S. Simulation and Modelling of a Heterojunction Bipolar Transistor Mixer. In Proceedings of the IEEE MTT-S International Microwave Symposium Digest; Publ by IEEE, June 1992; Vol. 1, pp. 333–336.
47. Antognetti, P.; Massobrio, G. *Semiconductor Device Modeling with SPICE*, 2nd ed.; McGraw Hill: New York, USA, 1993.
48. Pozar, D.M. *Microwave Engineering*, 4th ed.; Wiley: Hoboken, USA, 2012; pp. 637–655.
49. Maas, S.A. *Nonlinear Microwave and RF Circuits*, 2nd ed.; Artech House: Norwood, USA, 2003; pp. 497–514.
50. Robertson, I.D.; Lucyszyn, S. *RFIC and MMIC Design and Technology*, 1st ed.; The IET: London, UK, 2001; pp. 316–321.
51. Kang, S.; Choi, B.; Kim, B. Linearity Analysis of CMOS for RF Applications. *IEEE Trans. on Microwave Theory and Techniques* **2003**, *51*, 972–977. <https://doi.org/10.1109/TMTT.2003.808709>
52. Liu, Z.; Dong, J.; Chen, Z.; Jiang, Z.; Liu, P., et al. A 62-90 GHz High Linearity and Low Noise CMOS Mixer Using Transformer-Coupling Cascode Topology. *IEEE Access* **2018**, *6*, 19338–19344. <https://doi.org/10.1109/ACCESS.2018.2814062>.
53. Syu, J.S.; Meng, C.; Wang, C.L. 2.4-GHz Low-Noise Direct-Conversion Receiver with Deep N-Well Vertical-NPN BJT Operating near Cutoff Frequency. *IEEE Transactions on Microwave Theory and Techniques* **2011**, *59*, 3195–3205, doi:10.1109/TMTT.2011.2169421.

8. Paper 4 – 28 GHz Portable Channel Sounder and Close to Ground Usage

{Reproduced as published - author accepted version.}

© 2023 IEEE. Reprinted, with permission, from Edward A. Ball, and Sumin David Joseph, “A Portable 28-GHz Channel Sounder Platform and Measurement Results from Close-to-Ground Field Tests”, IEEE Open Journal of Instrumentation and Measurement, published 20th March 2023.

DOI <https://doi.org/10.1109/OJIM.2023.3259025>

(Published version [4].)

A Portable 28 GHz Channel Sounder Platform and Measurement Results from Close-to-Ground Field Tests

Edward A. Ball, *Member*, IEEE, and Sumin David Joseph

Abstract This article describes a novel, bespoke, and low-cost 28 GHz RF TX and RX front end design that has been combined with a commercial Software Defined Radio and Raspberry Pi controller to realize a portable propagation measurement system for the 28 GHz band. The complete sounder system can resolve an impulse from RX powers down to -107 dBm (3 dB impulse SNR) and the sounder TX can generate a signal of -8 dBm. Therefore, using 20 dBi antennas supports path loss measurements of 139 dB. The sounder can resolve time domain reflections to 33 ns in a channel measurement bandwidth of 60 MHz, producing both time domain and frequency domain results. The complete sounding system has been used to perform close-to-ground RF channel measurements, with propagation loss models and time domain impulses extracted. Close-to-ground measurement is an underreported area of propagation research that is relevant for novel use-cases, such as in military applications or for mobile device-to-device communications. A key initial finding from the trials is that the path losses for 28 GHz indoor and outdoor links at circa 70 cm above ground seem close to that of free space, with very few strong reflections with delays exceeding 33 ns.

Index Terms—Radio propagation, Measurement, Millimeter wave circuits, Transceivers, Signal processing

I. INTRODUCTION

THE rise of 5G has shown the huge appetite for improved communication systems, underpinned by enhanced radio technology. With the number of 5G connections predicted to reach 1.3 billion by end of 2022 and reach 4.8 billion by end of 2026 [1], the pressure on radio resources will only increase with time.

A key part of designing a viable and efficient radio system is to fully understand the radio channel in the target deployment use case. This relies on measurements and models for the channel propagation characteristics. Often, the systems used to perform such channel measurements use traditional (and costly) RF lab equipment. Mobility, power and equipment cost issues limit their suitability in challenging use cases, where damage may result. In the past, novel propagation measurement systems using lower cost hardware have been described, such as for IoT applications in the VHF and UHF bands reporting path loss and delay spread [2], [3], [4].

At mmWave frequencies the required measurement equipment becomes very expensive and

heavy, though many valuable works have been reported using lab equipment and hybrid systems. For example, the authors of [5] present one of the early reports on 5G channel models and propagation experiments across the mmWave bands. However, such systems are often large and costly, thus out of reach for many researchers, impeding innovation. In recent years, commercial chip manufacturers have brought to production a range of mmWave RF chips in surface mount packaging. It is the availability of these chips (as opposed to bare dies) that has led to the work described in this paper; leading to a low-cost, battery powered, portable RF mmWave transceiver platform that is suitable for general use and specifically used here for 28 GHz channel sounding.

An area of interest for mmWave channel measurements is the performance of the radio channel when close-to-ground, both outdoors and indoors. This could represent future mobile to mobile use cases in commercial communications. It is also relevant for future battlefield communications, where the high bandwidth and narrow beams can be attractive for minimizing eavesdropping or interception, whilst handling large amounts of data over long distance.

The main contributions of the paper are as follows:-

This paragraph of the first footnote will contain the date on which you submitted your paper for review.

This work was supported by the UKRI under Grant MR/T043164/1.

E. A. Ball is with The University of Sheffield, Sheffield, UK (e-mail: e.a.ball@sheffield.ac.uk). S. David Joseph. is with The University of Sheffield, Sheffield, UK (e-mail: s.d.joseph@sheffield.ac.uk.)

- Development of a low-cost, battery powered and easily portable self-contained channel sounder system for the 28 GHz band (external band pass filter (BPF) defined range 27.5 – 29.5GHz), capable of reporting path loss and delay spread for path losses up to 142 dB (0 dB impulse SNR). The developed RF PCB design is presented and made available for others to copy and use [6].
- Example measurement of 28 GHz channel responses close to ground in an indoor office environment.
- Example measurement of 28 GHz channel responses close to ground over a 1 km outdoor scenario.
- Extracted path loss models for the measured scenarios are provided.

Section II presents related works; section III introduces the system and RF hardware design. Section IV presents the channel sounder algorithms. System verification tests are discussed in Section V. Indoor and outdoor field test results and models are presented in section VI. System and measurement findings are discussed in section VII. The paper concludes in section VIII.

II. RELATED WORKS

Previously, some researchers have used Vector Network Analyzers (VNAs) for channel measurements. In [7] the authors use a VNA at 38-40 GHz with external power amplifier (PA) and low noise amplifier (LNA), providing measured results to 15 m. However, as might be anticipated, these systems are limited by cable link requirements. Some authors have used fibre optic links to extend the testable distance of the VNA [8].

There have been some reported development and associated results for portable multiband systems, such as [9] operating in ISM and 60 GHz bands and using FMCW sounding signals. The Ettus Research USRP portfolio are popular systems for software defined radio (SDR) platforms. In [10] a USRP-N210 is used for indoor channel measurements at 2.2 GHz, with 12.5 MHz sounding bandwidth (BW) and 80 ns delay resolution. By using multiple overlapping tones, a 100 MHz total measurement BW and 10 ns delay resolution is supported.

In [11] various 28 GHz indoor channels are measured using a pseudo noise (PN) sequence at 250 Mchip/s and using commercial mmWave upconverter modules, boards and lab equipment carried on a trolley. Results for indoor path loss (log-normal models), delay spread, and angle of arrival are presented. The authors of [12], [13] and [14] have performed extensive outdoor measurements at 28 GHz (and above), with antennas on rooftops and using sliding correlator techniques with mains powered lab equipment. A Free Space Path Loss (FSPL) reference distance of 5 m was used, and log normal shadowing models are used to fit the data. The authors of [15] describe urban micro-cellular channel

measurements at 28 GHz with a 170 dB path loss measurement capability. The transmitter was mounted on a vehicle and the receiver on a lab trolley. A continuous wave (CW) based channel sounder was used in [16] to perform urban canyon and rooftop propagation measurements. A measurable 28 GHz path loss of up to 171 dB is reported, using a rotating horn receiver. Measurements at up to 800 m were made.

In [17] lab equipment, including an arbitrary waveform generator, is used to create a PN sounding system with 1 ns multipath resolution. This is used to measure room reflections in Line of Sight (LoS) scenarios using a steerable TX horn and omnidirectional RX. LoS tests showed similar path loss to FSPL predictions, but off-axis measurements showed significant reflections from indoor surfaces. It was also found that RMS delay spread of under 30 ns were common.

Corridor measurements are performed at mmWave frequencies in [18] using lab test equipment and 1 Gchip/s PN chip rate. Path loss exponents were found to be significantly lower than FSPL due to wave-guiding effects of the corridor. The RMS angular spread is also found to be up to 100 degrees. Many studies have investigated the propagation in office and university campus buildings [19], often using high performance lab RF test equipment [20]. In [21] the authors find a close link between room size and model extracted parameters and report delay spreads of 11.8 ns – 83.8 ns. In general, log-normal modelling has been used at 28 GHz, such as by [22] with 5 m reference distance and [23] with 1 m reference distance, though the floating intercept path loss model is also used [24].

In [25] extensive measurements of 28 GHz propagation path loss, delay spread, and angular spread of arrival were made in stadiums, subways, factories, and agricultural barns. In LoS tests in all settings they observed close to FSPL links. For path loss and angular profile channel measurements, CW was used and orthogonal frequency-division multiplexing (OFDM) was used for delay spread measurements (100 MHz BW). Measurement equipment was mobile on three trolleys and used lab test kit.

In [26] authors use a 250 Mchip/s Pseudo Random Binary Sequence (PRBS) based system at 28 GHz to measure the propagation in residential environments with foliage and vegetation. TX and RX systems are cable-linked for synchronization and a 145 dB path loss measurement capability is reported. The authors report that in addition to expected floor reflections, building walls and tree foliage also lead to significant clusters of delay spread. The authors in [27] perform suburban residential area Fixed Wireless Access scenario propagation measurements at 28 GHz at up to 200 m. CW test equipment is used and offers a 138 to 172 dB path loss measurement capability.

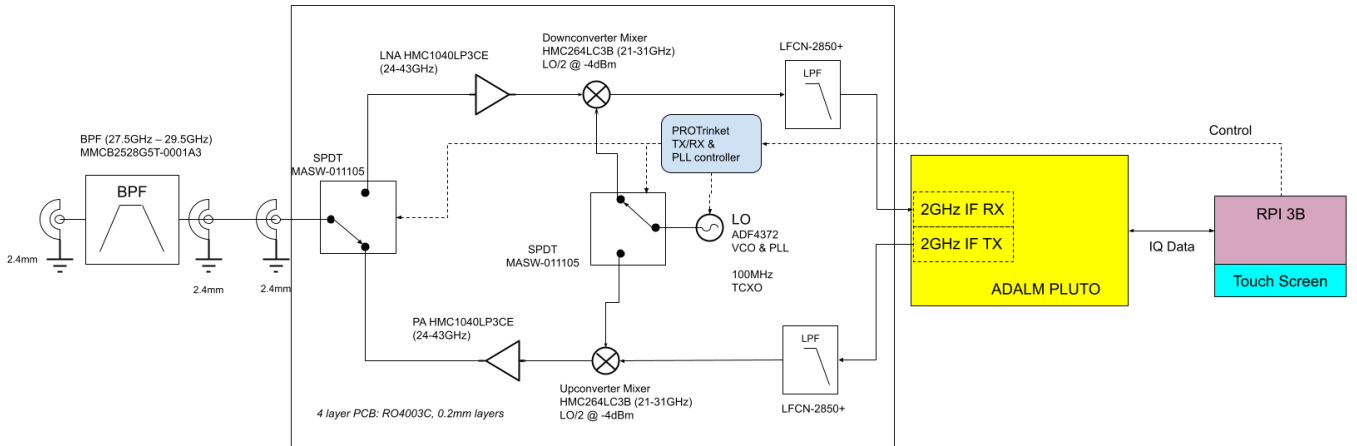


Fig. 1. Channel sounder system (two required: one as TX and one as RX).

The authors observed an excess path loss of up to 15 dB over FSPL expectations on LoS links.

Though the 28 GHz band is now important for 5G and future 6G links, there is little understanding of what the path loss models look like when close-to-ground. Indeed, in general there are few reported results for radio systems operating close-to-ground, with most research focusing on mobile or fixed communication links involving a high base station. However, there has been some military interest in UHF operation close-to-ground. In [28] ultrawideband (UWB) channel soundings (3-10 GHz) are taken at antenna heights including 10 cm and 2 m over various distances to 200 m. RMS delay spread, and path loss models are extracted.

Commercial lab equipment is used as the basis of the sounder and the TX and RX are linked by 200 m optical fibre for triggering. The authors report a strong dependence on antenna height to path loss, with data fitted to log-normal models. In [29] 27.7 GHz channel models at up to 26 m, for radar and communications operation involving a vehicle are reported, using lab equipment and antenna heights of 0.3 m and 0.5 m.

Measurements in the ISM bands (433/868/915/2400 MHz) are a common focus for near-ground propagation measurements. In [30] antenna heights of 50 cm are used in building corridors and compared to ray tracing models, with large differences seen compared to ITU models. Outdoor measurements for antennas at 5 cm to 1 m at 470 MHz are reported in [31] with data compared to reflective earth and log-normal shadowing loss models.

III. HARDWARE SYSTEM DESIGN

The developed 28GHz propagation measurement system is shown in Fig. 1. To maintain flexibility for future applications, certain architectural decisions were made early in the design. In receive mode, the incoming signals are routed through a single pole double throw (SPDT) switch (Analog Devices MASW-011105) and low noise

amplifier (LNA) (Analog Devices HMC1040) and then down-converted to a software adjustable 2 GHz IF, by an Analog Devices HMC264 mixer. The IF signal is then routed out to the SDR RX port. On TX, the IF signal from the SDR is up-converted to 28 GHz by a HMC264, amplified by a HMC1040 and routed out through the MASW-011105 SPDT. The limiting component defining the hardware RF frequency range is the HMC264 mixer, which can operate between 21 – 31 GHz. By placing the band select filter outside of the transceiver allows this range to be maintained. The local oscillator for the transceiver is generated by an Analog Devices ADF4372 integrated voltage-controlled oscillator (VCO) and phase locked loop (PLL). The PLL uses a 100 MHz temperature compensated crystal oscillator (TCXO) as master reference. It will be noted that the PCB includes TX and RX functions, though in practice when used as a sounder only the TX or RX function is used. However, having both functions available offers flexibility during field trials, with either unit able to work as TX or RX. If costs are an issue, then the unwanted circuit functions (one amplifier and a mixer) could be unpopulated during assembly, resulting in a dedicated TX or RX build, for a £ 97 saving.

The TX / RX circuit control and PLL frequency control is implemented within the transceiver by a PROTrinket [32] with dedicated code. External control of the transceiver is then via a simple interface between a Raspberry Pi 3B with touch screen (R-Pi) and the PROTrinket. The TX sideband selection and RX band selection is implemented in an external BPF, which is on a separate PCB for flexibility. For this application, a MMCB2528G5T-0001A3 from TDK, covering 27.5 GHz – 29.5 GHz was used. Although a 2 GHz IF is used, this could be reconfigured by changing the ADF4372 PLL register settings and IF low pass filters (LPFs) if necessary. The IF could be changed, if needed, to suit frequency ranges of alternative SDRs. The use of a 2 GHz IF here means the mixer image is 4 GHz away from the carrier and is properly removed by the external BPF. If a lower IF is used, care must be taken to manage the image susceptibility on RX and image generated on TX (which

must be removed to keep emissions in-channel) through consideration of the external BPF. Linear voltage regulators were used to generate the required circuit voltages. The PCB consists of 4 layers. Layers 1 - 2 use 0.2 mm of Rogers R4003C and layers 3 - 4 use 0.2 mm thick FR4.



Fig. 2. Fully assembled 28 GHz RF frontend PCB.

The central FR4 prepreg core is 1.2 mm, resulting in a total unpopulated board thickness of 1.6 mm. The PCB size is 16.5 cm x 9 cm. An example of a built 28 GHz transceiver PCB is shown in Fig. 2. Design files for the PCB and PLL software can be obtained via [6]. To make a functional transceiver, a SDR platform and controller are required. In this project an ADALM Pluto [33] was used as the SDR and R-Pi with touch screen was used as the controller. R-Pi sounder analysis code was written in Python. An example completed sounder (RF PCB, external BPF and SDR) is shown in Fig. 3a. An example completed full sounder system is shown in Fig. 3b: consisting of the sounder, R-Pi controller with touch screen and a 28 GHz horn antenna, with batteries. The small size of a built sounder is shown by Fig. 4, overall showing the system is easily hand portable. The PCB is powered at 6 V, which avoids the chips running hot and needing external heatsinking. The RF chips have thermal paddles in their package - it is important these are properly soldered for RF ground and thermal dissipation to the PCB. The sounders have been operated continuously for over 4 hours, with only minor internal temperature rise observed. To protect the sounder from rain, there are no cooling holes in the case. Reproductions of the sounder equipment should properly consider heatsinking requirements for their own use cases- vent holes or metal enclosures may be beneficial.

At the time of writing, the cost of one fully assembled RF PCB was circa £1,300 not including the SDR. Two test horn antennas were used (Quasar QWH21SB-UBR-K-F-20, with 17 degree beam width and 20 dBi gain), connected to the sounder using 2.4 mm connectorized coax cabling.

IV. SOUNDER ALGORITHM

The sounder uses a 511 bit PRBS modulated onto binary phase shift keying (BPSK) transmitted data as the

sounding signal. An efficient correlation procedure in the RX using circular convolution and FFTs [2] is used, based on (1).

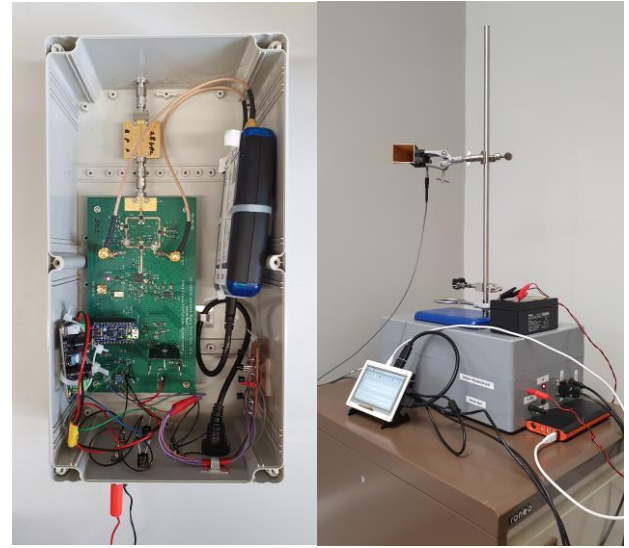


Fig. 3. Sounder: a) inside of a built sounder, b) example sounder system.



Fig. 4. Example of enclosed system (box size 30 x 16 x 12 cm).

$$C = IFFT[R(f)^*G(f)] \quad (1)$$

In (1), $R(f)$ and $G(f)$ are the FFTs of RX time sample series $r(n)$ and prior known TX sequence $g(n)$ respectively and $*$ denotes complex conjugation. C is the resulting cross-correlation array of the time series and thus is the channel impulse response in the time domain. From this, the system can provide accurate measurements of RF power and RMS delay spread. The PRBS is modulated by the SDR as an IQ signal with chip rate of 30 Mchip/s, which is sufficient to illuminate a 60 MHz channel and resolve delays to 33 ns. The maximum resolvable delay is 17 μ s. Since there is no synchronization between the TX and RX, absolute channel delay cannot be measured. However, usually in radio channel measurements, it is the channel frequency response and delay spread that is of primary interest, rather than absolute delay.

A. Equalization

The combined effect of the BPSK sinc shape of the TX sounding signal and the filters within the SDR RX chain require equalization before the measured channel spectral response can be properly presented. This equalization is performed on the spectrum of the recovered RX signal, after using (1). The required spectrum amplitude equalization is calculated using (2), for FFT spectrum bin m out of N .

$$Eq[m] = \left| \text{sinc} \left(\frac{m}{N} \right) \right|^r \quad (2)$$

Coefficient r must be found and is a function of hardware imperfections. The correct value of r to use was found by laboratory experimentation using a PRBS modulated RF signal generator at 28 GHz as the sounding source. The resolved spectrum from the sounder was monitored whilst r was adjusted, until the r giving a flat resolved channel response is found. It was found that r was a mild function of the RX signal power, and hence resolved impulse magnitude, so can be represented by a simple four term polynomial to scale the recovered spectrum (3), where x is the resolved impulse magnitude found in C using (1).

$$r = ax^3 + bx^2 + cx + d \quad (3)$$

For high impulse magnitudes beyond a level M_l , r can instead be fixed to a maximum value M_r using (4).

$$\text{if } (x) > M_l \text{ then } r = M_r \quad (4)$$

Two sets of coefficients are used, depending on which RX gain (RX_{gain}) is used by the SDR. Resulting found coefficient values used for (3) and (4) are shown in Table I.

TABLE I
EQUALIZATION COEFFICIENTS

RX_{gain}	a	b	c	d	M_l	M_r
50	$8.3x10^{-22}$	$-2.5x10^{-14}$	$2.3x10^{-07}$	0.75	$1.4x10^6$	1.8
20	$6.3x10^{-20}$	$-5.3x10^{-13}$	$1.5x10^{-06}$	-0.13	$5.5x10^6$	1.7

An illustration of the equalization action is presented in Fig. 5 showing the extracted channel response for an example PRBS modulated test signal (generated by a lab signal generator at 28 GHz, -75 dBm). Fig. 5a shows the channel response before equalization is applied, clearly showing the expected BPSK sinc shape dominating the spectrum plot. Fig. 5b shows the channel response after the equalization is applied, with the sinc response now removed and the true channel response remaining (from a coax cable in this case). The flatness of the resolved channel, both before and after equalization, can be analyzed by considering the maximum and mean channel magnitude offsets from the ideal flat channel

response of 0 dB (coax cable), over the full channel BW. Hence, in Fig 5a) before equalization the mean offset is 7.5 dB and the max offset is 30 dB. In Fig 5b) after equalization the mean offset is 1.0 dB and the max offset is 4.5 dB - both showing significant improvement due to the equalization.

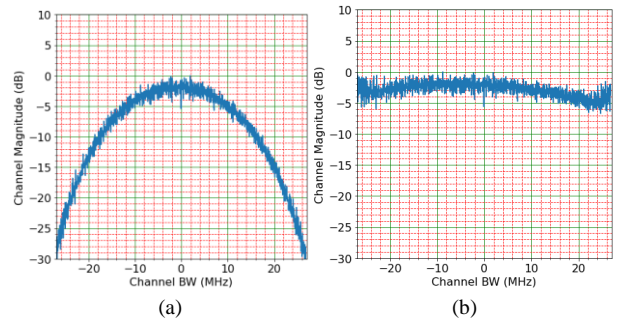


Fig. 5. Example channel response equalization for BPSK sinc and hardware shaping effects: a) no equalization applied, b) equalization applied: only channel response of coax cable remaining.

B. Signal Level & SDR RX_{gain}

During lab commissioning it was found that two gain settings were required for the RX SDR, RX_{gain} , to achieve best measurement dynamic range. The required gains are $RX_{gain} = 50$ for normal RX measurement from -110 dBm to -45 dBm (theoretical FSPL distances ~5 km down to ~6 m). For short range measurements, $RX_{gain} = 20$ is suitable between -90 dBm to -30 dBm (FSPL distances ~1 km down to 1 m). This lower gain setting is useful for initial lab calibration and tests prior to commencing a field trial.

Accurate RX power received signal strength indication (RSSI) readings are very important and a key output from the channel sounder. The output from (1) represents an accurate measurement of the resolved impulse amplitude, for a given RX input PRBS modulated carrier power. However, due to the frequency dependent RF hardware gain and cable losses, etc, a correction factor is needed to relate (1) back to an RF power in dBm as seen at the test port. Hence, the actual received signal power is related to the resolved impulse magnitude x from C in (1) using (5).

$$RSSI = RX_{powerscale} \cdot 20 \log_{10}(x) + RX_{poweroffset} \text{ dBm} \quad (5)$$

Where $RX_{powerscale}$ is approximately 1 and $RX_{poweroffset}$ approximately -180 for an RX_{gain} of 20 and approximately -200 for an RX_{gain} of 50. Parameter $RX_{powerscale}$ and $RX_{poweroffset}$ values also depend on specific channels used and so are found during initial lab commissioning calibration. This is done using a PRBS modulated sounder signal applied from a calibrated RF signal generator. Several RF test powers are applied across the dynamic range of the sounder and hence the parameters for (5) are

directly found. This calibration step needs only performing once, during equipment commissioning.

C. Carrier Alignment

It is important that the TX and RX systems are carrier aligned before a sounding event commences. The alignment is done by setting up the TX unit to produce a CW tone on the desired channel and then setting up the RX system to receive on the same channel, in CW mode. The RX sounder then uses an FFT to find the carrier centre and hence evaluate the overall carrier error. The found carrier error is then used by the sounding RX system to correct for all subsequent PRBS based soundings.

The following channels were identified during commissioning and are selectable in the system: ch1 (27 GHz), ch2 (28 GHz), ch3 (29 GHz), ch4 (27.2 GHz), ch5 (27.5 GHz), ch6 (27.65 GHz). In the UK ch2 & ch3 require an Ofcom Innovation and Trial Licence, but all other channels are in license exempt spectrum.

V. SYSTEM VERIFICATION TESTS

Two RF PCBs were built, commissioned, and tested for basic RF performance before integrating into the sounder system. An external switched mode buck converter was used to reduce the 12 V from the battery to 6 V for the PCB. The current drawn from the 12 V battery was 300 mA in both RX and TX modes. A 7 Ahr sealed lead acid battery is used to power the RF hardware during field operations, which should provide a service life of over 20 hours. Key metrics for the version 0.1 PCB design are reported in Table II.

TABLE II
THEORETICAL AND MEASURED RF PCB PERFORMANCE

Metric	Theoretical Design	Lab Measurements	
RX SSB NF	6.6	8.7	dB
TX gain	9	9	dB
RX gain	9	10	dB
RX IPP1dB	-15	-14	dBm
TX OPP1dB	6.2	1.0 DSB (<i>implies 4.0 dBm for SSB</i>)	dBm
RX BW	21 – 31 GHz	-	GHz
TX BW	21 – 31 GHz	-	GHz

The results in Table II are without the 28 GHz BPF fitted. It will be noted that the TX output 1 dB compression point (OPP1dB) is 5 dB lower than expectation and this is in part due to the lack of image filtering before the output stage, hence the output amplifier will limit on the total applied RF power from both mixer sidebands (i.e. double sideband - DSB). If an image reject filter had been fitted prior to the amplifier then circa 3 dB improvement would be possible (hence single sideband (SSB) figure also quoted), however this would require the filter to be mounted on the PCB and would limit system flexibility for future use. Therefore,

the necessary sideband selection filter is fitted at the output of the radio, as a separate PCB that is easy to swap. If higher TX powers are required, an outboard power amplifier (PA) can then be fitted after this BPF. It will also be noted that the RX noise figure (NF) is 2 dB worse than predictions, possibly due to power supply noise and the losses from 2.4 mm connectors and adapters used in the sounder.

However, overall, the RF frontend is close to predictions for the line-up and is suitable for generic 28 GHz use.

A. TX Power & RX Sensitivity Lab Verification

Next, the RF PCB was connected to the SDR and 28 GHz input BPF and the effective sounder operational RF performance measured. The SDR was configured to generate an IF TX power of -10 dBm, which places the TX IF input 2 dB below the PCB TX input 1 dB compression point.

Two systems were tested for RX level measurement accuracy, using a Rohde & Schwarz SMW100A dual arbitrary waveform signal generator (transmitting the sounder 30 Mchip/s PRBS). Testing showed good agreement between applied RF PRBS modulated power and sounder resolved power between -30 dBm and -110 dBm over all channels. Resolved mean RF power error is better than 0.7 dB and worst-case error is 2 dB, for resolved impulse signal to measurement noise floor (SNR) ratios greater than 4 dB.

Channel 1 was found to be susceptible to a clock spur at the RX IF, radiating from the R-Pi CPU, so was not used in the field. The expected impulse SNR is limited by the length of the PRBS sequence and is 27 dB for a 511 chip length sequence. An example time domain impulse and channel response from the tests are shown in Fig. 6.

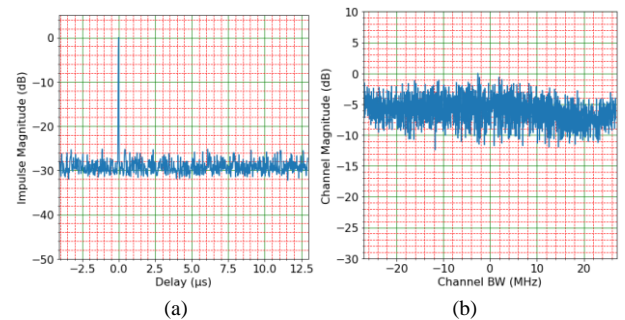


Fig. 6. Channel 5 (27.5 GHz) RX at -80 dBm using signal generator source: a) time domain impulse, b) channel frequency response.

The full sounder TX operation was also tested in the lab, with the conducted powers across all channels found to be between -8 to -10 dBm, apart from channel 3 at -19 dBm on both units. Additional loss was due to the BPF and associated cabling and adapters. The observed TX spectrum showed BPSK nulls at ± 30 MHz as expected for the PRBS chip rate. The 20 dB BW is 54

MHz, which represents a practical limit to the measured spectrum than can be equalized.

B. Reflection Emulation Using Coaxial Cable Delay

To confirm the sounder algorithm worked correctly with the SDR platform, a reflection path at the 2 GHz IF was emulated using a 1 m and 20 m length of RG316 coax (velocity factor~ 0.7) combined using resistive splitters and combiners, as shown in Fig. 7. The resolved time domain impulse for the single 1 m cable is shown in Fig. 8a and when the 20 m line is added in Fig 8b, clearly showing the two correlation peaks separated by 95 ns as expected.

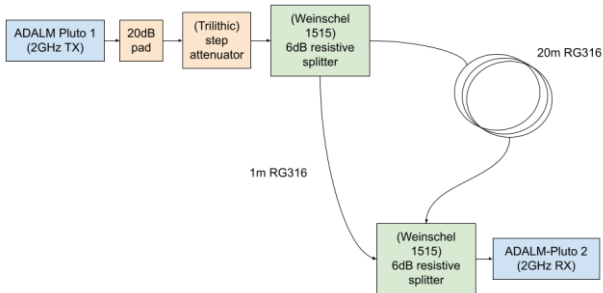


Fig. 7. Reflection emulation using coax delay line, for tests at the SDR IF.

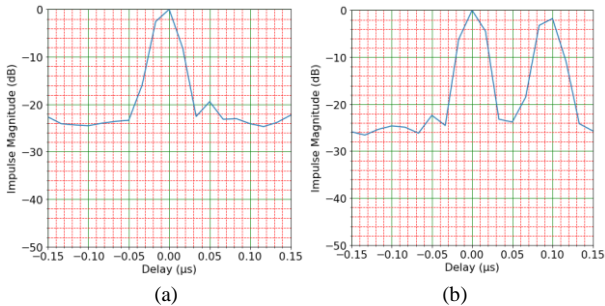


Fig. 8. Zoomed-in view of impulse for a) 1 m and b) additional 20 m line, showing expected 95 ns delay due to additional coax path.

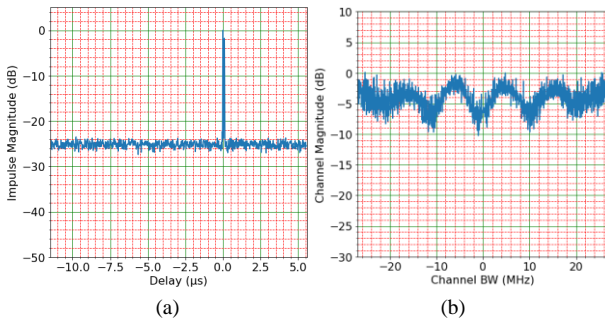


Fig. 9. Impulse response for test delay a) time domain, b) frequency domain, showing expected 11 MHz nulls due to coax cable lengths.

The full time-domain impulse response (with the two impulses) is shown in Fig. 9a and the resolved frequency response in Fig. 9b, which shows periodic nulls at 11 MHz, as would be expected for a 95 ns path delay difference.

VI. PROPAGATION SOUNDER FIELD TESTS

The sounder system was then tested in two scenarios, involving close-to-ground propagation. An indoor test and outdoor test were performed.

A. Field Test Sites

As a first test, indoor channel soundings were performed in the Mappin Building at the University of Sheffield, at various points (9 locations, 6 localized tests per location) along a 100 m corridor, with TX test set-up shown in Fig. 10. The horn antennas were both 70 cm above the corridor floor. All corridor obstructions were removed and all doors in the corridors were open.



Fig. 10. TX system during indoor soundings at The University of Sheffield.

Extended outdoor field tests were then conducted at a site on the outskirts of Doncaster in the UK (Lat.: 53.5222, Long: -1.0963), with the horn antennas 0.7 m above wet road and rough ground and with an overall testable distance of 1 km (21 test locations, 3 localized tests per location). Fig. 11 shows the test road surface. The TX system was set up at the side of the road with visibility down the road. The RX system was moved along the road using a small hand trolley, as also shown in Fig. 10. Results from the two measurement sites are presented in the following sections.



Fig. 11. Outdoor field tests site with wet road (1 km testable distance).

Collected data is compared to a simple FSPL model (6), and where appropriate a simple Reflective Earth (RE) with single reflected ray model (7), with

antenna height above ground h , measured distance d and wavelength λ .

$$PL_{FSPL} = 20 \log_{10} \left(\frac{4\pi d}{\lambda} \right) \text{ dB} \quad (6)$$

$$PL_{RE} = 40 \log_{10}(d) - 20 \log_{10}(h^2) \text{ dB} \quad (7)$$

Data is fitted to a standard log-normal path loss model of form shown in (8) where n is the distance log-scaling term and K the fixed offset (corresponding to a reference distance of 1 m).

$$PL_{model} = n \log_{10}(d) + K + X_{\sigma} \text{ dB} \quad (8)$$

Parameter X is a normal random variable with standard deviation σ dB for log-normal shadowing, calculated using (9), where N is the number of data points, PL_{data} is the path loss measured and PL_{model} is the path loss predicted by (8) with X_{σ} set to zero.

$$\sigma = \sqrt{\frac{1}{N} \sum_{k=1}^N \{PL_{data}(k) - PL_{model}(k)\}^2} \quad (9)$$

A sounding test takes under 1 minute per location. Multiple readings were taken at each measurement location.

B. Indoor Propagation Test Results

Extracted path loss (PL) results from the Mappin indoor corridor test are shown in Fig. 12, compared to FSPL model (6). The PL data has been fitted to the log-normal model (8) with 1 m reference distance, resulting in (10).

$$PL_{corridor} = 15.6 \log_{10}(d) + 69.1 + X_{\sigma_c} \text{ dB} \quad (10)$$

For the corridor measurement results $\sigma_c = 5.5$ dB. The fixed loss from a FSPL model at 1 m would be 61.4 dB. Thus, from (10) it can be seen that the fixed term K is 7.7 dB higher than for FSPL. In (10) it can also be seen that the fitted path loss exponent n is 15.6, which is lower than expected for FSPL.

This perhaps suggests that the wave is acting as if in a lossy waveguide formed by the corridor. Similar effects have been seen by [18].

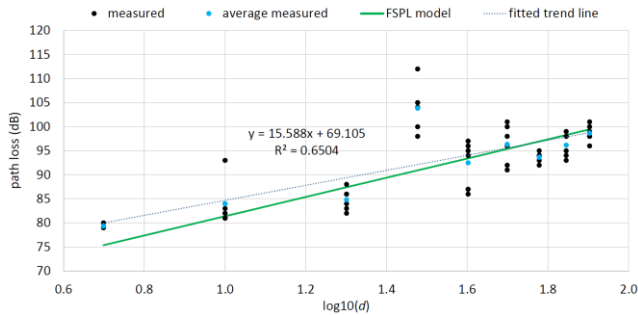


Fig. 12. Extracted path loss for 100 m in-building corridor: measured and FSPL comparison.

However, it is proposed that FSPL is a reasonable approximation to the corridor measurements since the overall path loss is within 5 dB of FSPL. Brief testing was also conducted to assess the extra loss due to closing one set of wooden fire doors. The additional loss was measured at 19 dB and also a second impulse from a delayed ray at 88 ns was seen. Reflections were seen on some of the corridor measurements, though generally more than 20 dB below the main ray. However, the most notable reflections were around the 30 m point, with an example shown in Fig. 13. This also corresponds to the anomalous channel loss seen at $\log_{10}(d) = 1.48$ on Fig. 12. A visual inspection of the corridor area showed no environmental causes for this anomalous high path loss. During subsequent analysis of the geometry of the test setup it was calculated that destructive interference from a simple two-ray model of ground reflection could be expected close to 30 m and so could explain this result.

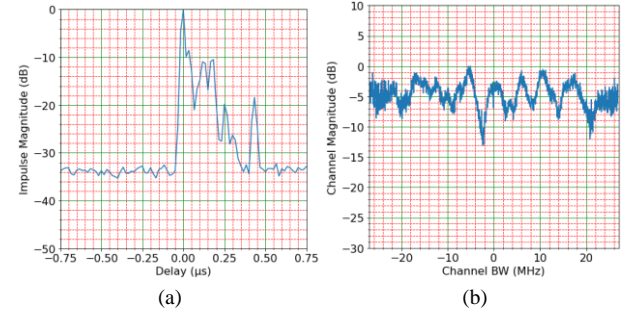


Fig. 13. Impulse response at 30m range: a) time domain, b) spectrum.

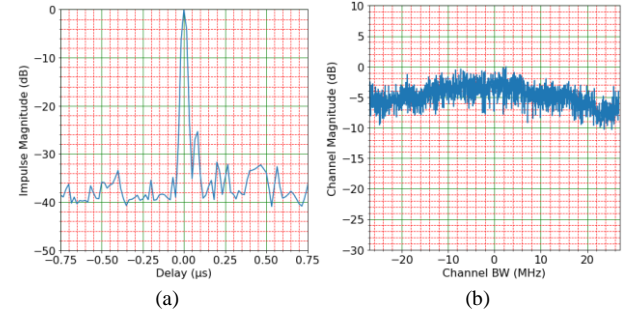


Fig. 14. Impulse response at 80 m range: a) time domain, b) spectrum.

There are clearly several strong time domain reflections present on Fig. 13a, spreading across 500 ns (producing an RMS delay spread of 70.2 ns calculated using [2]). The spectral nulls caused by these reflections are seen in Fig. 13b. Moving the sounder by 10 m moved it out of the reflective area. For comparison, the channel response close to the end of the corridor is shown in Fig. 14.

C. Outdoor Propagation Test Results

Outdoor tests were conducted over the 1 km LoS range. The TX was at a fixed site and the RX system was moved on a trolley to each test location, along a tarmac road. From Fig. 15 the extracted path loss model is very

close to that expected for FSPL, suggesting any reflections are minimal. A purely RE $40\log(d)$ model becomes valid after the first Fresnel zone distance of 183 m and is shown along with a FSPL model on Fig. 15. Although the data becomes more variable at this point it still seems to approximate to the FSPL model.

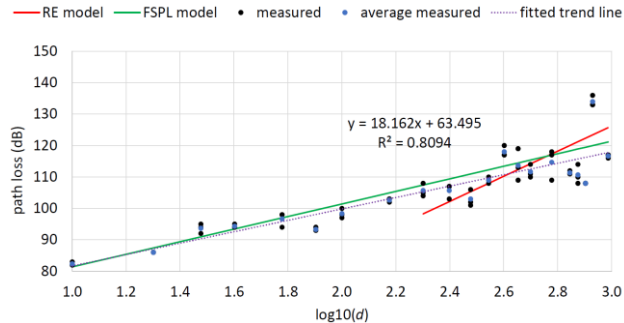


Fig. 15. Extracted path loss for wet road & rough ground over 1 km, compared to RE and FSPL models.

The large increase in path loss at 850 m (penultimate set of points) on Fig. 15 was caused by the path being obscured by several tree trunks after a bend in the road. A short distance further along the road and a move onto some rough ground returns the link to line of sight and the improvement in path loss is seen for the final reported result set (corresponding to 800 m over tarmac and then 170 m over wet rough ground). The path loss data has been fitted to the log-normal model (8), resulting in (11).

$$PL_{outdoor} = 18.2 \log_{10}(d) + 63.5 + X_{\sigma_r} \text{ dB} \quad (11)$$

From the measurement results, $\sigma_r = 5.4$ dB. The fixed loss from a FSPL model at 1 m would be 61.4 dB and it can be seen in (11) that this is now within 2.1 dB of the model. It can also be seen that the log-exponent of 18.2 is also close to the 20 expected for FSPL. Overall, the measured data agrees well with a FSPL model.

A lack of resolvable reflections throughout the trial was confirmed by inspecting the time domain impulse data. An example for the measurements at 971 m is shown in Fig. 16, showing a single resolved impulse and a flat channel (within the 60 MHz BW measurement capability).

Since the loss model (11) seems to fit a FSPL approximation, this also suggests that there is no polarization rotation over the tested distance.

It is also worth noting that the resolved impulse in Fig. 16a is 20 dB above the system measurement floor, suggesting that significant further distances could have been tested, though suitable field sites become hard to find in practice.

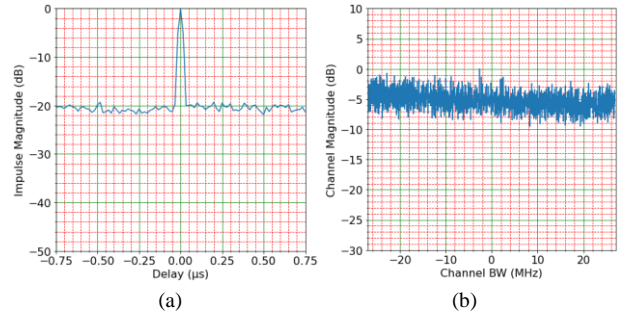


Fig. 16. Impulse response at 971 m range: a) time domain, b) spectrum.

VII. DISCUSSION

The sounder and the related recent field test results will now be considered in the context of the prior works. A brief comparison of the sounder system performance to existing published sounders is presented in Table III; considering Max Path Loss (MPL), Reflection Delay Resolution (RDR), Dynamic Range (DR), Sounding Results Latency (SRL), and TX sounding BW, where reported.

TABLE III
COMPARISON OF SOUNDER PERFORMANCE TO PUBLISHED WORKS

Ref	MPL (dB)	Equipment	RDR (ns)	DR (dB)	SRL (S)	TX BW (MHz)
[10]	-	USRP	10	-	-	100
[11]	145	lab kit	4	-	-	500
[12]	168	lab kit	2.3	-	-	800
[15]	170	lab kit	-	-	-	-
[16]	171	modules	-	75	-	CW
[17]	142	lab kit	1	-	-	1000
<i>This Work</i>	<i>142</i>	<i>PCB, SDR & R-Pi</i>	<i>33</i>	<i>80</i>	<i>40</i>	<i>60</i>

In [10] a USRP-N210 with 12.5 MHz sounding BW is expanded to an effective BW 100 MHz and 10 ns delay resolution through use of repeated and overlapping OFDM sounding pattern, though MPL is not reported. Since the instantaneous sounding BW at 2.2 GHz is still limited to 12.5 MHz, any fast artefacts could be missed, since 100 MHz is not the instantaneous full sounding BW. The RF front end PCB created as part of our paper could be used to extend the carrier frequency of the USRP or similar systems, if desired. In our proposed system the full 60 MHz channel is sounded instantaneously at 28 GHz.

A limitation of all other reported systems is the need for a PC to control and post-process the data (hence imposing measurement latency and potentially cumbersome in the field). Many of the reported systems use trolleys with mains powered equipment [11-14], severely limiting mobility and suitability for outdoor use in complex environments. Expensive lab equipment would be risky and inconvenient to move to field test sites in bad weather and powering would bring safety concerns. The proposed system is easily hand portable, fully self-contained using commercially available ICs and produces channel frequency response and impulse delay spread

measurement graphs on the touch screen within 40 seconds of the start of a sounding event (or 30 seconds if graphs not required) with no need for further data post processing. The compact and light-weight nature of the sounder, as seen in Fig. 4, could even support carriage by a suitably equipped drone, enabling many novel use-cases.

The use of circular convolution in (1) enables use of efficient FFT implementations in Python, hence the good achieved execution time. This rapid operation in the field allows direct insight into propagation effects during a field trial. This feature was beneficial during our outdoor field trials, allowing visual investigation of the channel environment when unusual results were observed and hence guiding retries.

Although 1 ns reflection resolution is provided by [17] this needs high performance and cumbersome lab signal generators. In-building measurements in [18-20], [25] similarly rely on high specification, large lab kit. In contrast, the reported system here uses a bespoke designed 28 GHz PCB that is cost effective, compact and can be battery powered. The system can resolve a discrete reflection down to 33 ns (limited by the SDR), which is sufficient to resolve a delay path delta of 10 m – sufficient for many large spaces. The proposed system has a measurement BW of 60 MHz (limited by the SDR) and is not a limitation of the RF PCB. A 60 MHz BW may be suitable for many IoT applications. The RF front end PCB has a modulation BW that covers 21 - 31 GHz, hence significantly wider channel illumination is possible, if a suitable SDR platform is available. As is, the presented PCB 2 GHz IF could support a sounding BW of up to 2 GHz, if suitable RF BPFs are used, which would be the widest of the sounders reported. The sounding algorithm is agnostic of SDR and could easily be adapted for different SDRs.

Lab trolley-based equipment in [15] offers a 170 dB path loss capability and [16] uses CW to achieve 171 dB, though without delay spread capability. In [27] CW test kit supports a measurement budget of 138 to 172 dB, without delay spread capability. Although our system has a link budget limit of 142 dB, (though similar to [11] and [17]) this does provide time domain delay spread measurements and was sufficient to measure to 1 km (and potentially beyond), in an outdoor line of sight scenario. Link budget capability could be enhanced using an external RF PA to boost the TX power. For example, an external PA with gain of 20 dB would increase the TX power from -10 dBm to +10 dBm, and thus offer a 162 dB link budget. Additionally, a longer PRBS sounder sequence could be used - offering improved processing gain, though carrier lock may become necessary to avoid the PRBS sequence rotating in carrier phase over long duration sequences, if the oscillators drift.

At 80 dB, the proposed system has the best dynamic range reported, representing beneficial tolerance of strong and weak signals during sounder operation.

Unlike some other reported systems, the RF system developed has been fully characterized and full RF performance is reported. The use of sinc equalization on the extracted spectrum, to compensate for both the BPSK sounding signal and also RF hardware shaping effects, is very beneficial in maximizing resolvable channel BW.

There is also importance in the field test results reported here using the instrument. The work in this paper is, to the best of the authors' knowledge, the first set of published data for propagation models within 1 m of ground at 28 GHz over rough ground outdoors at long distance. The prior work by [28] studied UWB frequencies to 10 GHz and only to 200 m, whilst requiring a fibre link for triggering and not reporting channel response spectral shape. In contrast, we measure to 1 km and at 28 GHz without need for external synchronization and report channel spectral features where notable. The upper measurement frequency of [28] is 10 GHz and our measurements at 28 GHz represent a significant shift in frequency band, requiring revised models. The UWB path loss exponent reported in [28] varies considerably between antennas at 50 cm heights ($n = 33.0$) and 2 m heights (closer to FSPL at $n = 21.4$) – hence the importance of our results showing that at 28 GHz for 70 cm heights the outdoor path loss is closer to FSPL at $n = 18.2$. This is a key result and suggests the higher carrier frequency we have tested offers an advantage for close-to-ground operation. The shadowing model parameter in [28] is 2.8 dB for antennas at 2 m and 4.39 dB for antennas at 50 cm, whereas in our outdoor 28 GHz tests we extracted a shadowing parameter value of 5.4 dB, again showing the importance of band-specific testing. In [29] the authors study channel models only to 26 m.

Measurement campaigns and models for propagation are always most relevant when in the direct band of interest, capturing all dependencies of the environment. The finding that outdoor path loss, when close to ground, approximates FSPL is quite surprising and was only possible thanks to the equipment's mobility. Similarly, the indoor model's closeness to FSPL with few reflections also suggests simple link budget models may be valid for many use cases.

VIII. CONCLUSION

A bespoke 28 GHz hardware platform consisting of a custom designed mmWave RF PCB and commercial SDR, both controlled by a R-Pi, is presented and described in the context of a channel sounder. The sounder hardware is low-cost (£1,300 for PCB & RF hardware) and the PCB design has been made available online to assist other researchers in the discipline, for their own adaptation and use. The sounder system is then used in two close-to-ground applications to measure path loss and inspect channel impulse responses.

Extracted log-normal models are provided for the measured propagation data, with measurements showing path losses close to FSPL can be achieved at antenna heights of 0.7 m for indoor and outdoor LoS tests. Apart from the one location specific case during the indoor corridor testing, there were no reflection paths observed exceeding the system's minimum resolvable 33 ns, further suggesting the suitability of the FSPL model, at least for the tested BW. Overall, this suggests that unobstructed mmWave signal transmission close-to-ground is entirely viable over communications bandwidths of circa 60 MHz. This could be useful for covert or low probability of intercept communications applications.

REFERENCES

- [1] Casetti, "The challenges of universal broadband connectivity [Mobile Radio]," *IEEE Vehicular Technology Magazine*, vol. 17, no. 3, pp. 5–11, Aug. 2022, doi: 10.1109/mvt.2022.3176414.
- [2] A. Ball, "Design and field trial measurement results for a portable and low-cost very-high-frequency / ultra-high-frequency channel sounder platform for Internet of things propagation research," *IET Microwaves, Antennas and Propagation*, vol. 13, no. 6, pp. 714–724, May 2019, doi: 10.1049/iet-map.2018.5827.
- [3] D. P. Wright and E. A. Ball, "Highly portable software defined radio test bed for dual band propagation studies," in *The Loughborough Antennas & Propagation Conference (LAPC 2018)*, Loughborough, 2018, pp. 1–6, doi: 10.1049/cp.2018.1472.
- [4] D. P. Wright and E. A. Ball, "IoT focused VHF and UHF propagation study and comparisons," *IET Microwaves, Antennas and Propagation*, vol. 15, no. 8, pp. 871–884, 2021, doi: 10.1049/mia.2.12101.
- [5] T. S. Rappaport, G. R. MacCartney, M. K. Samimi, and S. Sun, "Wideband millimeter-wave propagation measurements and channel models for future wireless communication system design," *IEEE Trans. on Communications*, vol. 63, no. 9, pp. 3029–3056, Sep. 2015, doi: 10.1109/TCOMM.2015.2434384.
- [6] RF PCB files. [Online]. Available: <https://www.sheffield.ac.uk/mm-wave/futuremmwave/downloads-pcb-design-files>.
- [7] Y. Wang, Y. Lv, X. Yin, and J. Duan, "Measurement-based experimental statistical modelling of propagation channel in industrial IoT scenario," *Radio Science*, vol. 55, pp. 1–14, Sep. 2020, doi: 10.1029/2019RS007013.
- [8] Y. Lyu, A. W. Mbugua, Z. Yuan, K. Olesen, and W. Fan, "Design and validation of a multilink phase-compensated long-range ultrawideband VNA-based channel sounder," *IEEE Trans. Microw. Theory & Tech.*, vol. 70, no. 10, pp. 4528–4543, Oct. 2022, doi: 10.1109/TMTT.2022.3194045.
- [9] S. Salous, A. Cheema, and X. Raimundo, "Radio channel propagation measurements using a multiband agile chirp sounder," in *2014 31st URSI General Assembly and Scientific Symposium*, Beijing, 2014, pp. 1–4, doi: 10.1109/URSIGASS.2014.6929650.
- [10] B. B. Harianto, M. Hendratoro, G. Ardiansyah, and A. Mauludiyanto, "Measurement of wideband indoor radio propagation channel using USRP," in *Journal of Physics: Conference Series*, vol. 1381, no. 1, pp. 1–10, Nov. 2019, doi: 10.1088/1742-6596/1381/1/012054.
- [11] J. Ko, S. U. Lee, Y. S. Kim, and D. J. Park, "Measurements and analyses of 28 GHz indoor channel propagation based on a synchronized channel sounder using directional antennas," *Journal of Electromag. Waves and App.*, vol. 30, no. 15, pp. 2039–2054, Oct. 2016, doi: 10.1080/09205071.2016.1239552.
- [12] M. Samimi *et al.*, "28 GHz angle of arrival and angle of departure analysis for outdoor cellular communications using steerable beam antennas in New York City," in *IEEE Vehic. Techn. Conference*, Dresden, 2013, pp. 1–6, doi: 10.1109/VTCSpring.2013.6691812.
- [13] H. Zhao *et al.*, "28 GHz millimeter wave cellular communication measurements for reflection and penetration loss in and around buildings in New York city," in *IEEE International Conference on Communications*, Budapest, 2013, pp. 5163–5167, doi: 10.1109/ICC.2013.6655403.
- [14] Y. Azar *et al.*, "28 GHz propagation measurements for outdoor cellular communications using steerable beam antennas in New York city," in *IEEE International Conference on Communications*, Budapest, 2013, pp. 5143–5147, doi: 10.1109/ICC.2013.6655399.
- [15] J. Lee, J. Liang, J.-J. Park, and M.-D. Kim, "Beamwidth-dependent directional propagation loss analysis based on 28 and 38 GHz urban micro-cellular (UMi) measurements," in *2017 IEEE 86th Vehicular Technology Conference (VTC-Fall)*, Toronto, 2017, pp. 1–5, doi: 10.1109/VTCFall.2017.8288370.
- [16] J. Du *et al.*, "Directional measurements in urban street canyons from macro rooftop sites at 28 GHz for 90 % outdoor coverage," *IEEE Trans. Antennas & Propag.*, vol. 69, no. 6, pp. 3459–3469, Jun. 2021, doi: 10.1109/TAP.2020.3044398.
- [17] A. M. Al-Samman, T. A. Rahman, M. H. Azmi, and S. A. Al-Gailani, "Millimeter-wave propagation measurements and models at 28 GHz and 38 GHz in a dining room for 5G wireless networks," *Measurement*, vol. 130, pp. 71–81, Dec. 2018, doi: 10.1016/j.measurement.2018.07.073.
- [18] A. M. Al-Samman, T. A. Rahman, and M. H. Azmi, "Indoor corridor wideband radio propagation measurements and channel models for 5G millimeter wave wireless communications at 19 GHz, 28 GHz, and 38 GHz Bands," *Wireless Comm. & Mob. Comput.*, vol. 2018, pp. 1–13, 2018, doi: 10.1155/2018/6369517.
- [19] S. Ju, Y. Xing, O. Kanhere, and T. S. Rappaport, "Millimeter wave and sub-terahertz spatial statistical channel model for an indoor office building," *IEEE Journal on Selected Areas in Comms.*, vol. 39, no. 6, pp. 1561–1575, Jun. 2021, doi: 10.1109/JSAC.2021.3071844.
- [20] M. A. Samad, F. D. Diba, Y. J. Kim, and D. Y. Choi, "Results of large-scale propagation models in campus corridor at 3.7 and 28 GHz," *Sensors*, vol. 21, no. 22, Nov. 2021, doi: 10.3390/s21227747.
- [21] Zhang *et al.*, "Experimental characterization of millimeter-wave indoor propagation channels at 28 GHz," *IEEE Access*, vol. 6, pp. 76516–76526, Nov. 2018, doi: 10.1109/ACCESS.2018.2882644.
- [22] S. Nie, G. R. MacCartney, S. Sun, and T. S. Rappaport, "28 GHz and 73 GHz signal outage study for millimeter wave cellular and backhaul communications," in *IEEE International Conference on Communications, ICC 2014*, Sydney, 2014, pp. 4856–4861, doi: 10.1109/ICC.2014.6884089.
- [23] D. He *et al.*, "Influence analysis of typical objects in rural railway environments at 28 GHz," *IEEE Trans. Vehic. Tech.*, vol. 68, no. 3, pp. 2066–2076, Mar. 2019, doi: 10.1109/TVT.2018.2840097.
- [24] R. MacCartney, T. S. Rappaport, S. Sun, and S. Deng, "Indoor office wideband millimeter-wave propagation measurements and channel models at 28 and 73 GHz for ultra-dense 5G wireless networks," *IEEE Access*, vol. 3, pp. 2388–2424, Oct. 2015, doi: 10.1109/ACCESS.2015.2486778.
- [25] S. Ito and T. Hayashi, "Measurement and evaluation of 28 GHz propagation characteristics in specific environments," *IEEE Access*, vol. 10, pp. 26242–26256, March 2022, doi: 10.1109/ACCESS.2022.3157063.
- [26] J. Ko *et al.*, "Measurements and analysis of radio propagation at 28 GHz in vegetated areas of typical residential environments," *IEEE Trans. Antennas & Propag.*, vol. 68, no. 5, pp. 4149–4154, May 2020, doi: 10.1109/TAP.2020.2968801.
- [27] J. Du, D. Chizhik, R. Feick, M. Rodriguez, G. Castro, and R. A. Valenzuela, "Suburban fixed wireless access channel measurements and models at 28 GHz for 90 % outdoor coverage," *IEEE Trans. Antennas & Propag.*, vol. 68, no. 1, pp. 411–420, Jan. 2020, doi: 10.1109/TAP.2019.2935110.
- [28] S. Sangodoyin, S. Niranjayan, and A. F. Molisch, "A measurement-based model for outdoor near-ground ultrawideband channels," *IEEE Trans. Antennas & Propag.*, vol. 64, no. 2, pp. 740–751, Feb. 2016, doi: 10.1109/TAP.2015.2505004.
- [29] D. Solomitskii, V. Semkin, M. Turunen, M. Allén, and M. Valkama, "Near-ground propagation in automotive radar and communication obstructed deployments: Measurements and

modelling,” *IET Microwaves, Antennas and Propagation*, vol. 16, no. 6, pp. 316–326, May 2022, doi: 10.1049/mia2.12241.

- [30] T. Rama Rao, D. Balachander, T. Nishesh, and M. V. S. N. Prasad, “Near ground path gain measurements at 433/868/915/2400 MHz in indoor corridor for wireless sensor networks,” *Telecommunication Systems*, vol. 56, no. 3, pp. 347–355, July 2014, doi: 10.1007/s11235-013-9848-1.
- [31] W. Tang, X. Ma, J. Wei, and Z. Wang, “Measurement and analysis of near-ground propagation models under different terrains for wireless sensor networks,” *Sensors*, vol. 19, no. 8, pp. 1-13, Apr. 2019, doi: 10.3390/s19081901.
- [32] Adafruit Ltd ProTrinket. [Online]. Available: <https://learn.adafruit.com/introducing-pro-trinket>.
- [33] Analog Devices ADALM Pluto SDR. [Online]. Available: <https://www.analog.com/en/design-center/evaluation-hardware-and-software/evaluation-boards-kits/adalm-pluto.html>.

Edward A. Ball (M 2008–present) Edward (Eddie) became a Member of IEEE in April 2008 and was born in Blackpool, United Kingdom in November 1973. Eddie graduated in 1996 with a 1st Class Master of Engineering Degree in Electronic Systems Engineering, from the University of York, York, United Kingdom.

After graduating, he worked in industry for 20 years, first spending 15 years working as Engineer, Senior RF Engineer and finally Principal RF Engineer at Cambridge Consultants Ltd in Cambridge, UK. He then spent 5 years as Principal RF Engineer and Radio Systems Architect at Tunstall Healthcare Ltd in Whitley, UK. In November 2015 he joined the Department of Electronic and Electrical Engineering at the University of Sheffield, Sheffield, United Kingdom, where he now works as Reader in RF Engineering. His research interests cover all areas of radio technology, from RF system design, RF circuit design (sub-GHz to mmWave) and the application of radio technology to real-world industrial and commercial problems. He has a particular passion for RF hardware design.

Mr. Ball is a member of the IET and is a Chartered Engineer.

Sumin David Joseph received the B.Tech. degree (Hons.) in electronics and communication from the CUSAT University, India, in 2012, M. Tech. degree (Hons.) in communication systems from the Visvesvaraya National Institute of Technology, India, in 2015, and dual PhD degree (distinction) in electrical engineering from the University of Liverpool, U.K., and National Tsing Hua University, Taiwan.

He is currently working as a Post-Doctoral Research Associate with The University of Sheffield. He was a Lab Engineer under CoE with the Visvesvaraya National Institute of Technology, India from 2015 to 2017, where he was involved in projects of national importance. He has authored or coauthored more than 25 articles in peer-reviewed journals and conference proceedings. His research interests include self-biased circulators, mmWave antenna arrays, rectifying antennas, MMIC circuit design, RF circuit design, rectifiers, integrated circuit designs, flexible electronics, wireless power transfer, energy harvesting and TMA antenna arrays.

Dr Sumin is a technical reviewer for leading academic journals and conferences, including IEEE Transactions of Antenna and Propagation, IEEE Antenna and Wireless Propagation Letters and IEEE Access.

9. Paper 5 – RX Subsampling TMA Prototype

{Reproduced as published - author accepted version.}

© 2023 IEEE. Reprinted, with permission, from Edward A. Ball, Sumin David Joseph, and Alan Tennant, "Receive Mode Time Modulated Antenna Array Incorporating Subsampling -Theoretical Concept and Laboratory Investigation", IEEE Open Journal of Antennas and Propagation, published 07 July 2023.

DOI <https://doi.org/10.1109/OJAP.2023.3293123>

(Published version [5].)

Receive Mode Time Modulated Antenna Array Incorporating Subsampling – Theoretical Concept and Laboratory Investigation

EDWARD A. BALL, MEMBER, IEEE, SUMIN DAVID JOSEPH, AND
ALAN TENNANT

Communications Research Group, The Department of Electronic and Electrical Engineering, The University of Sheffield, Sheffield, S1 3JD, UK.

CORRESPONDING AUTHOR: E. A. Ball (e-mail: e.a.ball@sheffield.ac.uk).

This work was supported by the U.K. Research and Innovation (UKRI) Future Leaders Fellowship under Grant MR/T043164/1.

ABSTRACT An eight element Subsampling Time Modulated Array (STMA) operating in receive mode with a carrier at 2.4 GHz is presented and demonstrated using bespoke Radio Frequency (RF) hardware. Each STMA cell incorporates subsampling functionality, with the sampling frequency significantly below the carrier frequency and requiring minimal additional hardware. By using this concept, the hardware required for a receiver incorporating an antenna array can be reduced and costs saved. STMA design equations and architecture strategies are presented, and a prototype hardware demonstrator is introduced. Laboratory measurements confirm that a received radiated signal, arranged to use the fundamental or a harmonic beam pointed at the radiating source, can be resolved from the subsampled intermediate frequency (IF) output. The concept demonstration hardware provides a measured array conversion gain of 11.4 dBi on the boresight beam, 7.8 dBi on the first positive and 11.3 dBi on the first negative harmonic beams, as resolved at the final combined IF output. The array IF output Signal to Noise and Distortion ratio is 69 dB. The dependence of array sidelobe level performance on STMA sampling switch rise time is also uncovered, though good performance with real, imperfect, hardware is still obtained.

INDEX TERMS Microwave circuits, RF hardware platform, time-modulated antenna arrays (TMAs), signal sampling.

I. INTRODUCTION

The design of the antenna array is always an important aspect of a radio communications system. The global adoption of 5G mobile communications continues, with over 1.3 billion connections worldwide [1]. Stimulated by this market, there continues to be significant research opportunities for 5G and future 6G systems, including mmWave [2], though often with a focus on massive MIMO for sub 6 GHz systems [3]. Propagation channels are often sparse at mmWave frequencies, so simple phased array antenna structures remain very relevant. Phased arrays systems are also important for many commercial and military communications scenarios at microwave frequencies.

The Time Modulated Array (TMA) [4], [5], [6], [7], [8] is a novel class of antenna array that does not use conventional phase shifters or vector modulators to apply a phase shift to each array radiating element. Instead, simple RF switching techniques are used, with simple controlling waveforms. Fourier analysis of the switch control waveforms

reveals a phase shifting property that results in an element-specific phase shift at the carrier, as required to realise a phased array. The TMA can be used in transmit (TX) or receive (RX) arrays and can also handle multiple beams of different data (e.g. for different target users) [9], [10], [11], diversity reception [12] or supporting polarization diversity [13]. The TMA can also be used to steer a null to minimise interference from an unwanted source [14], [15], [16], [17].

A TMA can be used in direction finding systems [18], [19] and radar systems [20], [21]. It has also been demonstrated that data transport using the harmonic beams and a radar function using the boresight beam can be supported [22], [23], [24], [25]. The TMA can also be used in reflector array applications [26], [27] or for generating circular polarization [28], [29] and for generating orbital angular momentum waves [30].

TMA hardware has historically been implemented using RF switches.

This work is licensed under a Creative Commons Attribution 4.0 License. For more information, see <https://creativecommons.org/licenses/by/4.0/>

Recent improved switch and control technologies have enabled improved RF bandwidth performance [31]. However, other advanced techniques using more RF hardware have adopted single sideband and IQ modulation to offer high RF performance [32], with some related hardware simplifications also investigated [33].

The TMA non-steered boresight beam results from the Fourier DC component (due to a non-zero average) of the switch control waveform. Recent work has shown that this boresight beam can be attenuated using simple hardware and digital control waveforms [34].

The TMA has also been demonstrated at mmWave frequencies, for secure communications applications [35]. As evidenced by the above examples, the TMA concept supports many useful and novel applications and remains important.

Although multiple concurrent harmonic beams can be generated by the TMA, the resulting beam magnitudes decrease with increasing harmonic [34]. In practice, most published works use just the boresight beam, first or second harmonic beams. The control of the TMA beams and their sidelobes is a major topic of research, such as in addressing suppression of sidelobes and sidebands [36].

The TMA is often considered in isolation from the communication system, with an RF carrier input that is processed by the TMA and results in steered beams, such as for an IoT system [37].

Software Defined Radio (SDR) applied to phased array beamforming has been researched over many years [38]. Analogue beamformers (ABF) require controllable phase shifters, such as [39] at 25 - 31 GHz and variable gain amplifiers (VGA), such as [40] at 22.8 - 35 GHz. ABFs have also now been realized in integrated front-end devices, such as [41] offering a four-element transceiver at 33.5 - 37.5 GHz. In [42] a four element 36 - 40 GHz ABF is realized for 5G. Other recent works in mmWave ABF include a single channel transceiver RF front-end [43], and quad-channel front-end [44]. Integrated, Digital Beamformer (DBF) systems have also been demonstrated, such as a 16 element RX [45]. TMA concepts have recently been applied to generate mmWave MIMO at 26 - 33 GHz through switching the LNA current, though the system still requires a VGA and phase shifter in an initial ABF stage [46].

However, to the best of the authors' knowledge, there is no reported work that incorporates the TMA directly within a SDR inspired downconverter with the intention to simplify overall hardware - which is stimulus and the focus of the work in this paper. By combining the carrier down conversion within the TMA operation, there exists the possibility to simplify and reduce cost in an SDR system. Although we demonstrate the principle in a RX array, it could also be applicable to a TX system, with appropriate circuit modification and filtering.

RX SDR systems commonly make use of an ADC to sample and digitize the RF signal. The sampling action generates Nyquist bands and it is well known that an RF signal presented in a higher Nyquist (alias) band can thus be down converted by subsampling via these sampling aliases [47], [48].

The sampling action can be considered separately from the digitization action and thus a dedicated sampler circuit can be used to perform the subsampling down conversion. The zero-order hold that would typically be the basis of such a circuit can be theoretically approximated by a simple ideal switch and sample hold capacitor. It is this concept that stimulates our work into combining a switch-based TMA with a sampler to form a single subsampler down converting TMA system. Hence, the key contributions of this paper are as follows:-

- Theoretical introduction of an RX subsampling TMA, leading to the new STMA concept,
- Theoretical performance predictions of the STMA and identification of key design criteria,
- Laboratory measured results from a 2.4 GHz hardware RX STMA prototype, compared to theoretical predictions.

The paper continues with the STMA concept and prototype described in section II, then the prototype tests and verification of the hardware platform is presented in section III. Chamber radiated antenna pattern measurements are presented in section IV and an overall discussion of findings in section V. The paper concludes in section VI.

II. SUBSAMPLING TMA CONCEPT

Since many modern radio systems are based on a SDR approach, it is interesting to consider how the TMA could directly apply SDR concepts and thus reduce hardware complexity and cost. In a conventional approach, the output of a passive RX antenna array may first be down converted to an IF and then sampled directly by an ADC and this is a widely used technique. When considering such a conventional sampler approach applied to the TMA output, it becomes interesting to consider what happens if the sampler gate is moved forward in the signal chain. Fig. 1 shows the sampler moved forward from the ADC / array interface and is now next to the TMA switches. Clearly, this is only an intuitive step and would be expensive in practice, but it is useful illustratively.

The subsequent step is to consider how the TMA switch and the sampler could be combined into one switch circuit function. In practice this is a relatively simple step, as represented in Fig. 2, which shows that by repurposing the already used TMA switch and addition of a hold circuit (a capacitor) the TMA can now perform the dual role of TMA and subsampler, though with a more complex control waveform required. The STMA concept thus makes use of the existing RF switch, as already required by the TMA, and a relatively simple addition to the circuitry to support sampling. However, as will be discussed later, the RF requirements of this combined function switch are now more demanding.

One issue is the maximum analogue bandwidth supported by the STMA switch, which must pass the incoming RF carrier signal and also switch at the desired sampling rate F_s . The optimal design of this switch is worthy of further research, but for expediency this article makes use of standard off the shelf parts to demonstrate STMA concepts.

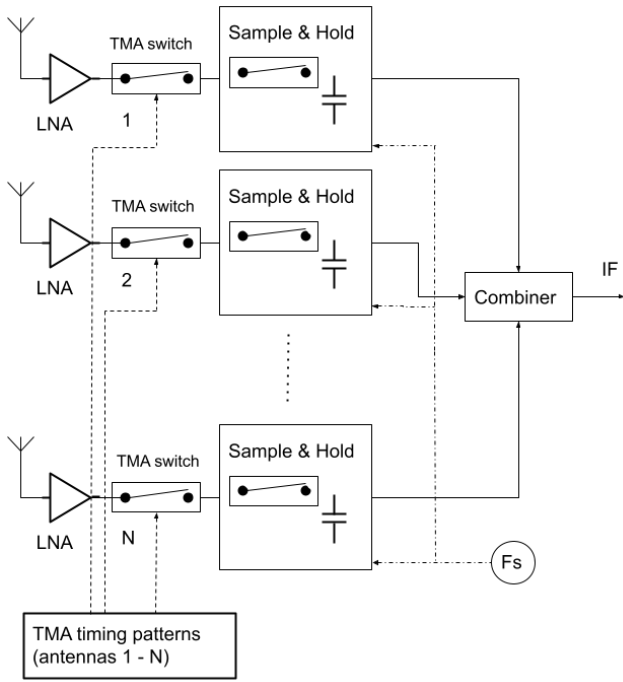


FIGURE 1. Illustrative concept - each TMA switching cell is followed by sampler, sampling at F_s .

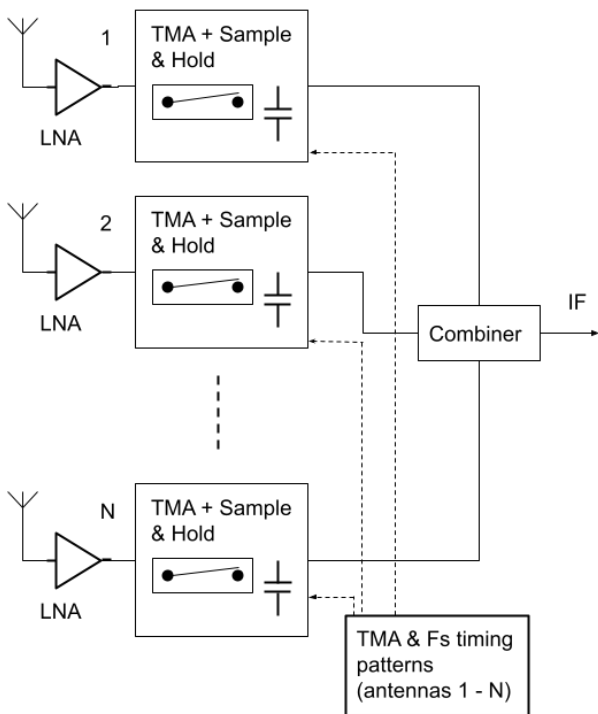


FIGURE 2. TMA and sampler function combined.

A. STMA RX PROTOTYPE CIRCUIT

In our demonstrator design we use an antenna array at 2.4 GHz and initially down convert using a conventional RF mixer to $IF1$, creating an IF signal suitable for the switches' limited input RF bandwidth (BW), as illustrated in Fig. 3.

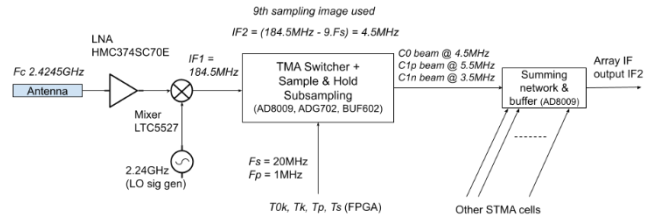


FIGURE 3. RX STMA concept demonstrator with frontend mixer down conversion.

If higher BW switches had been available this initial mixing stage would not be required.

After the TMA and subsampling operation, $IF2$ is produced as the final output from the system. In the demonstrator, the carrier frequency F_c is 2.2425 GHz, $IF1$ is 184.5 MHz and $IF2$ is centred on 4.5 MHz. To achieve this, the TMA frame period T_p is 1 μ s and the subsampler frequency F_s is 20 MHz (related design equations are presented later).

This two-stage (mixer first) conceptual approach could also be employed more generally if needed, such as at mmWave frequencies. This would allow the initial down conversion to be implemented using pragmatic low power and simple mixer technology and then employing the STMA at IF frequencies, where device switch technologies are more practical.

To demonstrate the STMA concept requires a practical hardware implementation. The choice of sampler switch dictates the maximum design frequencies for analogue BW and sampling rate and so defines the system.

Our demonstration prototype employs an Analog Devices ADG702 analogue switch [49] which has a 3 dB BW of circa 250 MHz thus defining the maximum upper limit for $IF1$. The conceptual block diagram of the prototype system at 2.4 GHz is presented in Fig. 3, with detail for one STMA cell. The full circuit diagram of one STMA cell is presented in Fig. 4, with eight copies used in the demonstrator system, integrated and combined as shown in Fig. 5.

The design of the STMA cell incorporates several important RF circuit aspects which will now be discussed, with reference to Fig. 4. The 2.4 GHz RX signal path from the antenna starts with the Analog Devices HMC374 [50] Low Noise Amplifier (LNA) U5 and then feeds the down conversion mixer LTC5527 [51] U3. The mixer LO (local oscillator) is provided through a corporate feed network on the PCB, feeding all the mixers from a single LO signal generator. Mixer U3 requires a 50 Ω termination at its $IF1$ output and this is provided by U2, a AD8009 [52] high BW opamp acting as an inverting amplifier and also conceptually translating the circuit operation from RF power signals from the antenna side to voltage signals as required by the sampler. In the U2 inverting amplifier stage resistor R1 provides the 50 Ω termination for the mixer, with a stage voltage gain of 12 dB. U2 also provides a low impedance drive to the ADG702 switch U1, which is important to help achieve a fast charge-up time for the sampling capacitor C22. U1 and C22 form the core of the STMA, performing both the array phase shifting and subsampling.

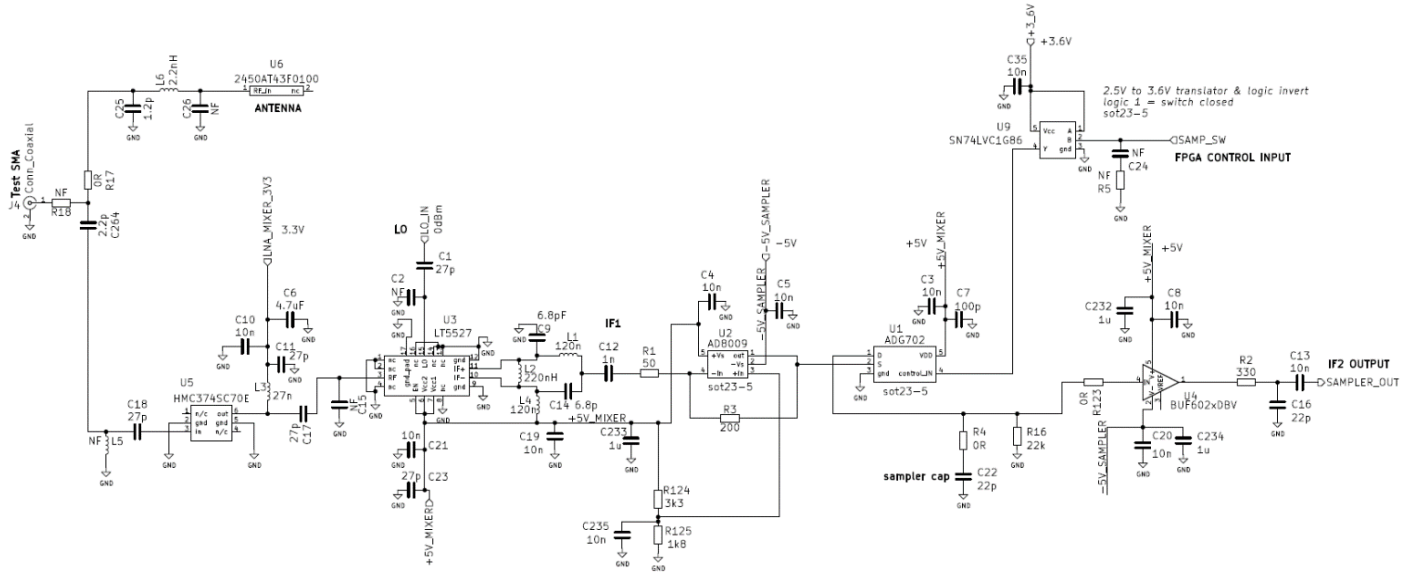


FIGURE 4. Circuit diagram of one STMA RX cell (antenna or test connector input to IF2 output).

The simple sampler R-C circuit based around C_{samp} must be considered in terms of its charge-up time and its hold time. The charge-up time constant T_{charge} can be approximated by (1), where C_{samp} corresponds to C22 and equals 22 pF, ADG702 $R_{switch_{ON}}$ is 2 Ω and AD8009 $R_{out_{opamp}}$ is 0.5 Ω .

$$T_{charge} = C_{samp}(R_{out_{opamp}} + R_{switch_{ON}}) \quad (1)$$

The discharge time constant T_{hold} can be approximated by (2), where R_p is the parallel combination of 1 M Ω due to the BUF602 input and the R16 value of 22 k Ω .

$$T_{hold} = C_{samp}R_p \quad (2)$$

FIGURE 5. Integration of 8 STMA cells into full STMA RX system (simplified representation).

The ADG702 switch has an on resistance of 2 Ω and the AD8009 has an output impedance of circa 0.5 Ω , leading to a combined series resistance of circa 2.5 Ω at 4.5 MHz (centre of IF2) supplying C22. The output from the sampler capacitor C22 must also be buffered to minimise discharge when the ADG702 switch is in its isolation (off) state. U4 is used as the buffer; a Texas Instruments BUF602 [53] with 1 M Ω input impedance. At the output of the STMA cell, the IF2 signal from U4 is then combined with the outputs from the other STMA cells using a AD8009 inverting opamp with 50 Ω output impedance and an eight-input resistive combiner, as shown in simplified form in Fig. 5. Note that the output is now at the subsampled signal IF2, not the carrier F_c or IF1.

In general switch U1, when used as a sampler, must provide a very high impedance in the off state and a very low impedance in the on state (high output drive current capability) as well as fast switching. This is to ensure the ‘hold’ capacitor C_{samp} (C22) charges quickly when the switch is enabled and then discharges only very slowly (ideally not at all) whilst the switch is off. It is desirable to only ‘blip’ the switch on, so it only samples the incoming signal for the briefest possible duration, as an approximation to a sampling impulse.

The ADG702 has a 10 pA leakage current when in signal isolation (off) state, so is not expected to significantly discharge C_{samp} . Hence, for the proposed circuit values $T_{charge} = 55$ ps and $T_{hold} = 484$ ns. Thus, the capacitor is expected to charge to 5 time constants in 275 ps, which is 0.55% of the sample rate period (since $F_s = 20$ MHz). In hold mode, with the ADG702 switch in isolation (off) state, capacitor C_{samp} is not expected to have significantly discharged over one sample interval since the 484 ns time constant is almost 10 times the sample period of F_s .

From the data sheet, the ADG702 has a minimum latency of 12 ns between the digital control signal changing and its analog output switching, which limits the maximum F_s . In practice, we have found that the minimum acceptable ‘on’ duration for the ADG702 is 7.9 ns.

The prototype system uses an FPGA to sequence the switches, with an internal clock running at 120 MHz and generating the TMA frame frequency F_p of 1 MHz (i.e. $1/T_p$) and F_s of 20 MHz. The 120 MHz master clock means the FPGA file has 120 STMA control words per one T_p frame. There are 6 words per subsample period T_s frame (i.e. $1/F_s$), hence 20 T_s events per one T_p frame. A single T_s sample duration event (i.e. ADG702 control bit on-time) lasts 8.33 ns and represents the maximum switching speed possible. During lab tests it was observed that switching the ADG702 faster than this leads to

unreliable performance. Each FPGA control word consists of the bit pattern for the full STMA at that instant in the STMA frame-with each bit corresponding to the state of each associated STMA cell switch.

B. FREQUENCY PLANNING FOR STMA

To understand the frequency domain operation of the STMA, consider an incoming RX signal presented to the TMA cell, as represented by Fig. 6. Where required due to switch BW limitations the initial conversion down from F_c to $IF1$ can be performed by a conventional mixer, as already discussed. If higher performance switches are available, then this initial down conversion stage could be removed and the STMA operate directly at F_c .



FIGURE 6. Incoming TMA RX signal in frequency domain.

The output signal from an ideal TMA switch, such as in Fig. 1, will consist of $IF1$ mixed with harmonics of the TMA switching frequency F_p , as illustrated in Fig. 7. The $C1p$ harmonic is at $IF1 + F_p$, $C1n$ harmonic is at $IF1 - F_p$, $C2p$ harmonic is at $IF1 + 2F_p$ and $C2n$ harmonic is at $IF1 - 2F_p$.



FIGURE 7. RX signal after generic TMA operation - beam harmonics for phased array use created.

Each resulting harmonic ($C0$, $C1n$, $C1p$, $C2n$, $C2p$, ...) will have a different phase shift due to the TMA control waveform timings. This phase shift implements the required phased array for receive array coherence at a particular wavefront angle of arrival, for that harmonic - hence creating an RX harmonic beam. The designer's task is to select which of these harmonic beams is of interest and to down convert it using the subsampler. The subsampling process uses the images that are created by the sampler operation, as represented in Fig. 8. The RF signals from the TMA placed in a high Nyquist band are thus translated down to a low IF ($IF2$) and so realize the STMA. Due to the subsampling, care must be taken to ensure unused Nyquist bands are clear of any input signals.



FIGURE 8. RX sampling spectrum of STMA showing Nyquist alias bands from subsampling.

The important relationship between the TMA switching frequency and sampling rate will now be discussed. It is important to consider how all the generated spectral components

are handled by the subsampling process, to avoid unwanted imaging and aliasing problems which may corrupt the desired harmonic beam RX signal. The resulting subsampled $IF2$ signal can be predicted by (3),

$$IF2 = (IF1 + nF_p) - pF_s \quad (3)$$

where F_s is the sampling frequency, F_p is the STMA frame rate ($1/T_p$), $IF1$ is the input down converted carrier frequency, n is the TMA harmonic beam being used to implement the array phase shift ($\dots, -2, -1, 0, 1, 2, \dots$) and p is the sampling frequency harmonic being used for subsampling. For simplicity, the input signal to subsample is assumed to be fully contained in the normal Nyquist bandwidth $[0, F_s/2]$.

In the prototype RX system, we use $F_s = 20$ MHz, $F_p = 1$ MHz, $IF1 = 184.5$ MHz, $p = 9$, $n = 0$. This results in the $C0$ RX beam being subsampled to 4.5 MHz, the $C1p$ beam to 5.5 MHz and $C1n$ beam to 3.5 MHz, the $C2n$ beam is resolved at 2.5 MHz and the $C2p$ beam at 6.5 MHz. Care must be taken to avoid the subsampled signals landing on system clock switching harmonics, most notably due to F_p . This is avoided by choice of F_c , F_s and F_p to ensure that the desired $IF2$ signals all land in between harmonics of F_p . Corruption from aliasing is also avoided by down converting all negative and positive beams from the STMA process to $IF2$, hence the $C0$ beam appearing at 4.5 MHz and not at 0 Hz. If a narrow band pass filter (BPF) was provided in between the TMA switch and a subsampler switch any unwanted TMA harmonic beams could have been removed before down conversion. However, this would require two switches with a BPF in between - which is more complex and so reduces the benefit of the proposed STMA technique. Therefore, here all the generated STMA harmonics must be handled by the subsequent RX system.

C. STMA CONTROL WAVEFORMS

The RX (or TX) beam pattern Array Factor (AF) for a conventional TMA using isotropic radiating elements can be predicted based on the time domain control waveforms controlling the RF switches [7], [34]. The AF can be calculated using (4) where N is the number of antenna elements, $F_n[U_k(t)]$ is the Fourier coefficient of the n th harmonic ($\dots, -2, -1, 0, 1, 2, \dots$) of the time domain switching waveform U on the k th antenna element.

$$AF(\theta, t, n) = e^{j[\omega_c + n\omega_p]t} \sum_{k=1}^N F_n[U_k(t)] e^{j\phi_k} \quad (4)$$

The time modulation of the incoming RF signal at element k can be represented as a series of Fourier coefficients, multiplied with harmonics of the switching frequency $\omega_p = (2\pi F_p)$, mixed with the carrier frequency $\omega_c = (2\pi F_c)$. The term $e^{j\phi_k}$ is an element-specific phase shift, due to antenna element spacing and evaluated beam angle and can be expressed using (5), where d is the spacing between the elements, θ is the azimuth beam angle direction being evaluated and λ is the carrier wavelength.

$$\varphi_k = (k - 1) \frac{2\pi}{\lambda} d \cdot \sin(\theta) \quad (5)$$

The n th Fourier coefficient of the switching waveform (n th harmonic), for a particular element k , is $Cn_k = F_n[U_k(t)]$ and the overall magnitude of the combined AF due to the n th harmonic is Cn , which can be for a positive beam steer ($C1p$, $C2p$) or negative beam steer ($C1n$, $C2n$) or boresight $C0$. The AF for a given applied switch timing set, at a given harmonic n , and resulting in a beam at $[\omega_c + n \cdot \omega_p]$ is found using (6) [34], where T_k is the on duration of the element switch and T_{0k} is the delay before the switch turns on.

$$AF(\theta, n) = \sum_{k=1}^N e^{j\varphi_k} \frac{\sin\left(n \cdot \frac{T_k}{T_p}\right)}{n \cdot \pi} e^{-jn\pi\left(2\frac{T_{0k}}{T_p} + \frac{T_k}{T_p}\right)} \quad (6)$$

The timing parameters for a conventional TMA switched element are illustrated in Fig. 9.

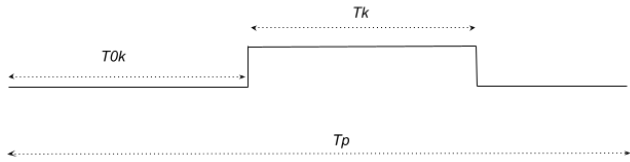


FIGURE 9. TMA switch control timings (no subsampling).

Therefore, in a conventional TMA, the individual switches in the RF path are turned on and off according to a required pattern to achieve a desired beam steer on a selected harmonic at an angle of interest, such as using (6). The required switch timings T_k and T_{0k} to steer a harmonic beam of interest can be calculated using the techniques described in [34].

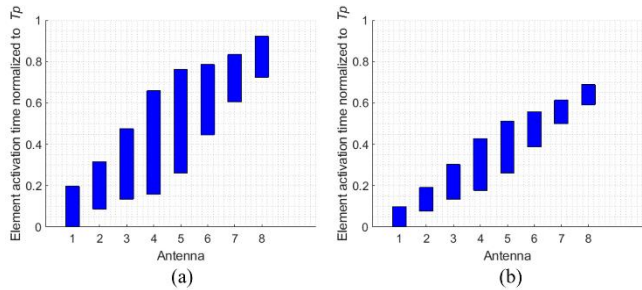


FIGURE 10. Conventional TMA antenna element timings (blue bar defines switch is on) (a): beam $C1p$ steered to 15 degrees, (b): beam $C2p$ steered to 25 degrees.

An example of such a control pattern for an 8 element TMA steering the positive first harmonic beam ($C1p$) to +15 degrees is shown in Fig. 10(a). Another example is shown in Fig. 10(b) for a positive second harmonic beam ($C2p$) steered to +25 degrees. In a subsampling TMA, with the sampler and TMA function combined, the resulting STMA switch control pattern must now incorporate both the expected TMA element timings and also the sampling event at F_s . This is pragmatically achieved by the product of both these timing sequences. An example of this is shown for a $C1p$ harmonic beam steered to +15 degrees and with a F_s/F_p ratio of 20 in Fig. 11(a).

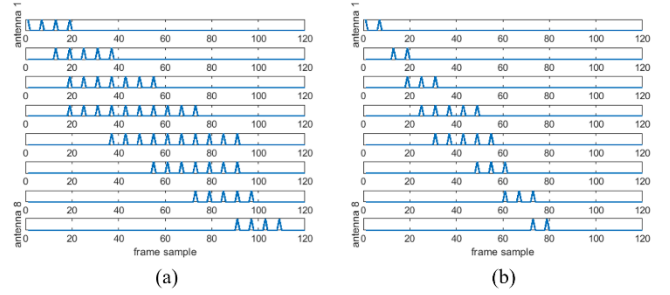


FIGURE 11. STMA antenna element switch timings (T_s sample instants shown) (a): beam $C1p$ steered to 15 degrees, (b): beam $C2p$ steered to 25 degrees.

In Fig. 11(b), the switch control pattern is shown for harmonic beam $C2p$ steered to +25 degrees. Notice that there are fewer on events in the $C2p$ harmonic pattern of Fig. 11(b) compared to Fig. 11(a). This leads to a reduction in $C2p$ recovered $IF2$ power compared to the $C1p$ power, due to the average on time affecting the magnitude of received power as will be discussed next.

D. STMA ARRAY CONVERSION GAIN

Since the STMA incorporates a frequency conversion action, we will refer to the system gain as resolved at $IF2$ relative to a known applied EIRP RF power at the antenna as the Array Conversion Gain (ACG). The subsampling action, when not using the TMA mode, has a negligible effect on the ACG when comparing the magnitude of recovered $IF2$ vs $IF1$. However, when the TMA mode is also used there is a reduction in effective ACG seen on higher harmonic beams due to the limited number of sample events per STMA element within frame T_p . This Harmonic Level Reduction (HLR) factor is approximated by (7), where $C2p_{tot_on}$ is the total number of sampling switch on events summed across all antennas when considering $C2p$ beam and $C1p_{tot_on}$ is the total number of on events summed across all antennas when considering $C1p$ beam, in period T_p . In our implementation as seen in Fig. 11, $C1p_{tot_on} = 52$ and $C2p_{tot_on} = 25$, with (7) then predicting a 6.4 dB reduction in the $C2p$ received beam power compared to the $C1p$ beam.

$$HLR = 10 \log_{10} \left(\frac{C2p_{tot_on}}{C1p_{tot_on}} \right) \quad (7)$$

The sampler circuit used has an implicit low-pass response, due to combination of C_{samp} , R_p , $R_{switchON}$ and $R_{out_{opamp}}$. This results in an amplitude slope as function of $IF2$ frequency so that resolved RX beams with IFs below the $C0$ beam frequency (4.5 MHz) are received at a higher signal level than the beams above the $C0$ frequency. One solution to this frequency response slope would be a smaller R_p value but this would directly impact the hold performance of the sampler, which is very undesirable. Spice simulation of only the sampler circuit allows the roll off to be predicted, with resulting expected $IF2$ beam levels with respect to the $C0$ beam presented in Table 1.

TABLE 1. Sampler-induced harmonic beam levels relative to $C0$ beam (used as $SGRF$).

$C2n$ level relative to $C0$ (dB)	$C1n$ level relative to $C0$ (dB)	$C1p$ level relative to $C0$ (dB)	$C2p$ level relative to $C0$ (dB)
5.1	2.2	-1.7	-3.2

The Sampler Gain Reduction Factor ($SGRF$) results of Table 1 are used later when validating the lab measured gains.

III. STMA HARDWARE PLATFORM

To allow the RX STMA to be evaluated in the laboratory, a hardware prototype was created, using the circuitry described in section II. Eight ceramic monopole antennas, 2450AT43F0100 from Johanson Technology Ltd, were used to feed the RX STMA. The PCB is standard 1.6 mm thick FR4, measuring 39 cm x 30 cm. The antenna spacing is 45 mm, with TMA control waveforms designed to suit this element spacing.

Based on device data sheets, the expected STMA cell conversion gain (F_c RF input to $IF2$ out, including AD8009 combiner circuit of Fig. 5) is 6.0 dB. The expected ideal ACG for eight elements is 15 dB. The STMA control waveforms are designed using the techniques of [34] for a sidelobe level of -20 dB, using Dolph-Chebyshev weightings.



FIGURE 12. Built PCB showing 8 STMA RX cells (antennas and test connector for cell calibration visible at top, $IF2$ output and LO input connectors towards bottom).

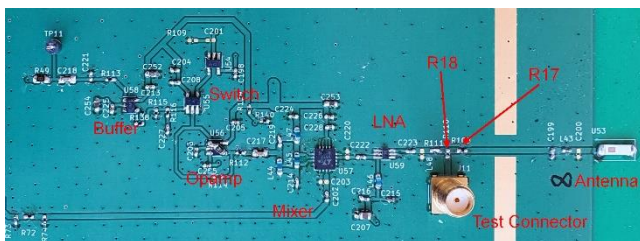


FIGURE 13. Detail of built PCB showing 1 of the 8 STMA RX cells with antenna, RF test connector used for calibration and key circuit functional blocks marked.

The timing control signals were created in matlab and loaded into an Intel EK-10M50F484 FPGA development board which was then plugged directly into the back of the STMA RF PCB to sequence it. The fully built STMA PCB is shown in Fig. 12 and the detail for one STMA cell and associated RF down converting front end is shown in Fig. 13.

A. HARDWARE PLATFORM VERIFICATION

The conducted gain, from the cell antenna test port connector, was measured by lifting the antenna link resistor R17 and fitting R18 and feeding in RF F_c signals. The $IF2$ output was measured for each cell in turn when operating only in T_s mode with no TMA pattern loaded, with results shown in Table 2. From Table 2, the T_s mode average conversion gain was measured to be 8.4 dB, which compares well to the theoretical line-up value of 6.0 dB based on data sheet nominal values. After including estimates of PCB routing losses and the gain of the ceramic antenna, the overall 8 element radiated ACG is expected to be 13.0 dBi as measured at $IF2$ combined output. The average measured 1 dB input compression point (IP1dB) at F_c was -30 dBm, at the RF input test connectors.

TABLE 2. Lab measured STMA cell conversion gains when only in subsampling mode (no TMA pattern applied).

STMA cell	Conversion gain in subsampling mode (dB)
1	8.2
2	10.3
3	8.8
4	6.1
5	8.0
6	8.9
7	8.5
8	8.4

The operation of the sampler circuit was also investigated. An example captured waveform of the voltage across C22 from one of the cells is shown in Fig. 14, for a sinusoidal $IF2$ frequency of 4.5 MHz and F_s of 20 MHz.

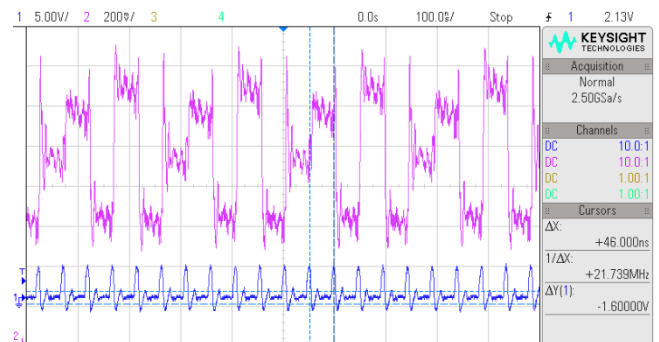


FIGURE 14. Example time domain capture of sampler waveform when processing a signal at $IF1$ (upper trace showing voltage on C22 and lower trace showing T_s sample event).

The general expected operation of the sampler can be seen, with the sampled signal changing to a new value at each sampling instant, though also with other artefacts visible.

The time domain operation was further investigated, with a zoom in view of 3 sampling events shown in Fig. 15. The peak in the centre of the plot has a rise time is 17 ns from the previously ‘held’ value and so the hold time appears to be 33 ns in the 50 ns sample period. Though this may seem worse than the circa 8-12 ns switchover latency expected from section II, note that the sampled signal is sinusoidal so will not be a steady value during the finite and non-zero period the sampling switch is on. The longer slope effect is also suspected to be due to non-ideal switching within the ADG702. However, in Fig. 14 and Fig. 15 the sampler is seen to be holding the value once charged and the switch turned off. Hence, the circuit is an acceptable approximation of a sampler for the purposes of the STMA demonstrator, though it does affect overall performance as is seen later.

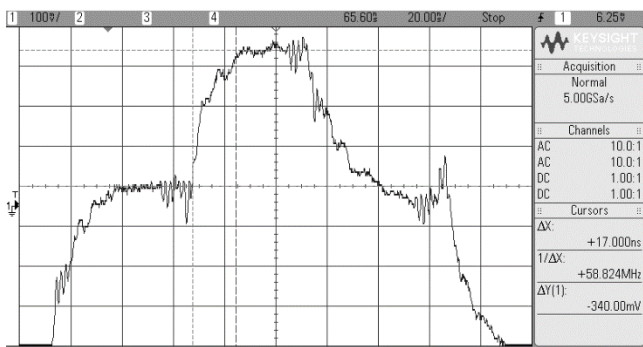


FIGURE 15. Example time domain capture of 3 cycles of T_s sampler capacitor C_{22} voltage, showing 17 ns rise and 33 ns hold times in a 50 ns sampling interval.

The non-ideal time domain nature of the sampled waveform is clear. However, an example of the spectrum seen at the IF_2 combined output when receiving a radiated signal at F_c with TMA mode disabled and subsampling is shown in Fig. 16.

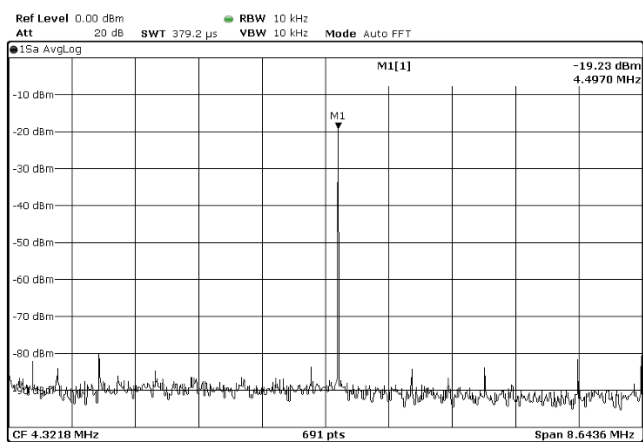


FIGURE 16. Output spectrum showing IF_2 centred at 4.5 MHz for an F_c radiated test signal at 0 degrees (TMA mode disabled).

The signal was captured using a Rohde & Schwarz FSV40-N Spectrum Analyser and suggests that the subsampler, though not using ideal waveforms, is functional, usable and gives a good signal at IF_2 .

When the TMA mode is enabled, the output spectrum at IF_2 contains additional components, but the desired output is still present, centered at 4.5 MHz for the C_0 beam, along with expected components at C_{1p} , C_{1n} , C_{2p} , C_{2n} , etc, as shown in Fig. 17. Harmonics of F_p are also seen to be present. Care must be taken in selecting the IF frequencies and switching frequencies to ensure images and spurious clock harmonics do not land on the desired beam IFs. Fig. 18 shows the output at IF_2 when no signal is being received (only noise and internally generated F_p switching harmonics are seen).

The Signal to Noise and Distortion Ratio (SNDR) was measured at the IF output of the STMA with an input signal at IP1dB. In sampling mode, the SNDR was measured to be 61 dB for a single cell (10 kHz measurement BW). The SNDR for the full array operating in STMA mode and processing a radiated RX signal was measured to be 69 dB. This improvement in SNDR due to TMA array operation has also been observed and predicted by others [46].

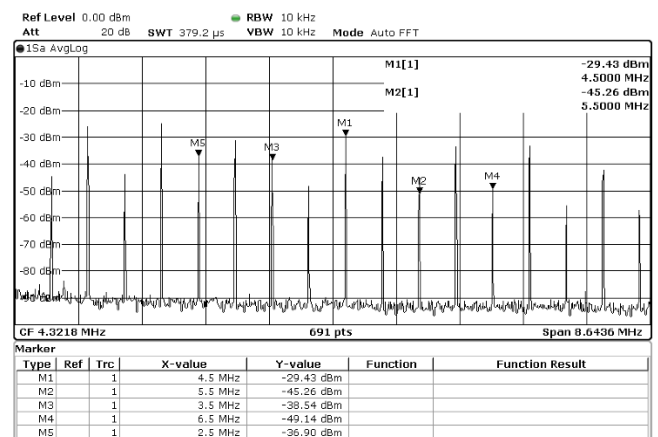


FIGURE 17. IF_2 output with C_0 centred at 4.5 MHz, for an F_c radiated test signal at 0 degrees (TMA mode activated, C_{1p} steered to +15 degrees).

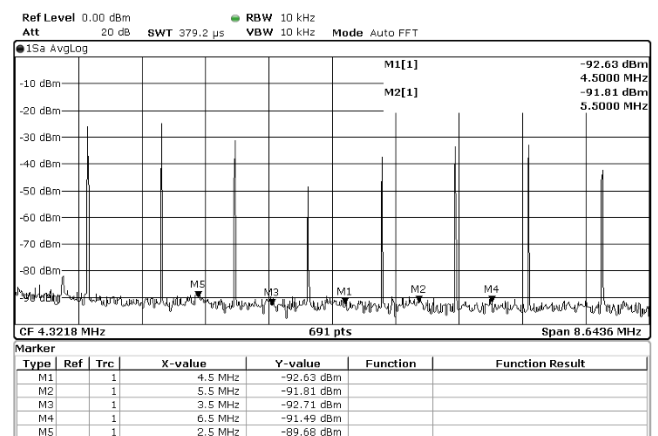


FIGURE 18. IF_2 output with C_0 centred at 4.5 MHz, RF radiated source beam off, C_{1p} steered to +15 degrees (only RF noise and spurious clock signals present).

The mutual coupling between adjacent antennas was measured to be -13 dB. Between second adjacent antennas the mutual coupling was -20 dB. However, improvements to mutual coupling may be possible with a patch array.

IV. CHAMBER ARRAY CONVERSION GAIN & PATTERN MEASUREMENTS

The STMA system was evaluated in The University of Sheffield's Communication Research Group's anechoic chamber. Prior to testing, the chamber background noise level in the band was checked and found to be sufficiently low to not cause interference. The measurement system included a Rohde & Schwarz FSV40-N Spectrum Analyser and AEL H-1498 measurement horn antenna with gain of 6 dBi at 2.4 GHz. The LO signal generator for the down conversion mixers was a Keysight E4436B set to 2.24 GHz. The RF signal generator providing the wanted radiated RF signal at F_c to receive was a Keysight E4437B set to 2.4245GHz. The STMA test system setup is shown in Fig. 19(a) and the STMA PCB being tested is shown in Fig. 19(b). The test horn antennas are on an arch that allows them to be positioned as required and the STMA PCB is in the centre of the axis of rotation. The $IF2$ output signals were measured using the Rohde & Schwarz FSV40-N spectrum analyser with 10 kHz resolution BW.

Radiated STMA ACGs are calculated and then reported in dBi, from the signals resolved at the subsampled $IF2$ centred on 4.5 MHz for $C0$. The measured RF powers were converted to STMA ACGs from knowledge of the applied TX RF power, test horn antenna gains, distance between test horn antenna and STMA PCB (converted to an equivalent free space path loss) following the technique used in [34].

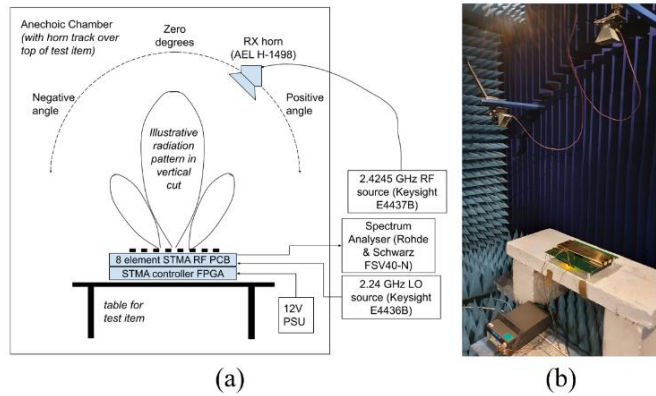


FIGURE 19. Laboratory radiated pattern measurement: (a) test system set-up, (b) example measurement.

A. STEERED FIRST HARMONIC BEAM ($C1p$, $C1n$)

The theoretically expected ACG is calculated based on the initial measured conducted conversion gain from section III and its resulting expected ACG of 13.0 dBi. However, this ideal ACG must now also include effects from the AF, the sampler low pass slope (i.e. $SGRF$) and pulse losses due to chosen harmonic (i.e. HLR), as described in section II. Thus, the overall expected radiated ACG as a function of harmonic beam and wavefront angle is found using (8), where $beam$ is the harmonic beam being

assessed ($n = -2$ for $C2n$, $n = -1$ for $C1n$, $n = 0$ for $C0$, $n = 1$ for $C1p$, $n = 2$ for $C2p$). $SGRF$ is zero for the $C0$ beam and HLR is only applied if $C2p$ or $C2n$ beams are being assessed.

$$ACG_{expected}(beam, \theta) = 13.0 + SGRF(beam) + HLR_{(only\ if\ C2p, C2n\ beam)} + 20 \log_{10}(AF(\theta, n)) \quad (8)$$

Tests were first performed with the STMA timings set to receive a radiated beam at +15 degrees on the $C1p$ harmonic, with results shown in Fig. 20 for the $C0$ beam and Fig. 21 for the $C1p$ beam, all compared to (8). The system was then configured to receive a $C1p$ beam at -15 degrees, with results show in Fig. 22, again compared to (8).

As discussed earlier, the sampler has an LPF response, and this means that the negative harmonic beams ($C1n$, $C2n$) have a higher $IF2$ output than the corresponding positive steered harmonic beams ($C1p$, $C2p$). This effect can be seen in Fig. 23 where the $C1n$ beam was steered to +15 degrees and shows a 3.5 dB higher gain than the $C1p$ beam steered to +15 degrees as seen in Fig. 21. This level difference agrees well with the 3.9 dB predicted for $C1p$ - $C1n$ level delta predicted in Table 1.

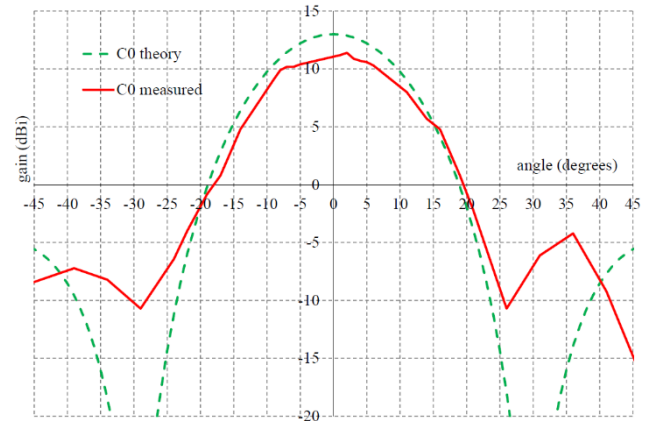


FIGURE 20. $C0$ beam ACG for $C1p$ steered to +15 degrees.

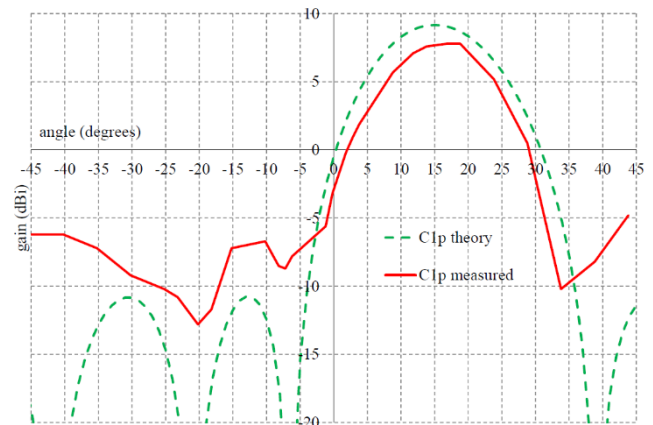


FIGURE 21. $C1p$ beam ACG for $C1p$ steered to +15 degrees.

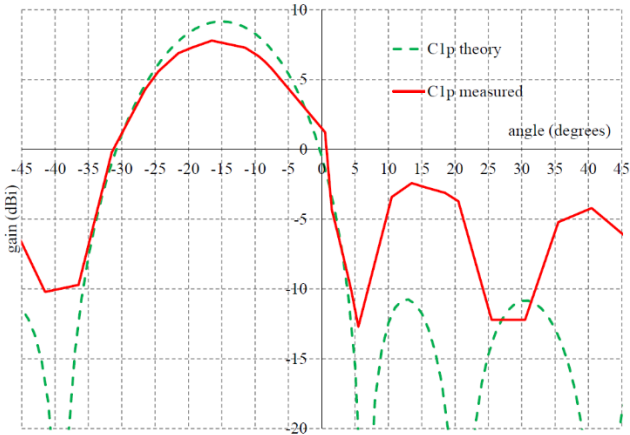


FIGURE 22. $C1p$ beam ACG for $C1p$ steered to -15 degrees.

Overall, for $C1p$ and $C1n$, the measured gain patterns for the main lobes agree well with theoretical expectation and show good conversion gain, though the sidelobe response is degraded compared to theoretical expectation.

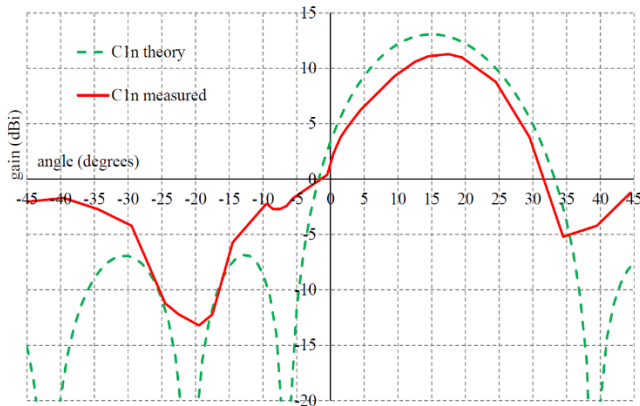


FIGURE 23. $C1n$ beam ACG for $C1n$ steered to $+15$ degrees.

B. STEERED SECOND HARMONIC BEAM ($C2p$, $C2n$)

Tests were then performed with the STMA timings set to receive a $C2p$ beam at $+25$ degrees, with results compared to (8) in Fig. 24 for the $C0$ beam and Fig. 25 for the $C2p$ beam.

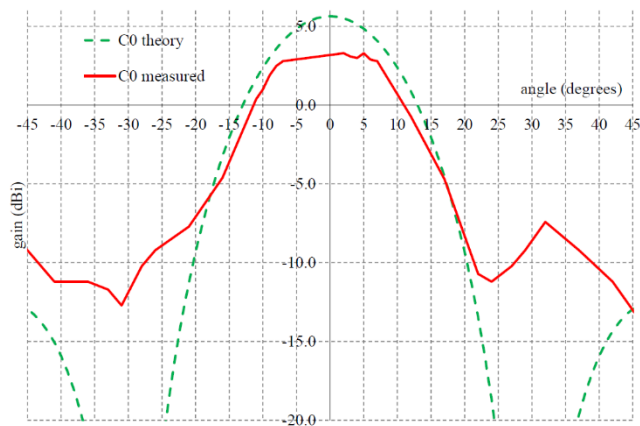


FIGURE 24. $C0$ beam ACG for $C2p$ steered to $+25$ degrees.

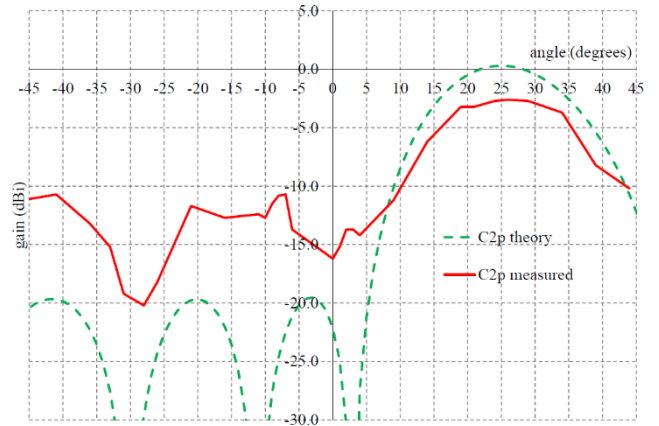


FIGURE 25. $C2p$ beam ACG for $C2p$ steered to $+25$ degrees.

The results for the $C2p$ beam steered to -25 degrees are shown in Fig. 26. The resulting gain when $C2n$ beam was steered to $+25$ degrees is shown in Fig. 27, showing a 7.9 dB higher gain is obtained compared to Fig. 25, due to the LPF response of the sampler as discussed earlier. This level difference agrees well with the 8.3 dB predicted for $C2p$ - $C2n$ level delta predicted in Table 1.

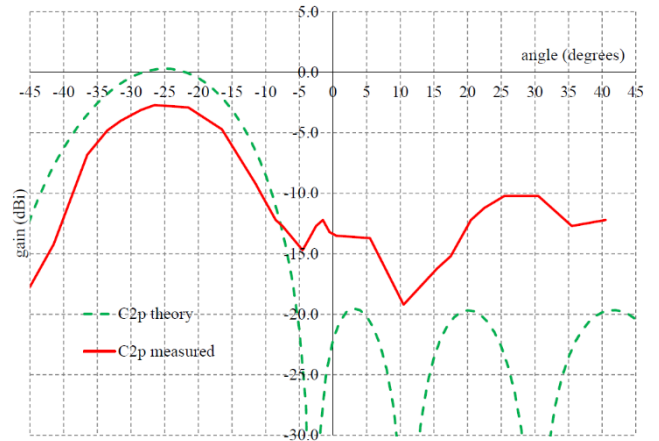


FIGURE 26. $C2p$ beam ACG for $C2p$ steered to -25 degrees.

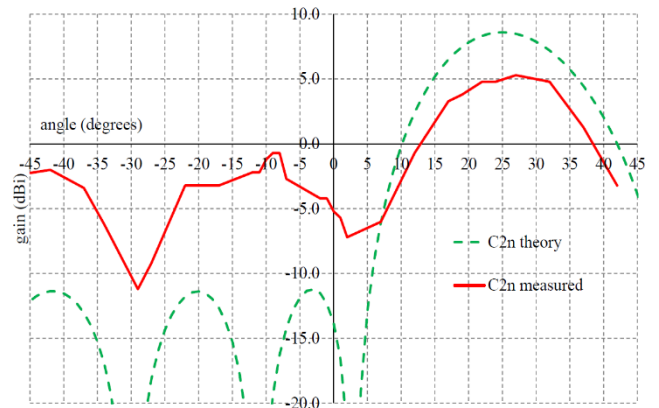


FIGURE 27. $C2n$ beam ACG for $C2n$ steered to $+25$ degrees.

Overall, for $C2p$ and $C2n$ RX beams, the measured gain patterns for the main lobes agree well with theoretical expectation and show usable ACG, particularly on the negative harmonic beams, though the sidelobe response is degraded compared to theoretical prediction.

V. DISCUSSION

Though the STMA is showing generally correct operation, analysis has been conducted to investigate possible reasons for the observed degradation in sidelobe performance. As an example, the observed sidelobe levels for the first harmonic beams are circa -10 dB to -15 dB, instead of the -20 dB as designed. From earlier, it is known that the ADG702 based sampler has a rise time of approximately 17 ns in a sampling period of 50 ns (i.e. 34 % of Tp). An investigation using techniques from [34] to investigate the dependency of sidelobe levels on rise time (Tr) and fall time (Tf) has shown that a 34 % Tr (with 0.1 % Tf) on a 1 MHz Fp leads to an increase in sidelobe levels to -12 dBc from a design target level of -20 dBc for the first harmonic sidelobes: similar to what was measured. From these same prediction simulations, a 2.5 % Tr would lead to a 1 dB reduction in sidelobe level performance from the design target. This shows that the performance of the sampler switch is very important in sidelobe control and is likely a significant contributor to the sidelobe results measured in the laboratory tests. It is also possible that the sidelobe degradation is affected by a smaller amount due to a) radiated leakage directly onto the PCB circuits from imperfect PCB screening enclosures and b) from the -13 dB to -20 dB measured mutual coupling between antenna elements.

However, the ability to steer the desired incoming RF receive beam at F_c and resolve it at the subsampled $IF2$ is demonstrated, validating the STMA technique and illustrating what can be achieved with imperfect hardware. Also, the main steered ACG lobe generally matches theoretical expectations well. The measured peak ACGs are 11.4 dBi for the $C0$ beam, 7.8 dBi for the $C1p$ beam, 11.3 dBi for the $C1n$ beam, -2.6 dBi for the $C2p$ beam and 5.3 dBi for the $C2n$ beam.

Achieved ACG is lower for second harmonic beams, as anticipated and also seen in other works [34], however is still useful. Also, as predicted, we note that negative harmonic beam ACGs are higher than positive harmonic beams, due to sampler circuit LPF response. This suggests that a practical system could benefit from using only the negative beams for steering, to minimise the impact of the SGRF. Alternatively, the $C0$ beam also gives good ACG and sidelobe performance and so could be used for a non-steerable STMA array.

One potential issue seen is the presence of the Fp harmonics in the output $IF2$ spectrum, requiring careful frequency planning to avoid them corrupting the wanted signals. The Fp harmonic components are due to the periodic switching of the $IF1$ signal which has a background DC component. It may be possible to reduce the magnitude of the Fp harmonics seen by use of differential switching techniques in the sampler, though this would increase complexity.

Cracking and subsequent failing of some ceramic capacitors in the RF signal chain was also experienced during tests and required occasional replacements. This failure mechanism is a well-known issue in industry and care was taken during tests to ensure results were always obtained from a fully functional system.

Overall, we propose that the STMA is a novel enhancement of a TMA, that could help reduce the hardware complexity of a conventional phased array receiver system by allowing the removal of a mixer stage prior to the ADC. Such a mixer stage would often usually be required to create an IF signal within the ADC passband. The use of the STMA concept also allows reduction of the ADC sample rate otherwise needed to directly digitise from a high IF (in the first Nyquist band), if subsampling of the ADC input had not been used. Our practical work verifies the expected operation of the STMA.

In our demonstration system we were forced to use down conversion mixers prior to the STMA cells, due to RF BW limitations of the sampler switch. If a switch was available that could pass carrier signals at F_c and switch at the desired F_s , then this mixer stage would not have been required. However, the strategy of a mixer-first STMA could be useful for mmWave systems, where suitable sampler switches are not yet viable but a phased array is needed.

Table 3 compares the performance of the STMA concept demonstrator to relevant published works in receiver DBFs and ABFs, operating with carriers below 6 GHz. Parameters compared include array Side Lobe Level (SLL), Effective Number of Control Bits (ENCB) and input 1 dB compression point (IP1dB). Although our demonstration system is primarily intended to illustrate the STMA concept (using commercially available generic components with associated power efficiency issues), it is still clear from Table 3 that the STMA performance for gain, SLL and SNDR is competitive. The low RF BW is due to FPGA maximum clocking frequency issues and the number of TMA pattern words used. This could be improved with different baseband hardware.

The simple (1 bit per cell) control interface and low IF output are key advantages. The STMA is the only work considered that has a low frequency IF output (4.5 MHz) from a high carrier frequency, which significantly simplifies the requirements for subsequent digitization.

The nearest conceptual work to ours is [54] but this does not subsample, so the down conversion is due to the switching harmonics. The harmonics in [54] will rapidly reduce in magnitude as they extend further from the carrier and so requires extremely high clocking rates to obtain a resultant low IF using only the first or second harmonic. Subsampling does not suffer from this effect.

TABLE 3. Comparison of STMA systems to prior works at sub 6 GHz.

	[55]	[56]	[54]	This work
Technique	IF sampling DBF	Time delay DBF	Microwave sampling	STMA
Carrier (MHz)	260	1000	5800	2420
RF BW (MHz)	20	100	6.49	1
Elements	8	16	4	8
ACG (dBi)	-	-	-	13
Cell Conversion Gain (dB)	-	-	Loss (due to pin diodes)	8.4
Cell IP1dB (dBm)	-	-	-	-30
SLL (dB)	-14 (single beam)	-13 (-30 degree steer)	-15.5 (SLL & scanning control)	-15 (C0) -10 .. -15 (C1p, C1n)
Sampler Clock	1040 MHz	4 GHz	6.49 MHz	20 MHz F_s , 1 MHz F_p (120 MHz FPGA)
Array SNDR (dB)	63.3	60	-	69 (10 kHz BW)
Array output	Digital	Digital	IF, 5.79351 GHz (1st lower harmonic)	IF, 4.5 MHz
Max. scan angle reported (degrees)	60	90	-50	+/- 15 (C1p) +/- 25 (C2p)
DC power	124mW (65 nm CMOS)	453 mW (40 nm CMOS)	8 – 14 mA per diode	978 mW / cell
Phase Resolution	240 steps using 12 bits (7.9 ENCB)	1 degree (10 bits)	1.4 degrees (8 bits)	6.9 ENCB (FPGA timing)
Amplitude Resolution	-	-	12 bits	6.9 ENCB (FPGA timing)

A. COST AND POWER CONSIDERATIONS

We will now consider the STMA cost and power, compared to an ABF in example beamformer implementations. As a first example, consider a 2.4 GHz phased array ABF with cell as shown in Fig. 28 and compare this to the STMA optimal approach (no initial down conversion mixer) of Fig. 2. For the sake of the illustration, we will ignore the upper frequency limits of the ADG702 switch and so assume the initial mixer of Fig. 3 is not required. The cost and power consumption for each commercial part used in the prototype 2.4 GHz system and their applicability to either the ABF or STMA are listed in Table 4, with a possible VGA and phase shifter.

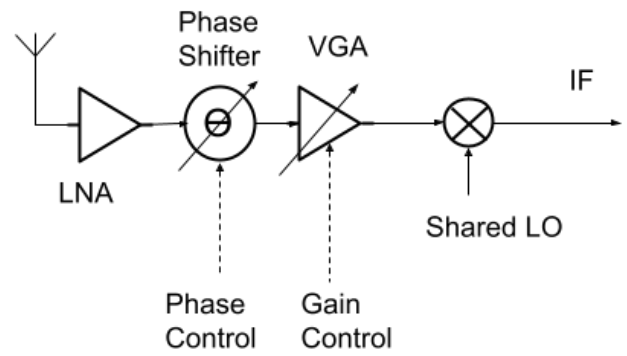


FIGURE 28. Conventional ABF cell (combination of cells can be before or after mixer).

TABLE 4. Cost and power model examples at 2.4 GHz using commercial parts (costings are based on current manufacturers' pricing for 500 off).

Function	Example part	Usage	Item cost (USD, 500 off)	Item power (mW)
LNA	HMC374	ABF + STMA	3.66	247.5
Phase Shifter	HMC647A (6 bits)	ABF	84.5	75
VGA	HMC742A (6 bits)	ABF	13.75	650
Mixer	LT5527	ABF	8.51	390
Buffer	AD8009	STMA	2.45	70
Sampler	ADG702	STMA	1.21	0.005
Buffer	BUF602	STMA	0.936	270

From Table 4, one cell of the ABF would consume 1021 mW and cost 103 USD. This assumes signal combination from all the cell branches occurs at the 2.4 GHz carrier and so only one down conversion mixer is required. In comparison, a single cell of the STMA would require 587 mW and cost 8.3 USD, representing a saving of 95 USD (92 %) and 434 mW (43 %) compared to the conventional ABF example. Though crude, the above example shows cost and power savings for a given semiconductor technology can be expected when using the STMA approach. It is also worth noting that the example phase shifter and VGA parts require 12 control bits in total, compared to the single digital bit for the STMA.

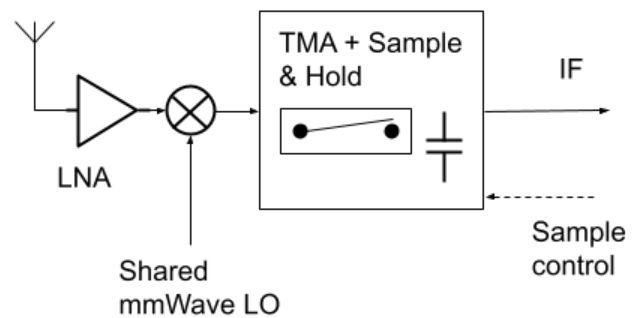


FIGURE 29. Prototype mmWave STMA cell with mixer-first down conversion to intermediate IF due to limited switch RF BW.

We now go on to consider the potential advantage of using the STMA at 28 GHz using recent published works to help illustrate. To realize a conventional ABF at 28 GHz would require a suitable phase shifter, for example [39] which requires 6 control bits, is passive and requires 0.53 mm² of wafer material. A VGA is also required, such as [40] which requires analogue control lines, draws 23 mW and consumes 0.103 mm² of wafer die. Alternatively, a combined phase shifter and VGA, such as [57] requiring both analog control and 6 digital bits whilst drawing 23 mW could be considered. In contrast, the STMA would likely require a mmWave to microwave down converting mixer, such as [58] requiring 6.4 mW and 0.52 mm² of die, which could be followed by a suitable ‘cold-FET’ zero-bias switch to implement the STMA sampler function, as illustrated in Fig. 29. If such a sampler switch were available and capable of sufficient switching speed, then a power saving of circa 16.6 mW (72 %) and area saving of circa 18 % could be obtained, (ignoring issues relating to wafer material differences). It would be more cost effective to have the sample-hold capacitor off-chip due to its large physical area. Power efficiency savings are increasingly important for large arrays, which are required for mmWave systems.

If the STMA mixer-first approach were not required for mmWave operation, then the wafer savings and DC power savings would be significantly greater, perhaps requiring only a few square microns of semiconductor material for the sampling switch and an off-chip sample-hold capacitor. However, significant research work is now needed in creating fast switches for use in a STMA, possibly via tail current switched amplifiers [46].

The STMA single digital control line to control the down conversion and beam steering is an important advantage. As illustrated above, conventional beamformers require multiple control lines for the phase shifter and VGA. For large arrays, arranging and routing sufficient control lines can be difficult.

VI. CONCLUSION

An STMA system which directly incorporates subsampling within a receive TMA is discussed and demonstrated. The system shows STMA receive array beams can be steered at the carrier F_c and resolved at the subsampled IF2, as predicted.

The concept could be applied to any frequency band, though the design of the sampling switch is a critical feature which dictates the maximum design frequencies and sidelobe performance. The STMA concept could be applied to carriers above the BW of the sampling switch by use of a simple down conversion mixer stage before the STMA cell, as demonstrated in our work. Such concepts could allow a pragmatic application of the STMA to mmWave or higher bands.

Potential power and cost savings for the STMA are presented using examples. The STMA concepts could also be applied to a TX system, with appropriate modifications to use the up-sampled Nyquist images from a DAC or similar.

ACKNOWLEDGMENT

This research was funded by UKRI, grant number MR/T043164/1. For the purpose of open access, the authors have applied a Creative Commons Attribution (CC BY) licence to any Author Accepted Manuscript version arising.

REFERENCES

- [1] Casetti, “The challenges of universal broadband connectivity [Mobile Radio],” *IEEE Vehicular Technology Magazine*, vol. 17, no. 3, pp. 5–11, Aug. 2022. DOI: 10.1109/mvt.2022.3176414.
- [2] W. Hong *et al.*, “The role of millimeter-wave technologies in 5G/6G wireless communications,” *IEEE Journal of Microwaves*, vol. 1, no. 1, pp. 101–122, Jan. 2021. DOI: 10.1109/jmw.2020.3035541.
- [3] R. Chataut and R. Akl, “Massive MIMO systems for 5G and beyond networks—overview, recent trends, challenges, and future research direction,” *Sensors*, vol. 20, no. 10, May 2020. DOI: 10.3390/s20102753.
- [4] W. H. Kummer, A. T. Villeneuve, T. S. Fong, and F. G. Terrio, “Ultra-low sidelobes from time-modulated arrays,” *IEEE Trans. Antennas Propag.*, vol. 11, no. 6, pp. 633–639, Nov. 1963. DOI: 10.1109/TAP.1963.1138102.
- [5] Y. Tong and A. Tennant, “Simultaneous control of sidelobe level and harmonic beam steering in time-modulated linear arrays,” *Electronics Lett.*, vol. 46, no. 3, pp. 200–202, Feb. 2010. DOI: 10.1049/el.2010.2629.
- [6] W. Q. Wang, H. C. So, and A. Farina, “An overview on time/frequency modulated array processing,” *IEEE Journal on Selected Topics in Signal Processing*, vol. 11, no. 2, pp. 228–246, Mar. 2017. DOI: 10.1109/JSTSP.2016.2627182.
- [7] G. Li, S. Yang, Y. Chen, and Z. Nie, “A novel beam scanning technique in time modulated linear arrays,” in *IEEE Antennas and Propagation Society, AP-S International Symposium (Digest)*, North Charleston, SC, USA, 2009, pp. 1–4. DOI: 10.1109/APS.2009.5171609.
- [8] P. Rocca, G. Oliveri, R. J. Mailloux, and A. Massa, “Unconventional phased array architectures and design methodologies - a review,” *Proceedings of the IEEE*, vol. 104, no. 3, pp. 544–560, Mar. 2016. DOI: 10.1109/JPROC.2015.2512389.
- [9] Y. Tong and A. Tennant, “A two-channel time modulated linear array with adaptive beamforming,” *IEEE Trans. Antennas Propag.*, vol. 60, no. 1, pp. 141–147, Jan. 2012. DOI: 10.1109/TAP.2011.2167936.
- [10] T. E. Bekele *et al.*, “Advances on time-modulated arrays for cognitive radio,” in *7th European Conference on Antennas and Propagation (EUCAP 2013)*, Gothenburg, Sweden, 2013, pp. 344–346.
- [11] L. Poli, P. Rocca, G. Oliveri, and A. Massa, “Harmonic beamforming in time-modulated linear arrays,” *IEEE Trans. Antennas Propag.*, vol. 59, no. 7, pp. 2538–2545, Jul. 2011. DOI: 10.1109/TAP.2011.2152323.
- [12] R. Maneiro-Catoira, J. C. Brégaïns, J. A. García-Naya, L. Castedo, P. Rocca, and L. Poli, “Performance analysis of time-modulated arrays for the angle diversity reception of digital linear modulated signals,” *IEEE Journal on Selected Topics in Signal Processing*, vol. 11, no. 2, pp. 247–258, Mar. 2017. DOI: 10.1109/JSTSP.2016.2609852.
- [13] M. H. Mazaheri, M. Fakharzadeh, M. Akbari, and S. Safavi-Naeini, “A time modulated array with polarization diversity capability,” *IEEE Access*, vol. 9, pp. 53735–53744, 2021. DOI: 10.1109/ACCESS.2021.3070492.
- [14] W. C. Barott and S. Fucharoen, “Experimental time-modulated beamformer for interference mitigation in a radio spectrometer,” *IEEE Journal on Selected Topics in Signal Processing*, vol. 11, no. 2, pp. 271–281, Mar. 2017. DOI: 10.1109/JSTSP.2016.2615268.
- [15] L. Poli, P. Rocca, G. Oliveri, and A. Massa, “Adaptive nulling in time-modulated linear arrays with minimum power losses,” *IET Microwaves, Antennas and Propagation*, vol. 5, no. 2, pp. 157–166, Jan. 2011. DOI: 10.1049/iet-map.2010.0015.
- [16] G. Bogdan, M. Jarzynka, and Y. Yashchysyn, “Experimental study of signal reception by means of time-modulated antenna array,” in *21st International Conference on Microwave, Radar and Wireless Communications (MIKON 2016)*, Krakow, Poland, 2016, pp. 1–4. DOI: 10.1109/MIKON.2016.7492030.
- [17] G. Bogdan, Y. Yashchysyn, and M. Jarzynka, “Time-modulated antenna array with lossless switching network,” *IEEE Antennas & Wire. Propag. Lett.*, vol. 15, pp. 1827–1830, March 2016. DOI: 10.1109/LAWP.2016.2538463.
- [18] J. Chen, R. Jin, H. Fan, J. Geng, X. Liang, and C. He, “Wideband direction-finding based on time-modulated antenna array,” in *Asia-*

- Pacific Conference on Antennas and Propagation (APCAP)*, Bali, Indonesia, 2015, pp. 48–49. DOI: 10.1109/APCAP.2015.7374266.
- [19] A. O'Donnell, W. Clark, J. Ernst, and R. McGwier, "Analysis of modulated signals for direction finding using time modulated arrays," in *2016 IEEE Radar Conference (RadarConf)*, Philadelphia, PA, USA, 2016, pp. 1–5. DOI: 10.1109/RADAR.2016.7485111.
- [20] Ni, S. Yang, Y. Chen, and J. Guo, "A Study on the application of subarrayed time-modulated arrays to MIMO radar," *IEEE Antennas & Wire. Propag. Lett.*, vol. 16, pp. 1171–1174, Nov. 2016. DOI: 10.1109/LAWP.2016.2626478.
- [21] Li, S. Yang, and Z. Nie, "A study on the application of time modulated antenna arrays to airborne pulsed Doppler radar," *IEEE Trans. Antennas Propag.*, vol. 57, no. 5, pp. 1579–1583, May 2009. DOI: 10.1109/TAP.2009.2016788.
- [22] J. Euziere, R. Guinvarc'H, M. Lesturgie, B. Uguen, and R. Gillard, "Dual function radar communication time-modulated array," in *2014 International Radar Conference*, Lille, France, 2014, pp. 1-4. DOI: 10.1109/RADAR.2014.7060416.
- [23] J. Euziere, R. Guinvarc'H, I. Hinostrroza, B. Uguen, and R. Gillard, "Time modulated array for dual function radar and communication," in *2015 IEEE International Symposium on Antennas and Propagation & USNC/URSI National Radio Science Meeting*, Vancouver, BC, Canada, 2015, pp. 806–807. DOI: 10.1109/APS.2015.7304790.
- [24] J. Euziere, R. Guinvarc'H, I. Hinostrroza, B. Uguen, and R. Gillard, "Optimizing communication in TMA for radar," in *2016 IEEE Antennas and Propagation Society International Symposium, APSURSI 2016 - Proceedings*, Fajardo, PR, USA, 2016, pp. 705–706. DOI: 10.1109/APS.2016.7696061.
- [25] C. Shan, J. Shi, Y. Ma, X. Sha, Y. Liu, and H. Zhao, "Power loss suppression for time-modulated arrays in radar-communication integration," *IEEE Journal on Selected Topics in Signal Processing*, vol. 15, no. 6, pp. 1365–1377, Nov. 2021. DOI: 10.1109/JSTSP.2021.3118896.
- [26] Y. Wang and A. Tennant, "Experimental time-modulated reflector array," *IEEE Trans. Antennas & Propag.*, vol. 62, no. 12, pp. 6533–6536, Dec. 2014. DOI: 10.1109/TAP.2014.2362129.
- [27] X. Cao, Q. Chen, T. Tanaka, M. Kozai, and H. Minami, "A 1-bit time-modulated reflectarray for reconfigurable intelligent surface applications," *IEEE Trans. Antennas & Propag.*, Mar. 2023. DOI: 10.1109/TAP.2022.3233659.
- [28] A. Reyna, L. I. Balderas, and M. A. Panduro, "Time-modulated antenna arrays for circularly polarized shaped beam patterns," *IEEE Antennas & Wire. Propag. Lett.*, vol. 16, pp. 1537–1540, 2017. DOI: 10.1109/LAWP.2017.2647900.
- [29] Bogdan, P. Bajurko, and Y. Yashchyshyn, "Time-modulated antenna array with dual-circular polarization," *IEEE Antennas & Wire. Propag. Lett.*, vol. 19, no. 11, pp. 1872–1875, Nov. 2020. DOI: 10.1109/LAWP.2020.2999643.
- [30] Tennant and B. Allen, "Generation of OAM radio waves using circular time-switched array antenna," *Electronic Lett.*, vol. 48, no. 21, pp. 1365–1366, Oct. 2012. DOI: 10.1049/el.2012.2664.
- [31] Bogdan, K. Godziszewski, and Y. Yashchyshyn, "Time-modulated antenna array for real-time adaptation in wideband wireless systems-part II: adaptation study," *IEEE Trans. Antennas & Propag.*, vol. 68, no. 10, pp. 6973–6981, Oct. 2020. DOI: 10.1109/TAP.2020.3008633.
- [32] Q. Chen, J. D. Zhang, W. Wu, and D. G. Fang, "Enhanced single-sideband time-modulated phased array with lower sideband level and loss," *IEEE Trans. Antennas & Propag.*, vol. 68, no. 1, pp. 275–286, Jan. 2020. DOI: 10.1109/TAP.2019.2938711.
- [33] Y. Ma, C. Miao, Y. H. Li, and W. Wu, "Harmonic beamforming based on modified single-sideband time modulated phased array and its enhanced version," *IEEE Access*, vol. 9, pp. 57819–57828, 2021. DOI: 10.1109/ACCESS.2021.3072777.
- [34] E. A. Ball and A. Tennant, "A technique to control the harmonic levels in time-modulated antenna arrays - theoretical concept and hardware verification platform," *IEEE Trans. Antennas & Propag.*, vol. 68, no. 7, pp. 5375–5386, Jul. 2020. DOI: 10.1109/TAP.2020.2978894.
- [35] X. Lu, S. Venkatesh, B. Tang, and K. Sengupta, "Space-time modulated 71-to-76GHz mm-wave transmitter array for physically secure directional wireless links," in *2020 IEEE International Solid-State Circuits Conference - (ISSCC)*, San Francisco, USA, 2020, pp. 86–88. DOI: 10.1109/ISSCC19947.2020.9062929.
- [36] O. Gassab, A. Azrar, A. Dahimene, and S. Bouguerra, "Efficient mathematical method to suppress sidelobes and sidebands in time-modulated linear arrays," *IEEE Antennas & Wire. Propag. Lett.*, vol. 18, no. 5, pp. 836–840, May 2019. DOI: 10.1109/LAWP.2019.2903200.
- [37] G. Bogdan, K. Godziszewski, and Y. Yashchyshyn, "Time-modulated antenna array with beam-steering for low-power wide-area network receivers," *IEEE Antennas & Wire. Propag. Lett.*, vol. 19, no. 11, pp. 1876–1880, Nov. 2020. DOI: 10.1109/LAWP.2020.3007925.
- [38] N. Singhal and S. M. R. Hasan, "Review and comparison of different limited scan phased array antenna architectures," *International Journal of Circuit Theory and Applications*, vol. 49, no. 10, pp. 3111–3130, Oct. 2021. DOI: 10.1002/cta.3118.
- [39] M. Wang, F. Ullah, X. Wang, Y. Xiao, and Y. Liu, "A 25-31 GHz 6-bit switch-type phase shifter in 0.13um SOI CMOS process for 5G mmWave phased array communications," in *2018 14th IEEE International Conference on Solid-State and Integrated Circuit Technology (ICSICT)*, Qingdao, China, 2018, pp. 1–3. DOI: 10.1109/ICSICT.2018.8565766.
- [40] Park and S. Hong, "Wideband bidirectional variable gain amplifier for 5G communication," *IEEE Microwave and Wireless Technology Letters*, vol. 33, no. 6, pp. 691–694, Feb. 2023. DOI: 10.1109/lmwt.2023.3244715.
- [41] P. Guan et al., "A 33.5–37.5 GHz four-element phased-array transceiver front-end with hybrid architecture phase shifters and gain controllers," *IEEE Trans. Microwave Theory Tech.*, 2023. DOI: 10.1109/TMTT.2023.3248175.
- [42] C.-N. Chen et al., "36–40 GHz Tx/Rx beamformers for 5G mm-wave phased-array," in *2018 Asia-Pacific Microwave Conference (APMC)*, Kyoto, Japan, 2018, pp. 756–758. DOI: 10.23919/APMC.2018.8617146.
- [43] W. Lv et al., "A 24–27GHz phased array transceiver with 6 bit phase shifter and 31.5dB gain control for 5G communication in 65nm CMOS," in *Proceedings of 2020 IEEE International Conference on Integrated Circuits, Technologies and Applications, ICTA 2020*, Nanjing, China, 2020, pp. 23–24. DOI: 10.1109/ICTA50426.2020.9331999.
- [44] T. Kanar, S. Zehir, and N. Yanduru, "Ultra-compact and modular 5G phased-array 4-channel beamformer front-ends with $\lt;2^\circ$ RMS phase error," in *2018 IEEE/MTT-S International Microwave Symposium - IMS*, Philadelphia, USA, 2018, pp. 1327–1329. DOI: 10.1109/MWSYM.2018.8439596.
- [45] R. Lu, C. Weston, D. Weyer, F. Buhler, D. Lambalot, and M. P. Flynn, "A 16-element fully integrated 28-GHz digital RX beamforming receiver," *IEEE Journal Solid-State Circuits*, vol. 56, no. 5, pp. 1374–1386, May 2021. DOI: 10.1109/JSSC.2021.3067504.
- [46] T.-Y. Huang, B. Lin, N. S. Mannem, B. Abdelaziz, and H. Wang, "A time-modulated concurrent steerable multibeam MIMO receiver array with spectral-spatial mapping using one beamformer and single-wire interface," *IEEE Journal Solid-State Circuits*, vol. 58, no. 5, pp. 1–13, Mar. 2023. DOI: 10.1109/jssc.2023.3253793.
- [47] E. C. Ifeachor and B. W. Jervis, *Digital Signal Processing - A Practical Approach*. Boston, USA: Addison-Wesley Ltd., 1997.
- [48] G. Wade, *Signal Coding and Processing*. Cambridge, UK: Cambridge University Press, 1994.
- [49] Analog Devices Ltd., "ADG702 datasheet," Accessed: Apr. 30, 2023. [Online]. Available: <https://www.analog.com/en/products/adg702.html>
- [50] Analog Devices Ltd., "HMC374SC70E datasheet," Accessed: Apr. 30, 2023. [Online]. Available: <https://www.analog.com/en/products/hmc374sc70e.html>
- [51] Analog Devices Ltd., "LT5527 datasheet," Accessed: Apr. 30, 2023. [Online]. Available: <https://www.analog.com/en/products/lt5527.html>
- [52] Analog Devices Ltd., "AD8009 datasheet," Accessed: Apr. 30, 2023. [Online]. Available: <https://www.analog.com/en/products/ad8009.html>
- [53] Texas Instruments Ltd., "BUF602 datasheet," Accessed: Apr. 30, 2023. [Online]. Available: <https://www.ti.com/product/BUF602>.
- [54] S. Farzaneh and A. R. Sebak, "Microwave sampling beamformer - prototype verification and switch design," *IEEE Trans. Microwave Theory Tech.*, vol. 57, no. 1, pp. 36–44, Jan. 2009. DOI: 10.1109/TMTT.2008.2009080.
- [55] Jeong, N. Collins, and M. P. Flynn, "A 260 MHz IF sampling bit-stream processing digital beamformer with an integrated array of continuous-time band-pass $\Delta\Sigma$ modulators," *IEEE Journal Solid-State Circuits*, vol. 51, no. 5, pp. 1168–1176, May 2016. DOI: 10.1109/JSSC.2015.2506645.
- [56] S. Jang, R. Lu, J. Jeong, and M. P. Flynn, "A 1-GHz 16-element four-beam true-time-delay digital beamformer," *IEEE Journal Solid-State Circuits*, vol. 54, no. 5, pp. 1304–1314, May 2019. DOI: 10.1109/JSSC.2019.2894357.

- [57] Zhang, Y. Shen, L. De Vreede, and M. Babaie, "A 23.8-30.4-GHz vector-modulated phase shifter with two-stage current-reused variable-gain amplifiers achieving 0.23° minimum RMS phase error," *IEEE Solid State Circuits Letters*, vol. 5, pp. 150–153, June 2022. DOI: 10.1109/LSSC.2022.3179661.
- [58] Y. T. Chang and K. Y. Lin, "A 28-GHz bidirectional active gilbert-cell mixer in 90-nm CMOS," *IEEE Microwave and Wireless Components Letters*, vol. 31, no. 5, pp. 473–476, May 2021. DOI: 10.1109/LMWC.2021.3061658.



EDWARD A. BALL (Member, IEEE) was born in Blackpool, U.K., in November 1973. He received the Master of Engineering degree (First Class) in electronic systems engineering from the University of York, York, U.K., in 1996.

After graduating, he worked in industry for 20 years, first spending 15 years working as an Engineer, a Senior RF Engineer, and finally a Principal RF Engineer with Cambridge Consultants Ltd., Cambridge, U.K. He then spent five years as a Principal RF Engineer and a Radio Systems Architect with Tunstall Healthcare Ltd., Whitley, U.K. He joined the Department of Electronic and Electrical Engineering, University of Sheffield, Sheffield, U.K., in November 2015, where he currently works as a Reader of RF Engineering. His research interests cover all areas of radio technology, from RF system design, RF circuit design (sub-GHz to mmWave), and the application of radio technology to real-world industrial and commercial problems. He has a particular passion for RF hardware design.

Mr. Ball is a member of IET and a Chartered Engineer.



SUMIN DAVID JOSEPH received the B.Tech. degree (Hons.) in electronics and communication from the Cochin University of Science and Technology, Cochin, India, in 2012, the M.Tech. degree (Hons.) in communication systems from the Visvesvaraya National Institute of Technology, Nagpur, India, in 2015, and the dual Ph.D. degrees (distinction) in electrical engineering from the University of Liverpool, Liverpool, U.K., and National Tsing Hua University, Hsinchu, Taiwan, in 2021.

He is currently working as a Postdoctoral Research Associate with The University of Sheffield, Sheffield, U.K. He was a Lab Engineer under CoE with the Visvesvaraya National Institute of Technology from 2015 to 2017, where he was involved in projects of national importance. He has authored or coauthored more than 25 articles in peer-reviewed journals and conference proceedings. His research interests include self-biased circulators, mmWave antenna arrays, rectifying antennas, MMIC circuit design, RF circuit design, rectifiers, integrated circuit designs, flexible electronics, wireless power transfer, energy harvesting, and TMA antenna arrays.

Dr. David Joseph is a Technical Reviewer for leading academic journals and conferences, including the IEEE TRANSACTIONS OF ANTENNA AND PROPAGATION, IEEE ANTENNA AND WIRELESS PROPAGATION LETTERS, and IEEE ACCESS.



ALAN TENNANT received the B.Eng. degree in electronic engineering and the Ph.D. degree in microwave engineering from The University of Sheffield, Sheffield, U.K., in 1985 and 1992, respectively.

He was with BAE Systems, Stevenage, U.K. He then joined DERA, Farnborough, U.K., where he worked on phased-array antenna systems before taking up an academic post with Hull University, Hull, U.K. He returned to Sheffield University in 2001 as a Senior Lecturer with the Communications and Radar Group, where he is currently a professor and involved in research into techniques, materials, and signal processing for adaptive radar signature management, novel 3-D phased-array antenna topologies, acoustic array systems, and new research into time-modulated array antennas. He has published over 100 academic articles, including several invited articles on adaptive stealth technology. His research has attracted substantial funding from both industry and government sources.

10. Paper 6 – TX TMA Channel Sounder

{Reproduced as published - author accepted version.}

© 2024 IEEE. Reprinted, with permission, from Edward A. Ball, Sumin David Joseph, and Alan Tennant, “The Time Modulated Array for Channel Sounding Measurements – Concept and Initial Field Tests”, 2024 18th European Conference on Antennas and Propagation (EuCAP), Published 26th April 2024

DOI <https://doi.org/10.23919/EuCAP60739.2024.10500956>

(Published version [6].)

The Time Modulated Array for Channel Sounding Measurements – Concept and Initial Field Tests

Edward A. Ball¹, Sumin David Joseph², Alan Tennant²

¹ Department of Electronic and Electrical Engineering, The University of Sheffield, Sheffield, UK, e.a.ball@sheffield.ac.uk

² Department of Electronic and Electrical Engineering, The University of Sheffield, Sheffield, UK

Abstract—We present a technique to use a Time Modulated Array as the transmitter in a 5.8 GHz propagation channel sounder. The 5.8 GHz signal is first modulated with a pseudo random binary sequence, to allow a correlation in the receiver to detect multi-beam relative path delays and powers, so supporting angle of departure measurements for the transmitter. The system can resolve delays down to 250 ns and the receiver measurement floor is -120 dBm. We present the system concepts and initial field test results.

Index Terms—microwave propagation measurement, microwave circuits, time-modulated antenna arrays.

I. INTRODUCTION

Propagation channel measurements often using lab-grade test equipment for the sounder. Measurements below 6 GHz in unusual scenarios remain very important: such as in a stairwell at 3.5 GHz [1] and near ground at 2.4 GHz [2]. Recently, software defined radio (SDR) platforms have become useful for propagation sounder use. When using a directional antenna in a sounder the effects due to the angle of departure or angle of arrival of a beam can be assessed, though the control of the test direction is an additional consideration.

An underused and novel method of steering an array, using RF switches instead of phase shifters, is the Time Modulated Array (TMA) [3], [4]. Such arrays can be applied to communication applications [5], including steering of the harmonic beams [6], and applied to direction finding [7].

However, to the best of the authors' knowledge, there has been no reported use of the TMA in a channel sounding application, using the harmonic beams in the sounding. This paper presents a concept system and test results for a TMA transmit (TX) and omni-directional receive (RX) SDR based system that extracts the path loss (PL) and propagation delay experienced by each of the harmonic beams. This allows a channel to be characterised in its angle of departure and PL with a single sounding. A key advantage of the TMA sounder is its simultaneous sounding of all TX beams at their various departure angles. In a conventional single beam phased array system, the sounding would have to be repeated at each steer, taking longer and potentially missing time sensitive artefacts.

II. THE TMA APPLIED TO CHANNEL SOUNDING

The array factor (AF) of an N radiating-element TX TMA is controlled by an element-specific switch on duration T_k , turn on delay T_{0k} and with frame period T_p [6], as shown in Fig. 1.

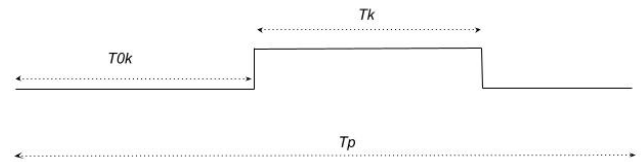


Fig. 1. TMA switch control for k th element.

In a channel sounding scenario, the k th RF switch timings producing equally spaced beams can be arranged by setting $T_k = T_p/N$ and $T_{0k} = (k-1)T_k$, thus defining a staircase control waveform where each RF switch turns on in sequence and leading to the example beam pattern of Fig. 2 for $N = 6$.

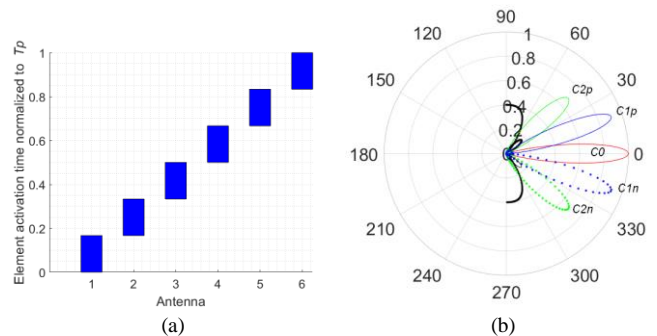


Fig. 2. TMA harmonic beams for $N = 6$: (a) time domain switch control, (b) resulting beam angles (linear scaling) also showing beam nomenclature used.

The TMA sounder AF is expressed by (1) where the time modulation of the RF signal at element k is represented as a series of Fourier coefficients, multiplied with harmonic n of the switching frequency F_p , where $\omega_p = 2\pi F_p$ and $F_p = 1/T_p$.

$$AF(\theta, t, n) = e^{j[\omega_c + n\omega_p]t} \sum_{k=1}^N e^{j\varphi_k} \frac{\sin\left(\frac{n\pi}{N}\right)}{n\pi} e^{-j\frac{n\pi}{N}(2k-1)} \quad (1)$$

The RF TX carrier frequency is F_c and $\omega_c = 2\pi F_c$. The TMA produces a set of steered harmonic beams at $(\omega_c + n\omega_p)$, spread in azimuth angle as shown in Fig. 2 (b). The AF calculates the magnitude of the radiated n th harmonic beam at azimuth beam angle θ . The term $e^{j\varphi_k}$ is an element-specific phase shift, due to antenna element spacing and evaluated beam angle, and is found using (2) where d is the spacing between the elements and λ is the carrier's wavelength.

$$\varphi_k = d(k-1) \frac{2\pi}{\lambda} \sin(\theta) \quad (2)$$

TX harmonic beams can therefore be used to all illuminate a channel and can be individually and uniquely resolved at the RX. This allows the instantaneous channel response at the various angles of departure from a TX TMA to be evaluated. It is desirable to keep F_p low, so all beams are close to F_c . We define the TMA beam nomenclature as follows: $C0$ beam is at F_c , $C1p$ beam is at $(F_c + F_p)$, $C1n$ beam is at $(F_c - F_p)$, $C2p$ beam is at $(F_c + 2F_p)$, $C2n$ beam is at $(F_c - 2F_p)$, etc.

A. Relationship Between TMA Beam Spacing and Modulation Signal Sounding Bandwidth

A 511 bit pseudo random binary sequence (PRBS) modulated carrier, with chip rate R_c and chip duration T_c , has a TX bandwidth (BW) of $2R_c$ between first spectral nulls. To avoid the modulated spectrum spanning into the adjacent TMA harmonic beams it is important that R_c is less than $F_p/2$, and so symbol shaping is required, as illustrated in Fig. 3.

B. Simulation of TMA Beam Delay Measurement

A conceptual baseband simulation representation of the TMA propagation sounder is shown in Fig. 4. The single PRBS signal is modulated onto carriers representing the TMA harmonic beam frequencies. The harmonic beams are at $-2F_p$, $-F_p$, 0 , F_p , $2F_p$ Hz relative to the RF carrier F_c . As a concept test, the signals from each beam can then be subject to a time delay $[D0..Dxn, Dxp]$, representing the channel delay that is to be simulated on that beam, and an amplitude scaling $[A0..Axn, Axp]$. The TX signal is thus represented at baseband by (4).

$$U_{TX} = U3p + U2p + U1p + U0 + U1n + U2n + U3n \quad (4)$$

The SDR RX samples are allocated to array $h(n)$ and the known ideal TX sequence U_{TX} is allocated to array $g(n)$. Using (5) [8], $H(f)$ and $G(f)$ are the Fast Fourier Transforms of time series $h(n)$ and $g(n)$ respectively and $*$ denotes complex conjugation performed on $H(f)$.

$$C = IFFT[H(f)*G(f)] \quad (5)$$

C is the resulting cross-correlation array of the time series, resulting from the Inverse Fast Fourier Transform (IFFT). Hence C is the time domain channel impulse response. The RX beams can either be correlated all at once by fully applying (4), or extracted individually to find a single beam. Due to the inherent TMA F_p mixing, the PRBS frame is rotated at the F_p harmonic of each beam - this effect is included in U_{TX} .

To demonstrate the sounder algorithm's ability to detect the individual beams, the following simulation was created (with respect to Fig. 4): $A0 = 0$ dB (reference level), $A1p = -2$ dB, $A1n = -4$ dB, $A2p = -6$ dB, $A2n = -8$ dB, $A3p = -10$ dB, $A3n = -12$ dB, $D0 = 30$ μ s, $D1p = 40$ μ s, $D1n = 50$ μ s, $D2p = 60$ μ s, $D2n = 70$ μ s, $D3p = 80$ μ s, $D3n = 90$ μ s with $R_c = 500$ kHz and $F_p = 1$ MHz. The resulting frequency domain TMA spectrum is shown in Fig. 5 (a), converted to a 10 MHz IF.

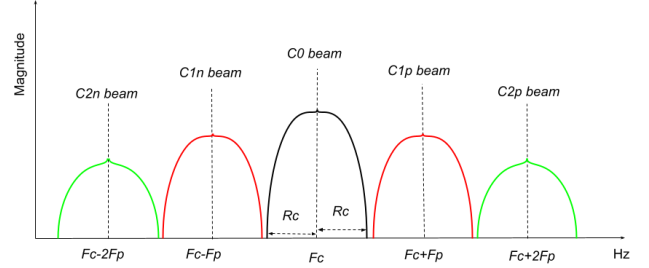


Fig. 3. TMA harmonic beams spectral planning related to R_c ($+ / - 2$ harmonics shown). It is important the TMA beam spectra do not overlap.

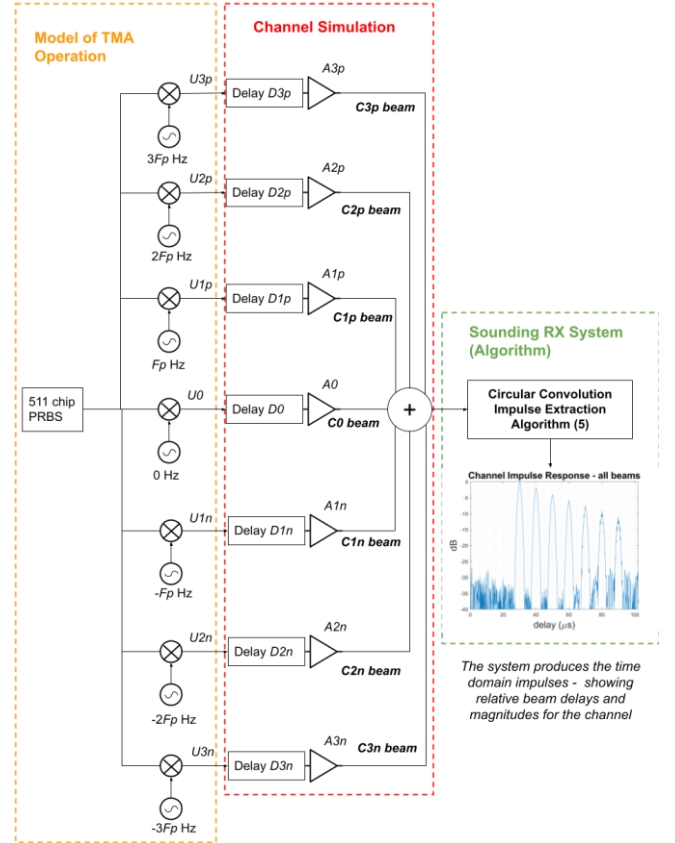


Fig. 4. TMA Sounder baseband conceptual model for beam delay tests.

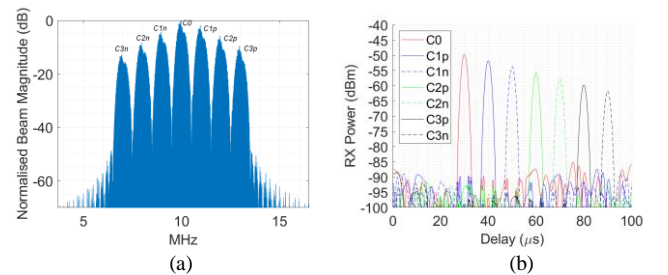


Fig. 5. Sounder test: (a) simulated TMA beams as seen in frequency domain (at a 10MHz IF), (b) recovered time domain impulses using (5), showing correct extraction of beam amplitudes ($A0$, $A1p$, etc) and delays ($D0$, $D1p$, etc) with 10 μ s increments. ($A0$ & $D0$ applied to beam $C0$, $A1p$ & $D1p$ applied to beam $C1p$, etc.)

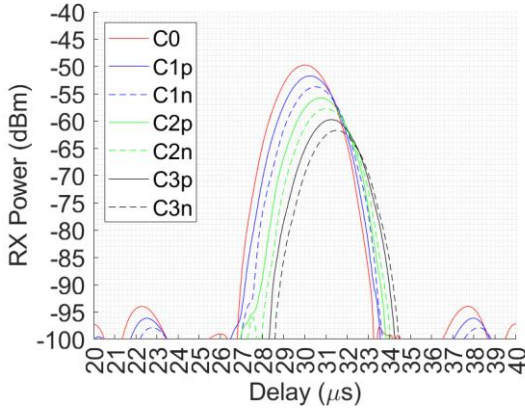


Fig. 6. Sounder test with $D0 = 30 \mu\text{s}$, $D1p = 30.25 \mu\text{s}$, $D1n = 30.5 \mu\text{s}$, etc, showing correct extraction of the time domain impulse beam delays.

The channel sounder algorithm described correctly extracts the channel time domain impulses for the above test scenario, with the recovered impulses shown in Fig. 5 (b). Beam impulse $C0$ is due to $A0$ & $D0$, $C1p$ is due to $A1p$ & $D1p$, etc.

In our system $Rc = 500 \text{ kHz}$, so the minimum reflection delay clearly identifiable by the system on an individual beam is $1/Rc = 2 \mu\text{s}$. However, it is possible to resolve delays less than this *between the beams*. Fig. 6 shows the time domain impulses extracted when the simulated TMA beams for the previous test are instead delayed by multiples of $0.25 \mu\text{s}$ ($D1p = 30.25 \mu\text{s}$, etc). This corresponds to a resolvable minimum propagation delay *between beams* of circa 75 m.

III. TMA SOUNDER HARDWARE AND TESTING

For generating the 5.8 GHz symbol-shaped PRBS TX signal we used an Analog Devices Adalm Pluto SDR controlled by a Raspberry Pi 3B (R-PI) with touch screen and bespoke Python code. The TX SDR signal is amplified by a Qorvo QPL9503EVB amplifier and then passed to our existing TMA TX array hardware [6], controlled by a bespoke FPGA platform (Intel MAX 10 FPGA EK-10M50F484).

The lab RX system consisted of a Adalm Pluto SDR and 5.8 GHz monopole antenna (Molex part 2144141001), controlled by bespoke Python code for IQ data capture. Subsequent signal analysis, using the algorithm based on (5), was then performed on a PC in Matlab. A concept diagram of the TMA sounder hardware is shown in Fig. 7.

The TMA FPGA generates a Fp of 1 MHz, to suit [6]. Due to this Fp , a maximum Rc of 500 kHz is imposed due to BW constraints as illustrated in Fig. 3. This defines a minimum resolvable path delay of 600 m on a single beam, but down to 75 m between beams. Even if delay information is not resolvable in a scenario, the system can still measure the RX power of the harmonic beams, for angle of departure PL.

Initial lab calibration was performed using a Rohde and Schwarz SMW100A signal generator and Rohde and Schwarz FSV40N spectrum analyser. Anechoic chamber measured TX radiated powers for the beams were: $C0$ (0 degree beam) = -7 dBm, $C1p/C1n$ (20 degrees) = -14 dBm, $C2p/C2n$ (40 degrees) = -16 dBm and $C3p/C3n$ (60 degrees) = -21 dBm.

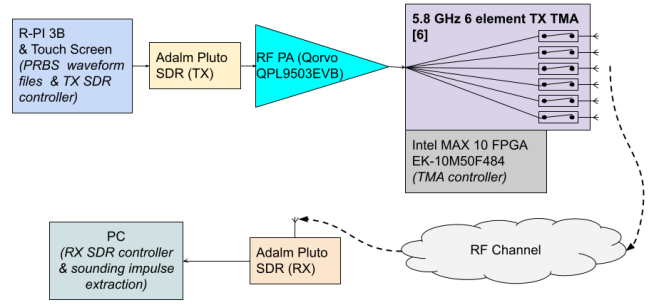


Fig. 7. TMA sounder hardware system (TX and RX).

As also shown in Fig. 2 (b), $C1n$, $C2n$ (and $C3n$) beams all emit to the right of the $C0$ beam and $C1p$, $C2p$ (and $C3p$) beams emit to the left of the $C0$ beam, when viewed from behind the TX array looking towards the RX. The RX system has a measurement floor of -120 dBm to resolve an impulse, and a maximum resolvable input of -50 dBm. This leads to a maximum resolvable PL of 113 dB on the $C0$ beam (assuming a 0 dBi RX antenna). During testing it was found that the SDRs' carriers can drift considerably; in one example showing a TX signal drift of 2 kHz in 4 minutes.

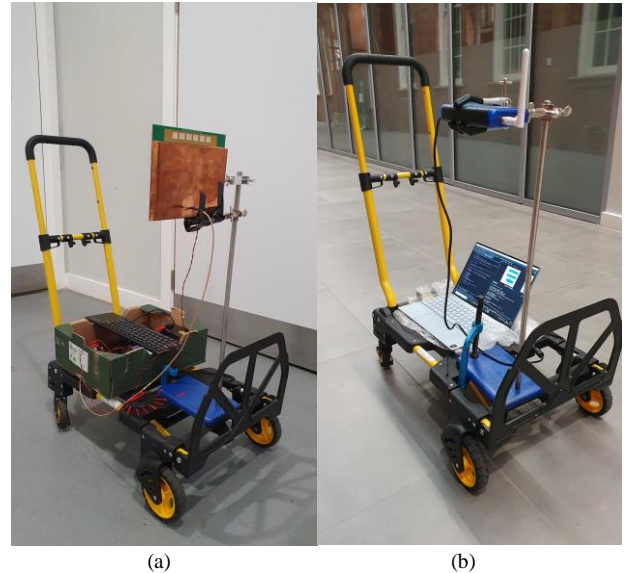


Fig. 8. TMA propagation system field test platform: (a) TMA TX, (b) RX.



Fig. 9. TMA TX propagation field test: (a) TX in café area, RX by rear wall (ringed), (b) Corridor test area: view from behind TMA towards RX (ringed).

Therefore, after warming up, it was necessary to incorporate an initial tone-based carrier calibration before each TMA sounding run. The field test hardware for the TMA sounder is shown in Fig. 8.

A. Field Test Sites – Café Area and Corridor Area

Field tests were performed in a 4-storey atrium and adjacent corridor area in The University of Sheffield’s Mappin Building (lat. 53.382, long. -1.479). Testing focused on an open-plan café shown in Fig. 9 (a), and a 78 m long corridor area at the back of atrium shown in Fig. 9 (b).

B. Field Test Results – Open Plan Café

The TX was sited at a far corner of the café 25m from the RX and with the TX antenna array 75 cm above the floor. The RX was on a table at the far side of the café, with antenna 170 cm above the floor. The café was closed and empty during the test. The TX array was pointed at the RX system and five RX SDR frames captured. The TX array was then rotated in +/-20 degree steps to ‘squint’ the TX and the tests then repeated. When the TX array is squinted to negative angles, the $C1p$, $C2p$, $C3p$ beams are the direct Line of Sight (LoS) beams. For positive squint angles the negative beams become LoS.

Sounder extracted measured data was compared to ITU-R P.1238-12 Line of Sight (LoS) and Non Line of Sight (NLoS) models for indoor environments [9]. The resolved PL for TMA harmonic beams $C0$, $C1p$, $C1n$, $C2p$, $C2n$, $C3p$, $C3n$ are shown in Fig. 10, compared to ITU-R.P.1238-12. The results agree well with the ITU-R P.1238-12 NLoS model. For each TX array orientation squint, the beam providing lowest PL was identified and found to be $C0$ when no TX squint was used (as would be expected). For positive TX beam squints, the $C1n$.. $C3n$ beams are LoS and hence should provide the lowest loss in reflectionless channels: $C1n$ is seen to observe this trend in Fig. 10. On the other hand, for negative beam squints Cp .. $C3p$ beams will be LoS: $C1p$ is seen to observe this at -40 degrees but the $C2n$ beam is also strong at -20 degrees, suggesting a strong reflection path for $C2n$ beam.

Fig. 11 shows an example of the extracted time domain impulse response for each beam, with the TX array pointing at +20 degrees (hence $C1n$ beam directly pointing to the RX).

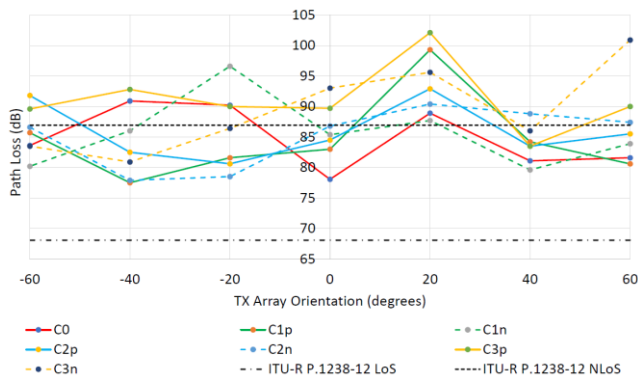


Fig. 10. Café area propagation results showing PL of all beams as function of TX array squint, compared to ITU-R P.1238-12 models.

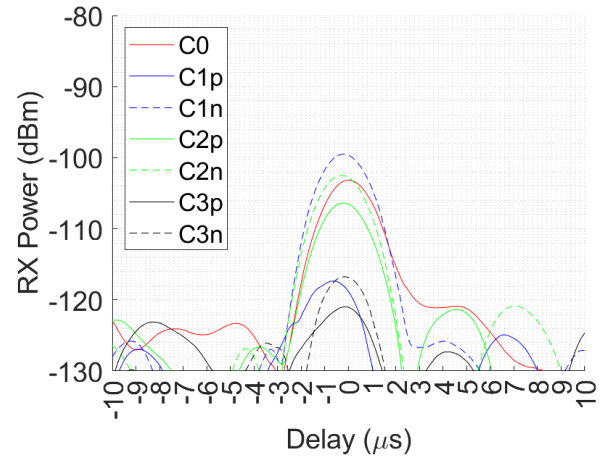


Fig. 11. Café area propagation results showing time domain impulse response RX powers for all beams with 20 degree TX array squint ($C1n$ beam is expected to be best beam for LoS and is the strongest here).

The resolved beam delays, with respect to the $C0$ beam timing, are $C1p$: -0.7 μ s, $C1n$: -0.2 μ s, $C2p$: -0.2 μ s, $C2n$: -0.3 μ s, $C3p$: -0.1 μ s, $C3n$: -0.2 μ s and $C1n$ beam is seen to provide the highest RX power (as would be expected for LoS). Hence, Fig. 11 shows a scenario where the system can resolve delays for short indoor paths, even though it uses a low R_c .

C. Field Test Results – Corridor Area

The TX was sited at one end of a 78 m long, high open corridor at the back of the atrium. The RX was mobile on a trolley and moved to each test location in 10m steps. Both TX and RX antennas were 75 cm above a concrete floor. The area was closed and empty during the test. At each location the TX array was first pointed at the RX system (i.e. no squint) and five readings captured. To implement a beam squint, the TX array was then physically rotated left to -20 degrees (direct beam now is $C1n$) and the RX capture repeated. The TX array was then physically rotated right to +20 degrees (direct beam is $C1p$) and the test repeated. The RX trolley was then moved to the next location and the three tests repeated. Example extracted PL are reported in Fig. 12 – Fig. 13 and compared to the ITU-R P.1238-12 LoS and NLoS models.

The RX beam providing the lowest PL at each location from 10 m to 78 m was found to be $C0$ when no TX squint was applied. When the left or right TX squint was applied, the expected direct beam ($C1p$ or $C1n$) was strongest for 75 % of results. In 25 % of the locations a reflected beam was strongest (likely mainly due to an adjacent dry brick wall).

From Fig. 12 the lowest PL is due to the $C0$ non-squinted beam, as may be expected. However, at 30 m there appears to be a strong reflection when the array is squinted right, providing a comparable PL to the non-squinted array. Also, the PL for the right squint on the $C0$ beam shows more variability, suggesting more reflective surface effects in that direction (i.e. due to walls). In Fig. 13 beyond 30m the lowest PL beam is $C1n$ when the TX array is squinted left, as would be expected for this direct LoS beam.

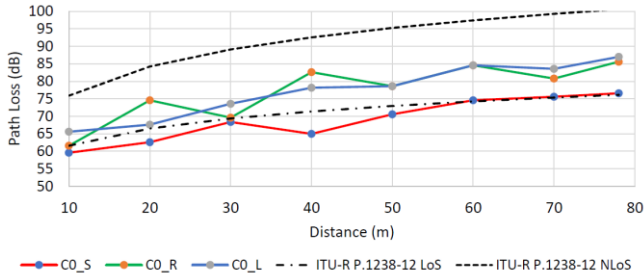


Fig. 12. Corridor propagation results showing PL of $C0$ beam as function of TX squint, compared to ITU-R P.1238-12 models. (Legend: no TX array squint = $C0_S$, left squint TX = $C0_L$, right squint TX = $C0_R$.)

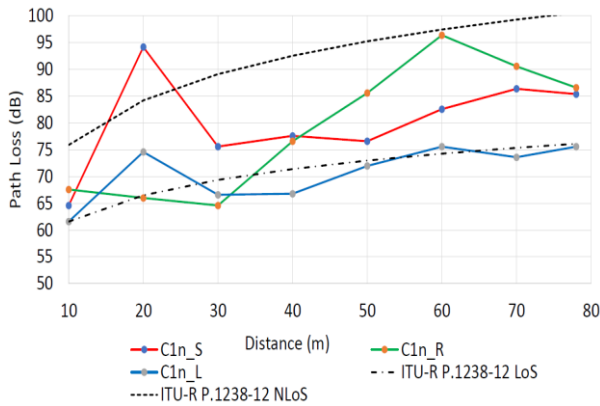


Fig. 13. Corridor propagation results showing beam PL as function of TX squint for $C1n$ beam. (Legend: no TX array squint = $C1n_S$, left squint TX = $C1n_L$, right squint TX = $C1n_R$.)

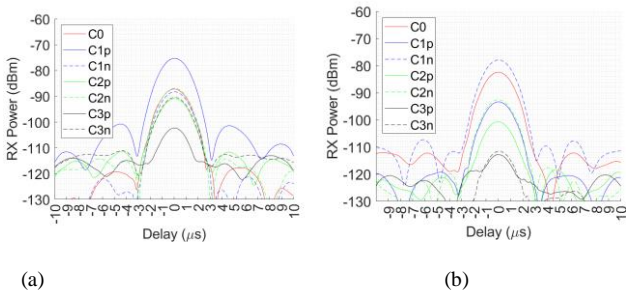


Fig. 14. Corridor propagation results showing example impulse response RX powers for all beams at 40 m: (a) right TX squint, (b) left TX squint.

However, for distances under 30 m a lower PL is seen when the array is squinted right – suggesting a strong wall reflection for that scenario.

Example channel time domain impulse responses are shown in Fig. 14 (a) for a right TX squint (showing $C1p$ as the strongest beam, as expected) and Fig. 14 (b) for a left squint (showing $C1n$ as the strongest beam, as expected). No delays between beams were resolved during the test, suggesting the relative reflections were less than 250 ns and direct beams were always dominant.

IV. DISCUSSION ON SYSTEM PERFORMANCE

Improving the impulse delay resolution requires a faster PRBS clock and faster TMA frame period, which is not possible with the current hardware using [6] but will be addressed in future versions of the system. With the -7 dBm

$C0$ beam TX power and -120 dBm RX impulse measurement floor, the outdoor testable range could be 650 m in a simple 2 ray reflective environment.

V. CONCLUSION

A propagation sounder system is demonstrated that can measure individual beam time delay and PL at 5.8 GHz, using a TMA as the sounding transmitter. The system can resolve all the beam paths in a single sounding measurement, with no beam scanning required. The TMA can thus enable a dynamic measurement of changes in a propagation environment in near real time. Due to hardware limitations, the minimum resolvable beam reflection delay is $2 \mu\text{s}$ for an on-beam delay, but circa $0.25 \mu\text{s}$ between beams.

The field tests show good agreement between measurements and ITU-R.P.1238-12, with measurement findings fitting close to either LoS or NLoS models.

ACKNOWLEDGMENT

This research was funded by UKRI, grant number MR/T043164/1.

REFERENCES

- [1] A. Al-Saman, M. Mohamed, and M. Cheffena, "Radio propagation measurements in the indoor stairwell environment at 3.5 and 28 GHz for 5G wireless networks," *Int. J. Antennas Propag.*, vol. 2020, 2020, doi: 10.1155/2020/6634050.
- [2] T. Rama Rao, D. Balachander, T. Nishesh, and M. V. S. N. Prasad, "Near ground path gain measurements at 433/868/915/2400 MHz in indoor corridor for wireless sensor networks," in *Telecommunication Systems*, Kluwer Academic Publishers, 2014, pp. 347–355. doi: 10.1007/s11235-013-9848-1.
- [3] P. Rocca, G. Oliveri, R. J. Mailloux, and A. Massa, "Unconventional phased array architectures and design methodologies - a review," *Proceedings of the IEEE*, vol. 104, no. 3, pp. 544–560, Mar. 01, 2016. doi: 10.1109/JPROC.2015.2512389.
- [4] W. H. Kummer, A. T. Villeneuve, T. S. Fong, and F. G. Terrio, "Ultra-low sidelobes from time-modulated arrays," *IEEE Trans. Antennas Propag.*, vol. 11, no. 6, pp. 633–639, 1963.
- [5] A. Ball, S. D. Joseph, and A. Tennant, "Receive mode time modulated antenna array incorporating subsampling-theoretical concept and laboratory investigation," *IEEE Open Journal of Antennas and Propagation*, 2023, doi: 10.1109/OJAP.2023.3293123.
- [6] A. Ball and A. Tennant, "A technique to control the harmonic levels in time-modulated antenna arrays - theoretical concept and hardware verification platform," *IEEE Trans. Antennas Propag.*, vol. 68, no. 7, pp. 5375–5386, Jul. 2020, doi: 10.1109/TAP.2020.2978894.
- [7] A. O'Donnell, W. Clark, J. Ernst, and R. McGwier, "Analysis of modulated signals for direction finding using time modulated arrays," in *2016 IEEE Radar Conference (RadarConf)*, 2016, pp. 1–5.
- [8] A. Ball and S. D. Joseph, "A portable 28-GHz channel sounder platform and measurement results from close-to-ground field tests," *IEEE Open Journal of Instrumentation and Measurement*, vol. 2, pp. 1–11, Mar. 2023, doi: 10.1109/ojim.2023.3259025.
- [9] ITU, "Recommendation ITU-R P.1238-12 (08/2023) Propagation data and prediction methods for the planning of indoor radiocommunication systems and radio local area networks in the frequency range 300 MHz to 450 GHz," Aug. 2023. [Online]. Available: <https://www.itu.int/publ/R-REC/en>

11. Conclusion

All the provided Papers are complete published works and so already include a focused conclusion in the article. However, it is now appropriate to consider and comment on their relevance and contribution to the theme of propagation sounding, associated techniques and hardware.

As a body of work, the thesis presents propagation sounder systems designed for microwave and mmWave operation, mmWave mixer analysis and design, and novel antenna array systems for TX and RX. Since a sounder is, in essence, an RF transmitter and an RF receiver, components and subsystems that are relevant to transceivers are also relevant and important to sounders.

The complete and novel propagation measurement systems in Paper 1 [1], Paper 4 [4] and Paper 6 [6] present their design, calibration and lab verification of correct operation. Then the systems are trialled in field test scenarios that would be very difficult to investigate using conventional lab equipment and approaches. In all cases they uncover novel channel propagation data and thus lead to new models.

The microwave transmitting array of Paper 2 [2] and receive array of Paper 5 [5] show that the TMA is a valuable technique for forming and steering a beam, which could be used within a sounder system. Key contributions in reducing an unwanted TX beam and hardware simplification for the RX array through novel signal processing help make the TMA an important enabling technology for future phased array implementation in sounders, and more generally in transceivers.

The mmWave SiGe BJT RX mixer analysis and prototype of Paper 3 [3] provides a way to initiate a mixer design and select operating conditions (bias & LO power), for the first time without relying on circuit simulation. This can aid a faster assessment of competing BJT semiconductor devices and their power efficiency. The resulting 26 GHz mixer prototype in itself is useful for mmWave RX channel sounders using a low frequency SDR.

The key contributions and findings of each Paper will now be discussed in turn.

11. 1. Paper 1 – Portable VHF / UHF IoT Sounder

Paper 1[1] showed the viability of using a low-cost SDR controlled by a Raspberry PI, with the addition of complex and bespoke signal processing code, could implement a highly portable, useful dual band IoT sounder RX. Although 71 MHz and 869 MHz were the focus of this investigation, the system could be used at any frequency over the operational range of the RTL SDR (0.5 MHz – 1.7 GHz), with only minor changes to the code and a change of antennas. At the sounding frequencies the current system has an RX measurement floor of -125 dBm at 71 MHz and -130 dBm at 869.525 MHz, for a 10 dB correlation peak above noise.

The measured channel responses can be displayed in the field, on the RX unit's screen. This can give important insight immediately in the field and allow a fast assessment of a location's channel (spectral and power delay profiles). This could be used to identify suitable target locations for a subsequent communications system deployment.

The produced channel models are useful for future IoT systems wishing to use the tested frequencies in similar scenarios. The lack of strong multipath reflections exceeding 1 μ s suggest that if long range IoT communication systems use symbol rates of circa 250 ksymbols/s or lower, the channel will appear approximately spectrally flat. Hence minimal (or no) equalisation is required, and simple single carrier modulation schemes are suitable and viable. This can enable simple IoT transceivers, with only a requirement for frequency agility (to move out of a PL null or away from interference). Since the sounder channel BWs are circa 1.5 MHz and show both some PL nulls but also lower loss portions of the spectrum, a set of narrow channels across 1.5 MHz may therefore be workable in an IoT wireless system in these bands.

11. 2. Paper 2 – TMA C0 Canceller and Beam Steering

Paper 2 [2] serves an important role in helping define the operation of the TMA and harmonic beam generation. This insight then led to, and was applied in, Papers 5 and 6. The key contribution of this paper is the technique to reduce the $C0$ beam emission, so only steerable beams remain in the radiated emission. The presented equations to control the steering of a chosen harmonic beam also are valuable. In practice, the level of $C0$ cancellation at 5.8 GHz was imperfect, limited to -16.5 dB due to the necessary simplifications and prototype hardware issues described. However, the $C0$ reduction and beam steering was demonstrated, achieving a gain of 2 dBi on the first harmonic beam and within 1 dB of theoretical prediction. The importance of fast slewing switches on the harmonic generation is also formalised with new equation models.

The maximum switching speed of the HMC7992 RF switches used in the lab prototype defined a limitation in the harmonic beam separation. This issue has subsequently led to work in MMIC design to implement faster switches [9] as well as adopting new FPGA controllers as used in Papers 5 [5] and 6 [6]. The design of fast RF switches is a key area of research for future TMAs.

In the context of a sounding system, as well as using the TMA to scan a single sounding beam in an obvious way, multiple RX stations in different locations could also be used- possibly each with directional antennas. This could allow a real time channel sounding between a fixed TMA TX and a set of fixed or mobile RXs. As discussed in Paper 6 [6], all the TX signals on the harmonic beams are time aligned, which allows time difference of arrival to potentially be measured between these distributed RX stations. PL variations over time could also be measured across the RX stations.

In Paper 2 only the $C0$ beam was suppressed, so all other TMA beams are being emitted ($C1p$, $C1n$, $C2p$, $C2n$, etc.) though with diminishing powers as harmonic order increases, as expected. This could be useful for future radio systems where orientation of a mobile device to a base station could be identified quickly since multiple available angles are all illuminated with a common signal. The handset could then detect which TMA beam it was able to hear and notify the base station to focus energy at this angle on subsequent communications. This could potentially be quicker than the base station having to scan a beam until it intercepted the handset.

11. 3. Paper 3 – Analysis of 26 GHz Downconversion Mixer Design

Beyond the presented mixer's measured results, the key findings of Paper 3 [3] are the presented analytical models that allows the DC bias conditions for a SiGe BJT mixer transistor to be calculated for a given LO drive, to meet a conversion gain or linearity criteria. This dependency has been seen experimentally before by others, but not described analytically from a circuit principles standpoint. The approach taken now allows the dependency to be considered properly at the design stage, before circuit simulation. Without this approach, a designer would have to completely rely on time domain or harmonic balance circuit simulators, which may not be available, or be expensive and time consuming for initial prototype purposes and device selection assessment. The detailed novel approach produces conversion gain results within 2.0 dB of circuit simulation and 2.5 dB of measured PCB results. IP1dB predictions are within 1 dB of the measured PCB result.

The ability to design a mmWave mixer at transistor level using commercial low-cost discrete parts is highly valuable for all prototype systems. When multiple mixers are required, such as for a MIMO RX sounder system, techniques to reduce the overall cost and power consumption become more important, as discussed in 4. 3. 1. Therefore, the mixer design strategy, circuit topology and analysis techniques outlined in this paper are very relevant to low mmWave prototype channel sounder RX systems.

The mixer concept investigated in the paper uses a low-cost commercial transistor that results in a mixer with circa 10 dB conversion loss and a similar NF, but a measured IIP3 of +20 dBm at practical LO powers. The NF, IIP3 and conversion gain can be scaled by changing the bias and LO power. A

further key finding was that the LO power could be reduced from 10 dBm to 3 dBm with only a 1 dB reduction in gain being suffered, as long as the DC bias was controlled as predicted.

The NF can be compensated (if needed for a sounding link budget) by use of an LNA before the mixer. Indeed, lossy mixers are already commonly used at mmWave frequencies, due to their good linearity and simplicity. If LNAs are used, it is important to use parts that can be re-biased, or switched out of circuit, to save DC power when lower gain / higher NF is acceptable in a sounding link budget. It is also worth noting that this was the first prototype of the mixer prototype, and so improvements may be possible in future PCB revisions.

11. 4. Paper 4 – 28 GHz Portable Channel Sounder and Close to Ground Usage

Paper 4 [4] shows that a self-contained and very compact, portable, low cost and reconfigurable channel sounder for mmWave bands is achievable using new commercial RF components, through the application of skilled bespoke hardware design. The resulting hardware designs have been made open source to allow others to apply and reuse the hardware RF front end – which represents removal of a significant design risk for newcomers to the field. The system’s 80 dB dynamic range is the best of those surveyed and supports a PL of up to 139 dB with its current 60 MHz sounding BW. The system’s RF hardware offers a 2 GHz sounding BW, which is the widest sounding bandwidth of published sounders surveyed.

A key finding from the sounder tested use cases is that a viable communication path at 28 GHz seems to exist in a 60 MHz channel over 1 km when close to ground (at 70 cm height above ground) – close to FSPL. No previous published data has been seen for comparable outdoor use cases.

The lack of observable reflections is in part due to the 33 ns measurement resolution limit of the instrument (corresponding to a 10 m delay path). If faster sampling SDRs and faster PRBSs had been used, it is possible that reflections may have been seen below 33 ns. However, any reflections that had led to path loss effects would have still been observed with the existing system.

The related sounding measurements performed at the NSC [55], [103] explored a more varied terrain and richer outdoor environment but also still show reasonable agreement to FSPL - if the LoS path exists. The test results through a wooded area suggest a random probability statistical model of path open / path closed could be developed to help PL planning in such environments.

11. 5. Paper 5 – RX Subsampling TMA Prototype

The genesis of Paper 5 [5] came from the early work in Paper 2 [2] fused with various earlier uses of SDR. The Paper is significant as it represents a new type of RX antenna array that can simplify the phased array implementation for a SDR based system and allow a much lower IF to the hardware.

The key contributions in combining the subsampling and TMA beam steering function are introduced, proven and demonstrated, with a practical demonstrator at 2.4 GHz benefiting from the convenience of commercially available parts. Lab measured results show a conversion gain of 11.4 dBi on the boresight *C0* beam and 11.3 dBi on the *C1n* beam. Measured array radiated gain results are generally within 2 dB of theoretical predictions.

The need for just a single digital line to be used in controlling the subsampling and beam steering for each element represents a simplifying benefit for large array systems in reducing the FPGA IO lines required.

The lab measured performance (steered beam angle and conversion gain) agree well with theoretical calculated predictions. The observed degraded SLL is recognised to be mainly due to the RF

switching slew rate and results confirm this. The issues associated with design of a fast switch with high RF operating frequency, as identified in Paper 2, once again come to the fore and in this paper is addressed by a mixer-first strategy. This new TMA architectural approach represents a format that could be applied to mmWave carriers and beyond.

If suitably fast RF switches are available in an RF band of interest, then the architecturally ideal scenario of removing the RF mixer can be achieved- with all associated cost and power savings. This could be possible in sub 6 GHz radios in the near future. Example cost and power savings for an STMA when compared to a conventional analogue beamformer are presented in the paper, identifying a 43 % power saving.

The STMA could be used in a sounder as a conventional RX phased array as it is. However, the RX STMA system could be used as the basis of a novel channel sounder RX and it shares the technical advantages of the sounder described in Paper 6 [6] related to the temporal coherence and measurement alignment between the beams. The incoming signal for such a sounder RX STMA could be a PRBS modulated carrier, with any channel reflections manifested as delayed version of the signal arriving at different angles. The required signal processing algorithms can be based on the new circular convolution algorithm introduced in Paper 6 [6], to include the effects of harmonic beam frequency offset with respect to the carrier. This means that delayed signals arriving within the boresight beam (CO) can be individually resolved in time if the delays exceed the PRBS bit duration. Additionally, reflections arriving at angles away from boresight will be resolved by the STMA in the harmonic beam frequencies corresponding to those angles of arrival and so be resolvable using a similar circular convolution approach as outlined in Paper 6 [6]. Overall, this means the RX STMA can be a novel and useful candidate for angle of arrival evaluation, also offering time of arrival comparison between the angles.

11. 6. Paper 6 – TX TMA Channel Sounder

Paper 6 [6] perhaps represents one of the most novel aspects of the TMA when applied to channel sounding – its ability to transmit time-aligned identical signals in multiple directions all at once. This allows a channel to be sounded in several angles of departure without any active beam steering at the TX.

A core contribution of this paper is the validation of the novel sounding algorithm, showing that the PRBS as transmitted by each harmonic beam (and so subject to a frequency rotation of multiples of Fp as seen at the RX IF) can be used as a decorrelation signal in the sounding RX. This is shown to result in unique extraction of each signal on each beam and so allows a time domain comparison of delays in arrival time, even though the absolute time of flight is unknown. A further feature is the ability to measure the delays between adjacent harmonic beams for fractions of a PRBS chip duration (which would not be possible on one beam). The 5.8 GHz prototype system transmits -7 dBm on the CO beam, can resolve path delays of 250 ns between the beams (limited by TX TMA hardware) and has an RX measurement floor of -120 dBm.

The measured results in an indoor test environment show that the extracted PL is a reasonable fit to ITU ITU-R P.1238-12 models, helping confirm correct operation of the system. Some interesting variations in the strongest available beam in various locations are seen, further proving the usefulness of the system and approach in evaluating an environment. After publication, application of the field measured data to provide indicative angular spread measurements has also been demonstrated in section 4. 6. 1.

Since spectrally the beams are offset by multiples of Fp , a trade-off exists between the value of Fp and the modulating sounding signal data rate Rc . This is discussed in the Paper and also in section 4. 6. A higher data rate is desirable to allow reduced delays in paths to be resolved (important for indoor sounding) but also requiring a higher Fp , and hence an increased frequency delta between the target

carrier (on CO beam) and the harmonic beams. In propagation-rich channels where this Fp imposed offset is a significant percentage of the carrier frequency, this may result in the sounded harmonic beams at the measured angle not fully representing the channel at the carrier if it were pointed in the same direction. A way forward would be to sound the channel with sets of Fp and related Rc and systematically, occasionally, physically reorientate the TX system to compare the carrier / beam dependency effects. Then, in sounder post processing the minimum Rc required to capture any reflective effects could be identified, and any beam and channel BW dependency also seen.

A useful increase in reflection resolution for indoor sounding could correspond to a delay distance resolution of 3 m, which implies a PRBS $Rc = 100$ Mbit/s. From the analysis in the Paper, this suggests that Fp would therefore have to be a minimum of 200 MHz.

12. Recommendations for Future Work

From the executed research activities, some specific recommendations for future work relating to each individual Paper have emerged. This is intended to improve the individual systems described and enable new measurement scenarios. New ideas to combine concepts from the Papers have also emerged.

This Chapter starts by outlining specific recommendations for future work for each Paper. It then goes on to propose new areas of research and finally a novel fusing together of some of the component paper concepts to create a new type of channel sounder.

12. 1. Recommendations per Paper

In this section, possible improvements to the systems in each individual Paper are discussed in turn.

12. 1. 1. Paper 1 – Portable VHF / UHF IoT Sounder

The sounder TX in the system of Paper 1 [1] is based on a standard laboratory dual arbitrary waveform signal generator. A useful enhancement would be to create a very small RF signal source that incorporates an PRBS BPSK modulator and so allow the TX also to be mobile and deployable in novel use-cases. Alternatively, a TX based around an SDR such as the Adalm Pluto of Paper 4 [4] could be employed, under Raspberry Pi control. The resulting sounding TX could be mounted to a drone or deployed in other interesting use cases more easily and so support further novel measurement scenarios. Additionally, the RTL-SDR could now be replaced with newer higher frequency and higher sampling rate SDRs, such as the Pluto.

12. 1. 2. Joint Consideration of Paper 2 and Paper 6 – TMA C0 Canceller and Beam Steering / TX TMA Channel Sounder

Here the next steps for the TMA systems of Paper 6 [6] which uses the hardware of Paper 2 [2] are considered, focused on propagation sounding usage. The TMA sounder of Paper 6 [6] is delay resolution limited due to the RF switches used in the TMA prototype of Paper 2 [2]. A vital improvement would be to create a new TX TMA prototype using modern RF switches with faster control capability. This would allow wider beam spacing and hence a faster PRBS to be used, and so allow a measurement of lower reflection delays. Additionally, a larger array with more active elements will enable narrower beam angular spacings, and this may be useful for a finer resolution in evaluating angle of arrival.

A further important next step for the TMA concept is to evaluate it a higher carrier frequency. This work has now commenced as part of another project, with initial high mmWave GaAs MMIC designs having been tested and showing good RF performance [9]. A subsequent step could be to create a TX demonstrator showing the usability of the TMA at mmWave frequencies, which can include channel sounding applications using a steered beam, thus taking the work of both Papers forward.

Future work on an FPGA TMA control platform can also investigate independent control of the harmonic beams and provoke research in new TMA timing control waveforms for sounding usage. The ability to use different numbers of active radiating elements is easy to support in the TMA (such as for a thinned array concept). This may allow novel control algorithms to be developed that result in less active hardware and so could save DC power in a set sounding scenario.

Finally, techniques to further cancel unwanted TMA harmonic beams could be useful, leaving just a single steerable beam remaining.

12. 1. 3. Paper 3 – Analysis of 26 GHz Downconversion Mixer Design

Paper 3 [3] focused on a SiGe bipolar transistor, which is also relevant to BiCMOS integration – an important topic for 6G radio systems. However, the FET device type is more commonly used in

MMICs - such as pHEMTs at mmWave frequencies. Therefore, a very useful activity would be to create a similar set of mixer analyses, design equations, and models for the pHEMT. The pHEMT device in a mixer has already been more widely studied, but actual models relating V_{gs} to LO drive are still missing from literature. Example candidate devices for use above 30 GHz could be the UMS Ltd PH10 and Win Semiconductors Ltd PP10-20 devices. This work could then align with ongoing MMIC development projects at The University of Sheffield.

The work of Paper 3 [3] solely addresses RX mixer design and so a similar analysis approach could be performed on the SiGe BJT device in a TX (upconverting) scenario for a sounder TX.

12. 1. 4. Paper 4 – 28 GHz Portable Channel Sounder and Close to Ground Usage

The test results from the NSC when exploring PL through a wooded area suggest a random model of probability of path open / path closed could be developed to help PL planning in such complex environments. Hence the development of this statistical PL model would be a useful next step.

The developed 28 GHz TX-RX PCB and Pluto SDR used in the published design are small and lightweight. They could be mounted to a drone, and so enable more exploratory height-based use cases and scenarios to be explored. Such tests could investigate the effectiveness of an antenna design in a scenario of interest, and extract height-based channel propagation measurements and PLs.

The chip rate (R_c) of the PRBS and sampling rate of the RX SDR limits the sounder's reflection time delay resolution. SDR implementations to improve both will be important to identify.

The 28 GHz coaxial connection to the sounder could be considered as an IF, and so higher frequency mixers and amplifiers could be attached to allow sounding at higher mmWave frequencies. One emerging area of interest in 6G is channel sounding in future mobile use cases at E band, W band, D band and upwards to sub-THz bands. PL at close to ground is interesting for military and civilian use cases. Use of external upconverter modules with this sounder is a way to access these bands. However, though PL can be extracted, improved time resolution of delay spread will require faster sampling SDRs. To conserve battery power, low power mixers, amplifiers and oscillators would also be needed for the external front end. This will avoid using lab equipment or conventional high cost, high power mmWave modules which would lose the advantage of the portability achieved with the present system. Appropriate upconverters will likely require a bespoke high mmWave PCB design using MMICs.

12. 1. 5. Paper 5 – RX Subsampling TMA Prototype

The RX STMA could be configured to evaluate RX angle of arrival of multiple signals by reapplying the signal processing techniques developed for Paper 6 [6]. This would not require hardware modification of the STMA demo platform. However, as the current platform is at 2.4 GHz and would at present likely use the Pluto SDR, indoor time reflection resolution will be limited to the delay resolution performance seen in Paper 6 [6]. Outdoor measurements with longer reflection delays, or general indoor angle of arrival PL, would be possible with the system and SDRs as used. As stated in the Paper, higher carrier frequency STMAs are also worthy of research.

The observed SLL degradation in the RX STMA is thought to be due to the RF sampling switch slew rate. To improve this will require faster switching speeds with faster slew rates. This will require research into RF switch and sampler architectures, possibly including dedicated novel MMIC and circuit designs.

The applicability of the TMA to angular spread (AS) measurements has been investigated after Paper 6 [6] publication for the TX TMA and is also relevant to consider for the STMA. This could allow the STMA to resolve AS as a function of beam MPC delay.

It is also very interesting to explore and apply the STMA concepts in TX mode. This would require a new hardware platform to be designed. Since TX sampling images would appear at all harmonics of F_p , narrow RF BPFs to select just the TX spectrum of interest would be needed after the sampler. These BPFs would be applied before the signal was passed to any TX amplification and individual antenna stages.

12. 2. New Sounder Concept Areas

In this section three new areas of research are proposed, including a new TMA based sounder concept.

12. 2. 1. Joint Sounding and User Traffic

At present the sounders described in this thesis all use PRBS data, which is not carrying any user traffic data. In addition to exploring new sounding waveforms (such as OFDM), it would be interesting to explore the tailoring of the sounding signal and waveform to also support transport of user traffic. This may then allow the sounder to be used in a mobile communication system and so allow sounding and data communications to occur *together*. This may save power since fewer transmissions could be required between a future mobile handset and base station.

A simple first exploratory step would be to reconfigure sounder hardware to accept user data once a channel sounding is complete and the best array configurations (TX and RX) have been identified. The interpretation of the sounding results, and rapid identification of optimum beam settings, could require machine learning techniques.

12. 2. 2. Sounders Operating At and Above mmWave Bands

Channel sounding at high mmWave and sub-THz, notably at W band (92 GHz to 114 GHz) and D band (130 GHz to 175 GHz), has risen to the fore recently for 6G and will require very compact equipment to support useful novel usage scenarios. These higher carrier frequencies are of interest to future communications systems since they can provide wider spectrum; needed to support future mobile user data rates in Gbit/s ranges.

Spectrum at E band (71 GHz to 86 GHz) is already used for cellular backhaul in the UK and broadband fixed point-to-point wireless in the US but is also now being considered for use in future mobile systems [30]. Spectrum beyond 90 GHz is being made available for future communications by the FCC, ETSI and the ITU.

New approaches to channel models are needed since the sub-THz and THz channel is different to lower bands [108]. The need for highly directional TX and RX antennas is clear at THz bands, to realise practical link budgets. Short channel coherence times require fast acquisition and scanning, perhaps implying from 2 to 8 GHz of sounding BW is needed [109]. Sounding systems that can detect the multipath components in very large path losses are needed. Outdoor, air to ground and vehicular sounding campaigns are now needed [110], which will all be difficult with conventional THz lab RF hardware which is bulky and expensive.

From a consideration of the above needs, mmWave and higher frequency channel sounders that are compact and power efficient will be a novel and important alternative to a VNA / signal generator and spectrum analyser / oscilloscope based SDR sounder system.

12. 2. 3. Joint TX TMA and RX TMA Sounder Concept

An interesting new concept to explore could be the creation of a joint TMA based AoD TX and TMA based AoA RX full sounder system, using the concepts already described in this thesis. This could also incorporate the STMA, to reduce RX complexity and SDR sampling rates, and mmWave mixers as designed in Paper 3 in the front end for higher bands.

To illustrate the new concept, consider the scenario illustrated in Figure 40 which shows the TX harmonic beams and RX harmonic beams that would be present in such a hybrid system.

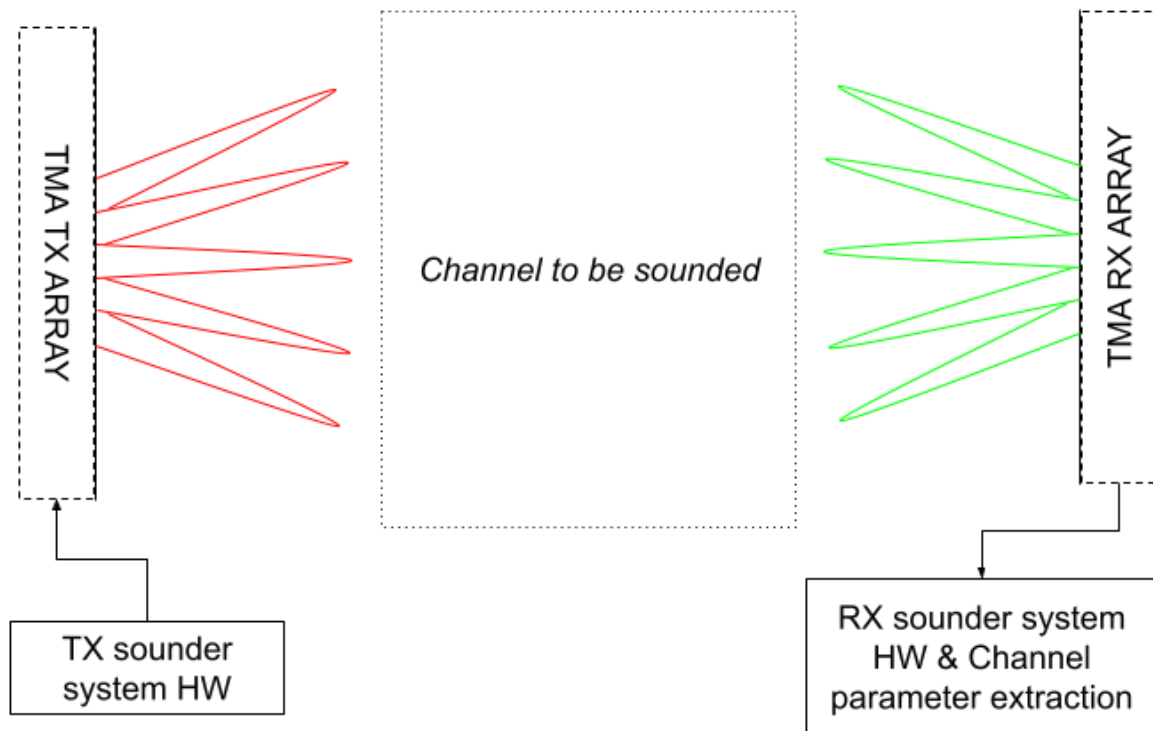


Figure 40. Joint TX and RX TMA sounder concept.

If the TX sounder uses a TMA frame period Fp_{tx} and the RX sounder uses a frame period Fp_{rx} and $Fp_{rx} > Fp_{tx}$ then it will be possible to uniquely resolve the resulting TX beams - since all will arrive in each of the RX beams uniquely. This is illustrated in terms of RX spectrum at the carrier frequency (centred on RX_{C0}) in Figure 41, assuming all TX beams are sufficiently reflected to be seen in all RX TMA beams.

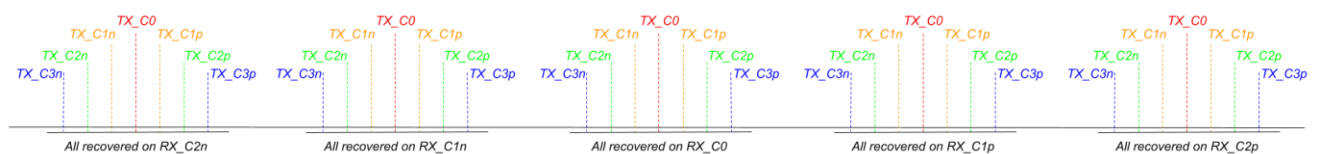


Figure 41. Joint TX and RX TMA sounder - recovered spectrum showing how all the possible TX TMA beams are received in each RX TMA beam (if a reflective path exists to support every reflection).

If we now consider example reflective scenarios as shown in Figure 42 and Figure 43 as an illustration, the possibility of combined joint measurement of AoA and AoD with unique identification (without any beam sweeping) becomes clear.

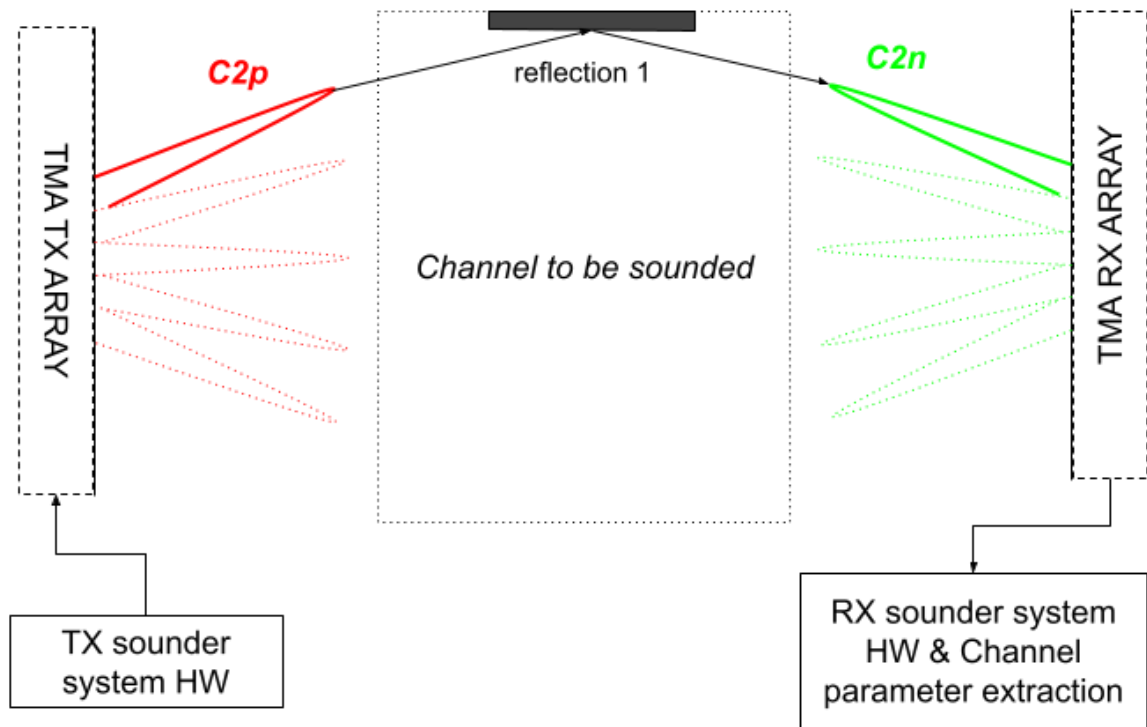


Figure 42. Single reflection example.

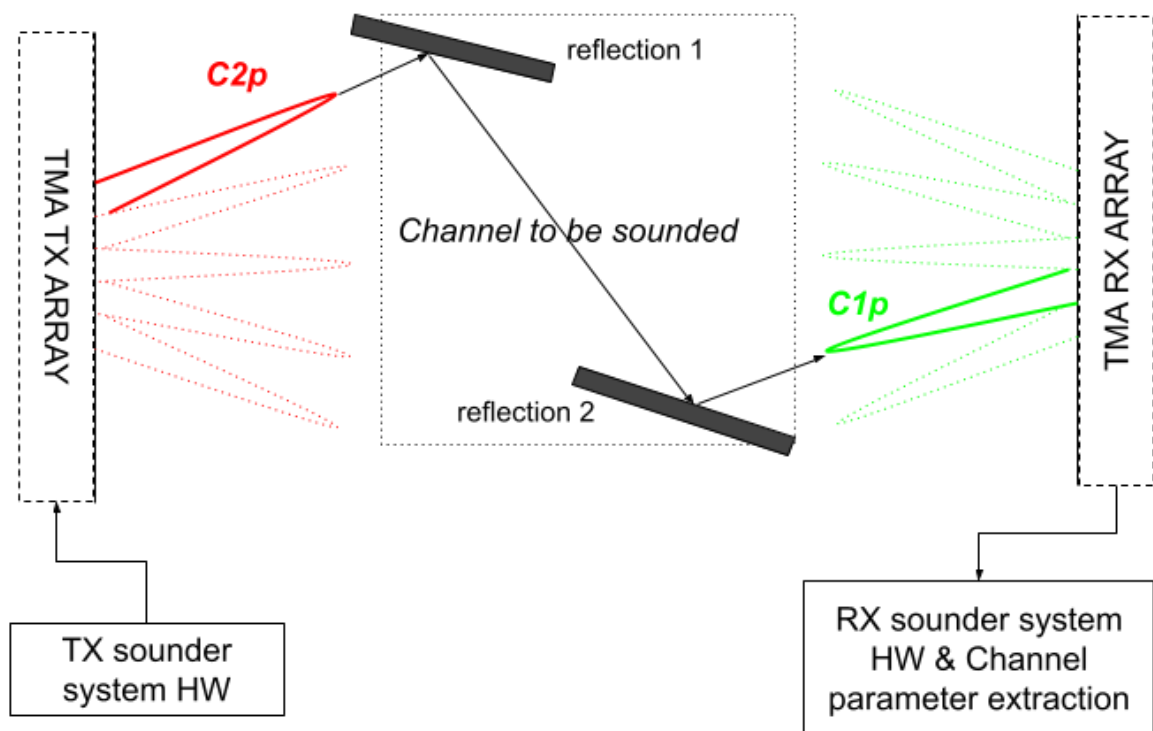


Figure 43. Double reflection example.

The single reflection situation in Figure 42 would be resolved by the RX TMA beams as shown in Figure 44. This allows the system to identify which TX beam and which RX beam has been used in determining the reflection. Hence a channel model could be extracted that included both AoD and AoA information.

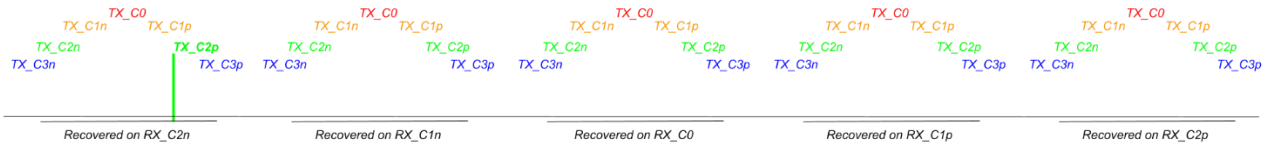


Figure 44. Resolved RX TMA spectrum showing single reflection spectral location - hence viable TX and RX beams can be identified.

The alternative example double reflection scenario in Figure 43 would be resolved by the RX TMA beams as shown in Figure 45. A double reflection scenario could result, for example, from a domestic mobile user operating in a highly reflective environment, such as adjacent to multiple metal structures or foil lined plasterboard.

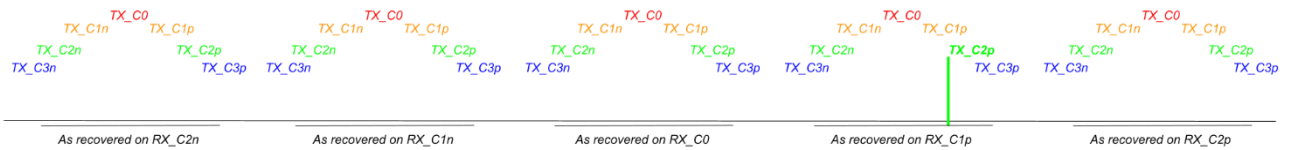


Figure 45. Resolved RX TMA spectrum showing double reflection spectral location - hence viable TX and RX beams can be identified.

The system could also process multiple reflection rays and extract the relative delays between the multiple received beams, as demonstrated already in Paper 6.

The arrays could have more radiating elements than in the present TMA systems, and so allow dynamic control of the number of active elements to best suit a sounding scenario and beam angles of interest. The angular nulls between the TX and RX available beams can be mitigated by controlling the number of active elements in the TX and RX arrays – more elements leading to a narrower illuminated span, as already shown in section 4.6 Figure 24 vs. Figure 25. For example, an array could switch from using N to $2N$ active elements during the sounding event, in a predetermined way. It is also possible to use the TMA timing control techniques described in Paper 2 [2] to systematically angularly steer a chosen beam, which would cause all other harmonic beams to also steer and hence nulls to be moved.

The TMA hardware could be based on a 2D array to allow beams to be pointed in various angles of departure / arrival in 2D, leading to more geometric aware models of the channel.

The sounder concept is frequency agnostic though the implementation will, by necessity, be tied to a band of interest. Such multi element systems would require power efficient RF hardware and could employ the mixer design concepts of Paper 3.

13. References Additional to those of the Published Papers

Here are references additional to those already provided in the published Papers 1 - 6. The references provided here are therefore used for only Chapters 1 – 4 and Chapters 11 – 12.

- [1] E. A. Ball, "Design and field trial measurement results for a portable and low-cost very-high-frequency/ultra-high-frequency channel sounder platform for Internet of things propagation research," *IET Microwaves, Antennas and Propagation*, vol. 13, no. 6, pp. 714–724, May 2019, doi: 10.1049/iet-map.2018.5827.
- [2] E. A. Ball and A. Tennant, "A Technique to Control the Harmonic Levels in Time-Modulated Antenna Arrays - Theoretical Concept and Hardware Verification Platform," *IEEE Trans Antennas Propag*, vol. 68, no. 7, pp. 5375–5386, Jul. 2020, doi: 10.1109/TAP.2020.2978894.
- [3] E. A. Ball, "Predicting the Performance of a 26 GHz Transconductance Modulated Downconversion Mixer as a Function of LO Drive and DC Bias," *Electronics (Switzerland)*, vol. 11, no. 16, Aug. 2022, doi: 10.3390/electronics11162516.
- [4] E. A. Ball and S. D. Joseph, "A Portable 28-GHz Channel Sounder Platform and Measurement Results From Close-to-Ground Field Tests," *IEEE Open Journal of Instrumentation and Measurement*, vol. 2, pp. 1–11, Mar. 2023, doi: 10.1109/ojim.2023.3259025.
- [5] E. A. Ball, S. D. Joseph, and A. Tennant, "Receive Mode Time Modulated Antenna Array Incorporating Subsampling -Theoretical Concept and Laboratory Investigation," *IEEE Open Journal of Antennas and Propagation*, 2023, doi: 10.1109/OJAP.2023.3293123.
- [6] E. A. Ball and S. David Joseph, "The Time Modulated Array for Channel Sounding Measurements – Concept and Initial Field Tests," in *Proceedings of 18th European Conference on Antennas and Propagation (EuCAP)*, Glasgow: IEEE, Mar. 2024, pp. 1371–1375. doi: 10.23919/EuCAP60739.2024.10500956.
- [7] S. D. Joseph, B. Gavin, and E. A. Ball, "28GHz Rural Close-to-Ground Propagation Field Test Results and Models," *IEEE Open Journal of Antennas and Propagation*, pp. 1–1, 2024, doi: 10.1109/OJAP.2024.3370968.
- [8] S. David Joseph and E. A. Ball, "Subsampling Time-Modulated Array for Reduced Hardware Down Conversion and Beamforming," in *Proceedings of 18th European Conference on Antennas and Propagation (EuCAP)*, Glasgow: IEEE, Mar. 2024, pp. 3727–3731. doi: 10.23919/EuCAP60739.2024.10501590.
- [9] E. A. Ball and S. D. Joseph, "Design and Measurement of a GaAs MMIC for use in a 73 GHz Time Modulated Array," in *2023 IEEE Conference on Antenna Measurements and Applications (CAMA)*, Institute of Electrical and Electronics Engineers (IEEE), Dec. 2023, pp. 560–563. doi: 10.1109/cama57522.2023.10352864.
- [10] C. Casetti, "The Challenges of Universal Broadband Connectivity [Mobile Radio]," *IEEE Vehicular Technology Magazine*, vol. 17, no. 3, pp. 5–11, Sep. 2022, doi: 10.1109/MVT.2022.3176414.
- [11] C. Casetti, "5G Standalone Deployments Are on the Rise [Mobile Radio]," *IEEE Vehicular Technology Magazine*, vol. 18, no. 1, pp. 5–11, Mar. 2023, doi: 10.1109/MVT.2022.3227710.
- [12] C. Casetti, "The Day 5G Came From Outer Space [Mobile Radio]," *IEEE Vehicular Technology Magazine*, vol. 17, no. 4, pp. 5–11, Dec. 2022, doi: 10.1109/MVT.2022.3205402.
- [13] J. C. Lin, "Health Safety Guidelines and 5G Wireless Radiation [Health Matters]," *IEEE Microw Mag*, vol. 23, no. 1, pp. 10-13+17, Jan. 2022, doi: 10.1109/MMM.2021.3117307.
- [14] J. C. Lin, "A Paradigm Shift? [Health Matters]," *IEEE Microw Mag*, vol. 24, no. 12, pp. 16–18, Dec. 2023, doi: 10.1109/MMM.2023.3313788.

- [15] C. X. Wang *et al.*, “On the Road to 6G: Visions, Requirements, Key Technologies, and Testbeds,” *IEEE Communications Surveys and Tutorials*, vol. 25, no. 2, pp. 905–974, 2023, doi: 10.1109/COMST.2023.3249835.
- [16] W. Saad, M. Bennis, and M. Chen, “A Vision of 6G Wireless Systems: Applications, Trends, Technologies, and Open Research Problems,” *IEEE Netw*, vol. 34, no. 3, pp. 134–142, May 2020, doi: 10.1109/MNET.001.1900287.
- [17] H. Tataria, M. Shafi, M. Dohler, and S. Sun, “Six Critical Challenges for 6G Wireless Systems: A Summary and Some Solutions,” *IEEE Vehicular Technology Magazine*, vol. 17, no. 1, pp. 16–26, Mar. 2022, doi: 10.1109/MVT.2021.3136506.
- [18] Samsung Research, “6G The Next Hyper Connected Experience for All,” 2020. Accessed: Sep. 21, 2024. [Online]. Available: <https://research.samsung.com/next-generation-communications>
- [19] Keysight Technologies, “Next-Generation Wireless: A Guide to the Fundamentals of 6G,” Jun. 2023. Accessed: Sep. 21, 2024. [Online]. Available: <https://www.keysight.com/gb/en/assets/7123-1050/ebooks/Next-Generation-Wireless-A-Guide-to-the-Fundamentals-of-6G.pdf>
- [20] J. Hayes, “6G and the Reinvention of Mobile,” *IET E & T Magazine*, vol. 15, no. 1, pp. 26–29, 2020, [Online]. Available: www.EandTmagazine.com
- [21] A. Behravan *et al.*, “Positioning and Sensing in 6G: Gaps, Challenges, and Opportunities,” *IEEE Vehicular Technology Magazine*, vol. 18, no. 1, pp. 40–48, Mar. 2023, doi: 10.1109/MVT.2022.3219999.
- [22] M. Marcus, X. C. Roman, and J. Jornet, “Millimeter-Wave Propagation: Spectrum Management Implications-An Update for >100 GHz [Speaker’s Corner],” *IEEE Microw Mag*, vol. 24, no. 1, pp. 91–94, Jan. 2023, doi: 10.1109/MMM.2022.3211599.
- [23] ITU, “ITU-R P.676-12 (Attenuation by atmospheric gases and related effects),” Aug. 2019. Accessed: Feb. 16, 2024. [Online]. Available: https://www.itu.int/dms_pubrec/itu-r/rec/p/R-REC-P.676-12-201908-S!!PDF-E.pdf
- [24] ITU, “ITU-R P.525-4 (Calculation of free-space attenuation),” Aug. 2019. Accessed: Feb. 16, 2024. [Online]. Available: https://www.itu.int/dms_pubrec/itu-r/rec/p/R-REC-P.525-4-201908-!!PDF-E.pdf
- [25] J. Borrill, “What is behind the drive towards Terahertz technology of 6G,” Sep. 2021. Accessed: Feb. 16, 2024. [Online]. Available: <https://apsr.anritsu.com/en-sg/tm/whatisbehind-drive6gtechnology>
- [26] T. Eichler and R. Zeigler, “Fundamentals of THz Technology for 6G,” 2022. Accessed: Feb. 16, 2024. [Online]. Available: www.rohde-schwarz.com
- [27] C. Han, W. Gao, N. Yang, and J. M. Jornet, “Molecular Absorption Effect: A Double-Edged Sword of Terahertz Communications,” *IEEE Wirel Commun*, vol. 30, no. 4, pp. 140–146, Aug. 2023, doi: 10.1109/MWC.016.2100704.
- [28] R. Nebuloni *et al.*, “Exploiting Numerical Weather Prediction Data for Radiopropagation Modeling of SatCom Links,” in *Proceedings of 18th European Conference on Antennas and Propagation (EuCAP)*, Glasgow: IEEE, Mar. 2024. doi: 10.23919/EuCAP60739.2024.10501034.
- [29] M. Vala, J. R. Reis, J. M. Felício, N. Leonor, C. A. Fernandes, and R. F. S Caldeirinha, “Wind-induced Backscatter Clustering from Vegetation at W-band,” in *Proceedings of 18th European Conference on Antennas and Propagation (EuCAP)*, Glasgow: IEEE, Mar. 2024. doi: 10.23919/EuCAP60739.2024.10501566.
- [30] P. B. Papazian, C. Gentile, K. A. Remley, J. Senic, and N. Golmie, “A Radio Channel Sounder for Mobile Millimeter-Wave Communications: System Implementation and Measurement

- Assessment,” *IEEE Trans Microw Theory Tech*, vol. 64, no. 9, pp. 2924–2932, Sep. 2016, doi: 10.1109/TMTT.2016.2592530.
- [31] T. S. Rappaport, G. R. MacCartney, M. K. Samimi, and S. Sun, “Wideband millimeter-wave propagation measurements and channel models for future wireless communication system design,” *IEEE Transactions on Communications*, vol. 63, no. 9, pp. 3029–3056, Sep. 2015, doi: 10.1109/TCOMM.2015.2434384.
- [32] T. S. Rappaport, *Wireless communication principles & practice*. NJ: Prentice-Hall, 1996.
- [33] Y. Huang and Kevin Boyle, *Antennas : From Theory to Practice*, 1st ed. Chichester: John Wiley & Sons Ltd, 2008.
- [34] A. Goldsmith, *Wireless Communications*, 1st ed. Cambridge: Cambridge University Press, 2005.
- [35] J. Sadowski, “Measurement of Coherence Bandwidth in UHF Radio Channels for Narrowband Networks,” *Int J Antennas Propag*, vol. 2015, 2015, doi: 10.1155/2015/985892.
- [36] R. Zhang, X. Lu, J. Zhao, L. Cai, and J. Wang, “Measurement and modeling of angular spreads of three-dimensional urban street radio channels,” *IEEE Trans Veh Technol*, vol. 66, no. 5, pp. 3555–3570, May 2017, doi: 10.1109/TVT.2016.2604394.
- [37] S. Salous, *Radio Propagation Measurement and Channel Modelling*, First. Chichester: Wiley, 2013.
- [38] K. A. Remley, C. Gentile, A. Zajic Line, and J. T. Quimby, “Methods for Channel Sounder Measurement Verification,” in *2017 IEEE 86th Vehicular Technology Conference (VTC-Fall)*, Toronto: IEEE, Sep. 2017, pp. 1–4. doi: 10.1109/VTCFall.2017.8288374.
- [39] J. Quimby, D. G. Michelson, M. Bennai, K. A. Remley, J. Kast, and A. Weiss, “Interlaboratory Millimeter-Wave Channel Sounder Verification,” in *2019 13th European Conference on Antennas and Propagation (EuCAP)*, Krakow: IEEE, Mar. 2019, pp. 1–5.
- [40] C. Gentile *et al.*, “Methodology for Benchmarking Radio-Frequency Channel Sounders through a System Model,” *IEEE Trans Wirel Commun*, vol. 19, no. 10, pp. 6504–6519, Oct. 2020, doi: 10.1109/TWC.2020.3003617.
- [41] S. Y. Jun, D. Caudill, J. Senic, C. Gentile, J. Chuang, and N. Golmie, “Over-The-Air Calibration of a Dual-Beam Dual-Polarized 28-GHz Phased-Array Channel Sounder,” in *2020 IEEE International Symposium on Antennas and Propagation and North American Radio Science Meeting, IEEECONF 2020 - Proceedings*, Institute of Electrical and Electronics Engineers Inc., Jul. 2020, pp. 1093–1094. doi: 10.1109/IEEECONF35879.2020.9330179.
- [42] S. Wittig, A. Schultze, M. Peter, and W. Keusgen, “Over-the-Air Verification of Angle-of-Arrival Estimation in Millimeter-Wave Channel Sounders,” in *IEEE Vehicular Technology Conference*, Institute of Electrical and Electronics Engineers Inc., 2021. doi: 10.1109/VTC2021-Fall52928.2021.9625085.
- [43] J. T. Quimby, D. F. Williams, K. A. Remley, D. Ribeiro, R. Sun, and J. Senic, “Millimeter-wave channel-sounder performance verification using vector network analyzer in a controlled RF channel,” *IEEE Trans Antennas Propag*, vol. 69, no. 11, pp. 7867–7875, Nov. 2021, doi: 10.1109/TAP.2021.3083737.
- [44] A. J. Heitmann *et al.*, “Observations and Modeling of Traveling Ionospheric Disturbance Signatures From an Australian Network of Oblique Angle-of-Arrival Sounders,” *Radio Sci*, vol. 53, no. 9, pp. 1089–1107, Sep. 2018, doi: 10.1029/2018RS006613.
- [45] T. Zhou, Y. Lin, Z. Yang, B. Ai, and L. Liu, “Radio Channel Measurements and Characterization in Substation Scenarios for Power Grid Internet of Things,” *IEEE Internet Things J*, vol. 10, no. 9, pp. 7691–7704, May 2023, doi: 10.1109/JIOT.2022.3195512.

- [46] D. P. Wright and E. A. Ball, "Highly Portable, Low-Cost SDR Instrument for RF Propagation Studies," *IEEE Trans Instrum Meas*, vol. 69, no. 8, pp. 5446–5457, 2020, doi: 10.1109/TIM.2019.2959422.
- [47] D. P. Wright and E. A. Ball, "IoT focused VHF and UHF propagation study and comparisons," *IET Microwaves, Antennas and Propagation*, vol. 15, no. 8, pp. 871–884, 2021, doi: 10.1049/mia2.12101.
- [48] V. Kristem *et al.*, "3D MIMO Outdoor-to-Indoor Propagation Channel Measurement," *IEEE Trans Wirel Commun*, vol. 16, no. 7, pp. 4600–4613, Jul. 2017, doi: 10.1109/TWC.2017.2700391.
- [49] R. Zhang, H. Xu, X. Du, D. Zhou, and M. Guizani, "Dual-polarized spatial-temporal propagation measurement and modeling in uma o2i scenario at 3.5 GHz," *IEEE Access*, vol. 7, pp. 122988–123001, 2019, doi: 10.1109/ACCESS.2019.2919377.
- [50] H. Kdouh *et al.*, "Double directional characterisation of radio wave propagation through metallic watertight doors on board ships," *Electron Lett*, vol. 48, no. 6, pp. 307–309, Mar. 2012, doi: 10.1049/el.2012.0310.
- [51] K. Mao *et al.*, "A UAV-Aided Real-Time Channel Sounder for Highly Dynamic Nonstationary A2G Scenarios," *IEEE Trans Instrum Meas*, vol. 72, 2023, doi: 10.1109/TIM.2023.3301592.
- [52] W. Hong *et al.*, "The Role of Millimeter-Wave Technologies in 5G/6G Wireless Communications," *IEEE Journal of Microwaves*, vol. 1, no. 1, pp. 101–122, Jan. 2021, doi: 10.1109/jmw.2020.3035541.
- [53] D. Shakya *et al.*, "Exploring Millimeter-Wave and Terahertz Circuits and Systems With a Novel Multiuser Measurement Facility: Multiuser Terahertz Measurement Facility (THz Lab)," *IEEE Microw Mag*, vol. 25, no. 2, pp. 68–79, Feb. 2024, doi: 10.1109/MMM.2023.3320820.
- [54] University of Sheffield, "UKRI National mmWave Measurement Facility." Accessed: Feb. 16, 2024. [Online]. Available: <https://www.sheffield.ac.uk/mm-wave>
- [55] S. D. Joseph, B. Gavin, and E. A. Ball, "28GHz Rural Close-to-Ground Propagation Field Test Results and Models," *IEEE Open Journal of Instrumentation and Measurement*, 2024, doi: 10.1109/OJAP.2024.3370968.
- [56] R. Charbonnier *et al.*, "Calibration of Ray-Tracing with Diffuse Scattering against 28-GHz Directional Urban Channel Measurements," *IEEE Trans Veh Technol*, vol. 69, no. 12, pp. 14264–14276, Dec. 2020, doi: 10.1109/TVT.2020.3038620.
- [57] E. A. Ball and A. Vasileiadis, "Constant Envelope Transceivers in Millimetre-Wave Massive MIMO: EVM and Link Budget Considerations," in *2018 IEEE 10th Sensor Array and Multichannel Signal Processing Workshop (SAM)*, Sheffield: IEEE, 2018, pp. 84–88. doi: 10.1109/SAM.2018.8448672.
- [58] J. Li, Y. Zhao, C. Tao, and B. Ai, "System design and calibration for wideband channel sounding with multiple frequency bands," *IEEE Access*, vol. 5, pp. 781–793, 2017, doi: 10.1109/ACCESS.2017.2649679.
- [59] C. Umit Bas *et al.*, "28 GHz Foliage Propagation Channel Measurements," in *2018 IEEE Global Communications Conference (GLOBECOM)*, Abu Dhabi: IEEE, Dec. 2018, pp. 1–6. doi: 10.1109/GLOCOM.2018.8647674.
- [60] C. Umit Bas *et al.*, "Outdoor to indoor propagation channel measurements at 28 GHz," *IEEE Trans Wirel Commun*, vol. 18, no. 3, pp. 1477–1489, Mar. 2019, doi: 10.1109/TWC.2018.2890239.
- [61] L. Wang *et al.*, "Channel measurement and characterisation for 5G multi-scenarios at 26 and 38 GHz," *IET Microwaves, Antennas and Propagation*, vol. 17, no. 14, pp. 1042–1055, Nov. 2023, doi: 10.1049/mia2.12421.

- [62] R. Sun, D. Viorel, W. Keusgen, and R. Gebremedhin, "Empirical Path Loss Model and Small-Scale Fading Statistics in an Indoor Office Environment in 6 and 37 GHz Shared Bands," in *Proceedings of 18th European Conference on Antennas and Propagation (EuCAP)*, Glasgow: IEEE, Mar. 2024. doi: 10.23919/EuCAP60739.2024.10500987.
- [63] E. Ben-Dor, T. S. Rappaport, Y. Qiao, and S. J. Lauffenburger, "Millimeter-wave 60 GHz Outdoor and Vehicle AOA Propagation Measurements using a Broadband Channel Sounder," in *2011 IEEE Global Telecommunications Conference - GLOBECOM 2011*, Houston: IEEE, Dec. 2011, pp. 1–6. doi: 10.1109/GLOCOM.2011.6133581.
- [64] Y. Lyu, A. W. Mbugua, Z. Yuan, K. Olesen, and W. Fan, "Design and Validation of a Multilink Phase-Compensated Long-Range Ultrawideband VNA-Based Channel Sounder," *IEEE Trans Microw Theory Tech*, vol. 70, no. 10, pp. 4528–4543, Oct. 2022, doi: 10.1109/TMTT.2022.3194045.
- [65] A. W. Mbugua, W. Fan, Y. Ji, and G. F. Pedersen, "Millimeter wave multi-user performance evaluation based on measured channels with virtual antenna array channel sounder," *IEEE Access*, vol. 6, pp. 12318–12326, Mar. 2018, doi: 10.1109/ACCESS.2018.2812304.
- [66] W. Fan, Z. Yuan, Y. Lyu, and G. F. Pedersen, "Enabling VNA Based Channel Sounder for 6G Research: Challenges and Solutions," in *Proceedings of 18th European Conference on Antennas and Propagation (EuCAP)*, Glasgow: IEEE, Mar. 2024. doi: 10.23919/EuCAP60739.2024.10501372.
- [67] L. Carslake, J. Skinner, and H. Loh, "Design and Preliminary Indoor Assessment of a Long-Range sub-THz VNA-Based Channel Sounder between 500 GHz and 750 GHz," in *Proceedings of 18th European Conference on Antennas and Propagation (EuCAP)*, Glasgow: IEEE, Mar. 2024. doi: 10.23919/EuCAP60739.2024.10501496.
- [68] R. J. Pirkl and G. D. Durgin, "Optimal sliding correlator channel sounder design," *IEEE Trans Wirel Commun*, vol. 7, no. 9, pp. 3488–3497, Sep. 2008, doi: 10.1109/TWC.2008.070278.
- [69] C. U. Bas *et al.*, "Real-Time Millimeter-Wave MIMO Channel Sounder for Dynamic Directional Measurements," in *IEEE Transactions on Vehicular Technology*, Institute of Electrical and Electronics Engineers Inc., Sep. 2019, pp. 8775–8789. doi: 10.1109/TVT.2019.2928341.
- [70] C. U. Bas *et al.*, "A Real-Time Millimeter-Wave Phased Array MIMO Channel Sounder," in *2017 IEEE 86th Vehicular Technology Conference (VTC-Fall)*, Toronto: IEEE, Sep. 2017, pp. 1–6. doi: 10.1109/VTCTFall.2017.8287875.
- [71] X. Yin, X. Chu, J. Chen, and Z. Zhong, "Performance Evaluation of A Hybrid-beamforming Sounder for 26 GHz Channel Measurements," in *2017 IEEE 86th Vehicular Technology Conference (VTC-Fall)*, Toronto: IEEE, Sep. 2017, pp. 1–5. doi: 10.1109/VTCTFall.2017.8287895.
- [72] G. R. MacCartney and T. S. Rappaport, "A flexible millimeter-wave channel sounder with absolute timing," *IEEE Journal on Selected Areas in Communications*, vol. 35, no. 6, pp. 1402–1418, Jun. 2017, doi: 10.1109/JSAC.2017.2687838.
- [73] Ó. Seijo, I. Val, and J. A. López-Fernández, "Portable Full Channel Sounder for Industrial Wireless Applications With Mobility by Using Sub-Nanosecond Wireless Time Synchronization," *IEEE Access*, vol. 8, pp. 175576–175588, 2020, doi: 10.1109/ACCESS.2020.3025896.
- [74] M. Li, R. Ma, and N. Behdad, "A compact, low-cost, ultrawideband direction-finding system: Techniques suitable for small-aperture designs," *IEEE Antennas Propag Mag*, vol. 60, no. 6, pp. 32–44, Dec. 2018, doi: 10.1109/MAP.2018.2870641.
- [75] R. Takahashi, G. Anirban, and M. Kim, "Double-Directional Angle-Resolved Wideband Channel Measurements and Path Loss Characterization in Corridor at 300 GHz," in *Proceedings of 18th European Conference on Antennas and Propagation (EuCAP)*, Glasgow: IEEE, Mar. 2024. doi: 10.23919/EuCAP60739.2024.10501117.

- [76] S. Kurokawa, M. Ameya, and M. Hirose, "Millimeter wave vector measurement system using low frequency band oscilloscope," in *Proceedings of 18th European Conference on Antennas and Propagation (EuCAP)*, Glasgow: IEEE, Mar. 2024. doi: 10.23919/EuCAP60739.2024.10501278.
- [77] M. Inomata *et al.*, "Sub-Terahertz MassiveMIMO Channel Sounder for 6G Mobile Communication Systems," in *Proceedings of 18th European Conference on Antennas and Propagation (EuCAP)*, Glasgow: IEEE, Mar. 2024. doi: 10.23919/EuCAP60739.2024.10501562.
- [78] D. Caudill, P. B. Papazian, C. Gentile, J. Chuang, and N. Golmie, "Omnidirectional Channel Sounder with Phased-Array Antennas for 5G Mobile Communications," *IEEE Trans Microw Theory Tech*, vol. 67, no. 7, pp. 2936–2945, Jul. 2019, doi: 10.1109/TMTT.2019.2910109.
- [79] M. Kim, S. Tang, and K. Kumakura, "Fast Double-Directional Full Azimuth Sweep Channel Sounder Using Low-Cost COTS Beamforming RF Transceivers," *IEEE Access*, vol. 9, pp. 80288–80299, 2021, doi: 10.1109/ACCESS.2021.3085325.
- [80] J. Hejselbak, J. O. Nielsen, W. Fan, and G. F. Pedersen, "Measured 21.5 GHz Indoor Channels with User-Held Handset Antenna Array," *IEEE Trans Antennas Propag*, vol. 65, no. 12, pp. 6574–6583, Dec. 2017, doi: 10.1109/TAP.2017.2742556.
- [81] P. Zhang *et al.*, "A Modular COTS-based High-Efficient Sub-THz Channel Sounder and Experimental Validations," in *Proceedings of 18th European Conference on Antennas and Propagation (EuCAP)*, Glasgow: IEEE, Mar. 2024. doi: 10.23919/EuCAP60739.2024.10501693.
- [82] J. Hu, A. Al-Jzari, and S. Salous, "Indoor Channel Characterization Based on Directional Measurements at 140 GHz," in *Proceedings of 18th European Conference on Antennas and Propagation (EuCAP)*, Glasgow: IEEE, Mar. 2024. doi: 10.23919/EuCAP60739.2024.10501502.
- [83] B. Wu, H. Mou, H. Yang, Z. Guo, X. Zou, and X. Gao, "E-Band Measured Propagation Characteristics for Urban Backhaul Communications," in *Proceedings of 18th European Conference on Antennas and Propagation (EuCAP)*, Glasgow: IEEE, Mar. 2024. doi: 10.23919/EuCAP60739.2024.10501018.
- [84] G. Chen, P. Yang, F. Lin, and K. Mouthaan, "X-Band Receiving Phased Array with Digital Beamforming Using RFSoc," in *Proceedings of 18th European Conference on Antennas and Propagation (EuCAP)*, Glasgow: IEEE, Mar. 2024. doi: 10.23919/EuCAP60739.2024.10501000.
- [85] V. Ariyaratna, A. Madanayake, and J. M. Jornet, "Toward Real-Time Software-Defined Radios for Ultrabroadband Communication Above 100 GHz [Application Notes]," *IEEE Microw Mag*, vol. 24, no. 8, pp. 50–59, Aug. 2023, doi: 10.1109/MMM.2023.3277362.
- [86] A. Sayeed *et al.*, "A Framework for Developing and Evaluating Algorithms for Estimating Multipath Propagation Parameters from Channel Sounder Measurements," *IEEE Trans Wirel Commun*, 2023, doi: 10.1109/TWC.2023.3318532.
- [87] R. Wang, O. Renaudin, C. U. Bas, S. Sangodoyin, and A. F. Molisch, "On channel sounding with switched arrays in fast time-varying channels," *IEEE Trans Wirel Commun*, vol. 18, no. 8, pp. 3843–3855, Aug. 2019, doi: 10.1109/TWC.2019.2919023.
- [88] Y. S. Yeh and B. A. Floyd, "Multibeam Phased-Arrays Using Dual-Vector Distributed Beamforming: Architecture Overview and 28 GHz Transceiver Prototypes," *IEEE Transactions on Circuits and Systems I: Regular Papers*, vol. 67, no. 12, pp. 5496–5509, Dec. 2020, doi: 10.1109/TCSI.2020.3026624.
- [89] D. Caudill, J. Chuang, S. Y. Jun, C. Gentile, and N. Golmie, "Real-Time mmWave Channel Sounding through Switched Beamforming with 3-D Dual-Polarized Phased-Array Antennas," *IEEE Trans Microw Theory Tech*, vol. 69, no. 11, pp. 5021–5032, Nov. 2021, doi: 10.1109/TMTT.2021.3104278.
- [90] Z. Ying, K. Zhao, E. Bengtsson, H. Tataria, and F. Tufvesson, "Design of Switched Antenna Arrays for a 28 GHz Propagation Channel Sounder," in *2020 IEEE International Symposium on*

- Antennas and Propagation and North American Radio Science Meeting, IEEECONF 2020 - Proceedings*, Institute of Electrical and Electronics Engineers Inc., Jul. 2020, pp. 55–56. doi: 10.1109/IEEECONF35879.2020.9329997.
- [91] G. Crupi *et al.*, “Nonlinear modeling of GaAs pHEMTs for millimeter-wave mixer design,” *Solid State Electron*, vol. 104, pp. 25–32, 2015, doi: 10.1016/j.sse.2014.11.001.
- [92] R. Levinger *et al.*, “High-Performance E-Band Transceiver Chipset for Point-to-Point Communication in SiGe BiCMOS Technology,” in *IEEE Transactions on Microwave Theory and Techniques*, Institute of Electrical and Electronics Engineers Inc., Apr. 2016, pp. 1078–1087. doi: 10.1109/TMTT.2016.2528981.
- [93] P. K. Saha, D. C. Howard, S. Shankar, R. Diestelhorst, T. England, and J. D. Cressler, “A 6-20 GHz adaptive SiGe image reject mixer for a self-healing receiver,” *IEEE J Solid-State Circuits*, vol. 47, no. 9, pp. 1998–2006, 2012, doi: 10.1109/JSSC.2012.2201284.
- [94] N. Mazor *et al.*, “Highly Linear 60-GHz SiGe Downconversion/Upconversion Mixers,” *IEEE Microwave and Wireless Components Letters*, vol. 27, no. 4, pp. 401–403, Apr. 2017, doi: 10.1109/LMWC.2017.2678426.
- [95] H. Li *et al.*, “Compact low-power 154 GHz receiver front-end in 0.13 μm SiGe BiCMOS,” *IET Microwaves, Antennas and Propagation*, vol. 14, no. 9, pp. 955–959, Jul. 2020, doi: 10.1049/iet-map.2019.0511.
- [96] J. M. Song, V. S. Trinh, S. Kim, and J. D. Park, “275 GHz Quadrature Receivers for THz-Band 6G Indoor Network in 130-nm SiGe Technology,” *IEEE Access*, vol. 11, pp. 138540–138548, 2023, doi: 10.1109/ACCESS.2023.3340023.
- [97] I. K. Aksoyak, M. Mock, and A. C. Ulusoy, “A Highly Linear D-Band I/Q Receiver With Active Mixer-First Architecture in SiGe Technology,” *IEEE Trans Microw Theory Tech*, 2023, doi: 10.1109/TMTT.2023.3328481.
- [98] D. Lal, M. Abbasi, and D. S. Ricketts, “A Broadband, Compact 140-170GHz Double-Side-Band Receiver in 90nm SiGe Technology,” in *Proceedings of the 46th European Microwave Conference*, London: IEEE, Oct. 2016, pp. 687–690. doi: 10.1109/EuMC.2016.7824436.
- [99] D. Lee *et al.*, “24-40 GHz mmWave Down-Conversion Mixer with Broadband Capacitor-Tuned Coupled Resonators for 5G New Radio Cellular Applications,” *IEEE Access*, vol. 10, pp. 16782–16792, 2022, doi: 10.1109/ACCESS.2022.3149311.
- [100] Y. Y. Wang, H. Duan, L. He, X. Wu, D. Wang, and L. Li, “Design of 39-GHz Up and Down-Conversion Mixers for 5G mmWave TDD Applications,” *Journal of Electromagnetic Engineering and Science*, vol. 23, no. 2, pp. 101–108, 2023, doi: 10.26866/jees.2023.2.r.149.
- [101] B. Bae, J. Jeong, S. Kim, J. Lee, K. Kwon, and J. Han, “24-40 GHz Dual-Band Highly Linear CMOS Up-Conversion Mixer for mmWave 5G NR FR2 Cellular Applications,” *IEEE Microwave and Wireless Components Letters*, vol. 32, no. 8, pp. 999–1002, Aug. 2022, doi: 10.1109/LMWC.2022.3161092.
- [102] “<https://www.sheffield.ac.uk/mm-wave/futuremmwave/downloads-pcb-design-files>.”
- [103] National Spectrum Centre, “<https://www.spectrum.aber.ac.uk/>.”
- [104] R. Zhang, S. Wang, Z. Zhong, J. Zhao, and B. Li, “Multipath DoA Estimation by Rotational Invariance on Array Channel Impulse Response,” *IEEE Antennas Wirel Propag Lett*, vol. 15, pp. 964–967, 2016, doi: 10.1109/LAWP.2015.2486624.
- [105] R. Zhang, S. Wang, X. Lu, W. Duan, and L. Cai, “Two-Dimensional DoA Estimation for Multipath Propagation Characterization Using the Array Response of PN-Sequences,” *IEEE Trans Wirel Commun*, vol. 15, no. 1, pp. 341–356, Jan. 2016, doi: 10.1109/TWC.2015.2473156.
- [106] M. R. J. A. E. Kwakkernaat, Y. L. C. de Jong, R. J. C. Bultitude, and M. H. A. J. Herben, “High-resolution angle-of-arrival measurements on physically-nonstationary mobile radio

- channels," *IEEE Trans Antennas Propag*, vol. 56, no. 8 II, pp. 2720–2729, 2008, doi: 10.1109/TAP.2008.927513.
- [107] J. Chuang, J. Senic, C. Liu, C. Gentile, S. Y. Jun, and D. Caudill, "Blind Calibration of Phase Drift in Millimeter-Wave Channel Sounders," *IEEE Access*, vol. 8, pp. 109557–109567, 2020, doi: 10.1109/ACCESS.2020.3001852.
- [108] T. S. Rappaport *et al.*, "Wireless communications and applications above 100 GHz: Opportunities and challenges for 6g and beyond," *IEEE Access*, vol. 7, pp. 78729–78757, 2019, doi: 10.1109/ACCESS.2019.2921522.
- [109] J. M. Eckhardt *et al.*, "Uniform Analysis of Multipath Components From Various Scenarios With Time-Domain Channel Sounding at 300GHz," *IEEE Open Journal of Antennas and Propagation*, vol. 4, pp. 446–460, 2023, doi: 10.1109/OJAP.2023.3263597.
- [110] A. Ghosh and M. Kim, "THz Channel Sounding and Modeling Techniques: An Overview," *IEEE Access*, vol. 11, pp. 17823–17856, 2023, doi: 10.1109/ACCESS.2023.3246161.